Syracuse University

SURFACE

The Role of Fluorescence and Human Factors in Quantitative Transdermal Blood and Tissue Analysis Using NIR Raman Spectroscopy

Bin Deng
Syracuse University

Follow this and additional works at: https://surface.syr.edu/bce_etd

Part of the Biomedical Engineering and Bioengineering Commons

ABSTRACT

The Role of Fluorescence and Human Factors
in Quantitative Transdermal Blood and Tissue Analysis
Using NIR Raman Spectroscopy

Bin Deng
Syracuse University, August 2012

This research is part of an ongoing project aimed at the application of combined near infrared (NIR) Raman and fluorescence spectroscopy to noninvasive *in vivo* blood analysis including but not limited to glucose monitoring. Coping with practicalities of human factors and exploring ways to obtain and use knowledge gained about autofluorescence to improve algorithms for blood and tissue analysis are the general goals of this research. Firstly, the study investigated the various sources of human factors pertinent to our concerns, such as fingerprints, turgor, skin hydration and pigmentation. We then introduced specialized *in vivo* apparatus including means for precise and reproducible placement of the tissues relative to the optical aperture, i.e., the position detector pressure monitor (PDPM). Based on solid instrumental performances, appropriate methodology is now provided for applying and maintaining pressure to keep surface tissues immobile during experiments while obtaining the desired blood content and flow. Secondly, *in vivo* human fingertip skin autofluorescence photobleaching under 200 mW 830 nm NIR irradiation is observed and it is characterized that: i) the majority of the photobleached fluorescence originates from static tissue not blood, ii) the bleaching (1/e point) occurs in 10^1-10^2 sec timescale, and also iii) a photobleached region remains bleached for at least 45 min but recovers completely within several hours. A

corresponding extensive but not exhaustive *in vitro* systematic study narrowed down the major contributors of such fluorescence and bleaching to collagen, melanin, plasma and hemoglobin: two major static tissue constituents and two major blood proteins. Thirdly, we established that measuring the inelastic and elastic emissions simultaneously leads to a sensitive probe for volume changes of both red blood cells and plasma. An algorithm based on measurements obtained while performing research needed for this thesis, as well as some empirical calibration approaches, was presented. The calibrated algorithm showed real potential to track hematocrit variations in cardiac pulses, centrifugal loading, blood vessel blockage using tourniquet, and even during as subtle an occurrence as in a Valsalva maneuver. Finally, NIR fluorescence and photochemistry of pentosidine, a representative of the advanced glycation endproducts (AGEs) which accumulate with age and hyperglycemia, was studied. The results indicate that oxygen plays a pivotal role in its photobleaching process. We hypothesized and offered proofs showing that pentosidine is a $^1O_2$ sensitizer that is also subject to attack by the $^1O_2$ resulting in the photobleaching that is observed when probing tissue using NIR. The photobleaching reaction is kinetically first order in pentosidine and ground state oxygen, and *in vivo* effectively first order with NIR irradiation also.

Syracuse University

The Role of Fluorescence and Human Factors
in Quantitative Transdermal Blood and Tissue Analysis
Using NIR Raman Spectroscopy

by

Bin Deng

B.S. Tianjin University, Tianjin, China 2004
M.S. Tianjin University, Tianjin, China 2007

Dissertation

Submitted in partial fulfillment of the requirements for the degree of
Doctor of Philosophy in Bioengineering

Syracuse University
August 2012

Dedicated to my parents,

Aiqin Cao and Lintong Deng,

for their unconditional love and continuous support

ACKNOWLEDGEMENTS

Sunshine in the summer time of upstate New York is gorgeous and I could not feel better to finish my five years of doctoral study in my favorite season of Syracuse. Along this fantastic journey there are many unforgettable moments I share with people who have helped, encouraged, and advised me. No truer words have ever been penned. And I would like to express my tremendous gratitude to those who have contributed to the final delivery of this thesis.

First and foremost, my utmost appreciation to my advisor, Prof. Joseph Chaiken, whose guidance and support from the beginning to the end I will never forget. Joe is not only the advisor who inspires and enlightens me as I hurdle all the obstacles in completion of this research, but also the mentor whose work ethics motivate me to be a better person. I am grateful that he lets me take initiative in research, respects my input into the project, and treats me like a colleague not a mere student. I appreciate his complete trust, confidence and belief in me which means more than words could express.

I am thankful to Prof. Julie Hasenwinkel for her continuous help and advice during my pursuit of doctoral degree. Prof. Patrick Mather is a role model, for I see in him a successful combination of science and artistic genius whose personality I greatly admire. I thank Prof. Jerry Goodisman for his belief and long-term constructive participation in this project. I am grateful to Prof. Daniel Clark for helping us understand the AGE chemistry. Prof. Rebecca Bader always reminds me the importance of a cheerful and positive attitude toward both life and career. I appreciate Prof. Gus Engbretson for

introducing me to this wonderful journey in Syracuse University and I am thankful for his guidance, confidence and trust in me.

I am especially grateful for the funding from LighTouch Medical Inc., the trust and support of Mr. Donald Schmucker, and the opportunity to work with the experienced "young" doctor Mr. George Shaheen, whose insightful opinions have always been the inspiration and fountain of new thoughts. It has been a great pleasure and honor to work with the sophisticated and experienced engineers in Critical Link LLC and mechanists in Physics Department Machine Shop.

I feel blessed to have so many dearest friends around. I want to thank my ex-roomies Yi Shi and Qianqian Cao for bringing me joy and certainty, and your support and care helped me overcome setbacks. I feel lucky to have two joyful souls, my roomies Yiqing Zhang and Hui Gong, who accompanied me through the most stressful time of writing up my dissertation. I am thankful to Erika Rodriguez and miss those days when we studied, ate, volunteered and almost did everything together. I want to thank Tarun Saxena for all the discussions on research, science, books; you awoke my thirst for reading. It is simply impossible to name everyone but my deepest gratitude is sent wherever you are. I also appreciate the help from these excellent undergraduates: Colin Wright, Anabel Simental, Ruben Guadalupe and Patrick Lutz.

Last but not the least, I would like to give my special thanks to my amazing parents for their unconditional love and support to me. I feel so blessed to have such understanding parents like them who believe in me and set me free to pursue my dream. You always say I make you proud, but I would like to say that I could not be more proud to have you, my dearest mom and dad!

TABLE OF CONTENTS

LIST OF SYMBOLS AND ACRONYMS

ADA   American Diabetes Association

AGEs   advanced glycation endproducts

ANSI   American National Standards Institute

ARF   acute respiratory failure

BP   blood pressure

BV   blood volume

CCD   charge-coupled device

CML   N-carboxy-methyl lysine

COPD   chronic obstructive pulmonary disease

CW   continuous wave

DI   de-ionized water

EE   elastic scattering emission

ET   electron transfer

FDA   U.S. Food and Drug Administration

GUI   graphical user interface

Hb	hemoglobin
HbA1c	hemoglobin A1c
Hct	hematocrit
HFs	human factors
HMI	human-machine interface
HPFS	high purity fused silica
IACUC	Institutional Animal Care and Use Committee
ICP	intracranial pressure
ICU	intensive care unit
IRB	Institutional Review Board
ISC	intersystem crossing
ISF	interstitial fluid
IE	inelastic scattering emission
LED	light emitting diode
MAP	mean arterial pressure
MIR	mid-infrared
NAD	nicotinamide adenine dinucleotiede

NADH	nicotinamide adenine dinucleotiede (reduced form)
NAS	net analyte signal
NICU	neurotrauma intensive care unit
NIH	U.S. National Institutes of Health
NIR	near infrared
OCT	optical coherence tomography
OPE	one photon excitation
PBS	phosphate buffered saline
PDPM	position detector pressure monitor
PLS	partial least square
POCT	point-of-care testing
QE	quantum efficiency
R&D	research and development
RBCs	red blood cells
RTE	radiation transfer equation
SNR	signal-to-noise ratio
SOSG	singlet oxygen sensor green

SOSG-EP	singlet oxygen sensor green – endoperoxide
TM	tissue modulator
TMX	tri-mixture of lysine, arginine and ribose
TPE	two photon excitation
TTA	triplet-triplet annihilation
UV/Vis	ultraviolet/visible
$^1O_2$	singlet oxygen (excited state)
$^3O_2$	triplet oxygen (ground state)

LIST OF FIGURES

LIST OF TABLES

1. INTRODUCTION

1.1 Motivation for Noninvasive Blood Analytes Monitoring

Today the physical principles behind the most common "state-of-the-art" medical instruments can be traced back decades with the main differences between the "old" and "new" devices entailing differences in the degree of automation involved. Such differences mostly affect the degree to which operating the devices are physical labor intensive, produce measurements that can be interpreted by less highly trained medical practitioners, e.g., medical assistants, or can be networked in order to interface with existing or planned patient telemetry systems. Essentially the current paradigms of medical practice conventional laboratorial tests provide sufficient accuracy and specificity to facilitate clinical diagnosis and treatment. But there are always increasingly challenging demands for new and improved medical products.

For example in these times, in acknowledgment of the benefits of earlier diagnosis and more prompt treatment, doctors and scientists are looking forward to subsequent rounds of innovation. Minimal or noninvasive approaches to decrease stress and discomfort, continuous monitoring to facilitate better disease control and therapy management, and transportable or portable test kits to support point-of-care testing (POCT) are a few examples of newly posed challenges in the medical device research and development (R&D) community. Triggered by these, we set out seeking spectroscopic applications in noninvasive continuous monitoring medical devices, especially those offering blood analyte information.

As a specialized transportation vehicle between cells and tissues, blood contains enormous critical health related information. Usually, blood is sampled through arterial puncture, indwelling arterial catheters, venous blood draw or fingerpricks, and then sent for lab test. These procedures suffer from drawbacks such as being clumsy during surgery, having insufficient monitoring capability, as well as providing delayed feedback. Therefore, such conventional laboratory techniques should certainly be improved in cases where blood analytes information could indicate life-threatening conditions.

For example, in neurotrauma intensive care unit (NICU) the cardiopulmonary monitoring of blood pH and bicarbonate concentration is particularly vital to high intracranial pressure (ICP) patients as an indicator of airway, breathing and oxygenation (1). Blood bicarbonate is also a critical diagnostic parameter for acute respiratory failure (ARF) among chronic obstructive pulmonary disease (COPD) patients (2). In another extreme scenario, internal hemorrhage after traumatic injuries, such as in the case of car accidents and battlefield wounds, is well documented to be one of the most avoidable common causes of death for all people between 18 and 45 years old (3, 4). However, as research has shown, the delay in pre-hospital and in-hospital hemorrhage control is the primary contributor to potential preventability (5, 6). A timely screening showing the existence and location of any hidden internal bleeding before the patient is transported to ICU will undoubtedly favor the rescuing of a life.

As examples speak for themselves, a *noninvasive* continuous fast *in-situ* blood analytes monitoring system is in immediate need. Having drawn the attention of many scientists, optical and spectroscopic methods are perhaps the most promising to achieve such a goal. By solving the so-called "inverse problem" for the radiation transfer equation

(RTE), Tuchin et al. (7-9) from Saratov State University modeled the propagation of light in turbid media, i.e., human tissue, thereby modeling the production of elastic emission (EE, including Rayleigh/Mie) that can be detected experimentally. The reasonable agreement between experiment and theoretical calculation suggests that such a treatment accurately and precisely describes the average propagation and production of externally observable, e.g., EE and fluorescence and Raman scattered light. Further, Chaiken and Goodisman (10) exploited this in order to calculate the EE in their unique probing geometry. This will be revisited in Section 3.3 of Chapter 3 in the context of testing the new algorithm for measuring hematocrit (Hct) in blood.

As shown in Figure 1-1, human tissue is relatively "transparent" in the near infrared (NIR) spectral range which gives us several "optical windows" (11-14) allowing NIR light to penetrate up to several hundred microns into the skin. However, chance or false correlations due to confounding factors and broad overlapping bands of NIR absorption spectra have largely limited its use in noninvasive *in vivo* monitoring. To address this obstacle, Arnold's group (15, 16) from the University of Iowa started in early 1990s using multivariate chemometrics, e.g., partial least square (PLS) and net analyte signal (NAS), to eliminate such influence.
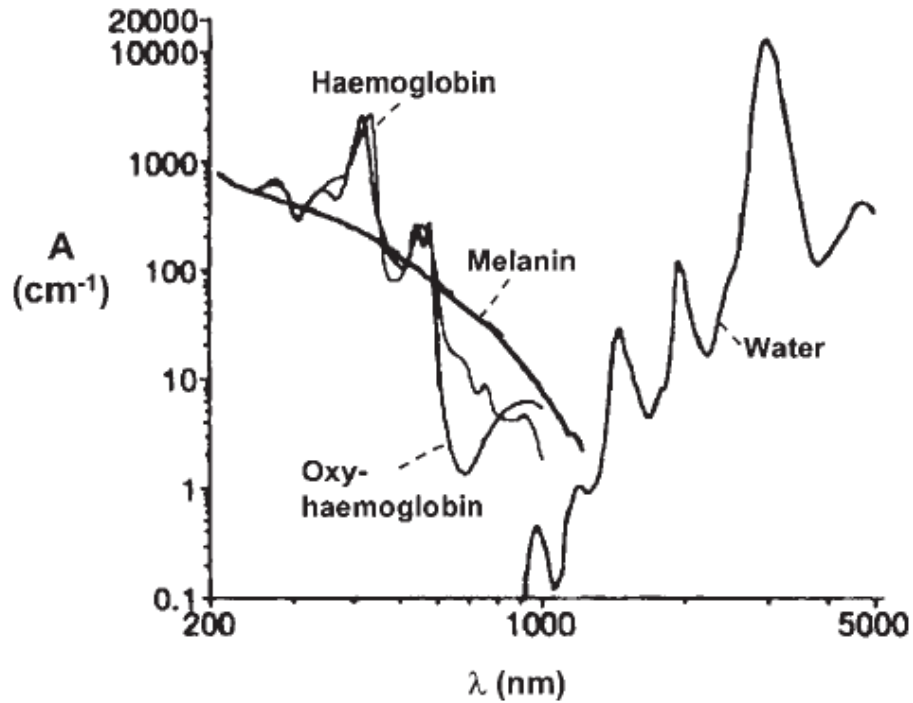
Figure 1-1: Principal light-absorbing molecules in the skin. Redrawn from Anderson (14). The most penetrating wavelengths are from 600 to 1300 nm, the so-called "optical window" of the skin.

Meanwhile, varieties of optical and spectroscopic approaches have been adopted to study wide range of medical applications. Puppels et al. from Erasmus Medical College Netherlands has applied Raman spectroscopy and microscopy in rapid identification of pathogenic microorganisms (17), determination of atherosclerotic plaque composition (18, 19), and discrimination of healthy (20, 21) and cancerous tissues (22). The Feld group from MIT has used endoscopic and optical tomography to image and diagnose cancer in addition to noninvasive blood analysis, e.g., glucose (23-25). The Michael Morris group from University of Michigan – Ann Arbor has done instrumentation (26) to analyze mineral composition and related progressive bone diseases (27, 28). The biomedical photonics lab from Vanderbilt University led by Prof. Anita Mahadevan-Jansen has

explored the optical imaging and diagnosis of cervical cancer (29), as well as optical stimulation of neural tissues (30, 31).

Most importantly, the aforementioned researches in biomedical optics and spectroscopy are largely depended on the advances in semiconductor, laser, high precision opto-mechanical industries. Major innovations over the past 20 to 25 years involving enabling technologies broke the old technical limits and significantly broadened the applicability of fundamental optical and spectroscopic principles to progressively more complicated problems. Recent advancement of NIR lasers, charge-coupled device (CCD) detectors, compact spectrographs and effective laser rejection filters have increased the instrumental sensitivity by factors as large as 10^5 plus decreased both interferences and noise (32). A revolution of biomedical optics and spectroscopy is on the nearest horizon.

Despite the fact that these various novel techniques have potential to be applied in sensing many physiologically valuable blood analytes, such as bicarbonate, urea, cholesterol and total protein, this project concentrates on noninvasive blood glucose monitoring. Glucose is the most important carbohydrate in biology: a ubiquitous source of energy and especially the *only* source of energy for the brain and nervous system. Because of such importance, whenever the blood glucose is not properly regulated various symptoms can occur. Metabolic homeostasis tightly controls the normal blood glucose level between about 3.6 and 5.8 mM (64.8 and 104.4 mg/dl). Sudden hypoglycemia (low blood sugar) hits the nervous system first and triggers drowsiness or impaired cognitive function. In severe glucose deficiency, temporary memory loss, and even fatal condition like coma could happen. In the short term, it is far more dangerous to

have too little glucose than too much. However in some diseases, diabetes mellitus for example, hyperglycemia (high blood sugar) can be chronic. Diabetes itself is not immediately lethal, but most diabetic patients actually die from the complications caused by this continuous elevated blood sugar such as cardiovascular disease, chronic renal failure, retinal damage, and neuropathy.

So far, diabetes is a serious disease that strikes 25.8 million, or 8.3% of the population in the United States, according to the American Diabetes Association (ADA) (33). Meticulous regulation of insulin intake based on intensive self-monitoring of the blood glucose concentration is still the first recommended tactic for management of diabetes mellitus by ADA. By far, the most widely adopted blood glucose self-monitoring technique is the U.S. Food and Drug Administration (FDA) approved finger stick capillary blood sampling method. However, few patients can comply with the recommended 5 to 6 measurements per day consistently using this painful and infection-risky approach. Even healthy people who might want to take some tests for prevention's sake are deterred. Sadly the truth is that early diagnosis has unfortunately been consistently overlooked and it plays a critical part in successful treatment and delaying or preventing some of the complications of diabetes. People's reluctance to endure extra pain and handle blood contributes to the failure of early diagnosis, leaving 27% of diabetes undiagnosed until it is too late.

Under the industry's current standard for point-of-care meters, readings may error up to 20% from standardized concentrations of 75 mg/dL or less. That means a meter reading of normoglycemia may actually be a failure to diagnose hypoglycemia, which as mentioned earlier is a very severe and dangerous situation, and serious consequences may

occur. Although those meters are considered home-use or over the counter *in vitro* diagnostic devices, some have been used professionally as a substitute for standardized plasma glucose measurements in clinical settings. Therefore, FDA is not satisfied with the performance of current commercial glucose meters and is recently considering tightening the standards. It is a challenge for the conventional finger stick meters, and also a chance for new technologies to step in.

The aforementioned opportunities and challenges comprise the motivations for the current project of utilizing combined Raman and fluorescence spectroscopy in the development of a noninvasive *in vivo* glucose monitoring system to assist in diabetes therapy.

1.2 Contemporary Technologies

The commercial opportunity, as well as the advancement in bio-optical technologies, drives the development of noninvasive blood glucose monitoring devices (34, 35). Table 1-1 lists the most popular contemporary technologies that have been adopted in pursuit this ultimate goal. However, in order to get FDA approval *as a substitute for finger stick meters*, noninvasive devices must provide straightforward glucose information from blood, rather than any other indirect information, e.g., interstitial fluid (ISF) glucose concentration. Therefore, products based on micro needle fluid harvesting, ocular spectroscopy and iontophoresis, which do not obtain a glucose measurement directly from blood, will have to face the public doubt concerning use of ISF or tear glucose as a substitute for blood glucose (36, 37). For other electrical signal based technologies, such

as electromagnetic sensing and impedance spectroscopy, their measuring precision can easily be influenced by minor temperature fluctuation (35). Similarly, thermal spectroscopy cannot work under physiological or pathological conditions which would also induce temperature variations (38).

Table 1-1: Contemporary noninvasive or minimal invasive blood glucose monitoring techniques – their underline principles and limitations.

TECHNIQUE	PRINCIPLE	LIMITATIONS
NIR	750 – 2500 nm absorption	Strong water absorption
MIR	2500 – 10000 nm absorption	Poor penetration
OCT	Interferometric signal	Motion sensitive
Raman	Laser induced	Confounding factors
Polarization change	Chiral molecule	Scattering depolarization
Ultrasound	Photoacoustic	Sensitive to environment
Fluorescence	Fluorescence intensity	Ultraviolet excitation
Thermal	Different approaches	Pathological temp change
Ocular	Chemical bond	Glucose in tears
Impedance	C_{Na}^+ & C_K^+ change	Various hydration status
Electromagnetic	Dielectric parameters	Temperature sensitive
Fluid harvesting	Microscopic holes	Glucose in ISF
Iontophoresis	Glucose transportation	Skin irritation, sweating

Major technological and scientific innovations over the past several decades have significantly broadened the applicability of spectroscopy in exploring this challenging project. Among all the optical and spectroscopic approaches, Raman spectroscopy is one of the most intensively explored technique (20, 23, 39, 40). As stated earlier in Section

8

1.1, in NIR spectral range, human tissue is relatively "transparent" which gives us several "spectral windows" (11, 12) to allow more light to penetrate into the tissue. For example, the penetration depth of the in-house LighTouch[TM] device is about 600 μm, which is deep enough to shed light on the epidermis and superficial part of dermis layer where the blood perfusion is acceptable (3 to 5%) particularly in fingertips (41-43). Furthermore, fundamental vibrations observed by Raman are sharper and have less overlap with other bands from the same and other molecules compared with NIR absorption or "diffuse reflectance" bands that predominantly involve overtones and combinations. Water, protein and lipids all have badly overlapping absorption bands in the NIR absorption spectra. But water, comprising 60% of body weight and 95% of blood (44), has a very small Raman cross section.

Nevertheless, major challenges for Raman spectroscopy include the presence of a strong background fluorescence signal and inherently low signal-to-noise ratios (SNR) (32). In general, the quantitative detection limit for spontaneous Raman scattering technology is roughly 10^{-3} M. However, the physiological glucose concentration, even for the hypoglycemic patient, is rarely less than about 2.3 mM. Our lab, from 1998 to recent years, published a sequence of papers (45-51) on the development of a novel tissue modulated NIR Raman spectrometer and in those cases demonstrated a detection limit of about 4.45 mM with a precision of 1.22 mM *in vivo* (50). These specifications are comparable to existing finger stick technology but better performance is possible.

1.3 Tissue Modulated Raman Spectroscopy

Transdermal *in vivo* spectroscopic analysis or imaging of tissue analysis involving NIR excitation always produces some broadband NIR fluorescence that, depending on what spectroscopy is being employed, can degrade SNR and dynamic range. Hardware and software have been devised to perform wavelength shifting, time gating, frequency domain first- and second- order derivatives, and simple or modified polynomial curve fitting (52, 53) for the purpose of fluorescence suppression. However, their implementation either relies on spurious assumptions, laborious spectroscopic system modification or user intervention, which makes them less reliable, time consuming and less commercially viable.

Tissue modulation as a methodology attempts to obtain more information in a measurement cycle and the measurement cycle is designed specifically for differentiating blood information from that of static tissue *in vivo*. Properly executed modulated spectra can reduce the fluorescence contribution to closer to that of the Raman contribution and also provide information bearing on the physiology of the probed tissue. As shown in Figure 1-2, tissue modulation is the use of spatiotemporally localized mechanical, thermal, chemical and/or other external influences to manipulate the mobile components, i.e., blood of the probed volume, relative to the static components. Thus, the resulting difference spectra could be used to isolate the spectral features of blood components from those of static tissues. The idea behind this approach is analogous to the difference spectroscopy which is widely adopted in infrared absorption spectroscopy to eliminate background interference and extract a signal of interest.
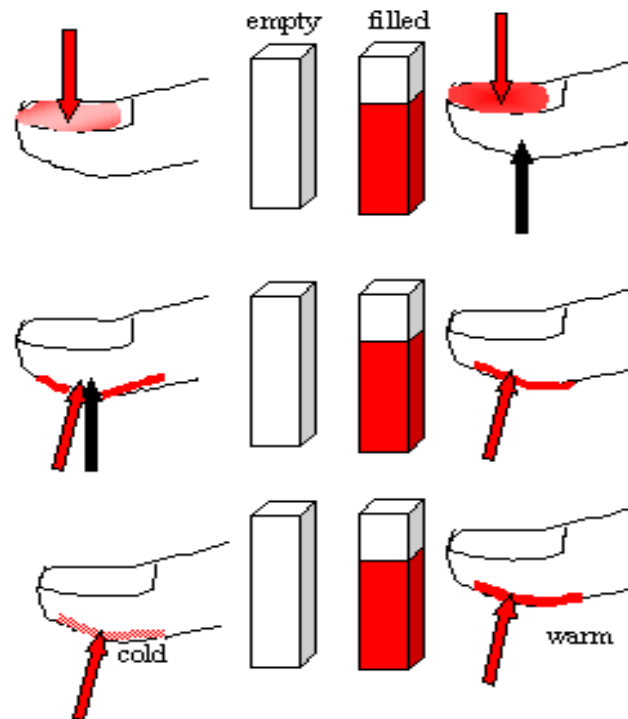
Figure 1-2: Schematic drawing of tissue modulation. Analogous to background subtraction widely used in NIR absorption spectroscopy, the purpose of tissue modulation is to separate the spectrum of blood from that of the surrounding static tissue. (Black arrows indicate the direction of applied pressure; red arrows indicate the direction of excitation/observation.)

Three tissue modulation schemes are shown in Figure 1-2. Top two panels illustrate the pressure modulation, while the bottom panel shows the temperature modulation. Temperature modulation is a slow process (38) since body temperature simply cannot be varied within seconds. And longer experimental time makes the measurement more prone to the influence of human factors. Therefore, this study is based on the pressure modulation scheme shown in the middle panel. *In vivo* the incident light probes the volar side of fingertips and the backward remitted light is collected. When pressure is applied

adjacent to the probed volume as suggested by the black arrow in the middle panel of

Figure 1-2, blood travels from the venous side to outside the probed volume creating an

effect analogous to an "empty cuvette". Therefore, by subtracting spectra with pressure

from the corresponding ones at lower pressure, i.e., a "full cuvette", one can get

differential spectra that manifest the effect of blood on the spectroscopy and tissue optics

of the whole probed volume.

To achieve a successful modulation, the ideal scenario is that in the unpressed part of

the measurement cycle the applied force is well below threshold so that sufficient blood

perfusion is guaranteed and the capillaries can maintain mechanical stability. While in the

pressed part of the tissue modulation cycle the force is only slightly above the threshold

of capillary collapse so that blood is modulated, i.e., moved, but limited deformation is

introduced to static tissue. The difference spectrum will thus contain a minimum

contribution from static tissue and be mostly composed of blood borne Raman and

fluorescence features. This additional contribution to the difference spectrum is due to

different light propagation, i.e., turbidity, because of the modulated blood. This

contribution is calculated using the same algorithm as for hematocrit to be described later

in Section 3.3 of Chapter 3.

1.4 Terminology

In the tissue modulated Raman spectroscopy, there are several terms that will be

frequently repeated in the following context. Therefore, it would be beneficial to make

the terminology clear first before we go in-depth justification and discussion in the

subsequent chapters. Figure 1-3 shows a typical 20 ms frame spectrum of a human volar side of fingertip under 200 mW 830 nm laser exposure. By scrupulously adjusting the laser line rejecting filter to make sure no signal saturation occurs at the Rayleigh line, two piece of separate information could be obtained simultaneously:
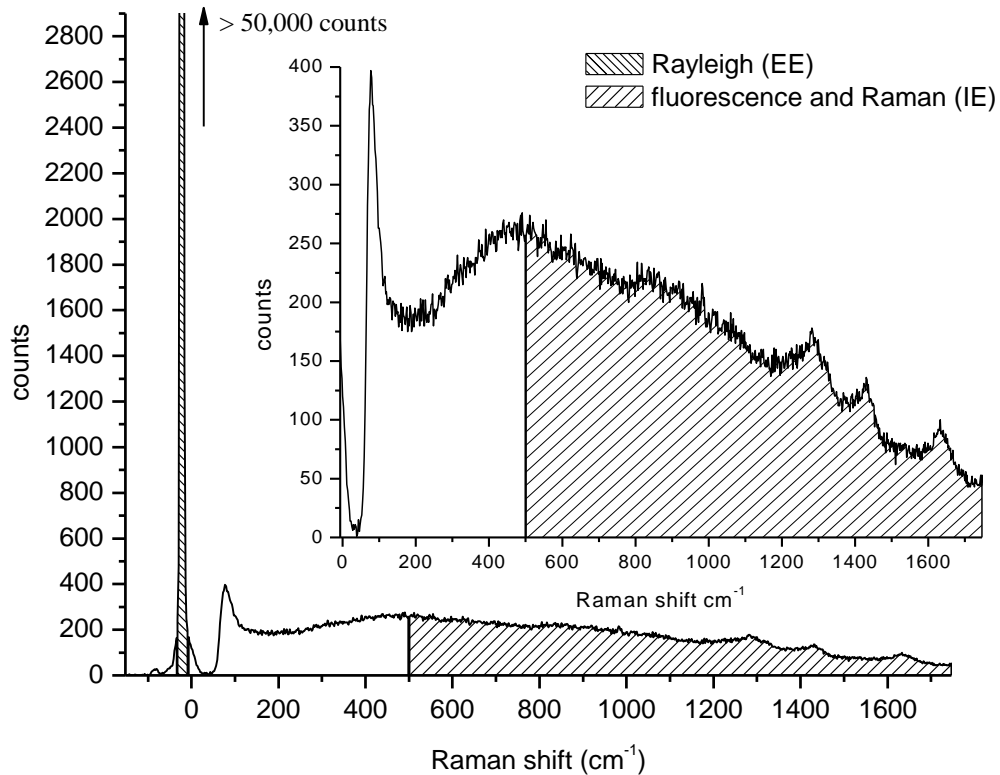
Figure 1-3: Raw typical single 20 ms frame of Andor CCD output for the volar side of human fingertip under 200 mW 830 nm exposure. Shaded areas show the integrals for IE (500 to 1750 cm^{-1}) and EE (-30 to +10 cm^{-1}) respectively. Insert: the same frame on an expanded scale to show the sections of emission integrated to obtain combined fluorescence and Raman emission, i.e., IE.

    i)   The elastically scattered light, or elastic emission (EE), contains only reflected or scattered light that no wavelength shift has occurred. The EE integral covers the Raman shift from -30 to +10 cm^{-1} on a spectrum and the overwhelmingly

majority of it is Rayleigh and Mie scattering light. EE, a probe based on physical optics, provides information relating to the presence and disposition of red blood cells (RBCs) in the probed volume.

ii) The inelastically scattered light, or inelastic emission (IE), is the spectral region that is chosen to exclude as much as possible of the Rayleigh line and off-axis reflected light from the outermost stratum corneum. Based on the current system setup, the Raman shift range from 500 to 1750 cm^{-1} which is comprised of undifferentiated Raman scattering and fluorescence is chosen to represent the IE integral. As a feature of vibronic spectroscopy, IE provides chemically specific and quantitative information concerning molecules in complex mixtures such as blood *in vivo*.

All of the *in vivo* data are exclusively collected using custom LighTouch^{TM} software programmed by Critical Link (Critical Link, LLC, Syracuse, NY, USA). A typical tissue modulated experiment takes 200 sec, however 20, 50 and 100 sec experiments are also performed based on the purpose of a study. The single frame exposure is maintained constant at 20 ms. Thus, for a typical 200 sec experiment ten thousand frames of such 20 ms spectrum like the one shown in Figure 1-3 are collected. Toward the end of each experiment the IE and EE integrals for each frame are calculated and plotted against frame numbers, which are basically the time axis. An example of such IE vs. frame numbers curve is shown in Figure 1-4.
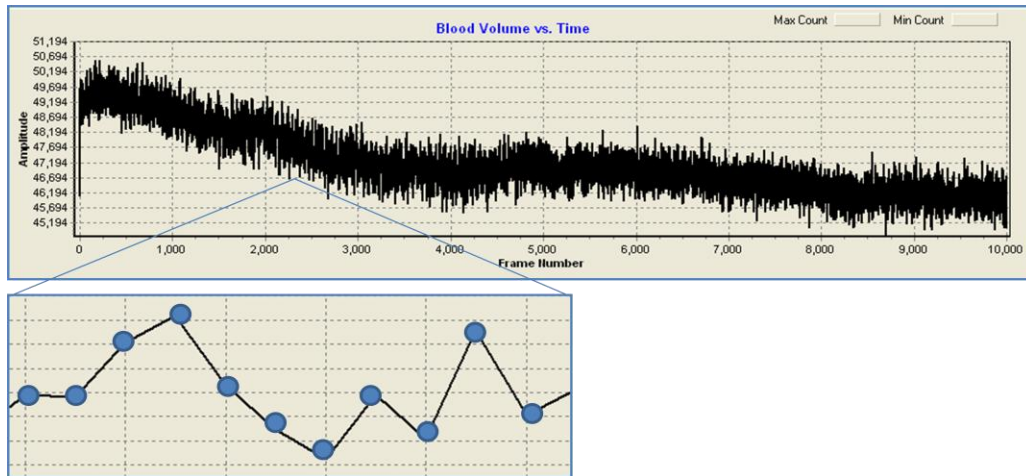
Figure 1-4: Screenshot of a BV vs. Time curve generated within the custom LighTouch^{TM} software. The panel below shows a close-up look of only eleven IE integrals from the curve. Each blue dot indicates an individual IE integral calculation based on a 20 ms single frame spectrum.

In earlier work with noninvasive glucose monitoring (54), using IE was proposed as a measure of probed volume or blood volume (BV) in a modulated approach. Despite the very low volume fraction (41-44) of RBCs, the optical constants of plasma, RBCs, and other skin constituent materials are such that the net propagation of light is mostly determined by the RBCs. Empirically, this is especially true for EE. Therefore, the IE vs. frame numbers and EE vs. frame numbers curves are thereinafter mentioned interchangeably as BV vs. Time and RBC vs. Time curves respectively. Detailed discussion will be continued in Chapter 3.

1.5 Previous Work and Limitations

Since 1998, most previous work (45-51, 54) has been done in the following aspects:

i) The earliest research was conducted to collect i*n vitro* evidence for

demonstrating the feasibility of the noninvasive spectroscopic approach to

quantitative glucose level determination. Raman spectra of various chemicals

presented in blood, such as glucose, hemoglobin (Hb), albumin, urea, tyrosine,

bicarbonate and glutathione have been investigated in either crystalline,

solution, or gelatin tissue phantom forms. (54) This comprehensive work led to

the selection of 373-686 cm^{-1} Raman shift range as an indicator of glucose

concentration. Since this range corresponds to two very strong Raman of

glucose skeletal modes at 423 cm^{-1} and 547 cm^{-1} and has little interference with

prominent protein peaks, quantitative measurements using these features

reached the resolution of ±1.5 mM *in vitro*. However, Raman spectroscopy's

millimolar sensitivity may not be achievable when applying to *in vivo*

physiological environment. It is also worthwhile to notice that despite the

chemical and optical similarities with human epidermal tissue gelatin phantom

can only be used as a calibration tool. Human factors, which will be elaborated

later in Chapter 2, need to be considered to further understand the limitations

and potentials of such technology.

ii) Earlier work applied the concept of tissue modulation to the *in vivo* glucose

concentration calculation. Previous work achieved acceptable results in a

clinical study on 41 individuals in cooperation with the Joslin Diabetes Center

at Upstate Medical University in Syracuse, NY. In this stage, to improve the

accuracy and sensitivity, a more rigorous approach should be sought to utilize

the information encoded in Raman, fluorescence, as well as Rayleigh scattering emission, rather than just a crude subtraction.

iii) The earlier research led to advanced instrument development including the tissue modulator (TM) (46). The previous prototypes made progress in maintaining the stable pressure applied to the back of fingertips, but there was no way to tell exactly how much force was exerted. Therefore, it was hard to fulfill the same setting across various test subjects. Besides, in the R&D phase of a product, it is important to monitor the changes in force and pressure in order to better control variables, design reproducible experiments and interpret any abnormal outcomes. A human-machine interface which can offer real-time force, contact area and pressure feedback and thus in turn perform better motion control is a necessity.

Aware of the limitation of previous research, the current work is to incorporate the human errors that have not been previously considered and interpret the modulated spectra in a much more systematic way. By interpreting a viable theoretical model we strive to engineer appropriate solutions that further improve the reproducibility, stability and sensitivity of this tissue modulated quantitative noninvasive *in vivo* Raman spectroscopy technique for blood analyte sensing.

1.6 Overall Scope of the Dissertation

This research is part of an ongoing project aimed at the application of combined NIR Raman and fluorescence spectroscopy to noninvasive *in vivo* blood analysis including but

not limited to glucose monitoring. Coping with practicalities of human factors and exploring ways to obtain and use knowledge gained about autofluorescence to improve algorithms for blood and tissue analysis are the general goals of the long term project. Based on the various results from this long-term project that was initiated in 1998, this doctoral research aims at tackling two main factors that can degrade the analyte specific spectroscopic signal: human factors and autofluorescence background. These are two different types of research challenges and so they will be introduced separately.

Previous research results show that the raw spectroscopic signals must be obtained from a well-defined location on stationary, perfusion controlled and monitored, plethysmographically confirmed tissue, and achieving this involves coping with the so-called "human factors". Human factors arise inevitably in the design and engineering of all medical devices that try to obtain signal from a transducer directly connected to the human body. In this thesis, we adopt a novel pressure based, tissue modulation methodology in order to exploit the spectroscopic benefits of differential spectra. Results have shown a dramatic improvement of stability by introducing an advanced human-machine interface, called "position detector pressure monitor" (PDPM). Given the PDPM we can methodically investigate the influences of skin tone, fingertip topography, skin hydration and possibly long term hyperglycemia on the precision, reproducibility and accuracy of the spectroscopic signals. PDPM measurements provide a synchronized plethysmographic record that complements the optical record.

The totality of the volume of tissue probed remits a background fluorescence signal, i.e., "autofluorescence", which cannot be removed from either the Raman scattered light or other identifiable, e.g., Hb, sources of fluorescence. Of the spectroscopic signals

available, usually any fluorescence background is not desirable when Raman is wanted. On the other hand it can be critical when or if it can be used as a measure of plasma volume and perhaps tissue volumes generally. Results have shown an interesting quenching of fluorescence which does not necessarily come from blood. Therefore, in-depth study *in vitro* and *in vivo* of potential fluorophores in static tissue and blood is performed. Pentosidine, an advanced glycation endproduct (AGE) that can be found in most tissues, has emerged as a central player and further study is conducted to uncover and quantify its fluorescence and quenching mechanism.

1.7 Specific Hypothesis

i) Some human factors, such as a) spontaneous tremor, and b) fingertip topography variance, can be controlled or coped with using an advanced human-machine interface, PDPM.

ii) Given that inelastic scattering emission (IE) and elastic scattering emission (EE) contain complementary optical information from the same skin constituents (static tissue and whole blood) through two different processes, relative volume percentage change of these constituents could be deduced from simultaneous EE and IE measurements.

iii) Autofluorescence quenching is due to laser exposure; potential candidates that contribute to the observed fluorescence include but are not limited to collagen, melanin, Hb, and albumin.

iv) Observed superabundant autofluorescence from aged and long-term

hyperglycemia subjects is related with the abundance of advanced glycation

endproducts (AGEs) within the skin. We further hypothesize that their

photodynamic characteristics are related to dissolved oxygen.

1.8 Layout of the Dissertation

The dissertation is organized in the following chapters:

Chapter 1 will first address the necessity and significance of this research for the

public health. This is followed by a brief introduction to the fundamental concepts of

tissue modulated NIR Raman and fluorescence spectroscopy in the context of other

published noninvasive human blood analytes sensing technology. A summary of previous

achievements of the Chaiken/LighTouch Group is followed by a statement of the scope

of the thesis and the hypothesis that is going to tackle.

Chapter 2 is designated, first of all, to demonstrate why human factors are relevant

to this study. Some specific sources of errors attributed to human factors are located.

Later on, the innovation of a human-machine interface, called PDPM, is introduced.

Performance of the PDPM is quantitatively evaluated. How the PDPM feedback

information could be used to guide *in vivo* experimental set-up is also discussed.

Chapter 3 relates various *in vivo* empirical observations regarding human volar side

fingertip fluorescence quenching that any model will need to explain. Qualitative analysis

indicates the potential origins of the so observed phenomenon. The *in vivo* calibration for

a proposed hematocrit (Hct) algorithm deduced by using combined elastically and inelastically scattered light is also described.

Chapter 4 puts the emphasis on a series of systematically performed *in vitro* experiments intended to supplement the database for known ultraviolet/visible (UV/Vis) chromophores to include their NIR excitation emission properties. Fluorescence of various endogenous molecules, such as antioxidants, blood proteins, skin and cellular pigments, are studied.

Chapter 5 focuses on the photochemistry of pentosidine, a specific representative of the AGEs family. Exogenously synthesized pentosidine tri-mixture (TMX) is used to study its NIR excitation induced fluorescence and bleaching characteristics. A hypothetical mechanism to account for the autofluorescence photobleaching behavior involving with dissolved oxygen is proposed and tested with multiple independent lines of evidence.

Chapter 6 concludes the thesis and proposes areas for future work. Considering the combined influence of human factors and photobleaching on quantitative analysis of tissue modulated Raman spectroscopy, a standard pre-experimental procedure is proposed to collect the spectral data in a much more systematic manner, thus greatly improves the reproducibility and comparability across various test subjects.

2. IN VIVO APPARATUS INNOVATION

2.1 Introduction

2.1.1 Haptics of Volar Side of Human Fingertips

To obtain spectroscopic information from blood embedded in dermis, the incident light must first penetrate the epidermis. How this occurs determines how the subsequently remitted light must be detected and processed to yield the desired information. Therefore managing, i.e., engineering, this initial process is essential to making *in vivo* spectroscopic probing of humans more technology than art. The term "haptics" refers to the sense of touch generally but often more specifically to the context of the human-machine interface (HMI). In this chapter a number of issues are raised relating to the specific and peculiar requirements that must be met by apparatus and procedures to allow methodical and reproducible probing of fingertip skin tissues *in vivo* noninvasively.

Initially the issue of choice of incident wavelength is discussed in some detail and it will be clear that this choice is influenced by considerations beyond simple propagation effects. The choice of which skin location to probe, detection schemes and apparatus among other such issues are discussed and subsequently, a substantial effort is made to describe the human factors engineering required to accommodate the highly irregularly shaped, highly variable sized fingers of human beings. In addition to the physical

dimension challenges, the hands are all connected to a human brain and that poses challenges of compliance that will also be discussed.

Propagation of light is affected by absorption and scattering losses and our goal is to obtain information from the vessels above the superficial dermal plexus, i.e., the capillaries *between* the skin surface and the superficial dermal plexus. One of the strong NIR absorbers in human tissue is Hb, and the red blood cells (RBCs) are the strongest Rayleigh/Mie scattering centers. As shown in Figure 2-1, despite the strong absorption between 400 nm and 450 nm, the molar absorptivity in the NIR range is three orders of magnitude less. Using a NIR excitation wavelength of either 785 nm, 805 nm, or 830 nm, the depth of penetration (1/e) could reach above 1.0 mm without the consideration of other factors.

However, melanin, which is another dominant absorber and also a strong scatterer, heavily influences how light will propagate within the turbid tissue and its strong absorption will further reduce the penetration depth. More importantly, the degree of pigmentation, i.e., the level of melanin, is quite variable across different ethnic groups and even across different individuals within the same group. Therefore, a testing site with relatively uniform pigmentation among people should be chosen. There are several candidates, namely the posterior chamber of eye, the tongue, the palm and the sole. First of all, tongue is not an easily accessible site and there are also problems related with hygiene concerns (11, 55). Secondly, areas around eyes are sensitive and pose special risks. Tightly regulated permitted power of laser radiation together with limited blood perfusion will produce a measurement with weak signal and low signal-to-noise ratio (SNR).
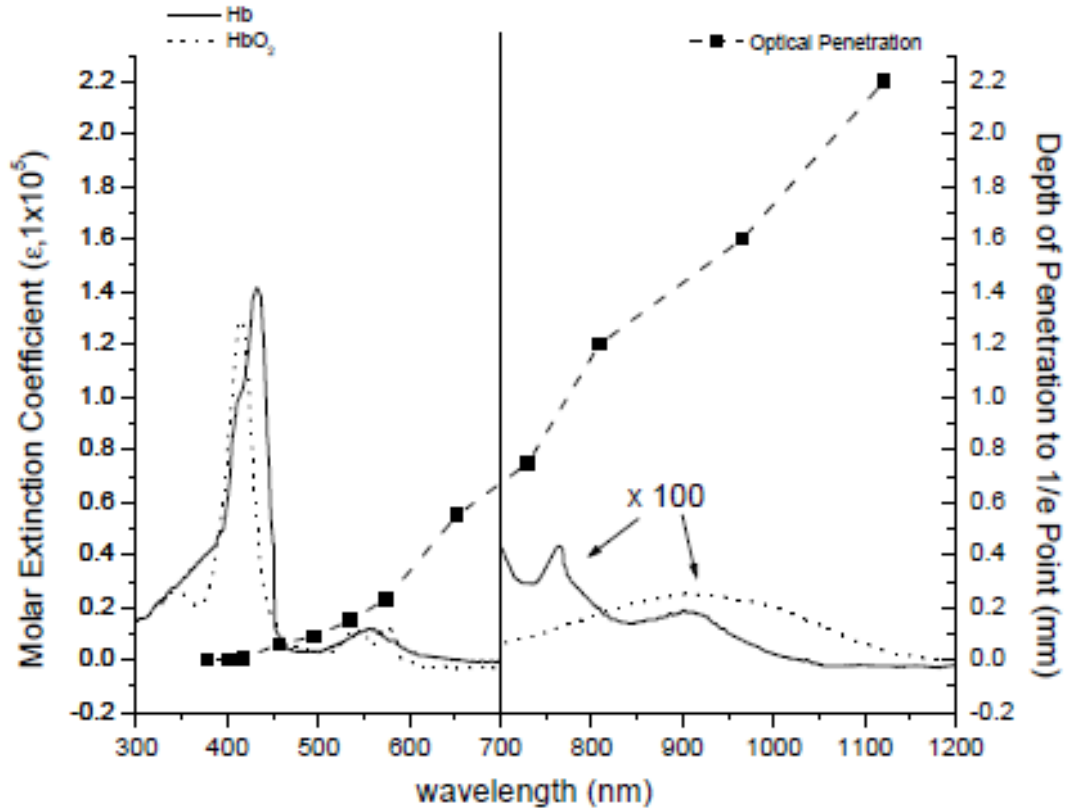
Figure 2-1: (left y-axis) Molar absorbability of Hb and oxygenated Hb (mm^{-1}/M) (56); (right y-axis) Depth of penetration of light to the 1/e point (57).

As shown in Figure 2-2(A), although the average thickness of epidermis is around 200 μm, on soles however, it can reach 1.5 mm, which is beyond the penetration of NIR excitation to get into dermis. Speaking to the probing volume of interest, i.e., blood, the capillary density of the palm is 2.5 to 3.5 times higher than that of the forearm, abdomen, or thigh (58), and the fingertip appears to have an even higher capillary density than the palm (59). A fingertip capillary blood vessels plastination model (60) is shown in Figure 2-2(B). As sensory probes to ascertain objects properties such as temperature, pressure, vibration, texture and moisture (61), fingertips possess the second highest concentrations of touch receptors and thermoreceptors among all areas of the human skin. Meanwhile,

anatomically speaking the fingertip is the second best perfused area in human body with a capillary density of almost 9 loops per mm (62, 63). At around 500 μm, capillary loops from the deeper layer vessels are already available. Previous calculation from our group (46, 54) shows that earlier prototype is capable of 600 μm penetration into the skin to get direct signal from blood. Therefore, volar side of human fingertip is practically the optimal site of detection.
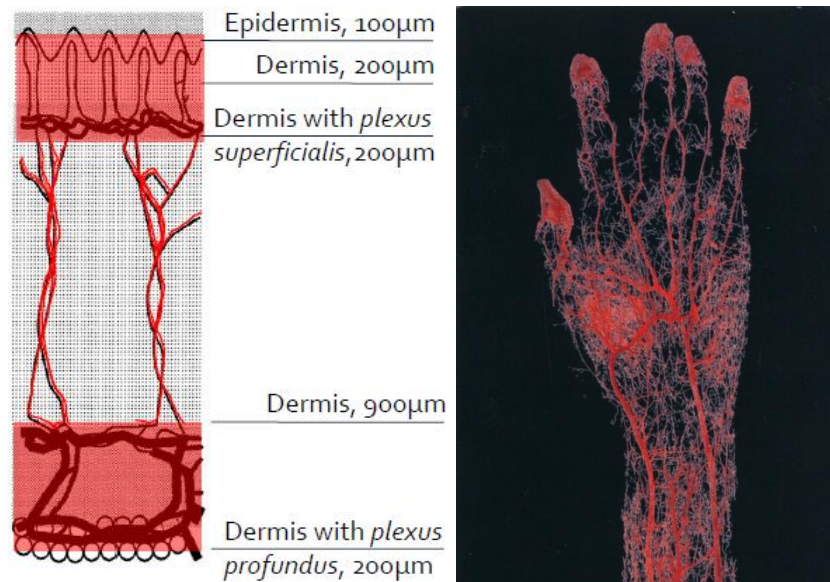
Figure 2-2: (A, left) A diagrammatic sectional view of human skin anatomy (62); (B, right) Tissue sample of palmar vascular system prepared by plastination (60).

2.1.2 Optical Layouts of the In Vivo Apparatus

Compared to the earlier versions of LighTouch^{TM} *in vivo* system (46, 51), the latest prototype, as shown schematically in Figure 2-3, keeps most of the geometric optical layouts but makes significant changes to both the optics and CCD detector. All the *in vivo* data presented throughout this paper, if not explicitly stated, are obtained using continuous wave (CW) external cavity diode lasers (Process Instruments, Salt Lake, UT,

USA and Sacher Lasertechnik Tiger Model, Marburg, Germany) with a clean-up filter (Semrock, Rochester, NY,USA). Due to the complicated errors caused by using an optical window, which will be discussed shortly, the 830 nm NIR excitation is free space coupled from the laser to the fingertip using a 15 cm focal length lens. In order to achieve reliable and reproducible optical registration the volar side of a fingertip is placed in contact with a rigid flat stiff spring steel surface having a 2 mm hole, chamfered 15 ° on the side facing the incident light. The size of this hole and the chamfering are chosen to minimize extrusion of tissue and to minimize the scattered light produced by interaction of the laser with the edges of the hole.
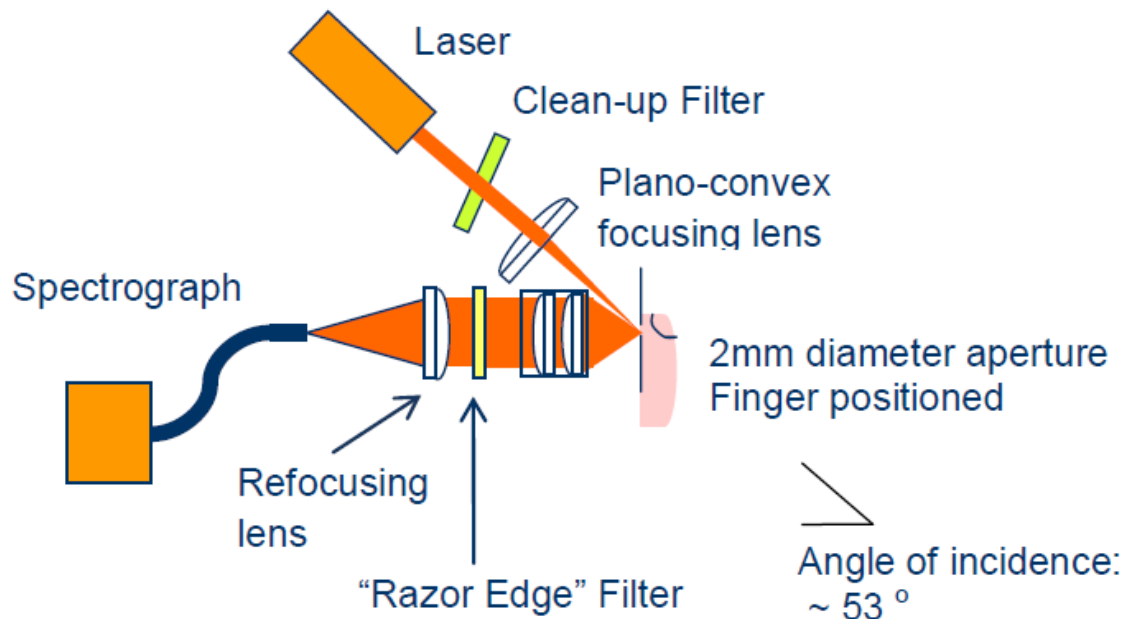
Figure 2-3: Schematic diagrams of optical layouts of the current *in vivo* apparatus.

Based on calculations (10), an angle of incidence of 53 °, i.e., the Brewster's Angle for an air-water interface, gives optimal results. It is primarily due to the fact that human tissue is mostly composed of water, and the Brewster's Angle from air to water allows

the best penetration into the skin instead of being scattered or reflected from the surface.

Therefore, the incident light that actually reaches the flat plane of the spring steel plate,

instead of being a perfectly round spot, produces an elliptical spot with a 100 μm minor

axis and 237 μm major axis. A microscope image of a ZAP-IT® paper burn hole is shown

in Figure 2-4. The hole is created by allowing a 20 μs blip of incident light onto the ZAP-

IT® paper to create a detailed mark of the laser. The measurement of the laser spot size is

made where the beam energy density is big enough to burn through the coated layer of

the paper. For the image shown, an 830 nm Process Instruments laser is driven by a 2300

mA current, which generates approximately 180 mW output emissions measured by an

optical power meter (Model 1830-C, Newport Corporation, Irvine, CA, USA).

Despite the capability of higher throughput capacity of the CW laser, the maximum

NIR power that we have ever used on any human subject is no more than 200 mW,

according to the Crouse Hospital Institutional Research Board (IRB) approval. Very rare

cases have been reported to cause small superficial tissue burns on unclean skin at 200

mW CW power at 830 nm after as much as 200 sec. Others (64) have been granted IRB

approval for using as much as 300 mW NIR laser on human forearm tissue and there

were no obvious safety issues. As will be shown in Chapter 3, at this power level, it is

readily sufficient to obtain spectra with good sensitivity and reproducibility in relatively

short time.
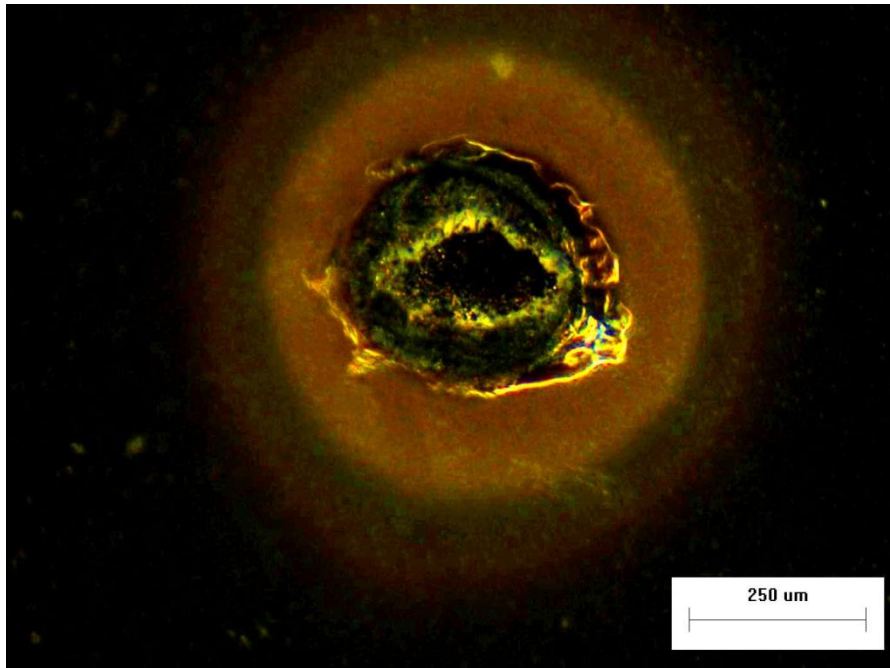
Figure 2-4: A microscope image of a ZAP-IT® paper burn hole. The driving current of 2300 mA (equivalent of 180 mW output) is applied to a Process Instruments 830 nm CW laser. Image is taken using a Stereo Discovery V8 Stereomicroscope (Carl Zeiss, Inc., Oberkochen, Germany).

All optics must be thin and fused silica, e.g., Corning HPF Series, particularly in the excitation side, to reduce background fluorescence and Raman originating with the lenses. However the optics can be thick on the collection side of the optical system because the total signal power incident on the first collection lens is very small, i.e., approximately equal to four to five orders of magnitude smaller than the incident laser power. Back scattered light containing physiological information is collected by an optical train consisting of a custom triplet collection lens (Avo Photonics, Inc., Horsham, PA, USA), followed by a laser line filter (Semrock 830nm Razor Edge, Rochester, NY, USA), and then a custom doublet refocusing lens (Edmund Optics, f=50 mm, Barrington, NJ, USA). A 61-fiber bundle presents an anti-reflection coated circular target to the refocusing lens

and a line configuration at the spectrograph (Process Instruments, Salt Lake, UT, USA)

entrance slit. The effective slit width is 70 μm and net collection of spectrograph is

approximately f/2.0. The wavelength dispersed light is imaged onto an Andor DU420-

BR-DD CCD camera (Andor Technology plc., Belfast, Northern Ireland) operating at

-65 ℃ or a Critical Link MityCCD-E3011-BICCD camera (Critical Link, LLC, Syracuse,

NY, USA) cooled to −30 °C.

Keeping all other optics the same, switching between CCD cameras with different

chip configurations will significantly influence the harvested spectra. Table 2-1 compared

the pros and cons of the most commonly used CCD chip configurations, including their

quantum efficiency (QE), dark current, etaloning issues and also prices.

Table 2-1: Comparison of characteristics of various CCD chip configurations.

CONFIGURATION	QE	PRICE	DEFECT
Front-Illuminated	$QE_{max} \approx 50\%$	Less expensive	Rugged, restricted detection range for 400 nm and above
Back-Illuminated	$QE_{max} \approx 95\%$	Twice of front-illuminated	Etaloning at longer wavelength (>700 nm)
Back-Illuminated Deep Depletion	Enhanced long wavelength response (> 50% at 900 nm)	Most expensive	Higher dark current (0.008 e-/pixel/sec)

Although the front-illuminated CCD sensor has a much lower dark current (0.0005 e⁻

/pixel/sec) under the maximum cooling, the silicon semiconductor materials become

increasingly transparent in the NIR. Thus the QE drops well below 10% for wavelengths

above 1000 nm. As a tradeoff, the Critical Link camera uses a back-illuminated configuration to gain extra QE in the NIR spectral range. However, etaloning at wavelengths above 700 nm is observed, which complicates the interpretation of the Raman features.

Most of the *in vivo* data before the end of 2009 were collected using the Andor back-illuminated deep depletion CCD camera. The deep depletion CCD chip is comprised of high-resistance silicon with a highly doped structure that boosts the QE to above 50% at 900 nm. Nevertheless, non-negligible thermal background noise hurts the SNR. Using extra coolant or liquid nitrogen cooling, the dark current density can be effectively lowered to around 0.008 e$^-$/pixel/sec. Dark current decreases approximately twofold for every 8 to 9 ℃ drop in CCD array temperature (32, 65). Especially, at low temperature ranges, 1 ℃ change of temperature changes a significant amount of dark current. This means that whenever deep cooling (-80 to -100 ℃) is desired, the temperature must be maintained with high precision. Therefore, besides the coolant circulation system, the Andor camera is also equipped with an extra temperature control box. It is thus unrealistic to make a portable version with such a bulky unit. By contrast, the Critical Link camera uses only a Peltier thermoelectric cooling to -30 ℃ with no need of precise temperature control. It is clear that tradeoffs in CCD camera selection are inevitable, and two cameras are used for different purposes of study.

Now it comes to the discussion of whether or not to use a window to attain optical registration with the probed tissue. When IE is used as a part of the measurement process, any fluorescence or Raman scattering from a window material, or even Rayleigh/Mie process involving the window that produces highly off-axis elastic photon emission (66),

adds a background to all measurements and thereby a shot noise contribution that cannot be eliminated. In the optical layout and configuration the depth of focus of the input coupling lens ensures that some of the incident light will be focused inside the window, at or very near the focus of our very fast emission collection system. It is not possible to include any window surface, or wire grid or other approach spanning the orifice, that is not a source of excessive stray light of all kinds, e.g., Raman, Rayleigh, fluorescence. It is possible to exclude a large proportion of light from the window-laser interaction using more optics and confocal apertures (67) in the collection train but not without sacrifice of simplicity, extreme loss of total signal, and imposition of spatial resolution that does more harm than good to the overall measurement process. Achieving maximum SNR is one strong reason to free space couple the probing light into the tissue without use of a window and thereby eliminate or at least minimize related noise contributions. Also, improved SNR by not using a window allows a decreased measurement time and shorter measurement times favor better control of human factors, i.e., extraneous motion, tremors, etc., which will be discussed in the following section.

2.1.3   Human Factors

Human factors (HFs), or cognitive ergonomics, involve the engineering of what we know about human capabilities and limitations to the design of equipment and devices in order to enable more productive, safe, and effective use (68). It has gained attention to increasing number of healthcare device manufacturers, such as Masimo, who recently release a new signal extraction technology (69, 70) to their pulse oximeters (the Masimo

"SET" series). This technology is mainly focused on using algorithm to eliminate the extreme motion artifacts.

One example of the most obvious HFs pertinent to our study is force or pressure maintenance. The delicate threshold force of blood flow disruption requires an active part to exert the additional force during modulation and the force needs to be controlled with a precision of ±0.1 N. However, due to the intrinsic limitations of human control, no matter how hard one would try, the human sense of touch is inadequate in the contact force range as low as 1-2 N. When trying to maintain 100 mmHg, the normal mean arterial pressure (MAP), for a 1 cm^2 fingertip, the total force needed will be 1.33 N. It is a substantially small force that needs additional assistance involving human factor engineering to maintain. Human factor engineering has become a notable part of the design of many modern safety critical systems, especially in the delivery of healthcare. In many cases it focuses on HMI, which by the definition of FDA (71) includes all components and accessories necessary to operate and properly maintain the device.

Apparently when tissue is pressed against an open aperture of the correct size the stress field is less a reflection of the shape of the underlying bone and the exact positioning of the tissues and more of the viscoelastic properties of the local tissue, including the possible motion of subsurface tissues, i.e., blood. Yet for a free space coupled interface like the current LighTouch^{TM} prototype, human factors are such that there is inherent variability in contacting different sized and shaped fingers or even the same finger at different times to the same aperture, no matter how the aperture is formed. Moreover, choosing to probe through an open aperture is at the expense of having to accommodate other HFs associated with some intrinsic characteristics of fingertip tissues:

i)   Fingerprints: All skin has surface topography, even relatively smooth forearm skin, and the effect on optical probing can be anticipated (10) using Fresnel's equations. Ridged skin (72) such as is found on volar side fingertips provides an important thermoregulation function and due to the uniqueness in patterns and minutiae of each person fingerprints are widely used in forensic science and security applications. However, depending on the relative size of the probing light beam and the scale of surface topographical features, the presence of topography may lead the results to have a strong dependence on the placement of the laser beam on the skin surface. As showed earlier in Figure 2-4, the size of the incident laser spot (100 μm in minor axis and 237 μm in major axis) is commensurate with the breadth of fingertip ridges (on average 480 μm for male and 430 μm for female with a depth of 200-300 μm) (73). Whether the light contacts the skin on top of a ridge or at the bottom of a furrow directly determines the local angle of incidence and thus the propagation into the tissue. Therefore, in any optical instrument including the LighTouch^{TM} apparatus the sample, e.g., the tissue, must be brought into reproducible registration with an optical system.

ii)   Fingertip doming: The collection side of the optical system is aligned to obtain the maximum emission from the collecting cone by assuming a flat surface. Although minor adjustment is made according to sample fingertip, the extrusion into the optical orifice moved the center of incident light. Dome height also varies among test subjects. Note that, now, in the context of probing skin through an open aperture, the depth of focus of the incident laser beam can be

an advantage. Being much longer than any motion or extrusion of tissue caused by doming or pressure in the direction of propagation of the incident laser, the properties of the incident laser can be taken as constant regardless of the motion of the tissue.

iii)   Turgor: Turgor is the normal state of turgidity and tension in living cells. In other words, it vividly shows the "puffiness" of a finger. The U.S. National Institutes of Health (NIH) define it as "the skin's ability to change shape and return to normal (elasticity)" and use it as a sign to assess the degree of fluid loss or dehydration. Turgor is also related with the extrusion into the aperture, but empirical experience shows it is more relevant to skin impedance and the resulting stability of the PDPM dots pattern (detailed in Section 2.2.3).

In an earlier study (50), the distribution of deviations between the noninvasive LighTouch™ measurements and the reference fingerstick measurements reflected various sources of random and systematic error. Better management of the measurement process with regard to the aforementioned human factors emerged as a strategy for improvement with feedback based on applied pressure and tissue placement.

2.1.4   Modulation Pressure

Research on human and machine haptics suggests that for contact forces below some threshold, probably around 0.5 N, the blood vessels in the finger pad are barely affected by compression (74, 75). Above that threshold, however, blood vessels in the region of compression collapse and the blood is driven away from the contact area. As shown in

Figure 2-5, decrease of grayscale color with increased force indicates less blood perfusion. Though not shown in the figure, there is a progressive 70% decrease in blood flow at 2.9 N as compared to 0.5 N (75). Notice the increase of fingertip contact area with the BaF$_2$ optical window as the increase of exerted force, which is also true in the free space coupled interface.

| 0.1N | 0.25N | 0.5N | 1N | 2N |
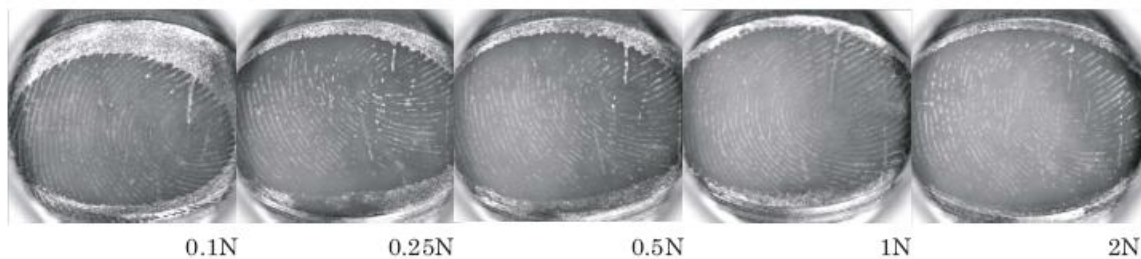
Figure 2-5: Typical images of fingertip deformation against a BaF$_2$ optical window at each target force (74). Notice the decrease of grayscale color, which indicating decreased blood perfusion, with increased force.

As stated earlier in Section 1.3, to achieve a successful modulation, the ideal scenario is that during the unpressed part of the measurement cycle the applied force is well below threshold so that sufficient blood perfusion is guaranteed and the capillaries can maintain mechanical stability. While in the pressed part of the tissue modulation cycle the force is only slightly above the threshold of capillary collapse so that blood is modulated but limited deformation is introduced to static tissue. Therefore, based on the research findings on human haptics (61, 74, 76, 77), the applied force should be in the range from 0.5 N to 2 N to obtain an optimal difference spectrum that contains a minimum contribution from static tissue but most blood borne Raman and fluorescence features.

On the other hand, *in vivo* collected data frequently reveal the occurrence of cardiac pulses both optically and mechanically. In Figure 2-6 the force sensor recordings of the real time exerted force on the aperture reveal an obvious pattern of cardiac pulses, while the simultaneously collected IE vs. Time curve demonstrate the same pattern but mostly in a complimentary way. This observation offers a pivotal evidence of the capability of our technology in collecting signals directly from blood. However, empirical observation also suggests that under various target pressures, for different test subjects, these pulses are not always observed and when observed, the amplitude of these pulses can be highly variable.
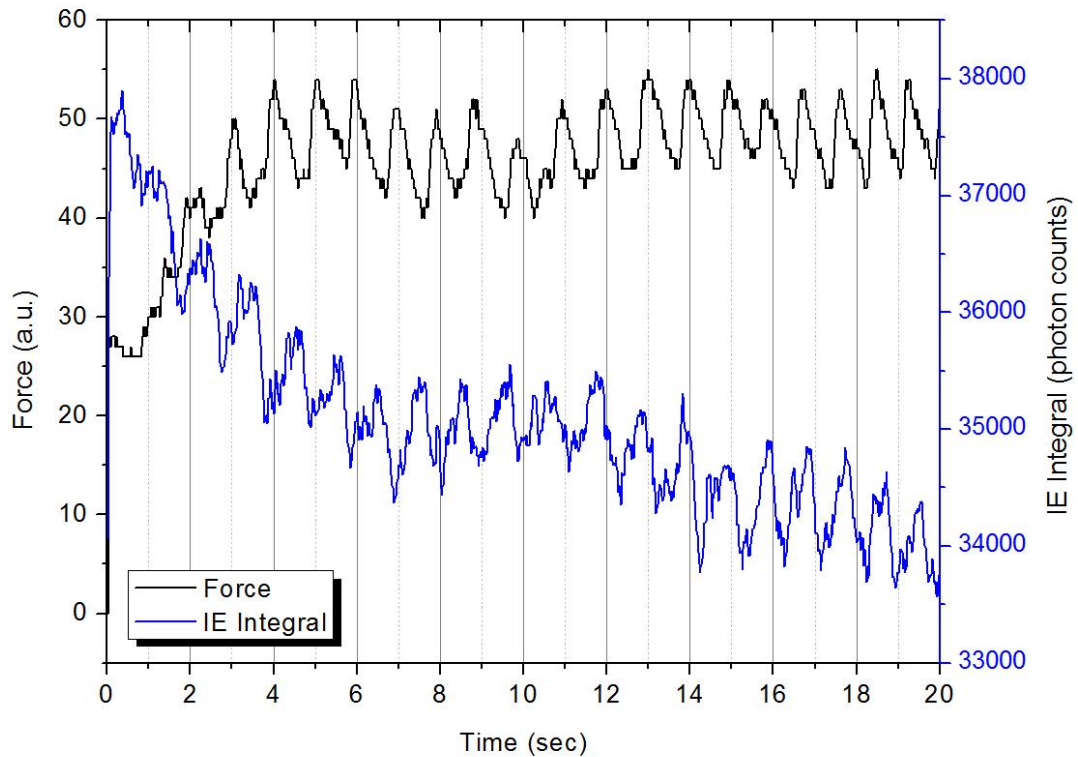
Figure 2-6: *In vivo* observed human cardiac pulses, both mechanically (black curve, left y-axis) and optically (blue curve, right y-axis). Although pulses are frequently observed among various populations under proper pressure registration, the plotted is based on a single measurement from a middle age Caucasian male. The pulse rate measured with a blood pressure cuff is 67 bpm.

We postulate that the mechanism of this phenomenon is similar to the principles applied in determining the blood pressure (BP). Generally speaking, there are three mostly used techniques to take BP measurement: auscultatory, oscillometric, and photoplethysmographic. The *in vivo* observed pulse response to the applied force or pressure works in a very similar way as the oscillometric method. When fingertip is in registration with the HMI that will be introduced in Section 2.2.2, the setup is analogous to the upper arm confined by a sphygmomanometer cuff. Therefore, the electronic force transducer senses the pressure fluctuations caused by the oscillation of blood flow. Nowadays, the oscillometric measurement has been used as a standard among various commercial automated noninvasive BP monitors.
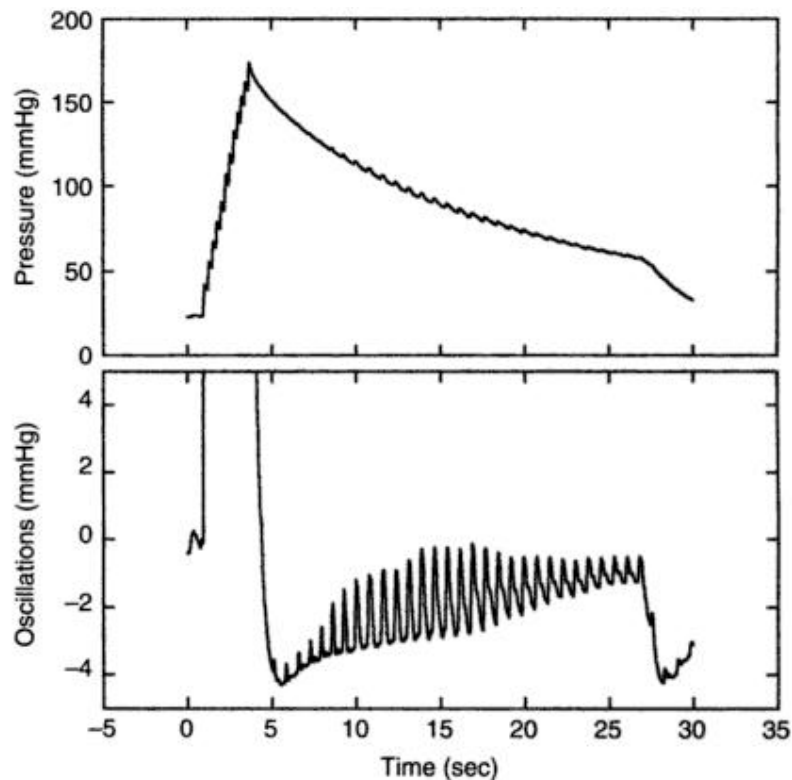
Figure 2-7: Sample recording of cuff pressure during oscillometric blood pressure measurements. Bottom panel shows oscillations in cuff pressure obtained by high pass filtering above 0.5 Hz (78).

The upper panel of Figure 2-7 shows a typical oscillometric measurement cycle (78). The automated pressure cuff is initially inflated rapidly above the systolic pressure as indicated by the complete cessation of pulses and then deflated gradually. The recorded cuff pressure is high-pass-filtered above 0.5 Hz to observe the pulsatile oscillations as shown in the bottom panel of Figure 2-7. Clearly, on one hand, the cuff pressure fluctuates with the pulses, while on the other hand the magnitude of the fluctuation varies with the applied cuff pressure also.

It has been shown that the pressure at which the pulse oscillations have the maximum amplitude is the mean arterial pressure (MAP). Knowing that MAP = 2/3 $P_{diastolic}$ + 1/3 $P_{systolic}$, the pulses are best sensed, i.e., the observed amplitude is maximized, when the applied pressure is roughly the average of diastolic and systolic pressure. When attempting to maintain a normal MAP of 100 mmHg for a test subject with 1 cm^2 fingertip contact area, the force needed is 1.33 N. Such force is in the 0.5 – 2 N range for optimal tissue modulation. Therefore, it is highly feasible to find a suitable applied pressure range for each individual in order to guarantee best blood modulation while maintaining a continuous flow. Last but not the least, it is worthwhile to note that after performing an absolute pressure calibration the potential exists to design a LighTouch^{TM} device to measure pulse rate and BP with other analytical goals simultaneously.

2.2 Position Detector Pressure Monitor (PDPM)

2.2.1   Features and Limitations of Previous Versions

HMI engineering has been considered important from the very beginning of this long-term project. At the birth of the very first LighTouch^TM system, a "Tissue Modulator" (TM) was already embraced in the design (46, 48). As shown in Figure 2-8, the TM contains an orifice in a metal plate, where the fingertip is placed so that tissue to be interrogated is accessible to the excitation light through the orifice (0.95 cm diameter). A spring loaded plunger module is placed in a retracted position for the "unpressed" half. Alternatively, the plunger can be released so that a padded complementary shaped "piston" presses against the back of a fingertip for the "pressed" half.
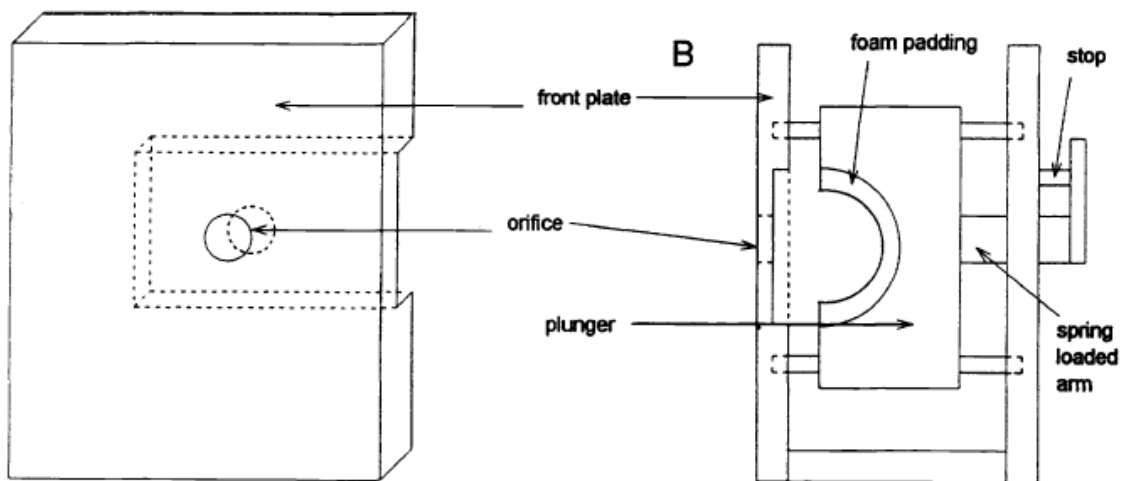
Figure 2-8: Schematic diagram of the 1st generation "Tissue Modulator". It comes with the very first LighTouch^TM prototype built around 2000. A spring loaded module is used to facilitate pressure modulation with no positioning guide or feedback.

At that time, all subjects were given minimal instruction (50) on how to perform tissue modulation and the data were collected using an essentially "double blind"

procedure. The 2nd generation TM comes along around 2006 and contains many improvements over earlier prototype. Firstly, rubber Braille-like "nubs" are arranged near the orifice to allow the test subject to orient the position of fingertip to the hole by way of touch. Secondly, the TM also employs a load cell to measure the force applied to the aperture. A linear array of several light emitting diodes (LEDs) in a pattern of red, yellow, green, yellow, and red. During the modulation cycle, an audio cue is given to the test subject while the LEDs light up depending on how much force is actually being exerted. Light-up of the green LEDs indicate the desired force is met; while yellow LEDs mean mediocre satisfactory force and red LEDs warn of way-off compliance. In this way, real time feedback to the test subject could be offered.

As aforementioned in the engineering of first two generation TM modules (46, 48, 51), we employed muscle memory, visual memory, and visual and audio cues in order to direct the test subject him/herself to apply the appropriate force and maintain an appropriate finger posture in order to modulate the blood content of the capillaries. Perhaps, not surprisingly, even when humans are given very accurate and precise feedback, they vary in their competence to execute the required actions. Further, even if compliance requires the test subject to be passive, as for an unconscious patient, the probability of involuntary tremor and the known occurrence of inadvertent or unconscious pressing or unpressing against the aperture by the test subject requires the instrumentation to play an active role in producing, measuring, and recording the actual position and actual applied stress field in the test subject.

It is also an empirical fact that pressure on the fingertip, even constant pressure, has at least two effects. As mentioned in Section 2.1.3, the pressure causes "doming" or

extrusion of tissues into the aperture, i.e., the exposed skin surface is not flat, independently of the presence or lack of ridges. In addition, over time, constant pressure causes some fluid, e.g., blood, to flow out of the irradiated region, without many changes to the static tissue. Note that as fluid moves in response to the applied pressure, the contact area between the tissue and the surface containing the aperture, i.e., the "modulating surface," must increase necessitating an external real-time contact area monitoring and pressure servo system in order to produce consistent results.

Thus, in addition to focusing our attention on the optical and spectroscopic issues of a particular experimentation, it is helpful to have a record of the test subject's actual compliance (or noncompliance) during the measurement process in order to help sort out motion and placement artifacts from actual spectroscopic content. Experience with each of these and the desire to have a device that would be applicable to unconscious people led us to seek a way to modulate the skin and blood automatically under external control.

2.2.2   Overall and General Description of Current PDPM

In what follows the current instrumentation and experimental methods used to obtain reproducible and reliable measurements on fingertip capillary beds will be described. The entire apparatus is coordinated using a C++ programmed graphical user interface (GUI), with embedded MityDSP for the PDPM and in the CCD camera control. All transducers are commercial-off-the-shelf and the circuitry needed to implement them is available from their manufacturers. Initially an overview of apparatus and procedures will be given

before specific discussion in more details of placement (or positioning), contact area

function, and force and pressure measurement and application.
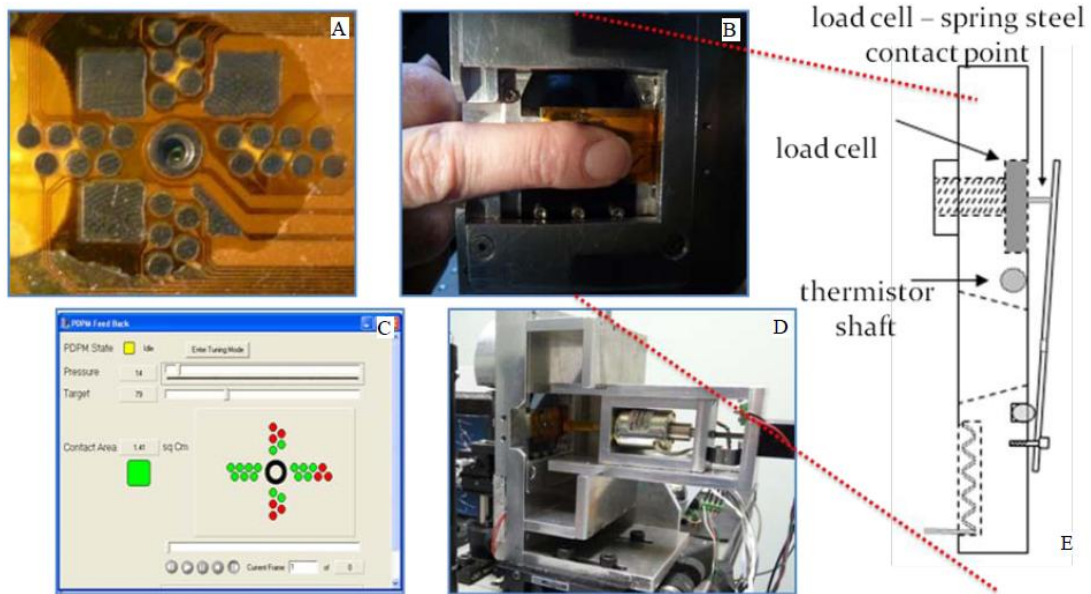
Figure 2-9: Details of the current used PDPM module and the control GUI. (A): close-up of the conductive dots on the flexible circuit board for contact area monitoring. (B): photo of the fingertip in place for measurement. (C): corresponding contact area and pressure feedback on the GUI software. (D): photo of the complete PDPM assembly including the stepping motor and the solenoid system for pressure servo. (E): side view of the load cell – spring steel lever system.

To give a general picture of the mechanical design of the currently used PDPM

module, Figure 2-9(A) shows that a conductive metal ring is oriented concentrically

around the orifice and surrounded by conductive dots at four different orientations. When

a finger is in contact with the circuit board (Flex Printed Circuit Sales, Redwood City,

CA, USA), PDPM detects the electrical resistance between the center ring and each of the

surrounding conductive dots. If there is a connection by finger, the resistance is below the

preset threshold and corresponding red dots in the GUI display turn green indicating

contact, as shown in panel (C). In this way, real time contact area (calculated from the number of covered dots) and force, which is measured by a load cell (LCGC-150G, Omega Engineering Inc., Stamford, CT, USA) through a lever system as shown in panel (B) and (E), can be obtained. Therefore, live applied pressure can be calculated to provide feedback into the LighTouch^{TM} software, providing a servo signal to drive a plunger (shown in panel (D)) against the back of the finger to establish and maintain the target pressure.

More specifically, to prepare to apply pressure after insuring appropriate placement with respect to the aperture, an actuator is brought to the threshold of contact with the dorsal surface of the distal phalanx coarsely using a stepping motor. When the load cell signals the threshold, the stepping motor stops (Figure 2-9(D)) and backsteps a predetermined amount relative to the dorsal skin surface. The solenoid can apply maximum force and fastest response, i.e., display optimum performance, when the shaft is positioned within plus or minus a few millimeters of the center of its range of motion. The stepping motor leaves the solenoid so that it can remake skin contact in the optimal shaft position. This process is mentioned as the pre-experimental "set-up" procedure thereinafter.

Contact between the actuator and the skin surface is always chosen to occur between the cuticle and the distal joint such that the actuator does not make direct contact with the fingernail. The exact point of contact determines the type of modulation that will occur and certain characteristics of the compliance information that will be available. Application of pressure onto the fingernail itself produces a reproducible modulation effect in the volar side capillary bed that is essentially the opposite effect of pressing on

the volar side soft tissue. Attempt has been made to contact the nail bed capillary blood through the fingertip for spectroscopic purposes before (46) but the difficulty in that approach is bringing the rigid nail surface into reproducible registration with the aperture. Thus, in the present context making contact between the cuticle and the joint ensures that the induced stress field does not produce opposing effects on the volar side.

Trial and error has shown that, once a measurement cycle has begun, the aperture must be stationary (in the direction of incident light propagation) with respect to the collection optics and the laser delivery lens to at most ±25 μm throughout any experiment to obtain consistent results. It appears that inconsistent aperture movement combined with inconsistent extrusion of tissue into the aperture produces an unmanageable spectroscopic response. However, all force transducers (in our case a 12-bit Omega LCGC-150 g transducer) require motion of some kind to produce an electrical signal. Therefore, a lever system, a simplified on-scale drawing is given in Figure 2-9 (E), is used to magnify the motion of the modulating surface at the transducer contact point and minimize the motion at the optical aperture so as to achieve sufficient sensitivity and stability with respect to knowing the total applied force at the aperture. Consistent with the specifications of the transducer no hysteresis in this system is detected, so the design seems acceptable.

The position of the aperture with respect to the fulcrum determines the largest finger size that can be used in this type of apparatus. Related to this is the fact that the fingertip is not a point load. The perceived force applied to a specific point on the fingertip increases as the distance between the fulcrum and the point of interest increases. The load cell does not detect any force applied to a region of a fingertip that overlaps the fulcrum.

Thus, since the fingertip must overlap the aperture, the distance between the aperture and the fulcrum is the largest width of finger that can be accommodated. In calibrating the force measurements of this design, it is important that any applied load, i.e., known test loads, have a contact area with the spring steel plate about half the maximum and be centered at the aperture. A fixture was designed that mounts the second reference load cell to the end of the solenoid shaft so that a chosen force/pressure setting can be tested in the instrument for independent calibration.

Various designs of this system have all required some temperature control of the modulating surface (spring steel) and nearby connected materials (aluminum and stainless steel) to control potentially random but usually periodic variation of the transducer output associated with zero applied force. The apparent zero of applied force can drift due to differential expansion of materials with respect to ambient temperature drift and, often, differential warming of the modulating surface itself by the *in vivo* tissue being modulated. Choosing to maintain the modulating system at or near 37 ℃ is advantageous and a thermistor (shown in Figure 2-9(E)) driven freestanding analog proportional-integral-derivative feedback loop is sufficient for this purpose.

2.2.3 Placement and Contact Area

The current PDPM system automatically measures the test subject's volar side contact area with the "tissue-modulating surface," i.e., the flat spring steel region surrounding the aperture, while providing feedback for initial placement and later a record of the actual placement during a measurement sequence.

The placement and contact area measurement needed as feedback for an actuator to maintain constant pressure is accomplished using an array of metallic gold spots on an insulating substrate as shown in Figure 2-9(A). This gold metallization pattern is deposited on a flexible Mylar™ circuit board that is glued to the spring steel surface. There is also adhesive on the Mylar™ surface *between* the metallic spots, so that when final placement and contact is achieved, the skin in contact with the adhesive cannot easily move parallel to the modulating surface. This raises a human factors issue since this flexible circuit board must be changed regularly due to fouling of the spots by skin borne fluids.

The electrical resistance between the gold annulus enclosing the optical aperture and each of the gold spots is relatively low when skin is in contact with both conductors and infinite otherwise. Each spot in a corresponding pattern displayed by the GUI is colored green or red depending on the resistance state sampled in real time every 20 ms. There are also two sliders produced in the same GUI window (Figure 2-9(C)) depicting in real time the actual applied pressure to the modulating surface and the target pressure for the modulating cycle. Based on which and how many spots are in the low resistance state (green), and the spacing and dimensions of the spots, an algorithm is devised to calculate the contact area between the modulating surface and the fingertip. The spot pattern, contact area, force, and pressure can be "played back" to allow examination of the measurement process frame by frame.

The electrical resistance of the skin perceived by the spots depends on many factors that can be distilled into two major but not completely orthogonal categories: hydration and turgor. Possibly there are two categories because there are two properties of the

tissues, electrical and mechanical, that determine the response of the gold spot system. Considerable experimentation with senior citizens shows that it is possible to have well hydrated skin and still have low net turgor causing the spot system to fail. Considerable experimentation with young people shows that it is also possible to have very high turgor but sufficiently dry skin so as to cause the spot system to fail.

All tissues in the mechanical train that starts with the spring steel and terminates at the opposing distal phalange bone surface inside the finger contribute to the apparent turgor of the whole assembly. Each tissue in the train has its own turgor properties but so long as the net turgor allows good mechanical contact between the skin and spots, only the outermost surface skin, i.e., the stratum corneum, contributes to the apparent electrical impedance sensed by the spot system.

"Hydration" is more than the simple presence of water. There is water in the stratum corneum, the interstitial spaces, and the cells themselves that affect the mechanical properties of the tissues as well as the electrical properties. In our experience, regardless of turgor, most commercial skin lotions and similar substances used regularly but not within a few hours of executing a placement will cause the apparent electrical resistance to decrease and the placement spots to work better than topical application of water or even electrolytes much closer in time to the initiation of the actual measurement cycle.

Turgor relates to water content of each cell and the oncotic pressure that keeps the water inside. This determines the apparent electrical resistance in that the skin must be brought into sufficient mechanical contact with the metal regardless of the availability of charge carrying capacity. Mechanical contact requires the tissues between the bone, i.e.,

the distal phalanx and the modulating surface, to resist further compression at some

applied pressure. When the oncotic pressure (79) is sufficiently low, all the tissues

between the bone and the Mylar™ surface are so compressible that the mechanical

contact is insufficient to allow adequate electrical current to flow, even though the

stratum corneum is sufficiently well hydrated to make the spots respond. Although better

approaches to this problem may emerge, with regular usage of almost any over-the-

counter skin lotion, the approach presented here allows a very wide variety of test

subjects to easily achieve proper placement and reliable contact area measurements

without any apparent spectroscopic consequences.

2.2.4   Force, Pressure and the Measurement Cycle

There are two modes for i) positioning the fingertip in proximity to the aperture and

ii) moving the actuator into proximity to the fingertip thereby initiating a measurement

cycle. In one (66) the test subject places his/her own fingertip against the modulating

surface, shown in close-up in Figure 2-9(B), achieving desired placement by visual

feedback using the GUI provided colored spot pattern. Or as shown in Figure 2-10, a

fixture is mounted on the solenoid, the finger is placed in a splint outside the device, and

then the finger with the splint attached is slid into the fixture all as described in greater

detail below. In this case positioning is followed by the "set-up" process, i.e., the stepper

motor/solenoid moves the fixture holding the passive splint-mounted fingertip toward the

aperture. If positioned without the splint, pressing a button in the GUI causes the actuator

to approach the stationary finger from the dorsal side using the stepping motor.
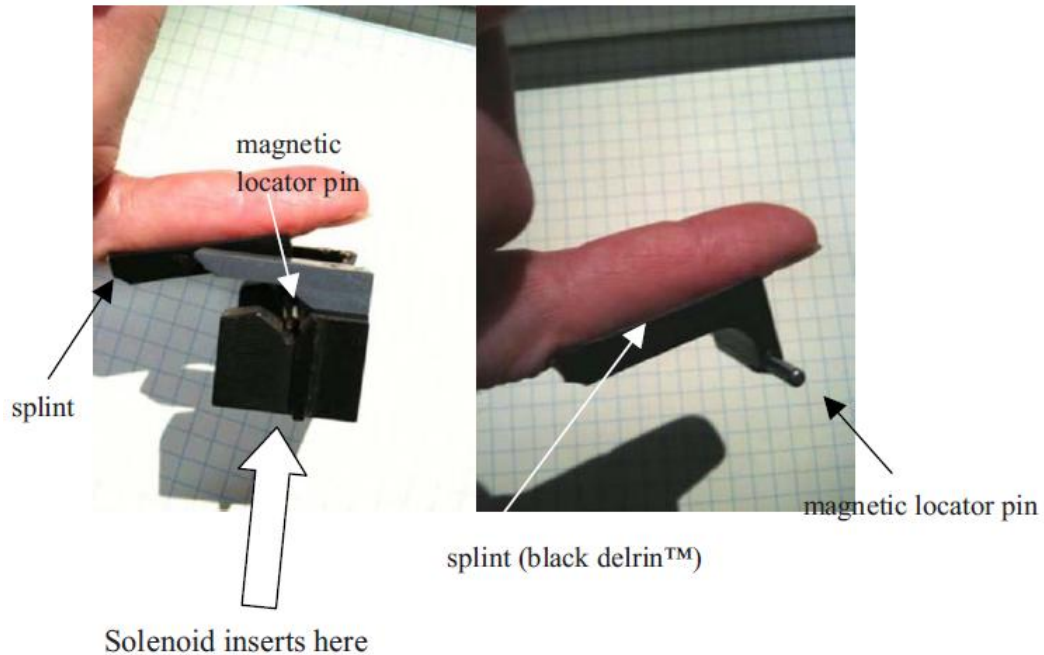
Figure 2-10: Splint fixtures for fingertip positioning. Right: splint is taped onto dorsal side of finger. Left: a finger is attached to splint that in turn is engaged into fixture.

In either case, upon first simultaneous three-way contact between the modulating surface, the finger and the actuator surface, the stepping motor stops and then retracts a few millimeters. The actuator position is then further adjusted using a solenoid to achieve a pre-unpressed pressure between actuator, finger, and spring steel of ≈ 10 gf/cm^2 pressure in the feedback system. This is very light pressure that most test subjects cannot discern. Utilizing the solenoid from this point forward allows continuous adjustment of actuator force and displacement, in order to keep the measured pressure, i.e., the ratio of the total applied force and the measured contact area, constant.

magnetic coupling plate

guides

double-stick tape
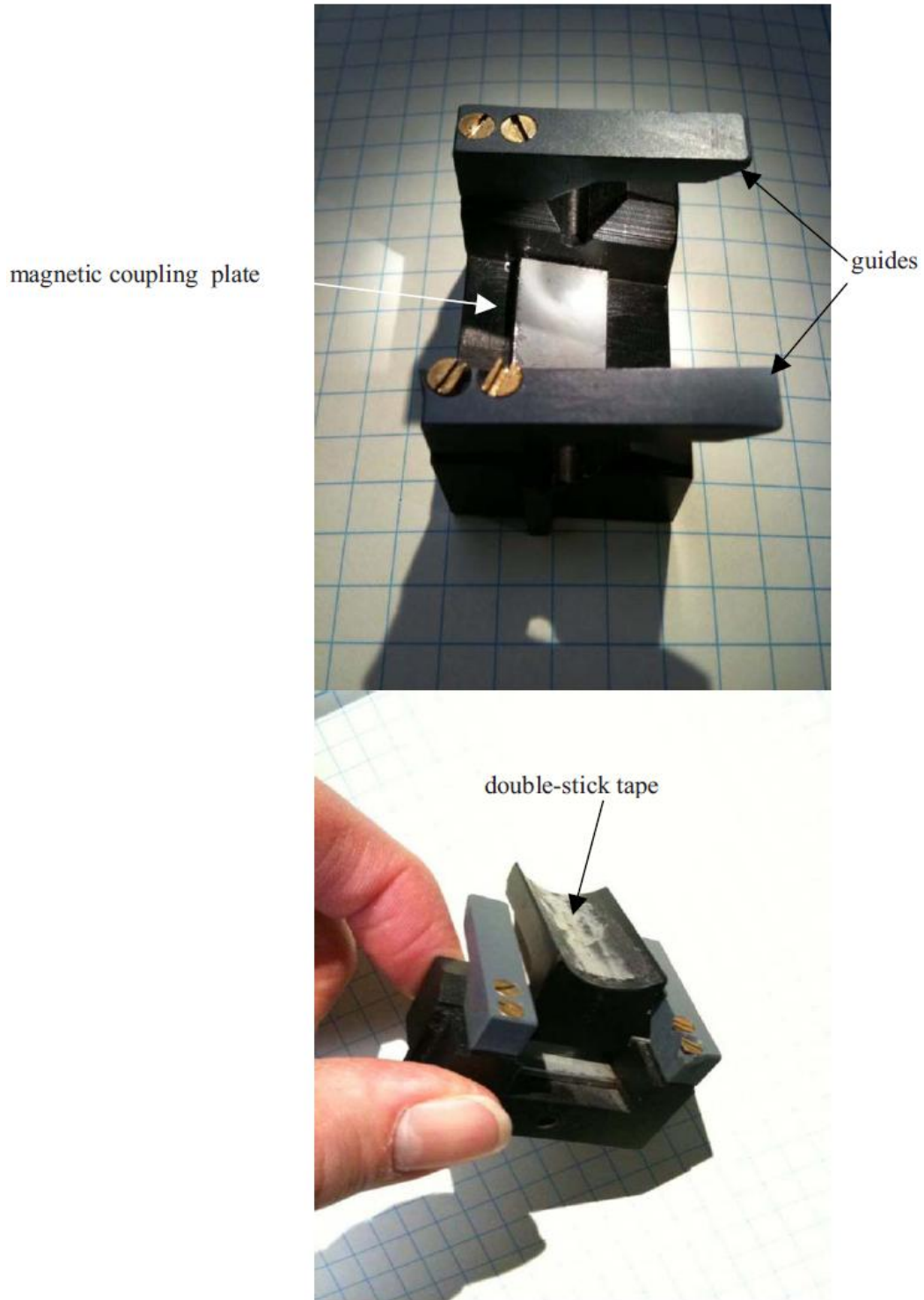
Figure 2-11: Coupling between splint, fixture and the back of fingertip. Top: fixture showing magnetic coupling plate and guides to locator pins. Bottom: view showing curvature of contact surface between splint and dorsal side finger and double stick tape.

The actuator for applying force can be made to contact the dorsal side of the distal phalanx between the nailfold and the first joint in a few different ways. This can be as basic as a simple cylinder, or a foam-pad-tipped cylinder attached to the end of the solenoid shaft. An example of mounting the finger to a "splint" is shown in Figure 2-10. The splint clicks into place on a fixture mounted to the end of the solenoid shaft. The splint is magnetically coupled as shown in Figure 2-11 and swivels with movement of the finger at the proximal joint. The splint, i.e., actual area of contact between the dorsal side and the actuator, is a shaped plastic piece that is fastened to the finger with double-stick tape.

This approach has the advantage that the splint can be positioned on the finger outside the aperture housing assuring appropriate alignment when subsequently engaged to the fixture, and unassisted compliance is possible for most test subjects. The fixture has guides that, once the locator pins are engaged, allow forward motion until the magnetic pins approach the magnetic plate embedded in the fixture and reproducible placement occurs. Providing comfortable support for the elbow and general posture of the arm and wrist greatly facilitates compliance. In addition, an easily adjusted vertical rod that fits into the webbing between thumb and forefinger placed in proximity to the modulator is also very helpful for hand stabilization.

The pressure servo has several sets of important details. When the measurement cycle is initiated, the existing contact area and the simultaneous total force between the volar side fingertip and the modulating surface is measured, divided by the contact area, to produce a pressure feedback signal for the actuator. The actuator is driven by the solenoid in contact with the dorsal side of the finger to achieve and maintain the preset

"unpressed" target pressure. Since the contact area between the volar side skin and the

modulating surface increases in time as the blood leaves the capillary bed, the force must

be increased in proportion to maintain constant target pressure. The placement spots and

the load cell are polled at 20 Hz giving the approximate bandwidth of the pressure servo.

The initial target pressure is achieved and the system becomes mechanically stable in

about 100 ms.

When a tissue modulation cycle is required, after a suitable "unpressed" collection

period, the target pressure is changed to reflect the transition to the "pressed" state, the

actuator applies more force to achieve the new target pressure and 20 ms CCD frames are

collected for an equal time period as the unpressed state. Afterwards, the actuator is

retracted, and the CCD frames are stored as a record of the applied force, applied

pressure, net contact area, and contact history of the individual placement spots. In a

separate step, the CCD frames are processed (46, 50) for calculation of glucose or

bicarbonate concentrations or hematocrit (Hct). Of course, other modulation schemes can

be employed for other purposes using the same apparatus (80).

2.3 Evaluation of PDPM Performances

2.3.1 History of PDPM Outputs

To clarify the two different measurement procedures and algorithms that are both

enabled in the LighTouch[TM] GUI, experiments for *in vivo* glucose and other blood

constituents monitoring is configured to be done under "Glucose" mode, while Hct

measurements are taken under "Hemo" mode. For both modes, all sensor recordings

including force, pressure, contact area and in-contact quadrant dots of the four directions, together with CCD spectra for each 20 ms frame are logged. The record of the measurement sequence provided by LighTouch^{TM} device allows deduction of the course of events. Human factor induced unexpected variations on the collected spectra could be verified by double checking with the sensor outputs. Therefore, rejection of unreliable data could be based on objective quantitative criteria and would ultimately help the glucose monitoring in making solid and trustworthy predictions.

While there are many types of motion and placement artifacts, Figure 2-12 and Figure 2-13 show data demonstrating two frequently observed motion artifacts made detectable by this instrumentation. In Figure 2-12, the sensor records of an intentional "rolling motion" of the type described by Asada (77) are shown. In this case the initial placement of the finger is skewed (uneven number of spots top and bottom, i.e., quadrants 1 and 0, at t=0) and apparently becomes acceptable (not equal but stable numbers of spots for each) for the last third of the experiment. But the asymmetry evident in the quadrant dot pattern in the middle graph shows that the finger rolled somewhat from top to bottom during the first part of the measurement.

The placement was skewed initially and remained slightly skewed after the rolling motion occurred, i.e., no twisting motion occurred simultaneously. We know it was a rolling motion and not a scraping motion because the quadrants 2 and 3 (spots are on either side of aperture along the axis of the finger) are relatively constant. The change in contact area was abrupt, so we know there was gross motion and not normal subsurface fluid movement due to the applied pressure. On this basis alone the data should be rejected. This record was generated intentionally but it also corresponds to the situation

when the well-meaning test subject suspected that something was wrong after the

measurement cycle started and tried to correct the placement without informing anyone.
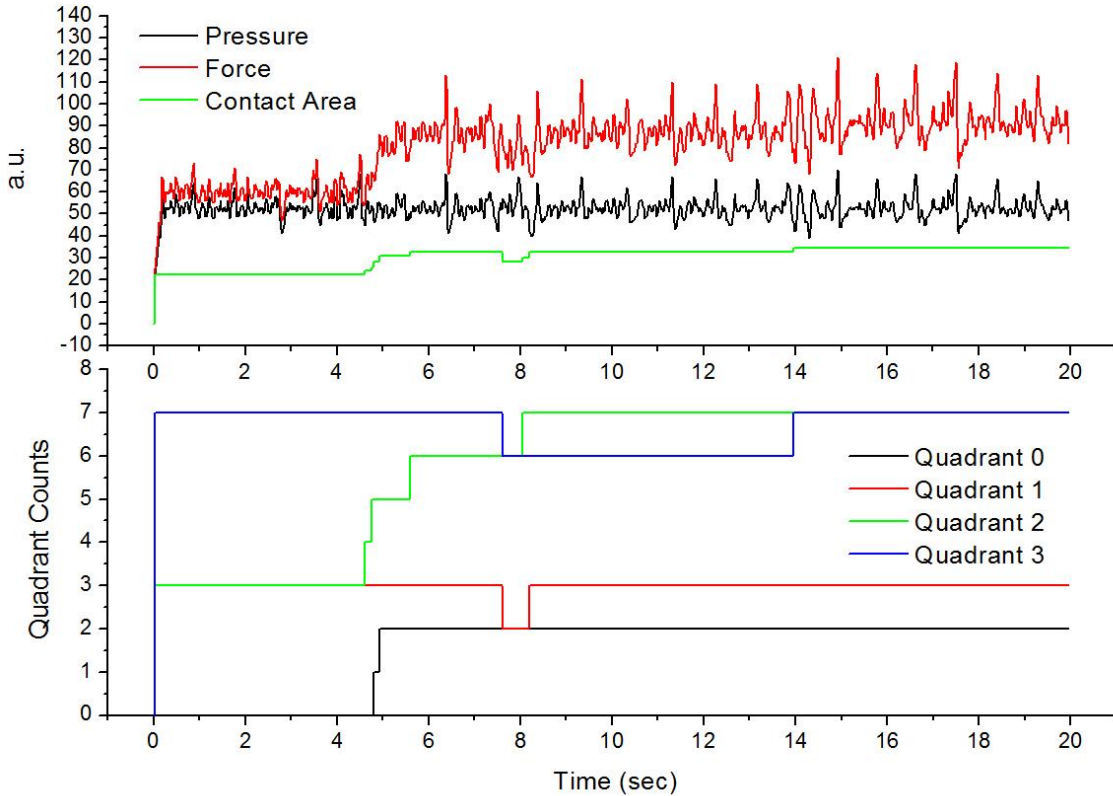
Figure 2-12: PDPM sensor outputs for a 20 sec measurement cycle showing the rolling motion of a fingertip. Top: actual pressure, force, and contact area (scaled to fit in the same plot) for a given measurement period. Bottom: plot of numbers of contacted dots in each quadrant showing that finger rolled at about 5 sec into measurement period. That contact is spatially skewed and abrupt motion occurs during the measurement and the data should be rejected.

Although the involvement of rolling motion disqualified the simultaneously

collected spectra for quantitative glucose concentration prediction purpose, the PDPM

did maintain pressure almost constant throughout the experiment cycle. Rolling motion

by nature is slow, subtle and is not necessarily accompanied by appreciable force changes.

The solenoid is thus able to compensate accordingly. However, as shown in Figure 2-13, stable force maintaining is always challenging for seniors and subjects with neural disorders even with the help of PDPM as involuntary tremors happen from time to time even if the test subjects are striving to be compliant.
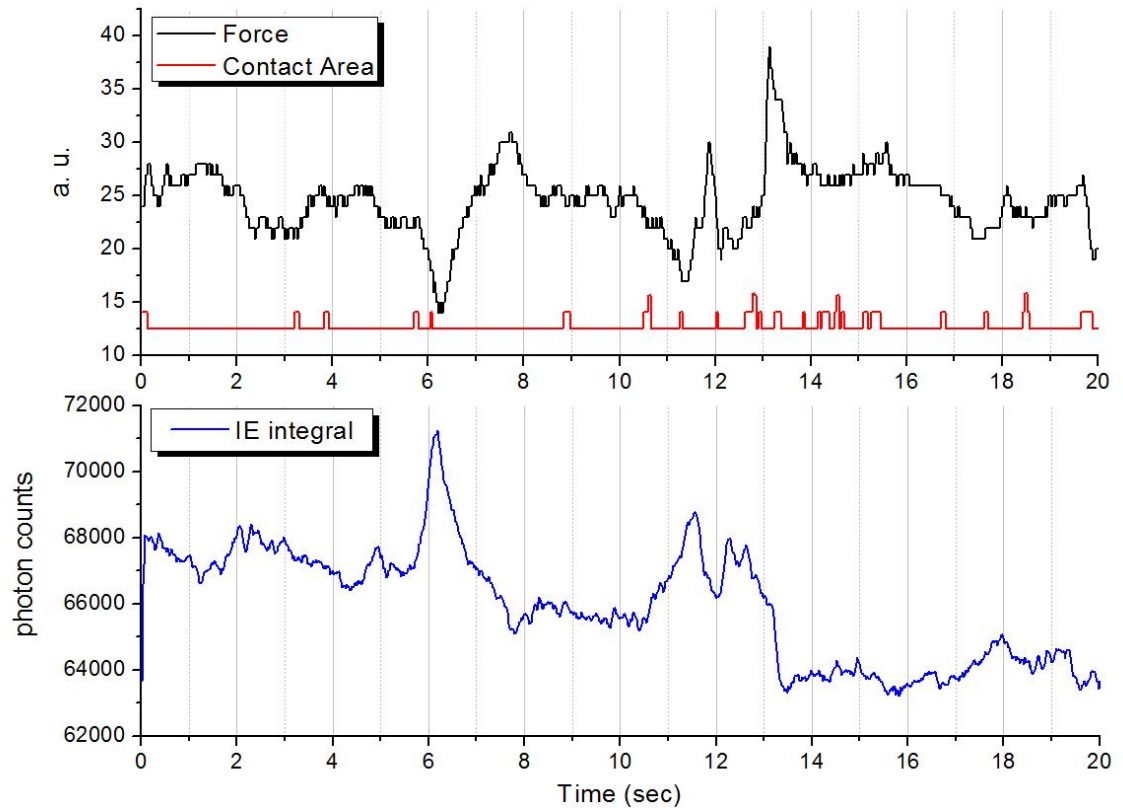
Figure 2-13: Tremor is shown on the logged force (black), contact area (red) and IE (blue) curves for a senior Caucasian male. Contact area is scaled ($\times25$) in order to be put with force in the same plot. PDPM failed to compensate when test subject is actively involved.

In the PDPM set-up, test subject is supposed to be passive and let the PDPM maintain and adjust exerted force based on preset target pressure. However, in the case shown in Figure 2-13, throughout the entire course of a 20 sec experiments the test subject waggled, causing erratic ups and downs on the force sensor recording. The

amplitude of such force variation exceeded the dynamic range of PDPM itself, therefore pressure compensation failed in this scenario. Even worse, several tremors happened right after 6 sec, before 12 sec and after 13 sec respectively. The abrupt push and releasing of force obviously interrupted collecting of spectra, as clearly shown in the IE vs. Time curve. Empirically, pulsatile blood flow usually causes 1000 – 2000 photon counts variation on IE curve. But these tremors made changes of almost 5000 counts, two times more than the pulses. Not shown in this figure is that the horizontal quadrant 2 increased as the quadrant 3 on the opposite direction decreased, meaning the tremor also resulted in a change of fingertip position. Without question, the collected spectra could not be used in glucose concentration calculation.

2.3.2 Pressure Registration

Acknowledging the benefits by keep a recording of the PDPM sensor outputs, it is even more important to feed this piece of information back into the loop and achieve automated pressure servo. It is already been shown in Figure 2-13 that involuntary motions like tremor deteriorate the spectra. Yet it is not surprising that slight skew of fingertip position could also be easily captured spectroscopically. Figure 2-14 shows the IE vs. Time curve collected corresponding to the rolling motion in Figure 2-12. Decrease of IE integral around 4 sec is induced by force compensation due to an increased contact area, while a brief increase at 7.5 sec corresponds to a sudden contact area drop that might result from a poor contact.
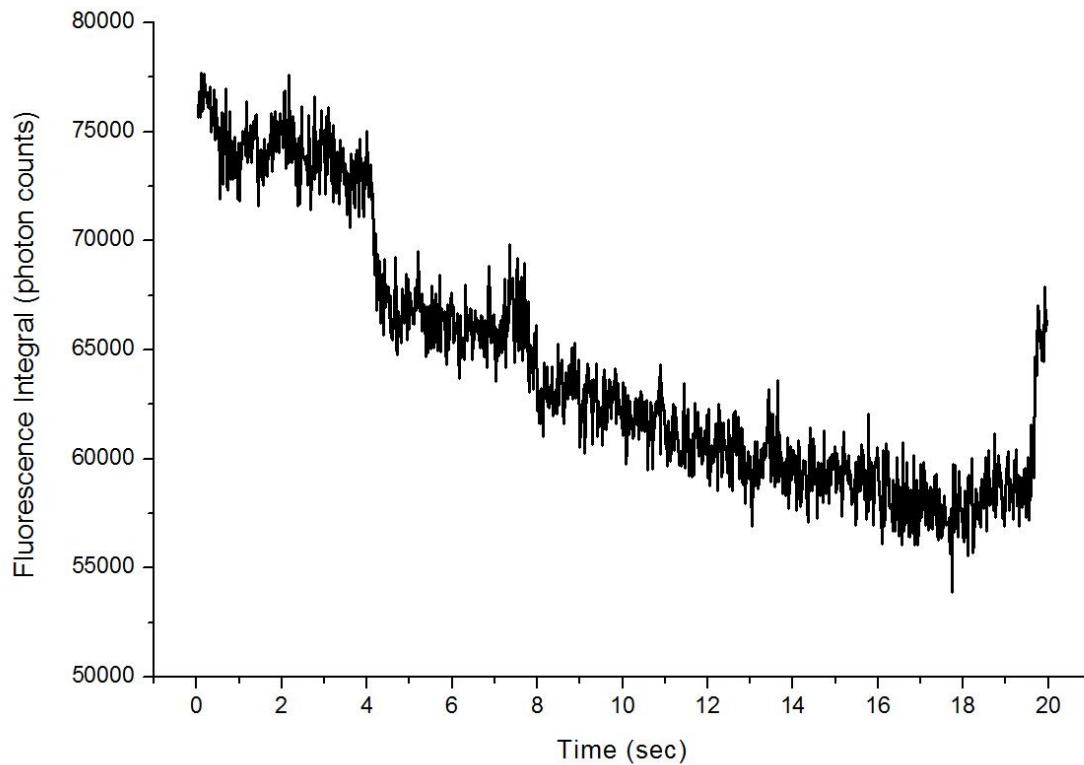
Figure 2-14: IE vs. Time curve collected corresponding to the sensor history in Figure 2-12. Rolling motion of fingertip, although not as detrimental as tremors, still produces a noticeable influence on the harvested spectra. Decrease of IE integral around 4 sec is induced by force compensation due to an increased contact area. A brief increase at 7.5 sec corresponds to a sudden contact area drop that might result from a poor contact.

Currently, the resistance change between the annular metal and surrounding gold dots is used as a measure of contact surface. Thus the issue arises when a fingertip is actually in contact, but due to lack of hydration or other possible reasons, e.g., very low turgor, flickering of the dots results in unstable contact area calculation. Frequent adjustment of force by PDPM will end up with undesired disturbance of blood flow. However, as mentioned in Section 2.2.3, application of a thin layer of any commercial

available lotion will make the patterned dots work better and to some extend help the measuring process.

To compare the performance of PDPM with the human sense of touch, four test subjects with various levels of familiarity (see Table 2-2) with LighTouch^{TM} apparatus participated in a series of designed experiments. For each subject, shorter than normal length experiments without tissue modulation, i.e., the pressure was maintained constant throughout the experiments, were perform either with or without PDPM. When PDPM is not used, test subject was asked to keep fingertip in position and do the push to the target pressure by him-/herself. Four target pressures were assigned, from 60 gf/cm^2 (44 mmHg) to 120 gf/cm^2 (88 mmHg). BP, together with pulse rate, of each subject was measured with a commercial automatic blood pressure cuff (HEM-712C, Omron, Osaka, Japan). Since the BP varies at different time of the day for each individual, the number listed in Table 2-2 is the average of multiple measurements taken at various times of the day.

Table 2-2: Test subjects summary for a PDPM performance study.

TEST SUBJECT	GENDER	ETHNICITY	AGE	PULSE RATE (bpm)	BLOOD PRESSURE (mmHg)	FAMILIARITY WITH PDPM
1	F	Asian	27	63	90/60	Well
2	F	Hispanic	20	59	122/76	New
3	M	Middle Eastern	78	48	126/78	Good
4	M	Caucasian	54	68	142/86	Well

Force records of eight short experiments, four with PDPM (black) and four without (red), of each test subject is plotted by stacking them with offsets in Figure 2-15. Other than the senior test subject, all three others show less random variations with the PDPM. Not shown in the graph, quadrants for subject 3 blinked on and off, thus resulted in poor performance even with PDPM. Clear cardiac pulses are also presented when PDPM is in registration with the finger, while the similar features are completely gone if test subjects tried to maintain the target pressures themselves, even for the experienced subjects.
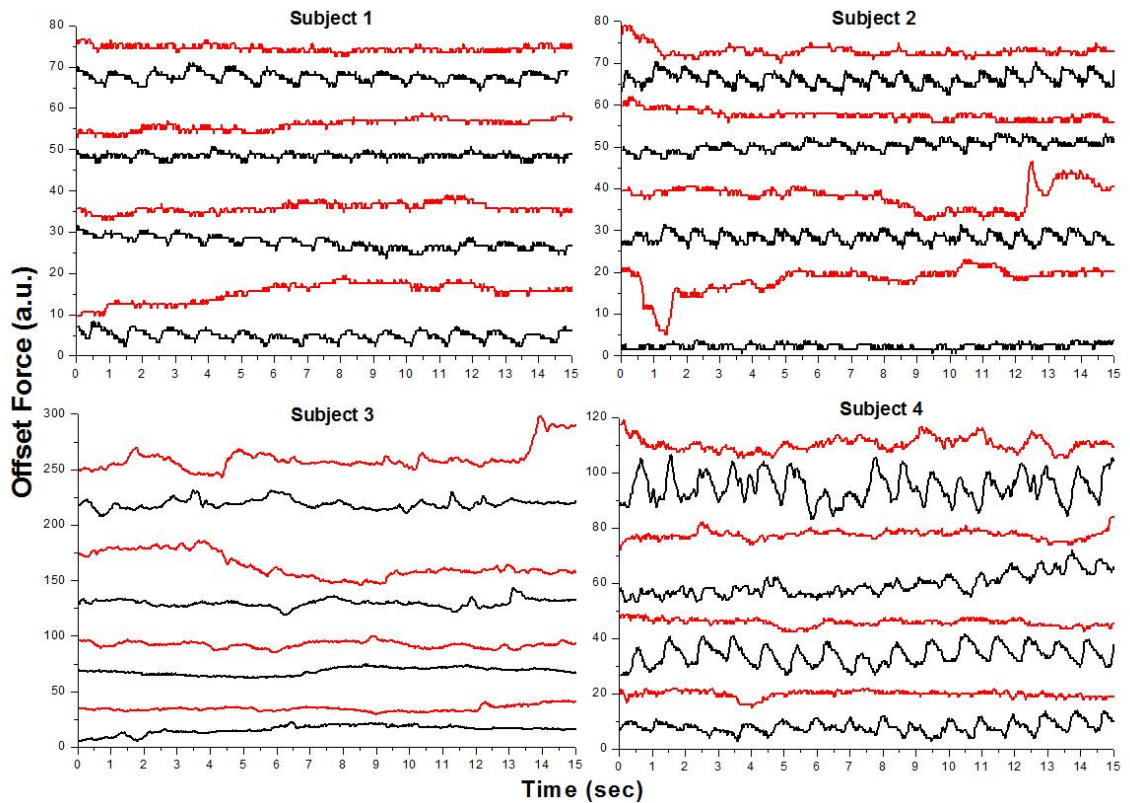
Figure 2-15: Force records of 4 subjects in a series of short *in vivo* experiments showing the difference between using (black curves) or not using (red curves) PDPM. Four pressures were applied, 60, 80, 100 and 120 gf/cm^2 respectively. For each subject, force curves are plotted by stacking them with arbitrary offsets but in a consistent force increasing manner, i.e., bottom two curves were taken under 60 gf/cm^2 while the upper two curves were taken under 120 gf/cm^2.

Although arbitrary offsets make the force axis lose its numeric meaning, relative

comparison indicates that for people with high BP such as subject 4 the maximum size of

pulses well exceeds that for lower BP subjects such as 1 and 2. Mechanical pulses are

always easier to be seen, which is not surprising. The y-axis span for subject 3 is almost 4

times bigger than that for the first two subjects, indicating a much more instability, as

shown in Figure 2-16.
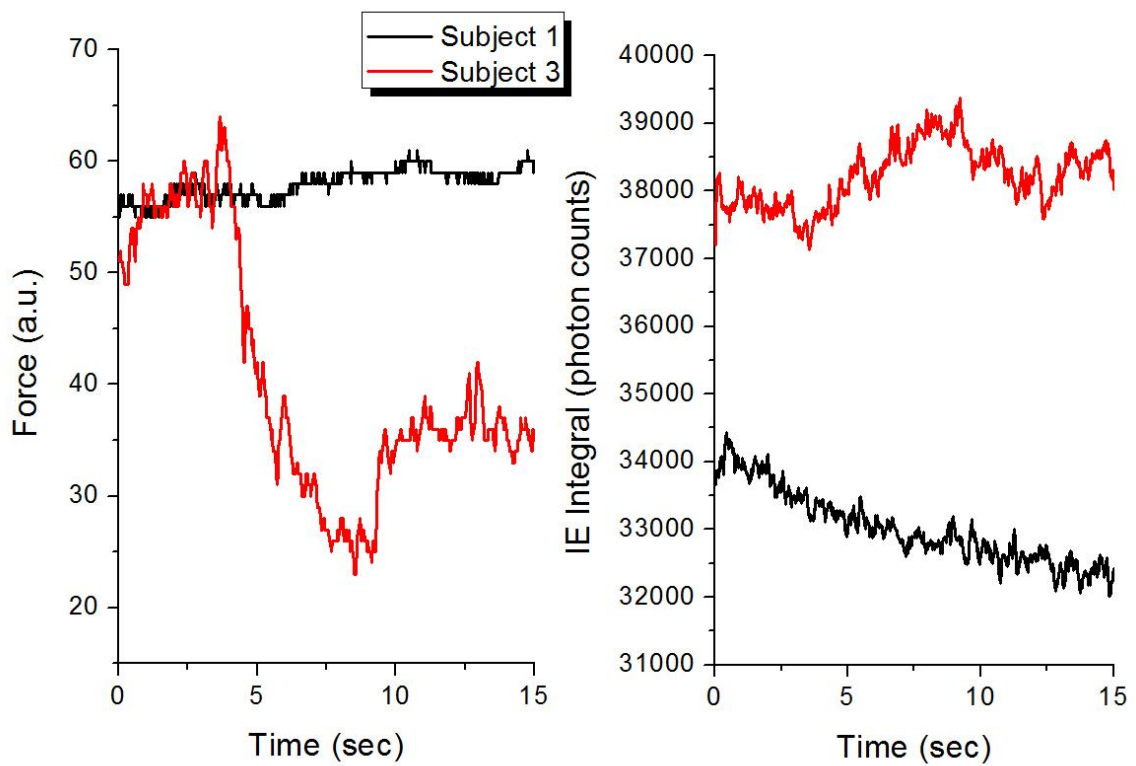
Figure 2-16: Comparison of force and IE variation between subject 1 and 3. For both subjects, no PDPM facilitation was supplied. Test subjects used their own sense of touch trying to maintain pressure at 100 gf/cm^2.

Usually, as shown in Figure 2-16, with a good contact the force varies within 5 units,

but this can be magnified up to 10 times bigger in situations like tremor or random finger

movements, which is more likely to happen among senior test subjects. As mentioned before, such motions are what we are trying to avoid. By either monitoring sensor or optical outputs, selecting rules can be developed and used to automatically screen out invalid data. By taking a scrupulous look at the IE curve for subject 1 in Figure 2-16, one may notice a trend of decreasing. Part of such decrease corresponds to the slowly increased force, but most of this quench is related with some photochemistry that will be discussed in detail in Section 3.2 of Chapter 3.

Most of the time, whenever mechanical pulses are observed, one could expect to see optical pulses. But they are not necessarily connected. Depending on how the fingertip is engaged with the PDPM, mechanical pulses could be easily invisible. For example, a simple cylinder (Nylon with a contact area of ≈ 0.27 cm^2) was once used to replace the splint and fixture design, shown previously in Figure 2-10 and Figure 2-11. The shaft could easily fit a wide range of fingertips, no matter how big the width and curvature. However, it is hard to detect mechanical pulses with this arrangement, even for subjects with high BP.

We notice that the way shaft is mounted to the solenoid makes it waggle, and the small contact with the back of fingertip causes it to slip off the finger from time to time. By contrast, the currently used design guarantees a much more solid contact, and that favors the sensitivity of force measurement. Moreover, load cell calibration also determines the sensitivity of the force detection. A poorly calibrated transducer will result in a limited dynamic range that may or may not enable us to see the mechanical pulses. The step-by-step instruction on how to perform a solid load cell calibration is elaborated in APPENDIX A.

On the other hand, spectroscopic signals explain the observation of pulses in a totally different way as mechanical force does. With our *in vivo* instrumental setup, as long as the photons collected have reached the depth of capillary layer and optically interacted with the molecules within blood, then optical pulses should be expected. Evidence is shown in Figure 2-17, where under the pressure of 60 and 80 gf/cm^2, optical pulses were still clearly observed even if no sign of mechanical pulses.
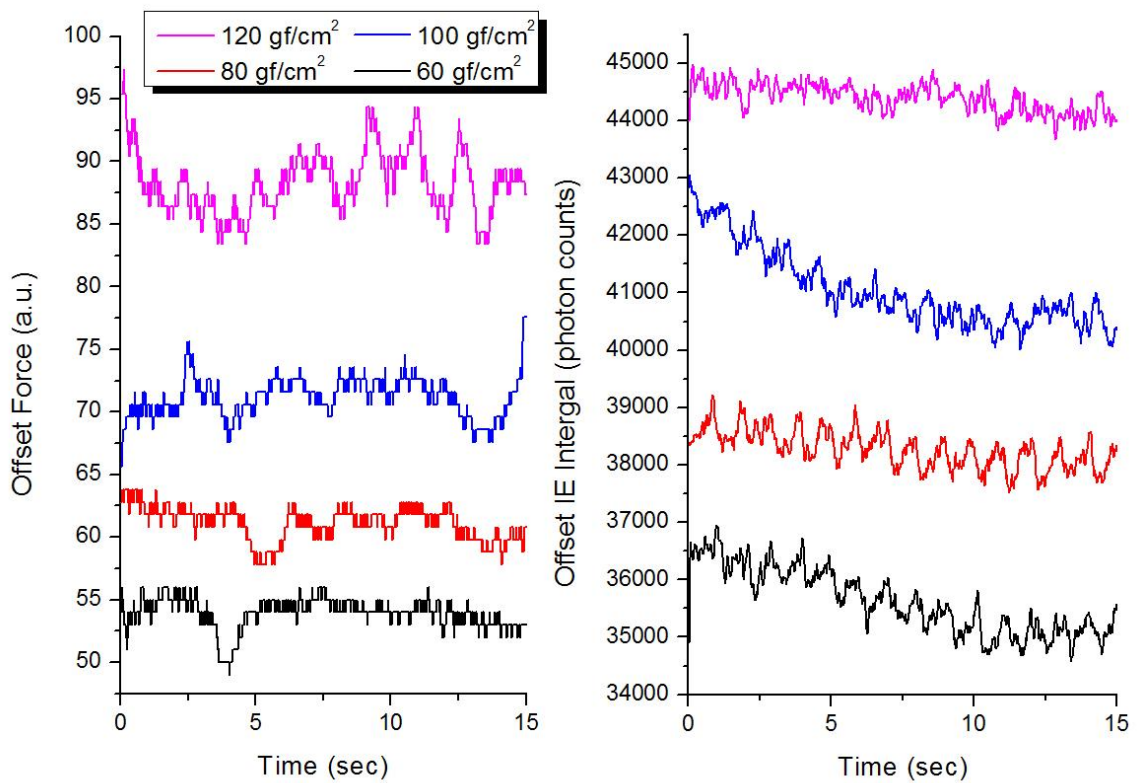
Figure 2-17: Offset force and IE curves under evenly spaced four increasing pressures for subject 4 who has the highest BP. No PDPM assistant in positioning and pressure maintenance. Under pressure of 60 and 80 gf/cm^2, optical pulses were still observed even if no sign of mechanical pulses.
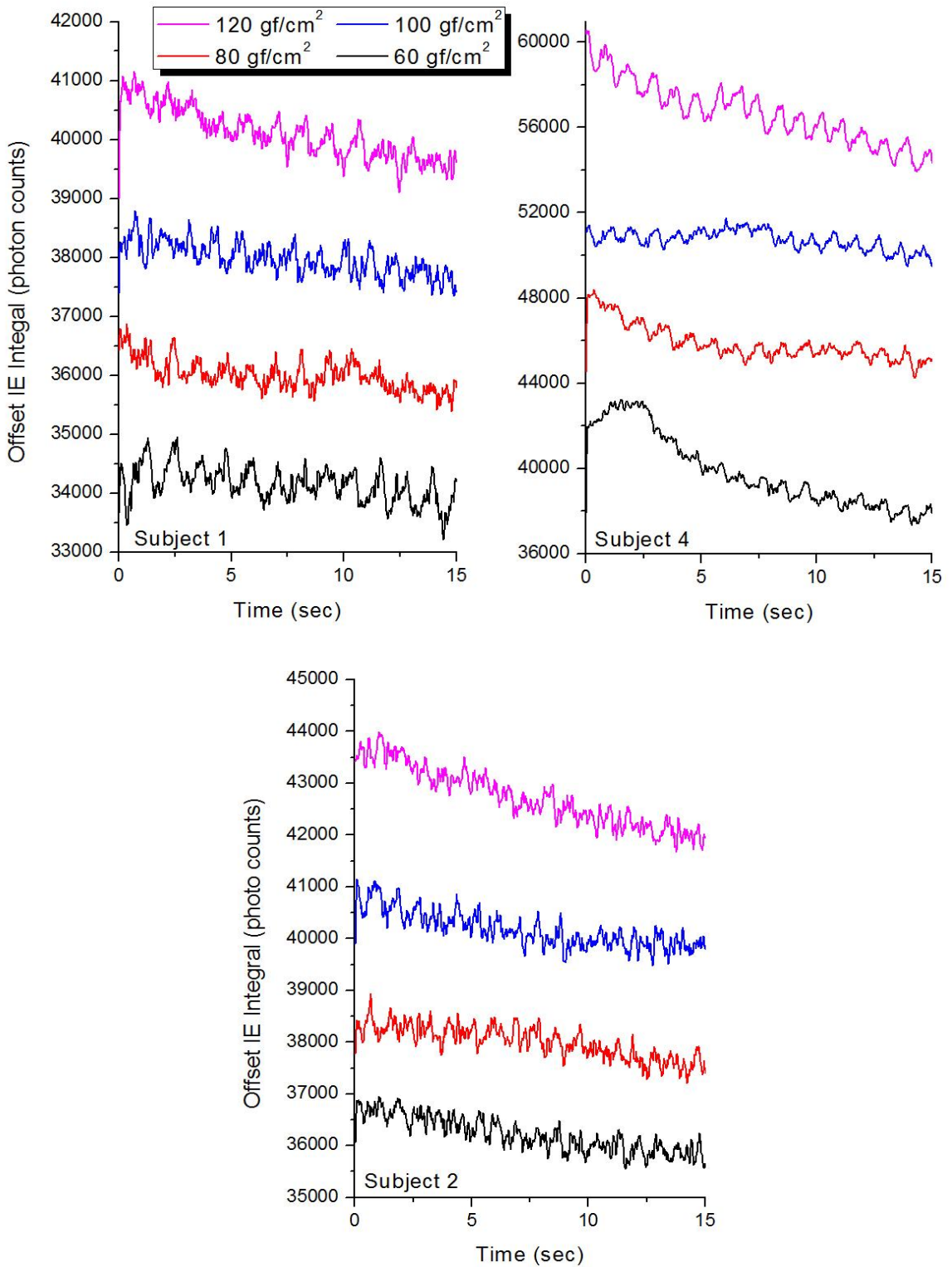
Figure 2-18: Optical pulses from subject 1, 2, and 4 showing various pulse amplitudes under different pressures. Spectra were all collected under PDPM registration.

Finally, as demonstrated in Section 2.1.4, principles in oscillometer indicate that while pulses can be detected within a relatively wide range of pressures, i.e., from below diastolic to well above systolic pressure, the best mechanically translated pulses can be achieved at MAP. Forces plotted in Figure 2-15 have already shown mechanical pulses for almost all test subjects in the pressure range of 44 to 88 mmHg. For comparison, optical pulses for subject 1, 2 and 4 are plotted in Figure 2-18. As expected, IE vs. Time curve also shows the existence of cardiac pulses, however slightly different amplitudes are observed.

Although it is subjective to judge the quality of pulses, for subject 1 under the pressure of 60 gf/cm^2 (44 mmHg) the IE curve shows the strongest pulses. Similarly, subject 2 shows best optical pulses under 100 gf/cm^2 (74 mmHg) and that pressure for subject 4 is 120 gf/cm^2 (88 mmHg). From Table 2-2, the MAPs calculated for subject 1, 2, and 4 are 70 mmHg, 91 mmHg and 105 mmHg, respectively. A reasonable connection could be found here that could be used to guide the selection of modulation pressure in order to reach the maximum optical pulses. Such a selecting standard will help in producing reproducible spectra for individuals and also make it possible to compare data collected from same person in different days.

2.3.3 Fingertip Topography

As mentioned in section 2.1.3, due to the commensurate size of the laser spot with the breadth of fingertip ridges, the incident light could either contact the surface skin on top of a ridge or at the bottom of a furrow. To validate this statement, images of fingertip

over the opposite side of the apertures were taken by inserting an ultra-thin semitransparent pellicle mirror after the triplet lens in the collection side. Additional white light illumination and neutral density filters were utilized to help visualize the bright laser spot and minimize blooming. The pellicle guided 10% of the reflected light into a CCD camera and frames of image were taken using Snappy video digitizer (Play Inc., Folsom, CA, USA). Over the time span of a week, images for seven individuals were collected and several typical images for a single subject are plotted in Figure 2-19.

Direct observation through the collection system shows that nearly all test subjects can remain stationary to within ±10 μm relative to the aperture for hundreds of seconds, not including inevitable involuntary tremors and similar random motions. In panel (B), fingerprints together with the sweat glands could be clearly seen and in this scenario the laser hits across the edge of a ridge into a groove. Despite of the over glow on the right side of laser spot, it is still clear that the size of laser is in the similar scale as fingertip ridges. When a different pressure was applied, the laser spot shifted and hit right on top of ridge. Attributed to the uneven topography of fingertips, the local angle of incidence could easily deviate wildly from 53 °, the angle to guarantee maximal penetration into the skin *if it were flat*. As a result, propagation into the tissue is to a nonnegligible extent dependant on the precise positioning of the fingertips of test subjects.
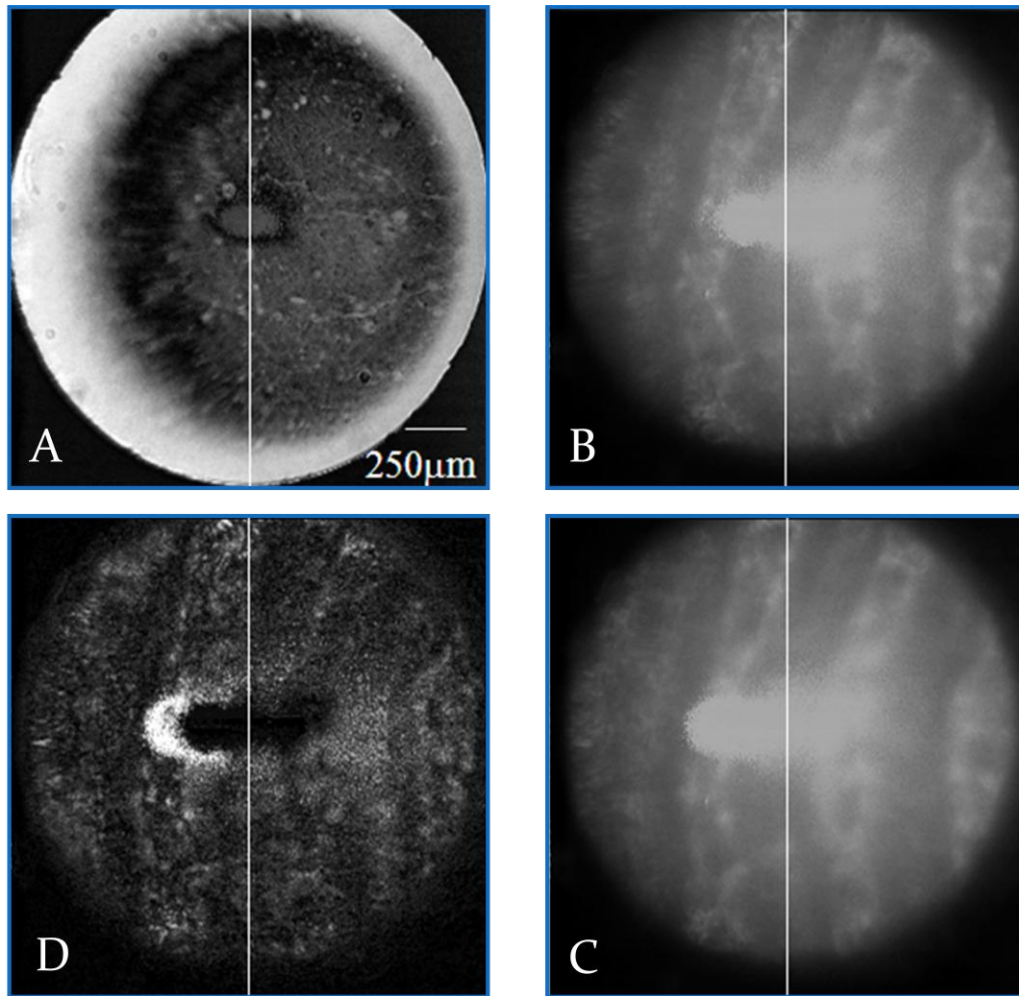
Figure 2-19: Imaging of the LighTouch^{TM} aperture. (A) Backlit flat Delrin^{TM} block. (B) Unpressed fingertip (pressure ≈45 gf/cm^2), showing illumination at center. (C) Fingertip pressed hard (pressure >140 gf/cm^2), showing displacement of illuminated area. (D) Difference between pressed (C) and unpressed (D). The images are taken by putting an ultra-thin semitransparent pellicle mirror right after the triplet lens in the collection train.

These images also show the doming issue that is mentioned in section 2.1.3. The optical system is initially aligned so that the light is incident at the middle of the aperture if the sample is flat and in the plane of the aperture, as can be seen in Figure 2-19(A) for a thick flat piece of light gray Delrin^{TM}. When a finger is registered into the aperture in an unpressed state, as in Figure 2-19(B), the ellipse of contact is slightly shifted to the side

of the tissue toward the incoming laser light. If additional pressure is applied, the point of contact moves farther toward the side of the incoming laser, as in Figure 2-19(C). This motion, as we discuss in detail in the following, is down the side of the extruded dome of tissue. However, Figure 2-19(D) shows the difference between images (B) and (C) and demonstrates that the total displacement, even for a very hard applied pressure, is only 10 to 30 μm.

In order to probe skin topography, the skin is translated relative to the laser beam, either by moving the finger relative to the aperture with the aperture stationary relative to the excitation and collection optics, or by moving the aperture relative to the excitation and collection optics with the skin stationary relative to the aperture. In the latter case, the amount of off-axis elastic light production depends on the location of the edges of the aperture relative to the laser. Figure 2-20 shows data obtained by the former approach. Here, a part of the fingertip was scanned where the ridges run perpendicular to the direction of motion. No precise control of distance translated per step was possible. Instead the total distance moved over the total observation time was divided into equal segments and displacement was assigned accordingly. While observing the color changes of the placement spots and the pressure slider on the PDPM feedback window, the fingertip was moved through a known distance in a known amount of time with relatively constant applied pressure. The calculated distance travelled was roughly 10 μm per step. The IE and EE integrals shown in Figure 2-20 are plotted versus steps taken. Both fluctuated by roughly 20% with a spacing of about 500 μm, characteristic of fingerprint ridges.
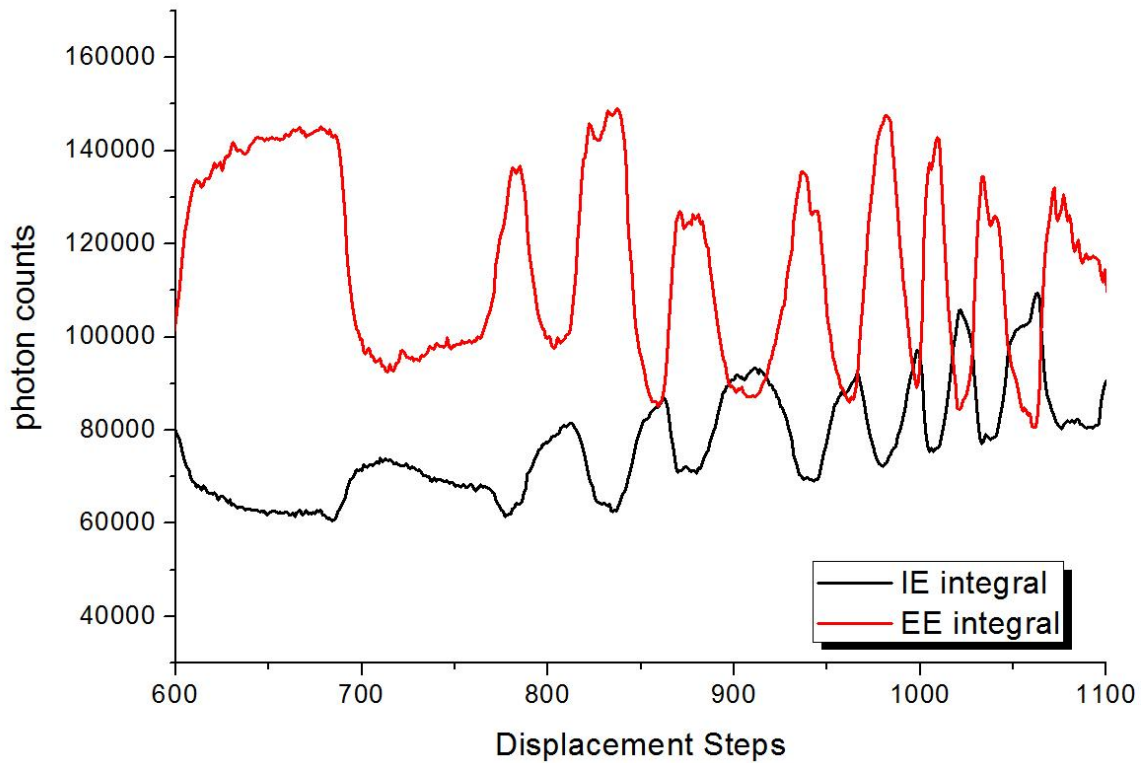
Figure 2-20: IE and EE integrals from scan of laser and detector across fingerprint ridges plotted against displacement of fingertip alone across a stationary aperture. The step size is roughly 10 μm per step.

Interestingly, the spatial fluctuations in the EE integral and the IE integral are complementary: one increases when the other decreases. Similar out-of-phase oscillations are observed in pulse modulated time-dependent measurements (81), in which the pulse causes a periodic increase in RBC volume fraction. Increased volume fraction of RBCs necessarily causes an increase in the IE, but this is accompanied by a decrease in the EE. A model built by Chaiken and Goodisman (10) predicts the temporal fluctuations due to both heart pulsing and the spatial fluctuations caused by fingerprint, although the explanations are different.
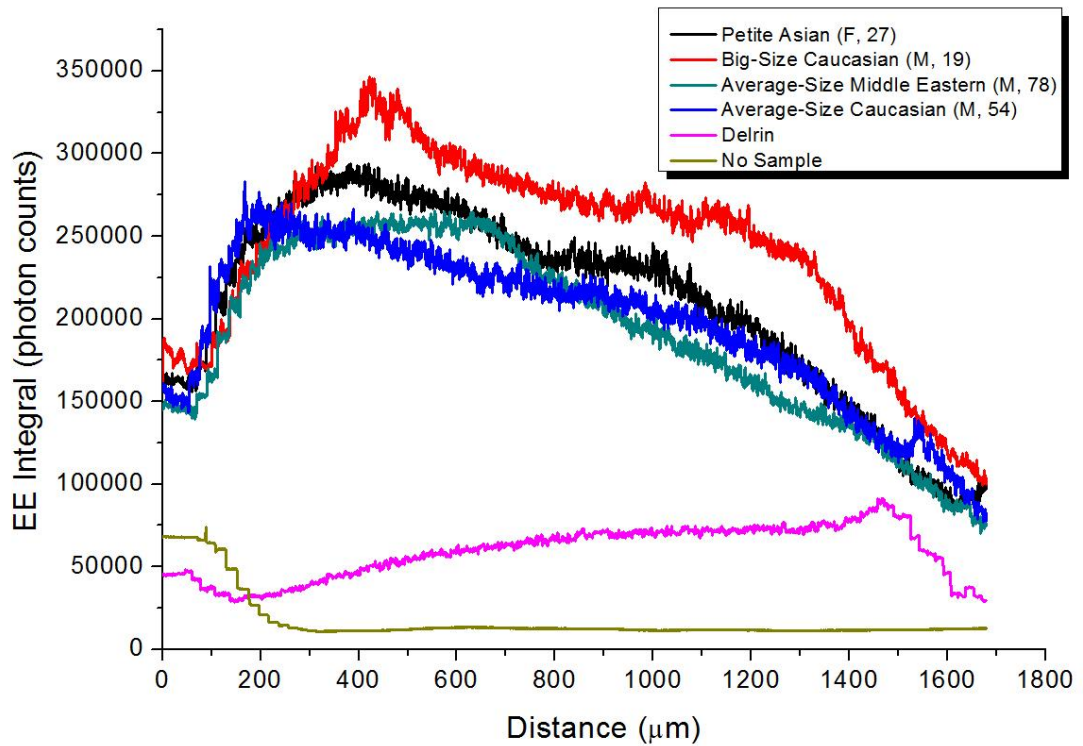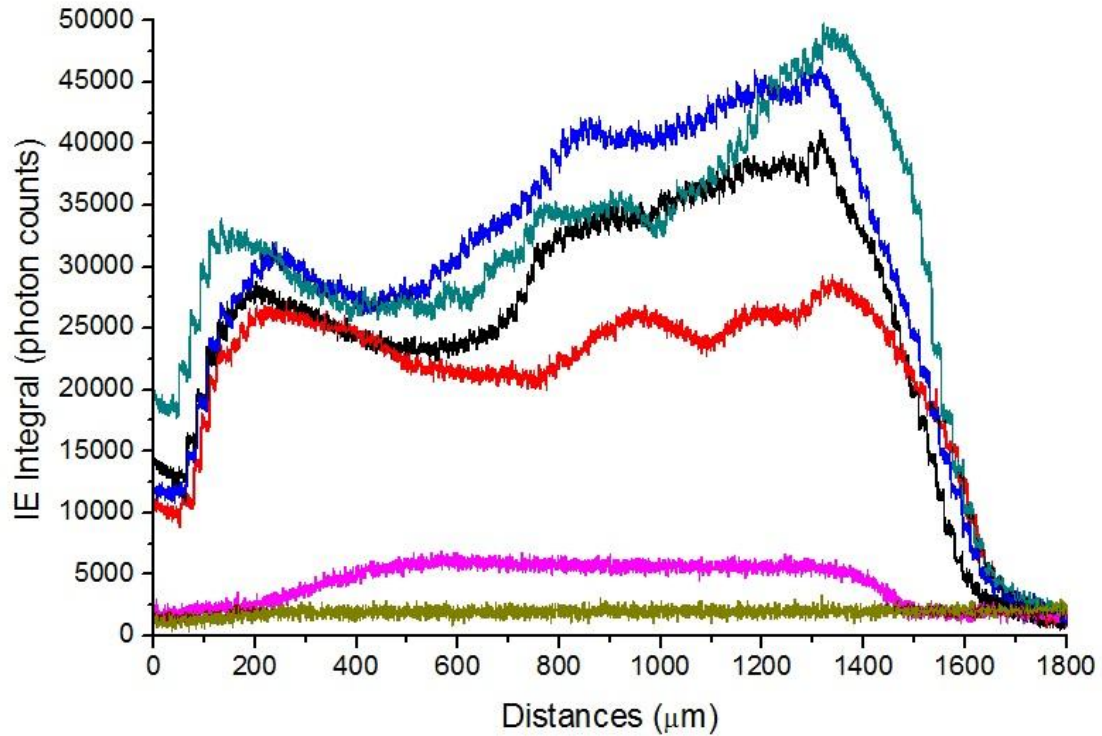
Figure 2-21: IE and EE curves as a function of displacement of aperture with respect to collection and excitation optics. In addition, a flat Delrin[TM] plastic sheet scan and empty aperture scan are shown. The subjects span three different ethnicities, 19 to 78 years old, from 110 lbs and 5'2" height to 260 lbs and 6'4" height, and both genders.

With our apparatus, a skilled test subject can scan his/her finger across the aperture, with known pressure and acceptable spatial precision and accuracy, using visual feedback from the apparatus. Nevertheless, this involvement of the test subject limits the reproducibility, precision, and accuracy of the results. Therefore, the data presented next were obtained using the second approach, in which the fingertip moves with the moving aperture driven by a micro-positioning actuator. The assembly containing the aperture is mounted on NSA12 motorized linear micro actuator (Newport Corporation, Irvine, CA), the step size of which could be programmed and tightly controlled to be 20 μm.

Figure 2-21 shows data obtained for four test subjects. In each case, the pressure used to maintain optical registration between the fingertip and the aperture was the average of the diastolic and systolic pressures measured with a commercial automatic blood pressure cuff. The laser has a 237 μm major axis while the aperture is 2 mm in diameter, therefore there are about 1750 μm (88 steps) effective displacement distance. A large increase in EE at the extreme right due to reflection as the laser beam strikes the outside of the aperture has been cropped. Oscillations apparently due to fingerprint ridges are evident, but so is a steady decrease or increase in intensity as one goes from left to right. This is associated with the doming of the fingertip pressed on the aperture (10). When the tissue extrudes a small dome is formed in the aperture and much of the difference between the Figure 2-20 and Figure 2-21 occurs because the position of the collection and excitation optics is locked on the same part of the dome for Figure 2-20 but the incoming lasers cans across the dome in Figure 2-21.

A wide variation in turgor, blood pressure, finger sizes, and skin tones are spanned by the selected test subjects with qualitatively similar results observed for all. Yet, Figure

2-21 shows consistent results using this instrument for a wide variety of test subjects. The consistency of these observations indicates that monitoring the variation in EE and IE with fine adjustment of the aperture position after the set-up procedure described above could allow the device to automatically find and interrogate the tissues at a location of consistent, predetermined topography and signal content. Specifically, positions of maximized IE and minimized EE are preferred because they correlate to the tops of primary fingerprint ridges (10).

2.4 Conclusions

Fingertip skin capillary beds are highly vascularized relative to other tissues and present a desirable target for noninvasive probing of blood. But human hands and fingers in particular are also highly idiosyncratic body parts requiring specific apparatus to allow rigorous and methodical spectroscopic probing. In an earlier study (50), the distribution of deviations between the noninvasive LighTouch™ glucose measurements and the reference fingerstick measurements reflected various sources of random and systematic error. Better management of the measurement process with regard to human factors emerged as a strategy for improvement with feedback based on applied pressure and tissue placement. Therefore, instrumentation for probing of volar side fingertip capillary beds with free space coupled near infrared light while collecting Raman, Rayleigh, and Mie scattered light as well as fluorescence is described in great detail in this chapter.

The apparatus includes means for precise and reproducible placement of the tissues relative to the optical aperture. Appropriate means are provided for applying and

maintaining pressure to keep surface tissues immobile during experiments while obtaining the desired blood content and flow. Soft matter, e.g., skin, extrudes into the aperture in response to any applied pressure, e.g., to keep the tissue in registration with the optical system, so the position, contact area, pressure, and force are continuously measured and recorded to produce feedback for an actuator applying force and to discern the compliance of the test subject. The compliance strongly affects the reliability of the measurement and human factors must be adequately managed in the case of *in vivo* probing. The present device is even more advanced since the actual application of pressure is automatic and could work for an unconscious test subject.

The digital quantitative records of the measurement cycle could be used for interpreting sources of errors in glucose concentrations in order to improve performance and better understand the total measurement process. Together with appropriate criteria based on general quantitative experience, any specific human factor data can be processed to allow objective rejection or acceptance of associated spectroscopic data before calculation of a glucose concentration for example *without* operator involvement.

Finally, despite the idiosyncratic aspects of *in vivo* human spectroscopic probing, the gross anatomy of ridged fingertip skin is constant across all but the most abnormal test subjects. The fingertip topographic results are reasonably consistent because the scanning of the different tissues samples, i.e., test subjects, has been relatively consistent. This general consistency suggests that the pressure is a universal variable appropriate for characterizing the state of perfused tissue and soft matter generally during spectroscopic probing. Thus it is important that the pressure be well defined in order to perform a spectroscopic experiment that can be executed reproducibly. It is possible that under

appropriate constant pressure conditions, the turbidity and relative density of the tissues in the probed volume do not vary much across individuals. Using this instrument, except for pulse driven motions and acoustic waves, the tissues can be isobaric and motionless during the measurement process. This does not necessarily mean that further processing of data acquired using this instrument for purposes of a turbidity correction (82-84) to the quantitative analysis of blood and other tissues are unnecessary. This must be ascertained with more experimentation, but using this instrument data collected for different test subjects or at different times for the same test subject can be compared and reproduced in an objective and quantitatively consistent manner. Many of the same ideas in this device would be applicable to spectroscopic probing of other types of soft matter, including *ex vivo* tissue samples for biopsy.

3. SIMULTANEOUS NONINVASIVE IN VIVO OBSERVATION OF IE AND EE

3.1 Elastic and Inelastic Emissions

3.1.1 Background

Figure 3-1 shows a Jablonski diagram that illustrates various vibrational and electronic states within a typical molecule with arrows to present scattering processes and electronic transitions associated with Raman, fluorescence and phosphorescence. Rayleigh scattering can happen when the incident photons hit an object, e.g., a molecule, which is much smaller than the wavelength of light with no energy transferred but only altered direction of propagation. Thus, this process is elastic. Not shown in the diagram, another similar elastic scattering i.e., Mie scattering, can happen when the size of the object is roughly the same as the incident wavelength. In our experiments we cannot differentiate between these two sources of elastic emission.

Of all the incident photons, roughly only one out of a hundred million will scatter from the sample at a shifted wavelength generating the extremely weak Raman scattering (32). A molecule in a very strong electric field, e.g., produced by a laser, has excited states, i.e., "virtual states", that only exist in the presence of the radiation field. Interaction with another photon from that same laser field in the manner indicated by the arrows can produce Raman scattered light as well as the aforementioned Rayleigh and Mie scattered light. Usually, part of the energy in an incident photon is transferred to the

molecule resulting in a remitted light that has a longer wavelength than the incident, which is called the Stocks emission. The Stokes Raman is the inelastic scattering that is observed in this study. Raman, Rayleigh and Mie are all *scattering* process and there is essentially no time delay between the incident radiation and the production of either elastic or inelastic emission.
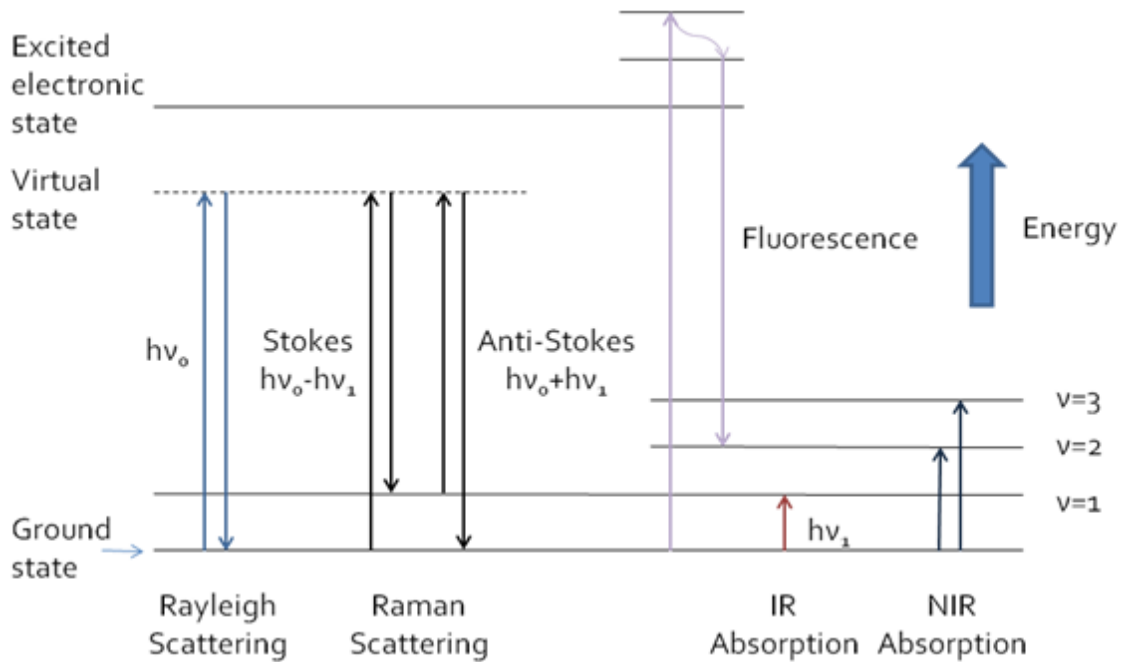
Figure 3-1: Jablonski diagram illustrating the electronic states within a molecule and transitions between them.

Similar to Raman, fluorescence and phosphorescence are inelastic processes. But for the latter two cases the incident photons must have enough energy to excite the molecule to an actual excited electronic state of the molecule, i.e., that is present regardless of an applied electric field, which is not necessary to produce Raman emission. Once excited, as a general rule, molecules in condensed phases, like the environment in the essentially water tissue, rapidly (10^{-12} – 10^{-15} sec) relax to the lowest vibrational level of the excited

electronic state and then give off an emission with a typical lifetime of $10^{-7} - 10^{-9}$ sec for fluorescence and $10^{-3} - 10^{-6}$ sec for phosphorescence (85). The excited state has different spin angular momentum from the ground electronic state for phosphorescence and it is the same for fluorescence. From the Jablonski diagram, it is obvious that both Stocks Raman and fluorescence processes involve energy loss and thus are both inelastic emissions. Experimentally we cannot separate the different sources of inelastic emission from each other without additional information, e.g., temporal properties.

In this study, the EE is Rayleigh and Mie scattered light, whereas the IE consists mostly of fluorescence and in absolute magnitude, only a small amount of Raman scattered light. The collected EE reflects the net absorption at the excitation wavelength but more importantly in terms of the relative amounts of collected EE, propagation losses due to physical scattering from structural and formed elements, e.g., collagen fibers and RBCs. Production of IE is initiated by absorption of the excitation light but there are other factors, e.g., the quantum yields for fluorescence and the cross sections for Raman, that contribute to determine the net collected IE. At least some of these factors would seem to be independent of the absorption process and thus for analytical purposes the measured EE and IE are effectively independent quantities with regard to their information content.

3.1.2   Potential In Vivo Application of EE and IE

In vivo, the NIR spectral range is the most advantageous for probing blood in human skin mainly because of the relatively low propagation loss and the low net absorption

such that the probing is nondestructive and therefore noninvasive. In the optical geometry as shown in Chapter 2 we believe we irradiate and collect light that mostly probes only to a depth of the capillaries in skin and with narrow bandwidth NIR excitation leads to easily separated EE and IE light.

The probed volume of human fingertip tissue can be modeled as a three-phase system: plasma and RBCs phases that are mobile, and a static tissue phase. The static tissue, different from the anatomic definitions of various skin layers, includes the cells in addition to the extracellular structural components and interstitial fluids, i.e., everything that does not move quickly under the influence of cardiac pulsing. The optical properties (86-88) of the three phases for 830 nm incident light are listed in Table 3-1. Static tissue has a tenfold larger scattering coefficient than plasma, and that of RBCs exceeds that of static tissue by *at least* a factor of 20. Thus, as will be demonstrated in a greater detail in the following context, the net propagation of light is mostly determined by the RBCs.

Table 3-1: Absorption and scattering coefficients at 830 nm for three phases, i.e., RBCs, plasma and static tissue.

PHASE	ABSORPTION COEFFICIENT	SCATTERING COEFFICIENT
r = RBCs	$\alpha_r = 4.5 \text{ cm}^{-1}$	$\mu_r = 300 \text{ cm}^{-1}$
p = plasma	$\alpha_p = 0.3 \text{ cm}^{-1}$	$\mu_p = 0.6 \text{ cm}^{-1}$
t = static tissue	$\alpha_t = 5 \text{ cm}^{-1}$	$\mu_t = 12 \text{ cm}^{-1}$

The IE that originates from fluorescence and Raman scattering contains overlapping components from all tissues in the irradiated volume, i.e., plasma, RBCs and static tissue.

Yet their fluorescence yields per unit volume are different. Resulting from fundamentally different physical processes, the apparent IE yields differ between RBCs, plasma, and skin in a manner that is uncorrelated with the variation in elastic scattering yields across the same tissues. Therefore, a model that takes these parameters into account should allow us to simultaneously estimate the relative volume fractions of the three phases in the probed volume, *in vivo* and noninvasively.
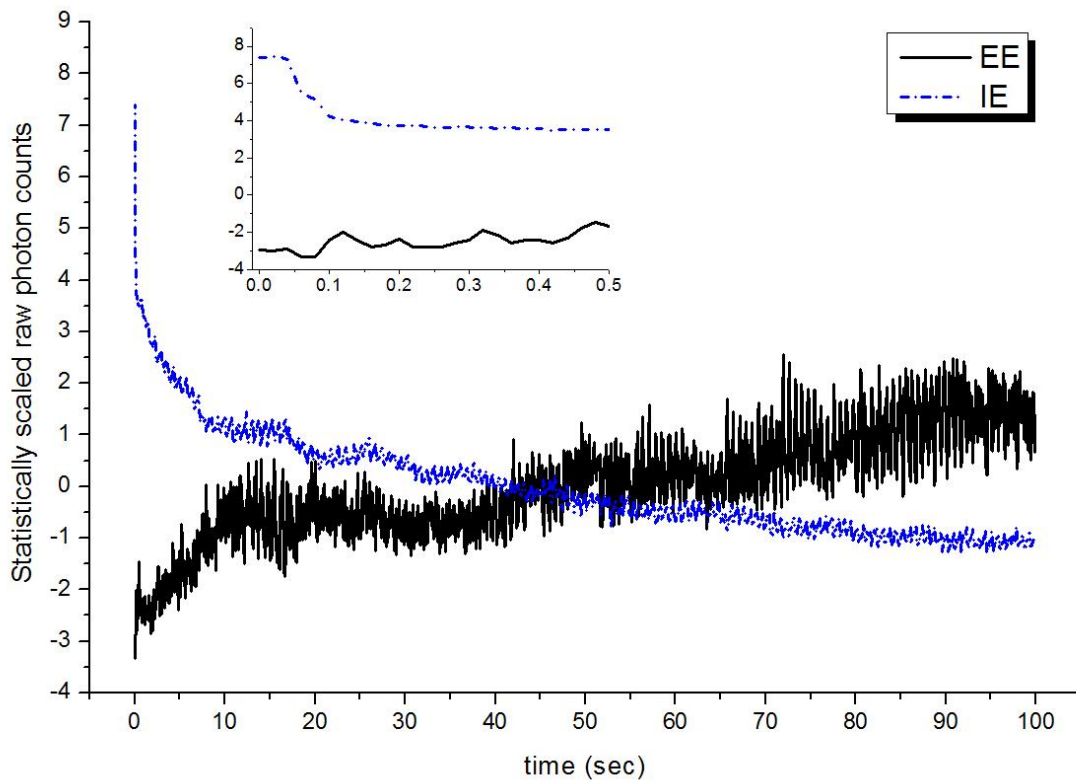
Figure 3-2: IE and EE as a function of time for a single very short and weak mechanical impulse starting at t=0 sec, followed by active pressure maintenance at 50 gf/cm^2. Inset: same data at shortest times.

Figure 3-2 shows the complete EE and IE curves collected for a typical 100 sec experiment with the pre-experiment "set-up" as described in Chapter 2. The IE and EE integrals are each plotted as a function of time. The data were transformed to have a

mean of 0 and standard deviation of 1 to facilitate their comparison. In the inset, we show the data for t<0.5 sec. Initially, the IE drops rapidly while the EE is nearly constant. Figure 3-3 shows some of the same data as Figure 3-2 but using an expanded temporal scale to show the complementary and very nearly proportional behavior of EE versus IE light.

To understand the relative time dependence of the EE and IE data on the time scale of the pulses and faster, two facts are important. First, the previously published (49, 50, 54) *in vitro* data for 785 nm excitation of methemoglobin over the concentration spanning the normal capillary blood range demonstrates that the integrated fluorescence, i.e., IE, increases linearly with increasing hemoglobin (Hb) volume percent. Moreover, as will be shown in Chapter 4, *in vitro* plasma fluorescence also increases linearly from infinite dilution in Normocarb™ to pure plasma. Thus, fluorescence measured *in vivo* is a measure of both plasma volume and Hb volume.

Second, the amount of elastically scattered light collected decreases as the volume percent of RBCs increases. In perfused skin, the volume percentages of the plasma, RBCs, and static tissues are constantly changing. A volume containing only static tissue and plasma would not scatter appreciably because the scattering coefficients are small. But propagation through a perfused volume may experience much larger changes because of changed RBCs volume fraction, because RBCs scattering coefficients are very large as shown in Table 3-1. If, for a heart-driven pressure wave, i.e., pulse, the volume percentage of plasma decreases, the volume percent of RBCs must increase, even if none actually moved, and the net elastically scattered light collected will decrease.
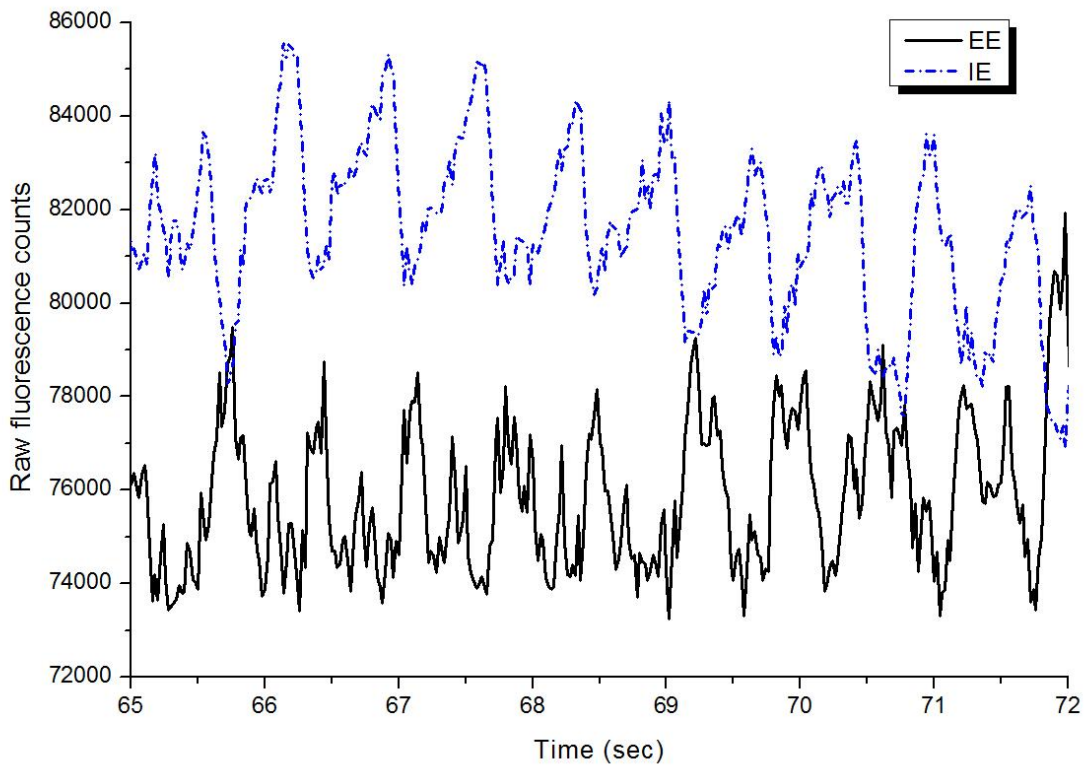
Figure 3-3: Same data as in Figure 3-2, shown at higher temporal resolution to show complementary behavior of EE versus IE.

At the shortest times as shown in the inset of Figure 3-2, when the actuator is establishing control over the pressure applied to the tissue, the behavior of the two plots (substantial decrease in IE with a *small* relative change in the EE) suggests that mostly plasma motion occurs. Because plasma motion out of the irradiated volume *decreases* the relative total blood volume percent and causes a decrease in the collected inelastically scattered light, we infer that the observed change in IE over the long timescale is due mostly to plasma removal. Apparently the small observed change in EE signal is due to a small movement of RBCs out of the irradiated volume, which keeps the change in volume percent of RBCs in the irradiated volume very small. This seems reasonable because, in the depth range we observe in Figure 3-2 plasma and erythrocytes are mostly

80

confined to narrow capillaries and the discharge and tube hematocrit (Hct) are very nearly equal (89). The effect of a relatively large change in IE due to plasma motion is compensated by a very small modulation of RBCs so the RBCs volume fraction is nearly constant.

Once the desired pressure value has been established, the pulses and other regular temporal oscillations in both the IE and EE data can be observed. The IE temporal behavior corresponds to the increasing and decreasing local blood volume as blood pressure pulses propagate through the capillaries in the irradiated volume. The capillaries become slightly distended as an increased volume of plasma and RBCs occupies the capillary lumen during the increasing pressure pulse. Because the RBCs have by far the largest scattering coefficient, change of EE collected light is most strongly associated with RBCs movement. Although most of the observed Rayleigh/Mie light originates from static tissue because that tissue has the highest volume fraction, the efficiency of *propagation* of the excitation light to the static tissue and of the elastically scattered light to the collection zone decreases as RBCs volume percent increases.

Therefore, simultaneous observation of elastic scattering, fluorescence, and inelastic scattering from *in vivo* NIR probing of human skin allows discrimination of the movement and presence of RBCs independently from plasma. Control of the mechanical force needed to obtain reliable optical registration of *in vivo* tissue with the optical system allows reproducible observation of blood flow in capillary beds of human volar side fingertips. The time dependence of the elastically scattered light is complementary to that of the combined fluorescence and Raman scattered light due to the changing volume fractions of the three phases in the irradiated volume with normal homeostatic processes

over time, i.e., heart-driven pulses, and the impeding effect of RBCs on optical

propagation. Thus, there is a potential to use these combined pieces of information to

calculate the volume fractions of the three phases, i.e., plasma, RBCs and static tissue,

which naturally leads to the Hct — the volume fraction of RBCs relative to whole blood.

This *in vivo* application will be further discussed in Section 3.3.

3.1.3   Negative Influences of Fluorescence Quench

For purposes of volume normalizing Raman spectroscopic signals that might be

associated with specific molecules in order to obtain concentrations of those analytes *in*

vivo, it is proposed earlier (46, 50, 51, 54, 81) to normalize the associated Raman signals

to the IE, the majority of which is fluorescence.
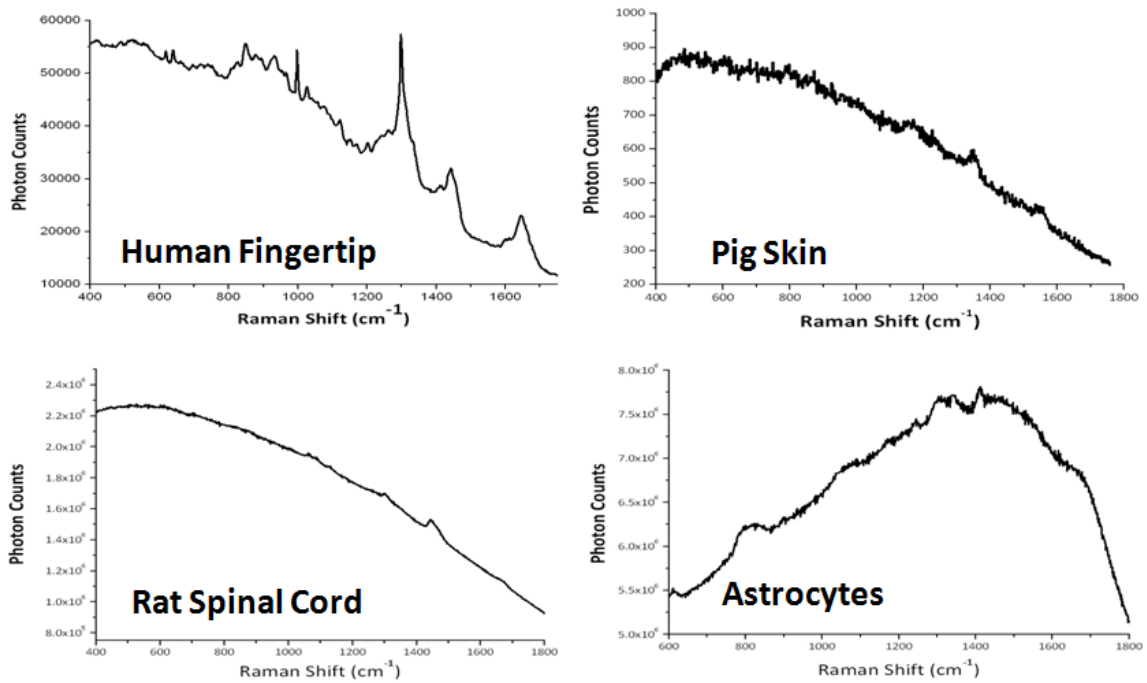
Figure 3-4: Fluorescence from various tissues and cells investigated *in vivo* or *ex vivo*
under NIR excitation.

As shown in Figure 3-4, for various tissues and cells that have been probed *in vivo* or *ex vivo*, fluorescence is ubiquitously observed and is related with the fluorophores within the probed volume. If all tissues produce fluorescence in proportion to the concentrations of fluorophores in those tissues and if the concentrations are constant in time then the hypothesis for volume normalization is supported.
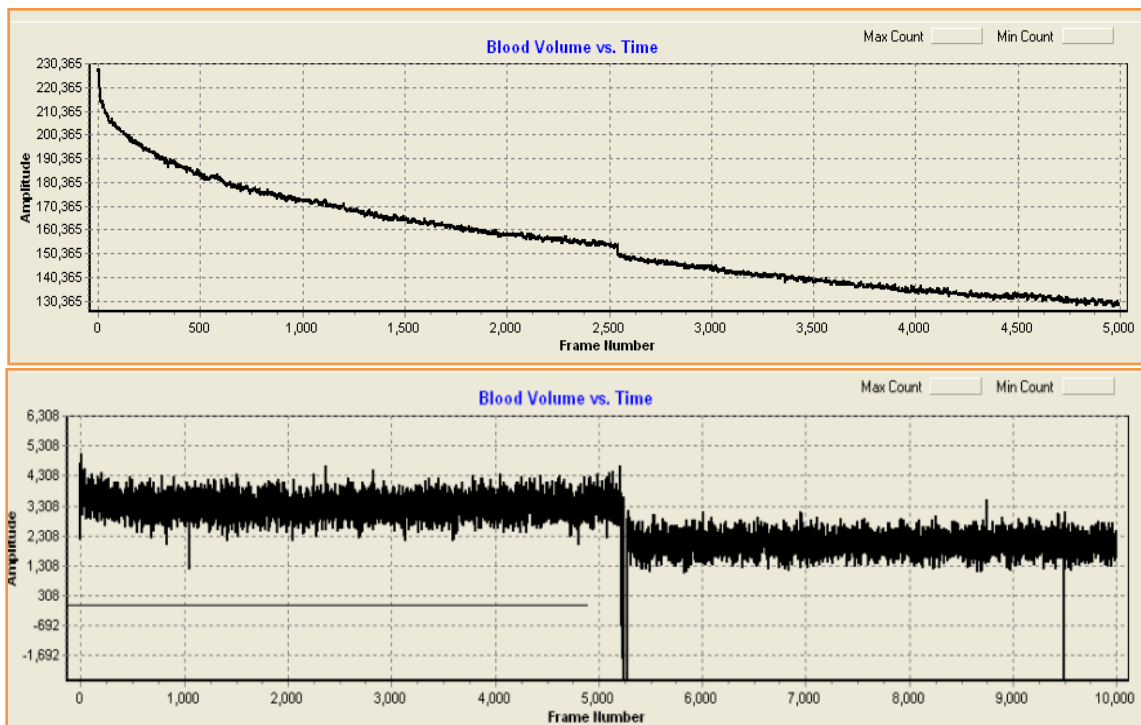
Figure 3-5: BV vs. Time curve screenshots of a typical *in vivo* collected human fingertip (A, top) and gelatin tissue phantom (B, bottom). Obvious trend of gradual IE decrease is observed in volar side human fingertip spectra.

Unfortunately, except for the drop of fluorescence in the middle of an experiment due to the pressure modulation of tissue, as shown in Figure 3-5(A), a typical *in vivo* BV vs. Time curve always shows an abrupt drop at the very beginning (usually within the first few seconds), and then slowly decreases with time. Ideally, as shown in the bottom panel of Figure 3-5, fluorescence change should only be observed when tissue

modulation occurs. Clearly, the *in vivo* decay indicates the change of fluorophore concentrations that is oppose to our hypothesis. Therefore, using the decreasing IE for volume normalizing will introduce uncertainties of inelastic emission that does not result from tissue modulation, which is detrimental to proper normalization.

To tackle the negative influences of such skin tissue fluorescence quenching, it is essential to study the origins and characteristics of *in vivo* human skin NIR fluorescence. Hopefully, the study in Section 3.2 provides an understanding to guide us in modifying our algorithm or experimental procedures to eliminate its detrimental effects. The relevance to the quantitative monitoring of glucose concentrations or Hct will be discussed in Section 3.3.

3.2 Characterizing Human Fingertip Autofluorescence

3.2.1 Dependence on NIR Irradiation

Besides the pressure administration exerted by PDPM, all the tissues of an organism are simultaneously under i) the oncotic pressure exerted by the osmotic pressure across physiological compartments due to changing electrolyte balance (44, 79), ii) the pressure exerted within the circulatory system, and iii) the hydrostatic pressure exerted by gravity on all the body tissues. From the outset we were suspicious that these pressure factors could be contributors to the gradual fluorescence drop as observed in the BV vs. Time curve in Figure 3-5(A). Thus, it is important to determine the timescale of possible fluid equilibration driven by hydrostatic pressure, if any, due to the changing body posture of the test subject in contacting with the apparatus, i.e., changing from a standing position to

a sitting position. In the extreme this can leads to the so-called "orthostatic hypotension", i.e., the dizziness upon standing sometimes experienced by people with low blood pressure. This process is also sometimes referred as "hydrostatic relaxation" (79). To appreciate and separate the effect of bringing the tissue into optical registration from that of changing the systemic hydrostatic pressure just before beginning the measurement process, the measurement sequence depicted in Figure 3-6 was executed.
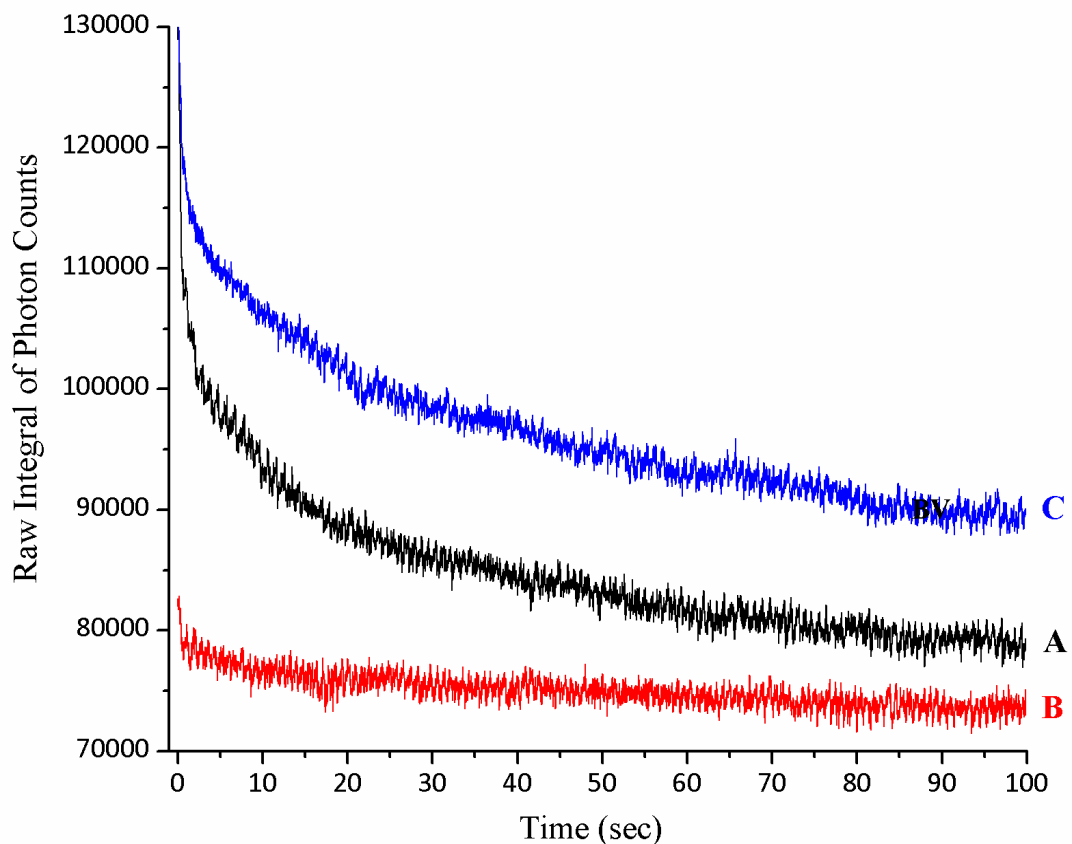
Figure 3-6: *In vivo* photobleaching and hydrostatic relaxation study. Condition: A) initial 100 sec experiment; B) a consecutive 100 sec experiment following immediately upon finishing of the initial experiment; C) a separate 100 sec experiment following initial 100 sec hydrostatic relaxation only, i.e., no laser exposure.

For the BV vs. Time curve A, a normally closed shutter placed immediately after the incident laser source was triggered open by starting the spectrum acquisition process following a quick "set-up" routine as described in Section 2.2.4, during which the finger was passively under the pressure administration fulfilled by PDPM. Immediately following the completion of curve A, the finger was maintained motionless (± 20 µm or less than about 10% of the physical dimensions of the laser spot) and the acquisition of curve B started.

To obtain curve C, the finger was retracted from the device and the test subject stood upright and walked around the laboratory for a total of at least 50 ft while executing movements of all appendages in order to re-equilibrate the blood in the entire body, thereby restoring normal hydrostatic status throughout. Then, with the laser blocked, the test subject re-registered with the device by selecting a slightly different spot with respect to the fingerprint ridges and running the same initial "set-up" routine. The hand was kept motionless and in contact with both the actuator and the aperture as the A run but not irradiated for 100 sec, a period of time equal to that of curve A collection. In this way, any fluid redistribution due to the changing hydrostatic pressure associated with assuming different body posture, i.e., sitting versus standing, would have the same time to occur but *without laser irradiation*.

As shown in Figure 3-6, obvious heart pulsing was observed throughout all the data. But in curve A, the initial value of the IE is large followed by a fast roughly 10^0-10^{-1} seconds decay and then a slower exponential decay over the next tens of seconds. In the case of curve B, however, the initial IE is nearly the same as the end of the A and not much drop in IE is observed. The dynamics of the C curve is nearly identical to that of

the A although the value of IE is greater than that of the A data. Since the difference in

data acquisition between curve B and C is only the 100 sec pre-experiment laser exposure,

we conclude that the drop in IE is associated with the presence of the laser and not due to

any change in hydrostatic pressure. Hereafter, such laser induced decrease of

fluorescence is mentioned as "photobleaching" and this photobleaching has been

observed for all subjects without exception.

The power dependence of the observed skin autofluorescence was also measured for

three test subject. Not surprisingly, the results shown in Figure 3-7(A) demonstrated that

the *in vivo* autofluorescence increases as the laser power increases. In addition to the

increased size of probed volume with greater incident laser power, higher power also

increases the penetration depth from which signal is obtained. Therefore, the observed

fluorescence at various powers could probably contain different relative contributions

from superficial static tissue and deeper blood components. This could in turn result in

change of rates and characteristics of photobleaching. Radiation transfer equation (RTE)

modeling including the correct probing and collection geometry (10) suggests that the

signal that is the IE has a power index of 1.0 when the excitation transition that produces

fluorescence is a one photon transition.

Recognizing that interpretation of the power dependence of the autofluorescence is

therefore complicated at best, we measured the quantity in order to i) satisfy engineering

needs, i.e., the scaling of signal with incident power is an important design parameter,

and ii) check for any evidence that the excitation process is a multiphoton process.

Measurement of the power index, i.e., the slope of a log power vs. log fluorescence plot,

is commonly used in the laser chemistry literature (90) to establish the order of the

slowest excitation step in any multiphoton process. While non-integral indices are commonly observed in complicated systems, e.g., representing an averaging over perhaps more than one excitation sequence, in well defined and simpler systems, such indices are rigorous proof in establishing the order of a multiphoton process.
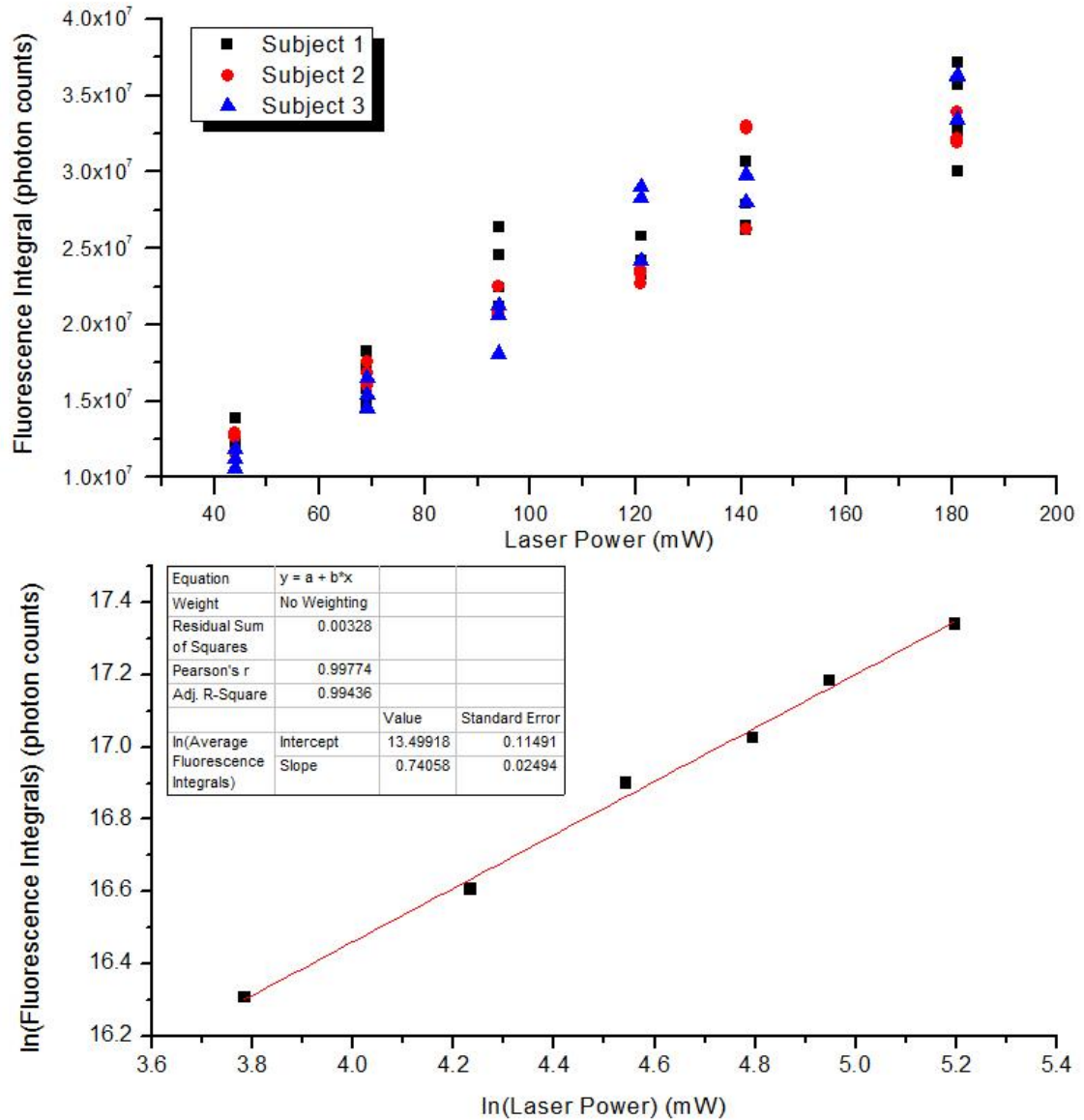
Figure 3-7: Laser power dependence of the skin autofluorescence. (A, top) IE integrals for three test subjects under six different laser powers. Data were collect on the same day. (B, bottom) Linear fit to the logarithmic values of both laser power and fluorescence integrals. Both panels show obvious IE increase as the increase of laser power.

As can be seen in Figure 3-7(B) the measured index was 0.74 for *all* the test subjects. While we have not yet tried to observe emission e.g. at 415 nm for 830 nm excitation, this index is consistent with the hypothesis that the autofluorescence is produced with NIR excitation of skin by a one photon absorption process. In analogy with simpler but possibly analogous systems, the power index could be less than 1.0 because in parallel with the excitation process, there is another laser induced process that causes a decrease in the collected fluorescence with increasing incident power.

Another study on the characteristics of photobleaching at different laser powers was performed on six test subjects. For each test subject, only one laser power was investigated a day to avoid any possible accumulative influence of such bleaching. Thus the data collected covered a relatively longer period of time. The firstly clear observation in Figure 3-8 is that the data collected for a diabetic patient stand out. The autofluorescence from the diabetic subject not only has almost three times bigger starting fluorescence, but also bleaches more than 60% toward the end of a 200 sec experiment. Similar excessive fluorescence and bleaching are observed for a senior subject, but not to an extent like the diabetic patient. For all the rest subjects, fingertip autofluorescence typically bleaches 15-20%, with a slight increase toward higher laser power to around 20-30%.
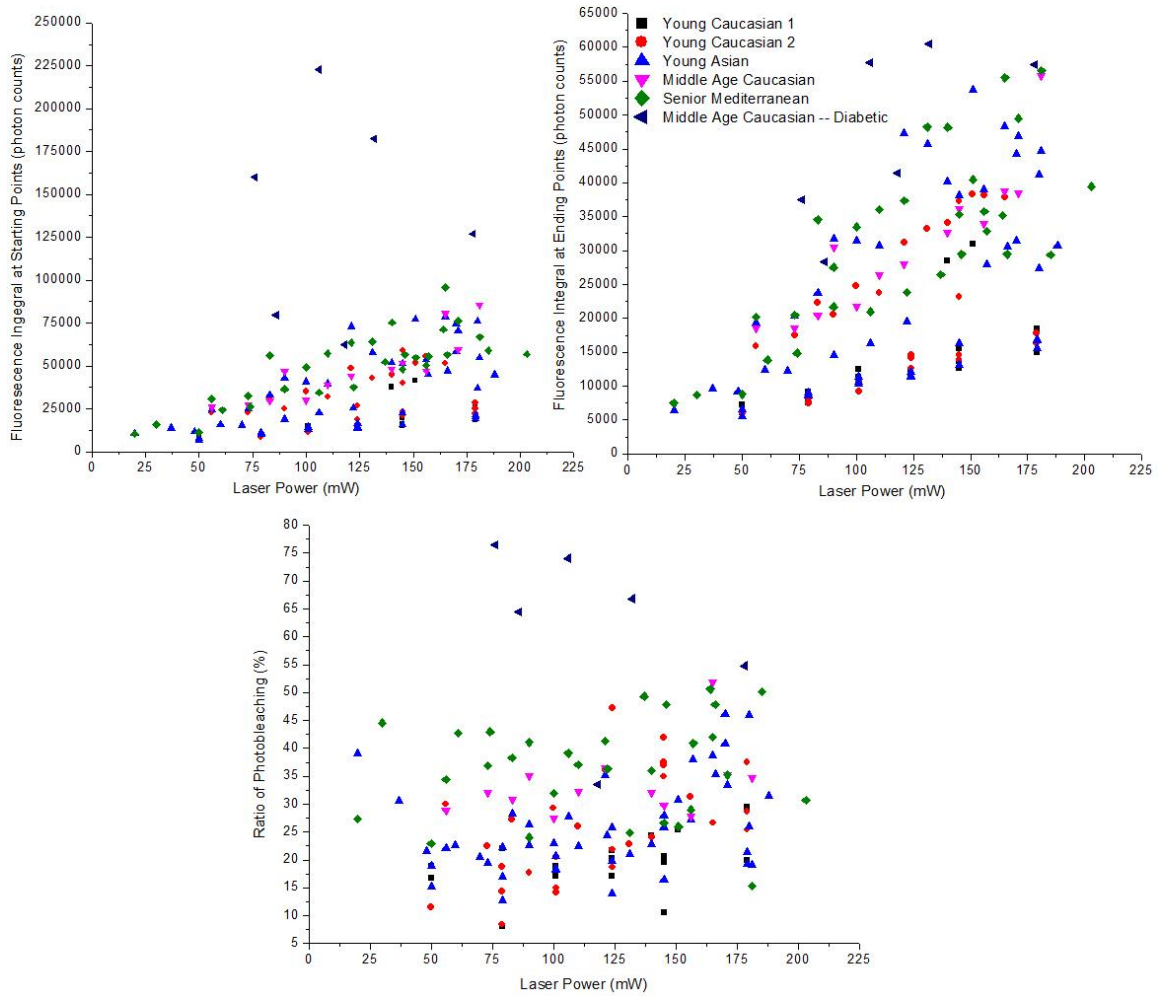
Figure 3-8: Photobleaching study of various test subjects at different power levels. (A, top left) Starting points of the skin autofluorescence; (B, top right) Ending points of fluorescence after 200 sec of 830 nm laser exposure; and (C, bottom) Ratio of the bleached fluorescence to the baseline, i.e., the equilibrium fluorescence after bleaching.

All fluorescence photobleaching curves were fitted into a two-component exponential decay equation to obtain the two lifetime τ_1 and τ_2 which is shown in Figure 3-9. Despite of the relatively large deviation and spread of the data, the two time constants definitely represent two separate processes, one quick and one slow. With not much difference among test subjects, τ_1 is of the order of magnitude of 10^1 to 10^2 sec, while τ_2 is typically below 10 sec. Lastly, although vaguely, τ_1 decreases slightly with the

increase of laser power, indicating a slightly quicker bleaching at higher power. This is
consistent with what Zeng et al. have reported (91), and they have related the fast
decrease term to laser induced photobleaching in stratum corneum and the slow decrease
term to fluorophore changes in the dermis. In our point of view, relating such processes
to constituents within stratum corneum and dermis, as will be demonstrated in Chapter 4,
might be more proper than a generate classification to skin layers.
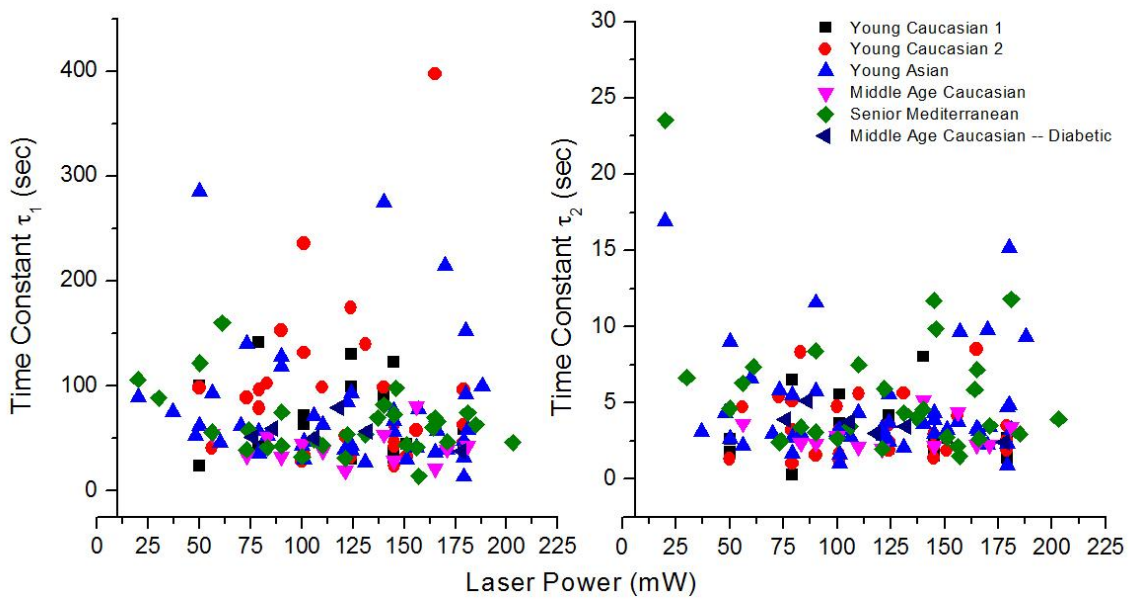
Figure 3-9: Time constants of the two-component exponential decay fit to the *in vivo* skin
autofluorescence photobleaching. (A, left) Time constant, τ_1, represents the slower part of
the photobleaching of 10^1 to 10^2 sec. (B, right) Time constant, τ_2, represents the initial
quick bleaching typically happens within 10 sec.

3.2.2 Relative Contribution from Static Tissue and Blood

The tissue under investigation is roughly divided into two major categories: static
tissue and blood. Knowing that the laser interacts with probed tissue, it is essential to
verify the relative contribution of static tissue and blood to the observed fluorescence and
photobleaching respectively.

In the experiment depicted in Figure 3-10 two shutters were included and programmed to control the laser exposure as shown in the upper right corner inset. In this case the fingertip was set-up and brought to 60 gf/cm^2 with laser blocked. The laser was unblocked at t=2±0.1 sec with pressure already equilibrated and the IE was observed to fall exponentially again in the first 27 sec. As shown in the lower left inset of Figure 3-10, pulses were shown in IE indicating that systemic circulation under modulation was not blocked. At this point the laser was again blocked for 8 sec in order for a dozen or more pulses to bring new previously *unexposed* blood into the irradiated volume.
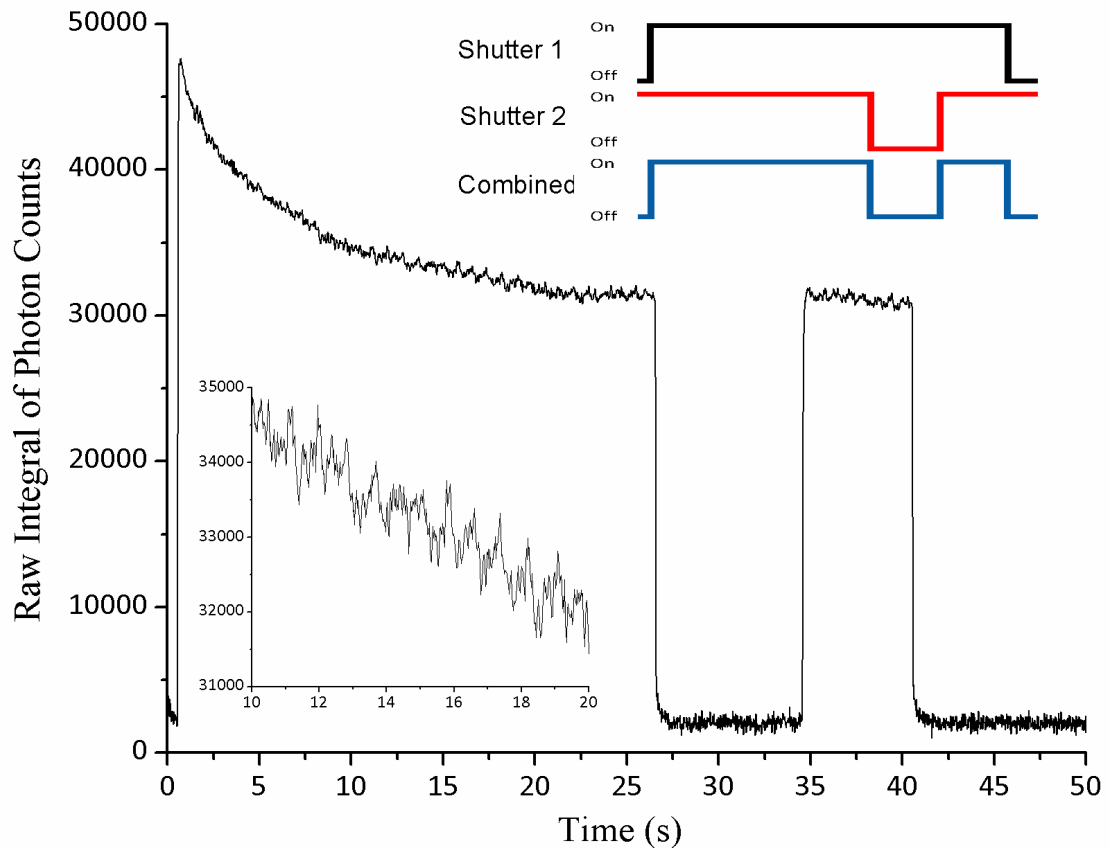
Figure 3-10: Shuttered *in vivo* IE profile of a human fingertip, attempting to observe fluorescence recovery by allowing fresh *unexposed* blood to flow into the probed volume. Lower left corner inset zooms in the 10-20 sec frames to show *in vivo* heart-driven pulses. Upper right corner inset illustrates the shutter programming sequences.

The hypothesis here is that static tissue remains the same either before or after the laser is blocked, while heart-driven pulses keep on pumping previously non-bleached blood into the illuminated zone. Therefore, after the 8 sec "dark time" it is expected that the bleaching effect on static tissue remains, if there is any, but now fresh unbleached blood components are present. Checking the IE curve on the point of reopening the shutters enables us to differentiate the influence of laser on the two separately. If blood is the main contributor to the bleached fluorescence observed at t=2 sec of the test, then fluorescence should recover back to the previous level on reopening of the shutters. As shown in Figure 3-10, fluorescence returned to where it was before the shutter was closed but not to a significantly greater level than where it was at the initiation of the experiment. Also noticeably, upon reopening of the shutters no exponential decay was observed. Thus it is evident that using 830 nm excitation most of the bleachable NIR autofluorescence originates in the static tissue.

Figure 3-11 also shows a typical BV vs. Time curve collected by a precious colleague using 805 nm excitation (51). Actually, under either 805 or 830 nm excitation, the blood, i.e., the sum of plasma and RBCs, and unbleached static tissue fluorescence per unit volume are comparable with the blood being somewhat greater. If the fluorescence per unit volume of the blood and the static tissue were the same, then pulses would not be observable. If the blood fluorescence were twice that of bleached tissue per unit volume then increasing the perfusion due to a cardiac pulse by 2% would increase the fluorescence by 2% and this is very roughly what has been observed. The appearance of the dichotic notch (51) compared with that observed using photoplethysmography also shows that the blood fluorescence per unit volume is larger than that of the tissue.

Despite of the low Hct in the capillaries probed, e.g., 0.1 – 0.3, the fluorescence per unit volume of Hb is greater at 805 nm (66) than 830 nm, thus resulting in the differences in the pulses in Figure 3-11 and Figure 3-12 with the expanded scale. Under 805 nm excitation the pulses are more visible throughout even at the very beginning. Nevertheless, the fluorescence fluctuation due to cardiac pulses either under 805 nm or 830 nm excitation is of the very similar size relative to the baseline fluorescence, i.e., around 2% in both cases, suggesting the same fluorophore(s) of the pulse fluorescence.
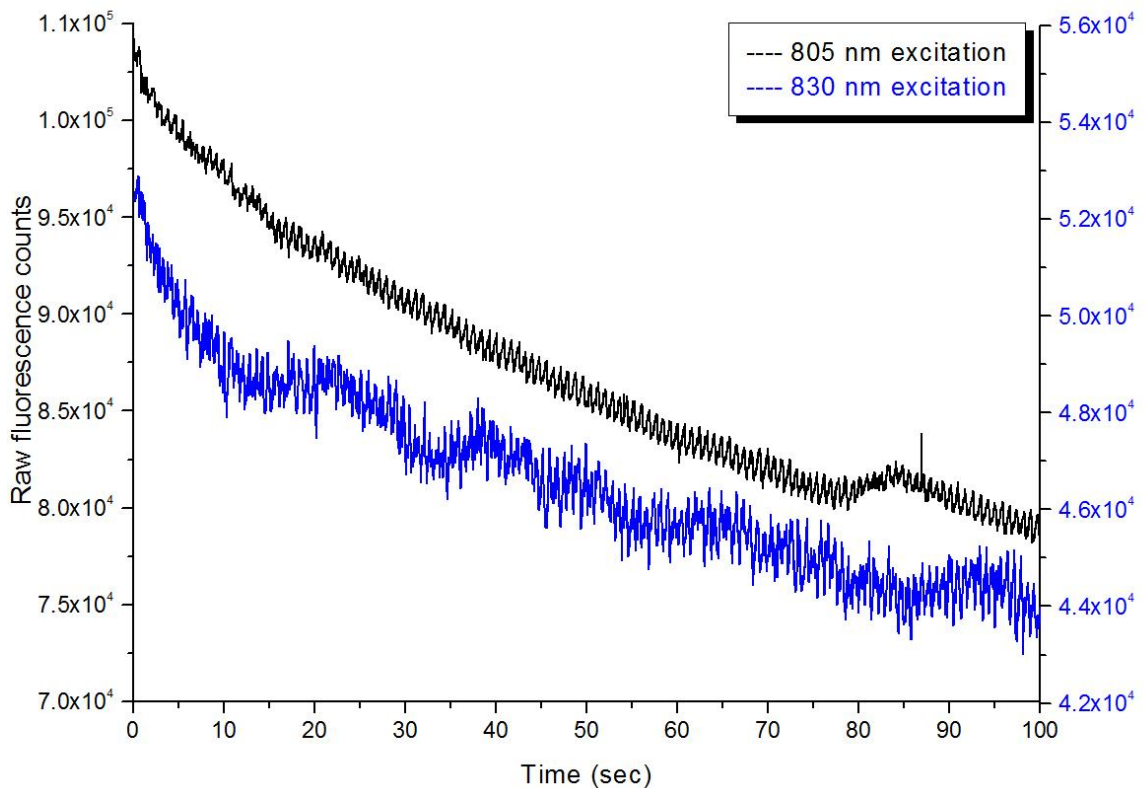
Figure 3-11: Comparison of two 100 sec IE vs. Time curves obtained under 805 nm and 830 nm excitation respectively. Although cardiac pulses are clearly shown on both curves, these under 805 nm excitation are less noisy and much easier to discern.

It is also noted that working at 830 nm, averaging among different test subjects roughly 10-15% of the initial fluorescence from tissue *in vivo* bleaches away in the first

several tens of seconds. The fresh blood in a background of bleached tissues adds little

additional baseline fluorescence. Therefore, it is concluded that at least 15% of the

fluorescence originates within the static tissue. Although bleaching of blood cannot be

totally settled at this point, it is safe to say that the photobleaching of the static tissue

contributes majority of the observed exponential fluorescence decay and once bleached it

does not recover in a couple seconds of no irradiation.
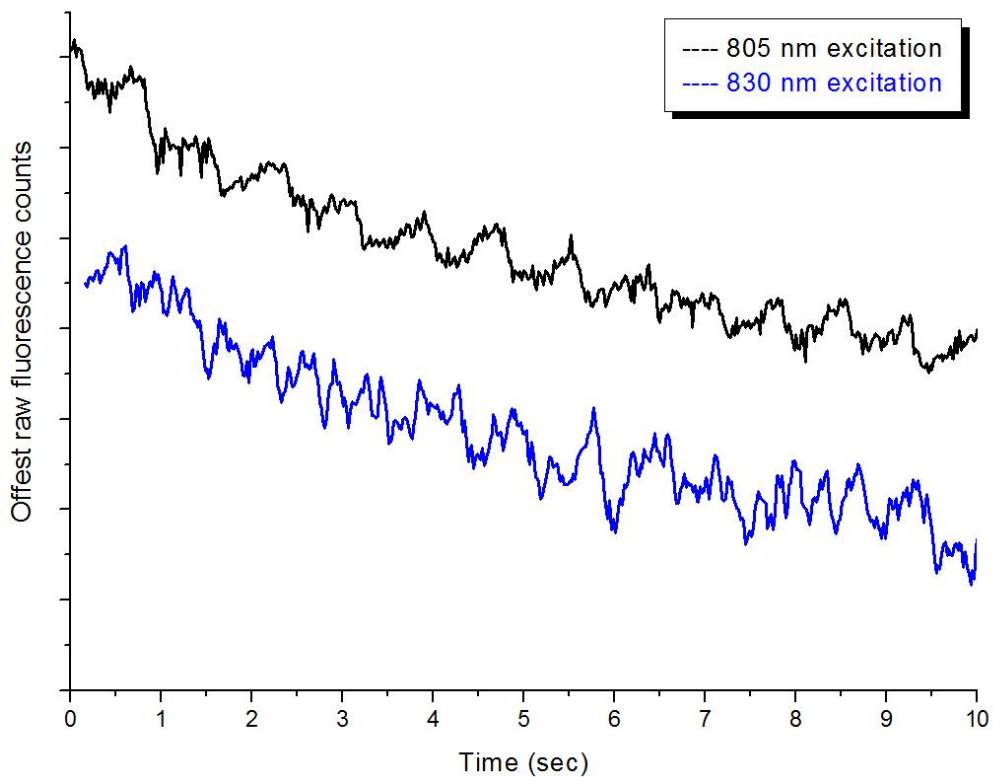
Figure 3-12: Re-plot of the IE vs. Time curves with expanded x-axis range from 0 to the
first 10 sec. Under 805 nm excitation, discernible optical pulses could be seen
immediately upon the start of the experiment, while pulses gain visibility gradually under
830 nm excitation.

3.2.3 Recoverability of Quenched Fluorescence

To observe whether and if so to what extent the laser bleaches the static tissue, two shutters were used to allow only 60 ms slices (chosen based on the 20 ms frame sampling time) of the CW laser to contact the skin during the scanning across the fingertip from tip to joint for the length of the entire aperture. The same setup described in Section 2.3.3 in Chapter 2 was used to obtain the fingertip topography. Driven by a NSC200 controller, both fingertip and the aperture were moved simultaneously relative to the stabilized laser source. At a scanning rate of 1 sec/spot, the actual duty cycle of laser exposure to skin was only 6%, which is hoped to greatly reduce the bleaching at each spot and offer unbiased fingertip topography.

A typical scan obtained in this manner is shown in Figure 3-13. The concave up gross appearance of the scan is an artifact of the tendency of the tissue (and all soft matter) to extrude into the aperture when held under any pressure as explained in Chapter 2 and previously published theory paper (10). After a first low duty cycle pre-scan was obtained, the laser was allowed to contact and thereby photobleach the motionless skin at the center of the aperture for 50 sec at 200 mW with 100% full duty cycle. Immediately following this and at various times afterwards, low duty cycle scans were conducted to reveal the effect of the photobleaching step. The fluorescence in the irradiated region is decreased by about 15-20% in the case of the non-diabetic test subject shown in Figure 3-13.

It is also observed that for all test subjects the bleaching effect persists for as long as 45 min without any notable recovery. However, it does not seem possible to detect the spot 24 hrs later. Since interstitial fluid exchanges materials with the blood stream and

the lymphatic system on a time scale of only a few tens of minutes, it could be concluded that at 830 nm and the power levels used the bleaching is faster than the interstitial fluid exchange between the bleached and unbleached static tissue constituents. Although many more test subjects need to be included to produce a statistically meaningful result, so far test subjects with diabetes photobleach roughly twice as deeply as the non-diabetic test subjects, regardless of age.
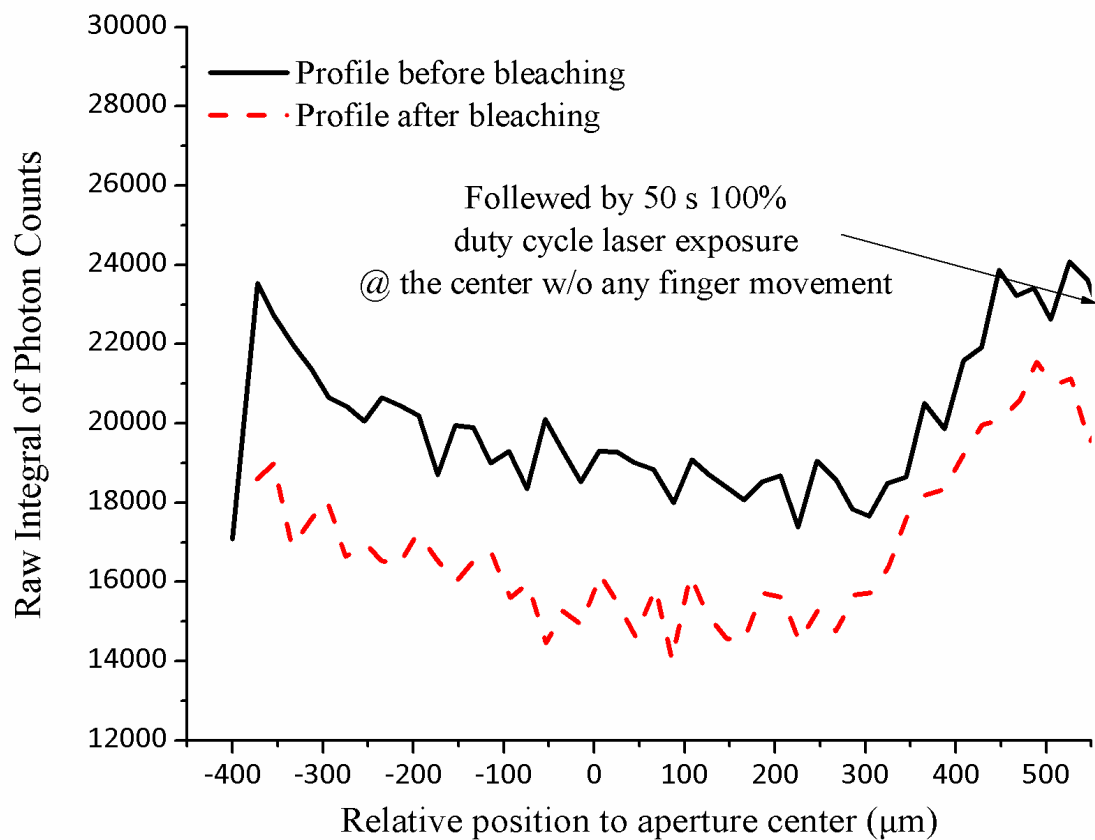
Figure 3-13: Two individual IE fingertip topography scans performed on the same subject w/o moving hand out in between. The second scan (dotted line) is performed after 50 sec bleaching under 200 mW laser exposure in the center of aperture at the end of the first scan (solid line).

3.2.4 Summary

A series of measurements *in vivo* intended to establish some of the basic empirical properties of the autofluorescence and photobleaching phenomena are described. To summarize, *in vivo* results show that the observed bleaching of human fingertip skin with 830 nm excitation is laser induced coming mostly from the static tissue rather than blood components, and is unrecoverable within the time span of 10^1-10^2 min. On a given trial the exact amount of tissue fluorescence varies from person to person in manner that we and others are actively studying (91-96). And an initial bleaching process always occurs and the magnitude is roughly as what is suggested. Therefore, for a single test subject in comparison with him or herself, utilizing a reasonable pre-bleaching period in a consistent manner could still allow for using IE as a volume normalizer.

3.3 Hct Monitoring Using Combined EE and IE

3.3.1 The Theoretical Model and Algorithm

Since we are interested in using fluorescence for volume normalization, in this section we first briefly review a new algorithm Goodisman and Chaiken developed to include turbidity changes simultaneously with fluorescence changes in order to consistently estimate plasma and RBC volumes. As we do we mention engineering issues which are now important to consider. As briefly introduced in Section 3.1.2, probing tissue with NIR radiation simultaneously produces IE plus EE that noninvasively give chemical and physical information about the materials and objects within. Therefore, it is reasonable to presume that EE and IE represent two independent observations that can be

used to obtain the volume fractions of two independent phases: the plasma and the RBCs. Having these two quantities is equivalent to having the Hct and the total blood volume, as shown in Equation 3-1and Equation 3-2 with ϕ being the volume fraction of each phase.

$$Hct = \frac{\phi_r}{\phi_r + \phi_p}$$ Equation 3-1

$$Total\ Blood\ Volume = \phi_r + \phi_p$$ Equation 3-2

Goodiman and Chaiken proposed a model (10) for the propagation and scattering of radiation through skin based on radiative transfer equation (RTE) that includes the attenuation of incoming radiation by scattering and absorption, the scattering of the radiation from all tissues, and the propagation of scattered radiation from scattering centers to the detector. As shown in Table 3-2, the model divides the structure of skin into three layers: a relatively thin (100 μm), static, bloodless, and nonviable outer layer a, covering a somewhat thicker (200 μm) relatively blood-rich layer b that is bounded from below by dermis, a less blood-rich layer c whose depth is essentially infinite. Of course, in reality the thicknesses of all the layers vary across all test subjects. But what is critical here is the ability to reach the 200 μm thick layer b which is a contiguous volume containing the perfused viable epidermis.

Table 3-2: Assumed volume fractions of the three phases in the three layers based on estimates (41, 42) of average capillary density, dimensions and an Hct of 0.10 for the blood in the most vascularized layer b.

Phase	Layer a	Layer b	Layer c
r = RBCs	0.00	0.0040	0.00067
p = plasma	0.00	0.0360	0.00600
t = static tissue	1.00	0.9600	0.99333

In vivo, any volume of tissue naturally experiences spatial and temporal fluctuations of blood plasma and RBCs content. Assuming there is no void volume in viable tissue, or that void volume is constant. Then, this could be summarized in Equation 3-3 and Equation 3-4.

$$1 = \phi_r + \phi_p + \phi_s \qquad\qquad \text{Equation 3-3}$$

$$0 = d\phi_r + d\phi_p + d\phi_s \qquad\qquad \text{Equation 3-4}$$

Chaiken and Goodisman have also proposed an algorithm (80) for calculating these volume fractions based on their theoretical RTE-based model. Using literature absorption and scattering coefficients as shown in Table 3-1, the RTE calculated contribution of IE and EE from the three phases vary linearly with the various volume fractions of plasma (ϕ_p) and RBCs (ϕ_r). This linear relation enables the prediction of two unknowns, i.e., ϕ_p and ϕ_r, from the two known quantities, i.e., EE and IE, using Equation 3-5 and Equation 3-6.

$$\phi_r = a + b\left(\frac{EE}{EE_0}\right) + c\left(\frac{IE}{IE_0}\right) \qquad\qquad \text{Equation 3-5}$$

$$\phi_p = d + e\left(\frac{EE}{EE_0}\right) + f\left(\frac{IE}{IE_0}\right) \qquad \text{Equation 3-6}$$

In these equations IE_0 and EE_0 represent the average IE and EE for a specific test subject and real time measured IE and EE will be fed into the model. Hct is then calculated using Equation 3-1.

3.3.2   In Vivo Calibrations

There are six parameters *a–f* for which numerical values must be obtained by using constraints based on empirical data or assumptions. First, consistent with Jacques (88) and our own geometrical approach for very well-perfused skin, it is reasonable to assume that $\phi_r = 0.004$ and $\phi_p = 0.036$ on average and that $EE_{ave} = EE_0$ and $IE_{ave} = IE_0$. A cursory examination of other parameter sets suggests that some flexibility in choosing these values could be exercised because only deviations from the baseline values, not the absolute Hct, are the interested values to be monitored. According to Equation 3-5 and Equation 3-6, this gives two constraints: $\underline{a + b + c = 0.004}$ and $\underline{d + e + f = 0.036}$.

Additional constraints can be obtained from changes in EE and IE that can be correlated with known physiology. Normally with each cardiac pulse (97) about 75 ml of 0.45 Hct blood is injected into the arterial side of the 4000 ml total supply. Uniformly distributed, this would result in a 1.9% transient increase in blood volume, i.e., in both ϕ_r and ϕ_p assuming constant Hct. Thus, it could be assumed that with each pulse ϕ_r and ϕ_p increase by 0.000076 and 0.0006.84, respectively. Meanwhile, the raw spectral data in Figure 3-3 show −2.08% and +2.63% changes in EE and IE, respectively, with each cardiac pulse, i.e., systolic EE and IE minus diastolic EE and IE. By taking derivatives of

Equation 3-5 and Equation 3-6, the changes of pulse ϕ_r and ϕ_p can be expressed using the two equations below:

$$\Delta\phi_r = b\left(\frac{\Delta EE}{EE_0}\right) + c\left(\frac{\Delta IE}{IE_0}\right) \qquad\qquad \text{Equation 3-7}$$

$$\Delta\phi_p = e\left(\frac{\Delta EE}{EE_0}\right) + f\left(\frac{\Delta IE}{IE_0}\right) \qquad\qquad \text{Equation 3-8}$$

Therefore, the two aforementioned conditions can be inserted into Equation 3-7 and Equation 3-8 to generate two more constraints on the values of the parameters *a–f*: _b = -0.00365 + 1.264 c_ and _e = -0.0329 + 1.264 f_.
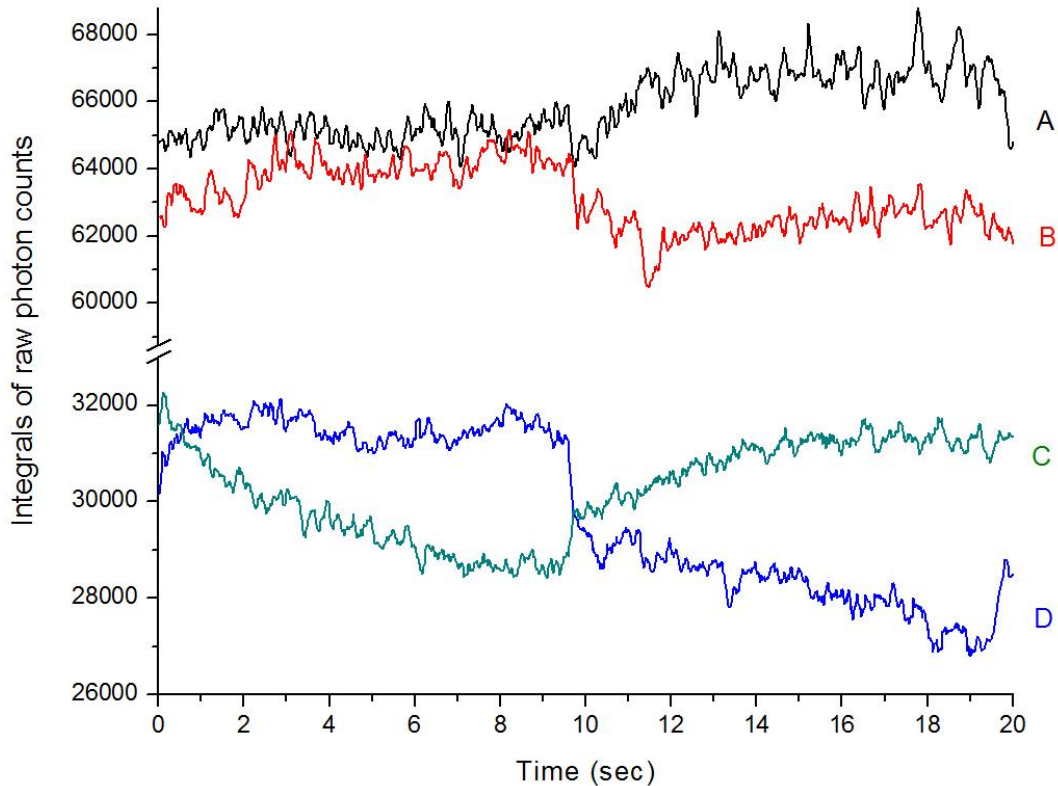
Figure 3-14: IE and EE as functions of time for two different modulation cycles. In one cycle, the pressure went from low = 60 gf/cm^2 to high = 200 gf/cm^2; and in the other, went the opposite. (A) EE for low to high, (B) EE for high to low, (C) IE for high to low, and (D) IE for low to high. Trials (A) and (D) were used to provide the calibration.

Finally, it has been shown in Chapter 2 that tissue modulation could significantly redistribute the blood flow. Figure 3-14 shows IE and EE integrals of a test subject whose fingertip was modulated between 60 and 276 gf/cm^2 of pressure. As shown, EE increased by 3.03% and IE decreased by 9.6%.

In obtaining these results, the maximum applied pressure was three to four times the normal systolic blood pressure; thus, the amount of blood displaced is roughly three to four times the amount displaced by a pulse. The changes in ϕ_r and ϕ_p are estimated based on: i) the applicability of the Poiseville–Hagen equation to optimization in the cardiovascular system (98), and ii) the variation in appearance of tissue-modulated spectra with varying amounts of modulating pressure (99). Although we probe the capillaries, they are fed by the superficial dermal plexus, with vessels large enough to demonstrate well-known microcirculation anomalies (100, 101), i.e., plasma skimming and the Faraeus and Faraeus–Lindquist effects, associated with nonproportional plasma and RBC movement. Under greater applied pressure, relatively more plasma is expected to move than RBCs because the viscosity of plasma is less than that of RBCs.

Under our experimental conditions, we estimate the discharge Hct as 0.075. The decrease in ϕ_r is therefore $3 \times 0.019 \times 0.004 = 0.000228$ and the decrease in ϕ_p is $4 \times 0.019 \times 0.036 = 0.002736$. This corresponds to three and four times the amount of RBCs and plasma moved by a single pulse. Again, by putting these volume fraction changes together with IE and EE changes in Equation 3-7 and Equation 3-8, two more constraints could be obtained: _b = −0.00752 + 3.168 c_ and _e = −0.0903 + 3.168 f_.

The above examples yield four constraints on the six parameters. The remaining two parameters could be determined by minimizing the standard deviation of the Hct from the mean over some time range of measurements when no blood interference is introduced in any form. This is justified because, normally, Hct is constant under homeostasis (98). The mean value will be ≈0.1 because the assumed reference values of ϕ_r and ϕ_p are 0.004 and 0.036, respectively. Again, it is emphasized that the assumed capillary Hct values are not important – what matters is the deviation of the calculated ϕ_r and ϕ_p from the reference values.

With no doubt, there are various more approaches involving empirical observations of IE and EE modulations that are associated with known physiological effects that could be applied to obtain constraints on the six parameters. Already, the *empirical* calibration of the Hct model as described above could apparently lead to very stable results with sufficient sensitivity. However, it is imported to obtain steady IE_0 and EE_0. From the study on *in vivo* tissue fluorescence in Section 3.2, it is known that photobleaching introduces artifacts. Therefore, to unambiguously and accurately observe and interpret effects of blood volume *changes*, it is important to reach photobleaching equilibrium before monitoring EE and IE for quantification. Nevertheless, the measurement of absolute Hct could be limited in accuracy and precision if we cannot account for and cope with the person to person variation in autofluorescence and photobleaching characteristics.

3.3.3　In Vivo Monitoring of Hct

3.3.3.1　Arm Swings

To utilize and evaluate the algorithm, experiments were performed in which the homeostatic blood volumes are intentionally perturbed in a manner that may be comparable to an autonomic response to hemorrhage, e.g., shifts in peripheral body fluids. Of a number of means for accomplishing such purpose (5), results for a method analog to "centrifugal loading" was shown in Figure 3-15. Before taking the measurements of Hct, test subject rotated the arm about the shoulder with the arm, elbow, and fingertips outstretched so that all joints and long straight members of the circulatory system have a projection along the centrifugal force direction. If the maneuver was properly executed, then the test subject could feel tingling in the fingertips after the swinging.

Estimating the rotating arm length as >30 cm and the rotator motion as 120 rpm, we calculate >4 G applied force using the standard relative centrifugal force equation. For the results that follow, the loading was continuous for a period of at least 30 sec. Because G-force induced loss of consciousness (102) is known to occur as a result of transient application of 2-4 G forces to the human body, 30 sec of continuous motion 4 G force could be expected to lead to transient minor hemoconcentration in the fingertips or leakage through the capillary walls, just as centrifuging leads to hemoconcentration in an Hct tube. And this is what has been observed in Figure 3-15. Several trials of soaking hand in hot water before making Hct measurement were also performed. The vessel dilation caused by heating, although does increase the blood volume fraction in the irradiation zone, is not necessarily to cause significant changes in Hct.
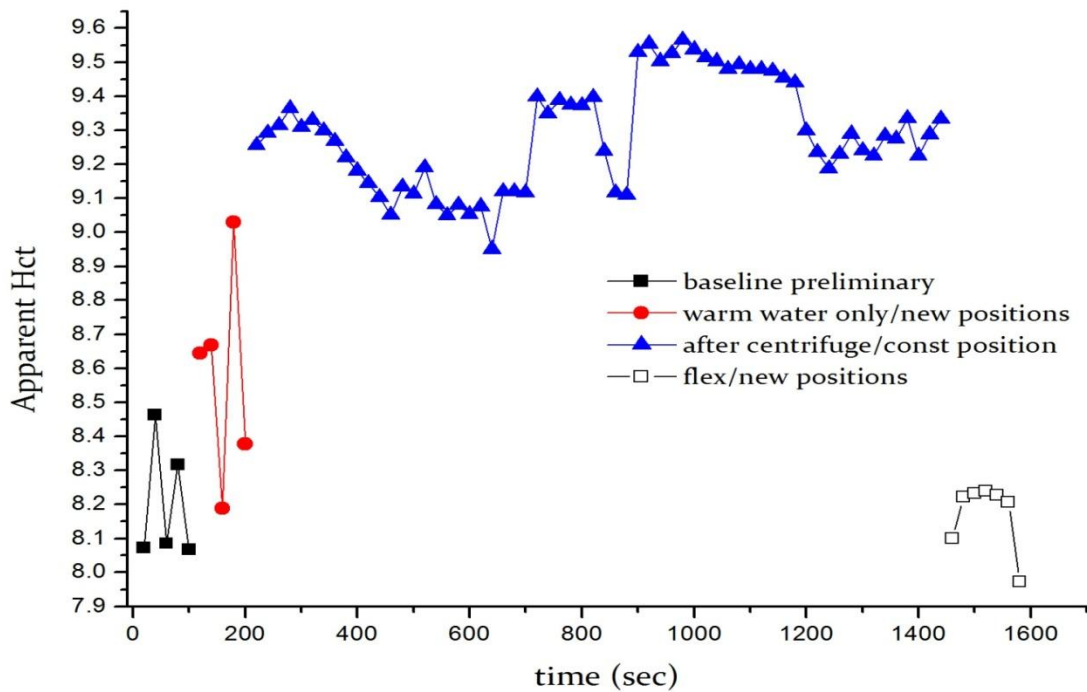
Figure 3-15: Calculated Hct based on the parameters predetermined by a separate calibration trial. Each point represents an averaged Hct of 20 sec of data. Baseline of the test subject was established before performing the arm swinging.

To correlate the noninvasive approach with Hct measurement gold standard, conventional centrifuge fingerstick Hct measurements were obtained (103, 104) using a UNICO centrifuge (UNICO PowerSpin BX C884, Dayton, NJ, USA). The standard 75 mm Drummond micro-hematocrit tubes (VWR, Radnor, PA, USA) were spun at 11000 rpm for 5 min. All of tubes were then read by the same person for consistency in estimating the buffy coat.

The conventional Hct measurements established that the absolute value of the difference between measurements of Hct before and after the centrifugal loading step is roughly three times greater than the variation in Hct readings obtained from consecutive samples going forward in time but without the loading in between. However,

hemoconcentration was not always observed for everyone. This might partially due to the fact that blood sampling by itself has various sources of errors (105). Moreover, the influence of swing arm on blood flow could also be easily dependent on the timing and execution of the procedure, and the time course is apparently variable. Nevertheless, the arm swinging procedure definitely causes blood imbalance in the fingertips.

3.3.3.2 Valsalva Maneuver

Another demonstration involves the Valsalva maneuver (106). The Valsalva maneuver refers to the test subject attempting to push air through any closed orifice. When executing the Valsalva maneuver the test subject must constrict the chest muscles and clench the abdominal muscles causing them to occupy a greater volume of the abdominal cavity. This expansion impedes the venous return of blood to the heart thereby decreasing net cardiac output and simulating central hypovolemia. The calculated changes in apparent Hct by a Valsalva maneuver are shown in Figure 3-16.

At around 135 sec, the test subjects started a Valsalva maneuver, and on Hct trace after a brief increase Hct gradually decreased in the first 5 sec of the maneuver. This could result from the rush of blood flow due to the initial pressure wave. Afterward, the held pressure impeded the venous return and thus caused a pooling of RBCs. Plasma movements, on the other hand, although is hard and slow but not completely blocked, therefore resulting a slow but obvious incline in the Hct. Correspondingly, upon releasing the pressure, sharp drop in Hct was observed but the pooling effect needed some time to regain equilibrium back to steady state.
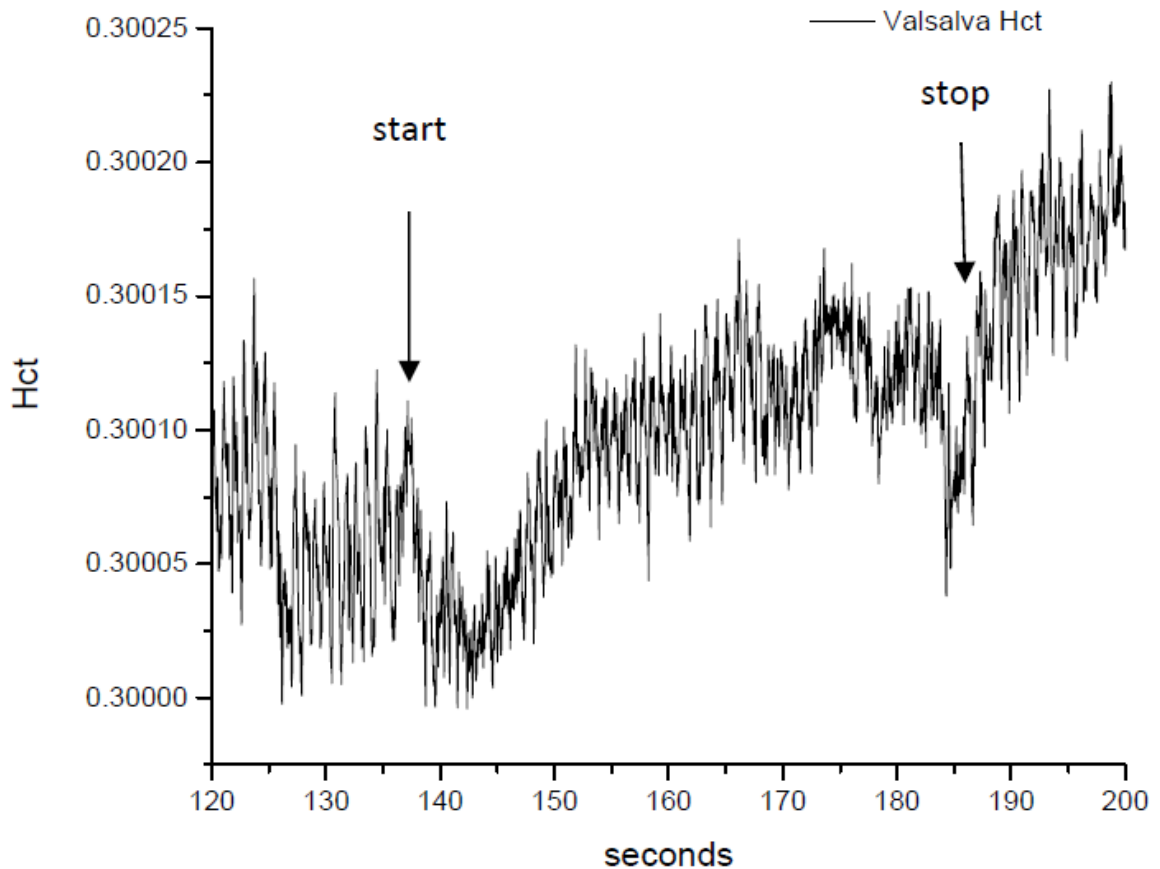
Figure 3-16: Typical Hct changes observed when executing the Valsalva maneuver. The test subject initiated the maneuver at about 135 sec and released at about 185 sec. The IE_0 and EE_0 were calculated from the prebleached data earlier in the experiment.

Valsalva maneuver is a fairly subtle physiological process whose influence is much more obvious in blood pressure and pulse rate than in Hct. Depending on how much pressure a test subject could exert and how long such pressure could be held, the amplitude of Hct change caused by a Valsalva maneuver could vary in a fairly large range but has been observed nearly every time. The fact that it is discernible at all using the proposed noninvasive Hct algorithm is surprising, which demonstrate the high sensitivity of the algorithm.

3.3.3.3   Blood Pressure Cuff

As a final experiment, a manual blood pressure cuff was used as a tourniquet to induce hemoconcentration for a sufficiently long enough time to make as much Hct change as possible. After determining the test subject's BP and pulse rate using an automatic cuff, IE and EE were collected with no applied tourniquet beyond that needed to maintain mechanical registration of the tissue with respect to the optical system, in order to define homeostasis for 60 sec.

Then, the tourniquet brought the pressure to its final planned value within five to seven cardiac pulses by a single increase in pressure (in several pumps on the manual bulb), at around 60 sec. The final pressure was chosen to be just above the systolic pressure in order to insure venous occlusion, which can be confirmed with a stethoscope. Once complete occlusion was established, it was maintained without modification for 60 sec. Thus, at 120 sec from establishing homeostasis, the tourniquet was released as quickly as possible. The associated changes in EE and IE can be seen in Figure 3-17. Both scattering intensities decreases gradually after the tourniquet is applied and rebounded quickly to their original values when the tourniquet is released. The decrease is ≈10% for EE and ≈20% for IE.
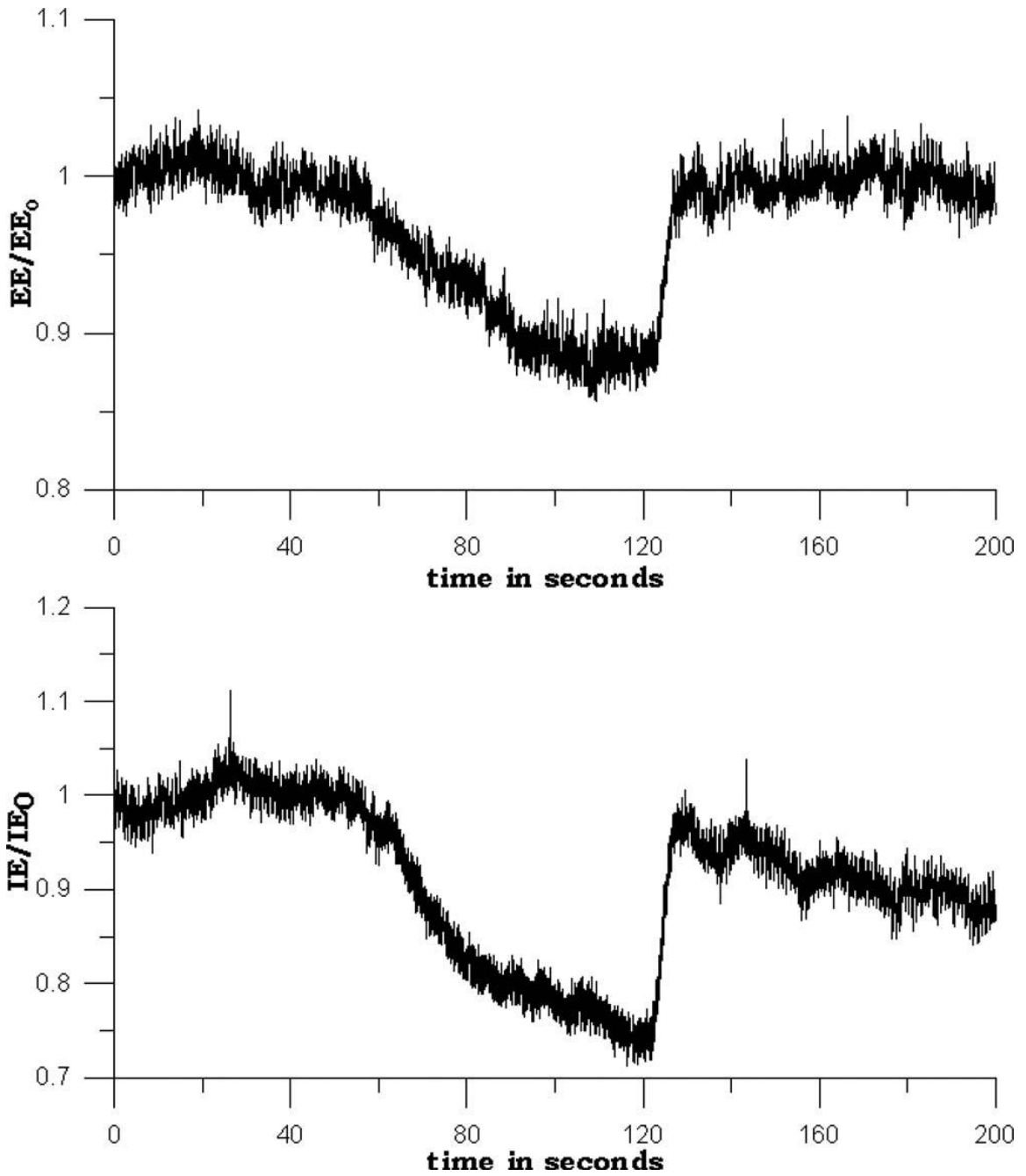
Figure 3-17: EE/EE_0 and IE/IE_0 versus time for application of tourniquet at $t \approx 60$ sec and release at $t \approx 120$ sec. Sufficient prebleaching was performed before data collection. Plasma and RBCs volume fractions and Hct, derived from this data, are shown in Figure 3-18.

The resulting RBCs and plasma volume fractions, and the Hct, are shown in Figure 3-18. Both volume fractions rise gradually during the period over which the tourniquet is applied, showing that the main effect is trapping blood in the irradiated volume. When the tourniquet is released, both volume fractions drop quickly to their pre-tourniquet values. The Hct, because of our parameterization, is much more constant, changing by only 0.5%, but also increases on application of the tourniquet and decreases on release. The increase, which is a little sharper than the increases in volume fractions, shows that relatively more red blood cells are trapped than plasma. Interestingly, the Hct shows some post-tourniquet effects. After release, the Hct drops to its original value, but then increases gradually to a value about 0.5% higher. By 200 sec, it has leveled off; the measurements do not go far enough to determine how long it takes to come down again.

For direct comparison, three test subjects exercised the tourniquet maneuver using a blood pressure cuff pumped above systolic pressure for 2 min four times in a week's time span, and meanwhile the conventional Hct determination technique was employed. For each subject, two to four blood samples were taken both before and after the maneuver each day, which yielded a total number of 61 data points, 30 before and 31 after. The average Hcts before applying tourniquet were 0.379, 0.372, and 0.406; whereas the averages after were 0.402, 0.381, and 0.414, respectively. The result is plotted in Figure 3-19. The statistics show a clear trend of increased Hct after the tourniquet is applied.
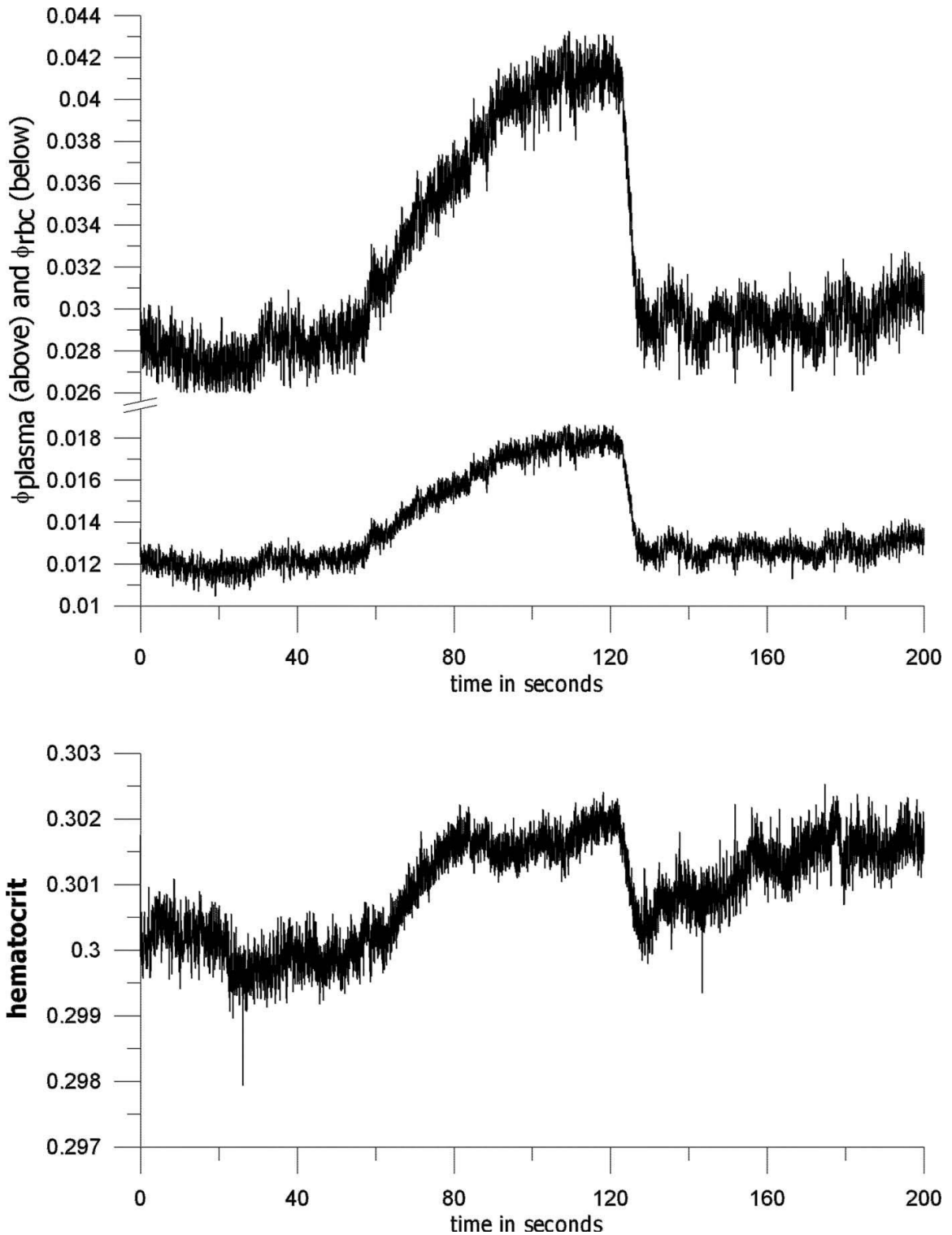
Figure 3-18: Volume fractions and Hct calculated from the data of Figure 3-17. Both calculated volume fractions increase gradually when the tourniquet is applied and drop quickly to their initial values when it is released. The Hct follows roughly the same pattern, but shows some residual effects after tourniquet release.

112

To support the statement in a more statistically meaningful way, the null hypothesis is tested by splitting the raw 61 data points into two sets, 30 before and 31 during application, without differentiating test subjects and the dates on which the experiments are performed. The result yields a p-value of 0.039, which is significant at >90% confidence to reject the null hypothesis that assumes there is no Hct change due to the tourniquet. It is important to be pointed out here that within any set of personal Hct values, the behavior is much more consistent; thus, the statistic just quoted tends to underestimate the Hct change on a single person basis. Therefore, personal average Hct was used as a normalizer for each individual. And instead of using raw Hct, the relative change of Hct was used to test the null hypothesis. A p-value of 0.0219 resulted, even more strongly supporting the probability that Hct increases with the tourniquet applied, as shown in Figure 3-18.
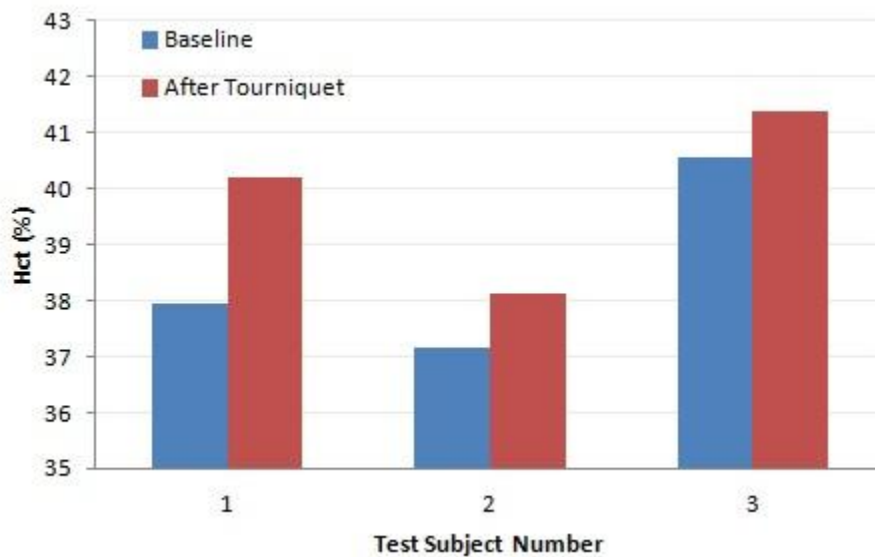
Figure 3-19: Box plot of Hct changes before and after the tourniquet experiment for three different test subjects. The Hct values were measured using conventional fingerstick method and the heights showed the mean values of about 7-10 Hct measurements for each bar.

3.3.4 Summary

Measuring the IE and EE simultaneously and applying the algorithm leads to a sensitive probe for volume changes of both RBC and plasma. Obviously, a number of approximations have been made to demonstrate calculation of volume fractions and Hct from EE and IE. The first assumption is the Hct of layer b in the model. As might have been noticed, the absolute Hct number assumption has been changed to generate different *a-f* parameters. In the deduction of the algorithm and arm swinging experiment, an Hct of 0.1 was assumed; while in the Valsalva and tourniquet experiments 0.3 was assumed. Nevertheless, in both cases meaningful Hct change predictions could still be produced. Since the immediate goal is to monitor changes in Hct over a long time period. Thus, the particular value assumed for the Hct is not very important.

What is essentially required in this model for the algorithm to work as designed is for all three phases to remit detectable fluorescence at different rates per unit volume. When the fluorescence per unit volume of any phase changes during a monitoring period, as when photobleaching that has been elaborated in Section 3.2 occurs, or if the parameters are not well chosen to properly balance the contributions from the different phases to each type of remission, the algorithm can produce inaccurate results. Therefore, unless we can quantitatively account for or otherwise cope with the effects of autofluorescence and photobleaching, absolute calibration of this technique across patients may not be possible. Nevertheless, Leypoldt et al. (99) have demonstrated potentially useful clinical information having the capability to monitor *relative* variation from homeostasis of Hct and fluid volumes.

Lastly but importantly, the same set of parameters *a-f* produces from a single calibration has been used for different test subjects in different days to produce Hct predictions as shown in Figure 3-16 and Figure 3-18. Although not shown in the graph, Hct results of similar experiments have show surprisingly identical qualitative responses for any number of different test subjects spanning a wide variety of skin tones and textures. It indicates that it may be possible to empirically calibrate the LighTouch^{TM} device once and still produce quantitatively accurate Hct changes across various subjects for a longer period of time, e.g., a month.

3.4 Conclusions

This chapter begins to tackle the empirical photophysical and photochemical properties of human skin autofluorescence, which are of pivotal importance to the implementation of volume normalization as proposed for the noninvasive *in vivo* human blood glucose measurement. The quenching of IE is laser induced photobleaching, the majority of which comes from the static tissue, not blood components. Nevertheless, blood fluorescence from RBCs and plasma under 830 nm excitation is of similar order of magnitude as that from static tissue, therefore optical pulses are always discernible. The *in vivo* observed photobleaching is a process that starts with a relatively quicker bleaching and follows a slower decay that could extend to hundreds of seconds. Once bleached, the tissue does not readily recover within 10^0-10^1 min. Therefore, a prebleaching process may allow for more effective use of fluorescence for *in vivo* data normalization.

The potential of utilizing combined IE and EE to noninvasively monitor Hct change is also introduced. Assuming constant blood perfusion, increase of Hct will cause an increase in IE and decrease in EE. However, as shown in Figure 3-17, this complementary IE and EE feature is no longer true when interference of blood perfusion and flow is introduced intentionally to an extreme level that exceeds the normal range of pressure that is typically applied by the PDPM. The empirical calibration of the Hct algorithm built based on RTE could monitor the Hct deviations reasonably well with high sensitivity that enables the observation of Hct changes due to Valsalva maneuver. It might be equally important that the algorithm also produces the plasma and RBCs volume. Notwithstanding the problems associated with autofluorescence photobleaching in producing absolute measurements, these two quantities could be used in glucose prediction as a better turbidity corrected volume normalizer.

4. IN VITRO STUDY OF ENDOGENOUS FLUOROPHORES

4.1 Motivation

Chapter 3 has shown that transdermal *in vivo* spectroscopic analysis or imaging of tissue analysis involving NIR excitation always produces some broadband NIR fluorescence. Depending on what spectroscopy is being employed, such fluorescence background can degrade SNR and dynamic range. Well known to originate from blood and various other endogenous materials associated with the static tissue, such NIR fluorescence of biological tissue is frequently mentioned as "autofluorescence" (107). The propagation of NIR light in tissue *in vivo* can be described reasonably well and in detail (10, 62, 108), nevertheless the production of fluorescence is much less so easily explained and little investigation is reported in the literature to clarify the exact origins and distribution of all of the NIR fluorophores in detail. The sources and characteristics of such NIR fluorescence are important to us because as stated in Chapter 3 fluorescence was proposed as a measure of the probed volume in the earlier work (46, 54, 81) for our long-term project of noninvasive glucose monitoring.

From a chemical substance point of view, a significant amount of fluorescence might be associated with the two biggest absorbers and scatterers in skin, i.e., Hb and melanin (14, 57). In addition, substantial fluorescence is ubiquitously observed for all tissues, therefore commonly existed proteins such as albumin and elastin are also suspected to

produce noticeable fluorescence. Advanced glycation endproducts (AGEs) which are the products of a chain of chemical reactions initiated with the Maillard reaction have long been found to fluorescence under UV/Vis excitation (109). Most importantly, AGEs level has been shown (110, 111) to correlate with UV/Vis fluorescence but no work has been done to extend the knowledge to the NIR. Therefore, it is also worthwhile to investigate AGEs fluorescence properties in NIR. This topic will be elaborated separately later in Chapter 5 due to the intriguing mechanism involved.

In fact there are probably a number of minor contributors, porphyrins and non-porphyrin, and this makes a complete description of the net fluorescence more difficult. From the experimental side, one difficulty in attempting to associate a specific amount of fluorescence with a particular volume of tissue *in vivo* is that the sample is perfused and so cannot be studied in the absence of blood, the single largest contributor to the net fluorescence on a per unit volume basis. Therefore, although it is unlikely to settle all relevant issues in this study, recent work directed at clarifying the origin and nature of such fluorescence will be presented.

4.2 Experimental

4.2.1 Methodology of the Study

From the previous chapter, it is learned that volar side human fingertips fluoresce copiously under NIR excitation. Not only that, but such fluorescence also gets quenched about 10-15% within 10^1-10^2 sec with 200 mW 830 nm laser irradiation. The photobleaching is not a quick process but it could finally reach a relatively steady state.

Once bleached, no recovery is observed up to 45 min. However, repeating the same *in vivo* experiment next day on the same test subject showed no sign of revisiting the bleached spot from *any* previous experiment. It is suggested that either the bleached species could partially recover slowly or it could be cleared from the probed volume and replenished through routine metabolic processes.

Trying to categorize the potential endogenous contributors and associate them with the observed NIR fluorescence, the *in vitro* study is guided by the aforementioned characteristics of *in vivo* human tissue fluorescence and carried out in the sequence as shown in Figure 4-1. First of all, for every compound under investigation the first thing to check is whether it fluoresces or not under NIR CW diode laser excitation. As shown later in Section 4.2.3.1, the concentrations used were relevant to their physiological levels although most of the species only have limited quantity in skin or blood. However, it is fundamentally the absorption ability and fluorescence quantum yield that determine and characterize the fluorescence activity per molecule. If these are zero or very small then the relevant concentration is almost always too small to make that fluorophore responsible for much *in vivo* emission. Therefore, experiments with much higher than physiological concentrations were also carried out to determine whether there was even weak fluorescence or not.

For those species that fluoresce, experiments were further performed to characterize their photobleaching properties. To do that, samples were exposed to 450 mW 785 nm irradiation for tens of minutes while continuous spectra were collected. Without repositioning, samples were left in complete darkness for up to 24 hours and revisited to

check if there was any occurrence of fluorescence recovery. To help better interpretation of the data, Raman and UV/Vis absorption spectra of some species were also presented.
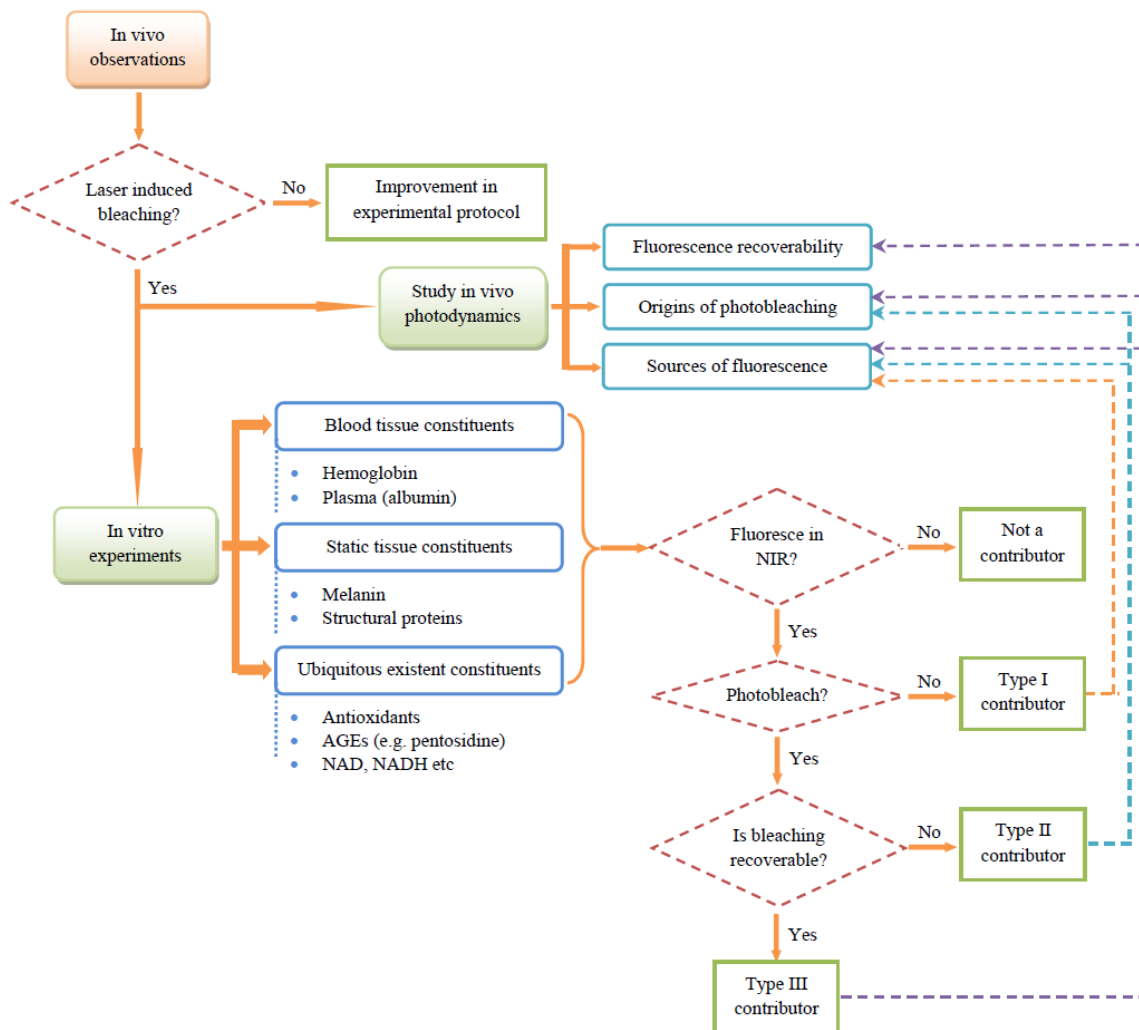
Figure 4-1: Flow chart showing the interconnection between the *in vivo* and *in vitro* photochemical studies of NIR fluorescence of various endogenous species.

As shown in Figure 4-1, potential contributors are divided into three different categories based on their NIR fluorescence properties. Type I fluorophores give significant fluorescence that does not bleach. Thus they participate in building up the solid and strong background as observed *in vivo*. Since autofluorescence is reported for

nearly all living cells, tissues and organs it seems reasonable to expect that type I

fluorophores include at least 2-3 strongly fluorescent species that could be found

ubiquitously throughout the whole body.

According to Figure 4-1, type II and type III fluorophores differ in whether or not

the bleached fluorescence recovers. Since different mechanisms may be involved for

different fluorophores and tissues, contributions from type II and III fluorophores to the

in vivo observed photobleaching phenomenon should be cautiously assigned bearing in

mind the physiological and anatomical issues as will be discussed below.

4.2.2   In Vitro Apparatus

All the *in vitro* spectra are collected using a separate Raman spectrograph, the

optical layout of which is shown in Figure 4-2 below. Most of the filters and focusing

lens serve the same purpose as they do in the *in vivo* setup shown in Section 2.1.2 of

Chapter 2. However, the most striking differences are the excitation laser wavelength and

the angle of incidence. A Process Instruments (Salt Lake City, UT, USA) external cavity

diode laser produces 785 nm excitation with a maximum power of 500 mW. The focused

incident light is steered 90 ° to the vertical by a periscope and reaches the sample surface

at normal incidence through a hole drilled in the center of a downward facing mirror. The

100% backscattered Raman and fluorescence emission is directed back to the horizontal

direction by the plane mirror and free space coupled by a pair of 2 inches diameter fused

silica plano-convex lenses into the dispersion apparatus (Kaiser Holospec, f/1.4, 100 μm

slit width, Ann Arbor, USA) after passing through a Kaiser Super-Notch laser line
rejection filter.
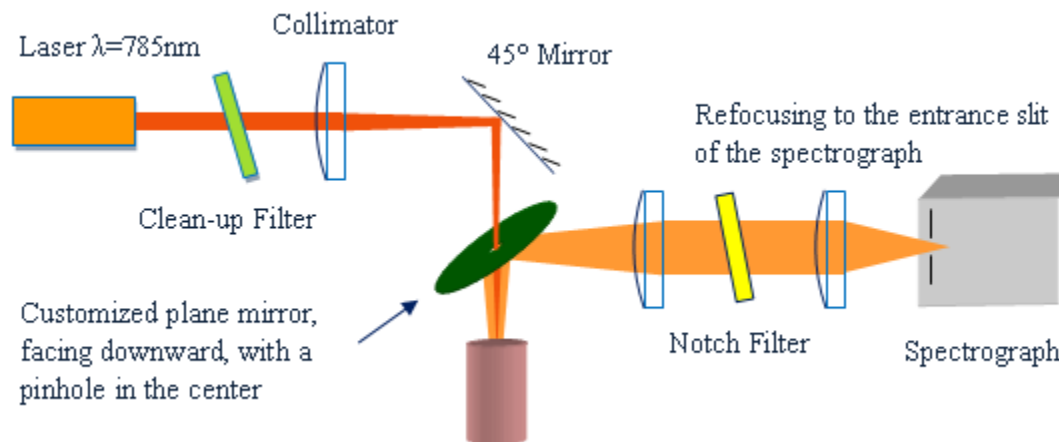
Figure 4-2: Schematic diagram of *in vitro* experimental setup. There are two major
differences between this and the *in vivo* apparatus: i) instead of 830 nm, the excitation
wavelength used *in vitro* is 785 nm, and ii) *in vitro* spectroscopic system collects 180 °
back scattered emission.

Fused silica cuvettes (2 ml or 5 ml capacity) fabricated with side filling tubes are
used for *in vitro* samples because they minimize the unwanted fluorescence and ensure
that there is ample sample along the whole depth of focus of excitation. This design
enables long experiment times without evaporation, thus guaranteeing a more constant
sample volume compared to open top cuvettes. However, the fluorescence of fused silica
requires background subtraction to isolate the sample fluorescence, and such correction is
performed on all displayed spectra unless stated otherwise.

So far, there is no knowledge based way to separate Raman from fluorescence other
than an arbitrary polynomial fitting based background subtraction (53, 112-114). The
methodology used in this study to extract Raman from the raw spectra was elaborated in

multiple previous publications (54, 113). Simply put, a 101-point adjacent average smoothing is performed on the background corrected raw spectrum which, based on known electronic spectroscopy and the condensed phase nature of our spectra, is dominated by fluorescence. Thus the wide window smoothed spectrum helps to establish the broadband fluorescence features. This smoothed spectrum is then subtracted from the raw and another narrower window 7-point adjacent average smoothing is applied to get the final spectrum shown in this thesis.

But in this study we do not concern ourselves with the Raman contribution to the fluorescence since by exciting with 785 nm light the amount of fluorescence produced relative to Raman is at least 6-7 times greater and even greater compared to that produced using e.g. 830 nm. Thus, photon counts in the Raman shift range of 400-1900 cm^{-1}, including undifferentiated Raman and fluorescence emissions, are integrated as one fluorescence data point.

Also notice that instrument function should be applied to harvested spectra for the purpose of comparing features like Raman peak sizes or ratios collected on different apparatus. However, in our application we pay attention only to broad band fluorescence, and mostly the relative change of fluorescence. Therefore, no attempt is tried or needed to implement the instrument function correction.

4.2.3   Materials and Sample Preparation

4.2.3.1   List of Materials

The specific materials chosen for study *in vitro* are certainly not expected to account for all possible sources of *in vivo* fluorescence. Fluorescence is very easily detected. Since a very tiny amount of fluorophore could have a strong emission and there are a multitude of potential *in vivo* sources, there will always be some doubt that all sources *in vivo* have been identified. The ultimate goal is to account for the *majority* of the total fluorescence on a volume basis and a process of elimination has been started to approach that goal. Certain specific materials chosen were intended to either i) sample *classes* of materials that are commonly found *in vivo*, ii) account for materials that occupy a significant volume of all tissues or iii) could contain chromophores with specific activity in the production of NIR emission. Thus protein is ubiquitous both as structural materials, e.g., collagen fibers in the extracellular matrix, and active molecular species in all tissues, e.g., enzymes and transport proteins like albumin.

Table 4-1 lists the cutaneous and subcutaneous constituents of human skin and blood tissue that are investigated. To get relevant result as reference for interpreting *in vivo* observed human skin autofluorescence, physiological concentration of each constituent was obtained (42). Yet, for those compounds that are found widely spread within the whole body, such as antioxidants, coenzymes, and collagen, the physiological concentrations refer to their levels in blood, interstitial fluid or in skin only. Some compounds, e.g., melanin, fat-soluble β-carotene and α-tocopherol, are poorly soluble in water as they are probably membrane bound or found in adipose tissues *in vivo*. In these

cases, stock solutions were made without knowing the exact concentrations. Various

dilutions however were made to offer a relative comparison of the absorption and

fluorescence capability. In this table, ×5 means five times of the physiological

concentration. Similarly, /2 means half the physiological or stock solution concentration.

Table 4-1: *In vitro* investigation of fluorescence and photobleaching properties of some
cutaneous and subcutaneous constituents of human skin tissue.

NAME	SOLVENT	CONCENTRATION		SOURCE	
		EXP.	PHYSIOL.	MFR	CAT. #
L-Glutathione	DI water	×5, ×125	≈1.09 mM	Sigma-Aldrich	G4251
Uric Acid	DI water	×2, stock	234-456 μM	Aldrich	16,118-7
β-Carotene	Cyclohexane	Stock, /2, /4, /25	1.23-1.75 μM	Sigma	C9750
Cholecalciferol	Cyclohexane	×5, ×125, ×3125, ×78125	40-80 nM	Sigma	C9756
L-Ascorbic acid	DI water	×5, ×125, ×3125	50-60 μM	Sigma	A5960
(±)-α-Tocopherol	Cyclohexane	Stock, /4, /25	≈24 μM	Sigma	T3251
Collagen	DI water	0.5-7.5 g/dL	N/A	Aldrich	27,160-8
Melanin	DI water	Stock, /2, /4	Various	Sigma	M8631
NAD/NADH	PBS	×10, ×50, ×100, ×500, ×1000	64 μM	Sigma	N3014
Hb	DI water	1.3-14.5 g/dL	12-17 g/dL	Freshly harvested	
Plasma	PBS	Stock, /2, /3, /4	N/A	Freshly harvested	

4.2.3.2 Antioxidants & Coenzymes

Water soluble materials, e.g., L-glutathione (reduced), L-ascorbic acid and nicotinamide adenine dinucleotiede (NAD/NADH), were readily dissolved either in de-ionized (DI) water or phosphate buffered saline (PBS) with pH adjusted in physiological level of 7.4 (44). The solubility of uric acid is dependent on both pH and temperature (115). At room temp (25 °C) neutral pH it only dissolves around 68 mg/L, which is about 404 µM. In order to prepare higher concentrated samples, pH of uric acid solution was adjusted to a little bit alkaline (pH=8). Stable solution with two times the upper physiological level could be obtained. More crystalline uric acid was added to form a stock of an even higher concentration. However, the absolute amount dissolved was not known.

For those that are not or are only barely soluble in water, such as β-carotene, cholecalciferol, and (±)-α-tocopherol, cyclohexane was used as the solvent because of its fairly flat baseline other than the six well-defined Raman peaks spanning the range of interest (116). Evidence of fluorescence growth could still be quite discernible even with the interference of cyclohexane Raman features. The nature of the study is for internal comparisons of fluorescence coming from one particular sample itself at various concentrations or under certain time of laser exposure. Therefore, constant Raman features from the solvent system will not bias the results in such a substantial way that would lead to misleading interpretation.

4.2.3.3 Collagen

Commercial product of gelatin produced from porcine skin was used. Though not a pure form of collagen, gelatin is 98-99% protein by dry weight extracted by boiling swine skin, tendons, ligaments and bones in water. The transparent, colorless solid substance dissolves in water when heated and gels when cooled down. In this study, 0.5 g of gelatin was dissolved in 10 mL DI water. The sample was contained in a cylindrical plastic cup and put onto a water-containing glass Petri dish. An electric heater was used to offer a warm "water bath" for the gelatin samples for 10 min. Then the samples were let cool in room temperature for another 2 min. During this process, the sample was frequently stirred to let the air bubbles release. It was then refrigerated for around 1 hr before the formed gel was taken out for tests.

4.2.3.4 Melanin

Synthetic melanin is purchased from Sigma-Aldrich. This skin pigment and photo-protector is isolated in the form of a biopolymer that does not easily dissolve in water and other commonly used organic solvents. Therefore, an excess amount of melanin was placed in DI water, stirred well and left overnight for maximal stock solution concentration. The stock solution produced has light brown color with black particles suspending throughout. Further filtration with various pore sizes filters, 20 nm, 100 nm or 200 nm (inorganic membrane syringe filters, Whatman Ltd., UK), was performed to avoid accumulating additional particles apparently by precipitating from unfiltered sample over a long experimental period.

As shown in Figure 4-3(A), raw spectra for filtered samples show significantly less fluorescence than the unfiltered one, apparently associated with the successful removal of larger aggregates. The sample without filtration shows broadband melanin Raman features at 1380 and 1580 cm^{-1}, the similar bands observed *in vivo* of cutaneous melanin (117). The Raman of filtered samples (Figure 4-3(B)) resemble with each other and both show less melanin Raman, indicating the dissolved melanin might have less degree of polymerization than that *in vivo*. Since the radius of melanin granules *in vivo* is estimated to be 40-50 nm (118) we used 100 nm or 200 nm filtration to preserve as much soluble melanin as possible.
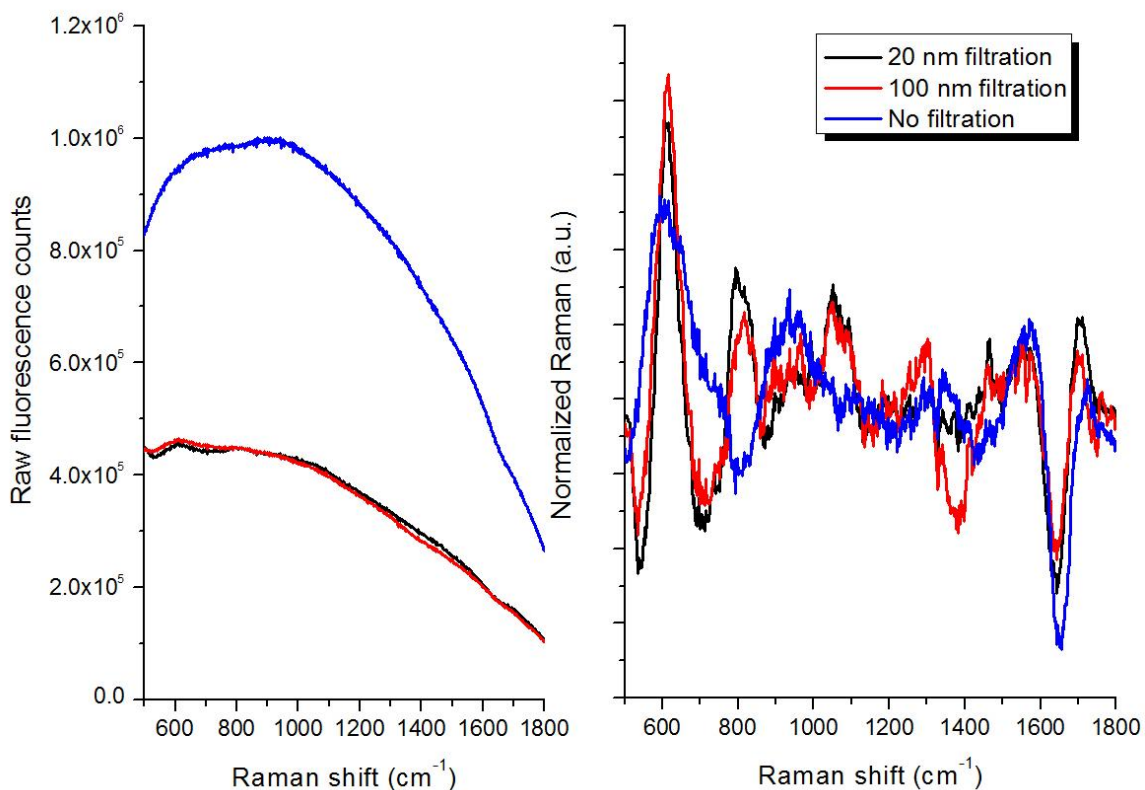
Figure 4-3: Raw (A, left) and normalized Raman (B, right) spectra for melanin solutions with various pore sizes of filtration.

4.2.3.5 Blood components

The blood sample was extracted from a healthy volunteer into a sodium heparin Vacutainer® tube (BD, Franklin Lakes, NJ, USA). The blood was centrifuged (3500 rpm for 12 min) to form a buffy coat. The supernatant plasma was removed and because it was not completely homogeneous, i.e., there were proteins and other materials that did not dissolve, a certain amount of glucose was intentionally added into it so that the stock plasma sample had a measurable glucose concentration (0-444 mg/dL) using HemoCue D-glucose meter (HemoCue Inc., Lake Forest, CA, USA). Using this as an internal reference provided dilution information for later sample preparation. Several drops of normal saline solution were then added into the remaining RBCs to wash off any lipid or proteins. Finally, Hb was released by adding DI water directly into hematocrit and Hb concentrations were measured by HemoCue Hb meter for different dilutions. Before the spectra were taken, Hb samples were further processed by passing through a 450 nm glass fiber low protein binding Durapore ® (PVDF) membrane syringe filter (Millex, Millipore Corporation, Billerica, MA, USA) to remove any cell debris which might introduce additional turbidity into samples.

4.3 Results

4.3.1 Antioxidants & Coenzymes

Raw spectra of all the six antioxidants and the coenzyme NAD are shown in Figure 4-4, Figure 4-5 and Figure 4-6.
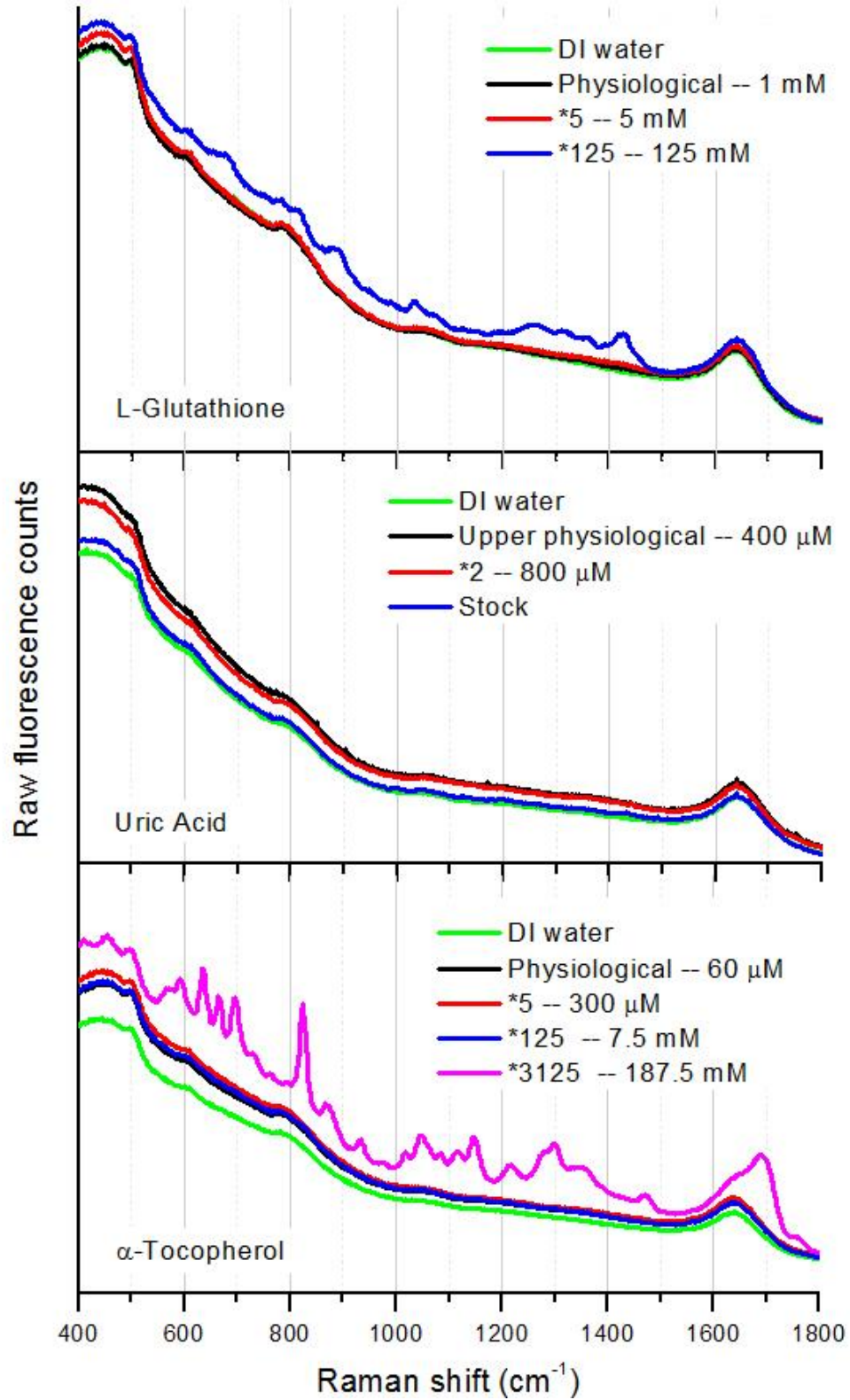
Figure 4-4: NIR spectra of three water soluble antioxidants, namely L-glutathione, uric acid and α-Tocopherol.
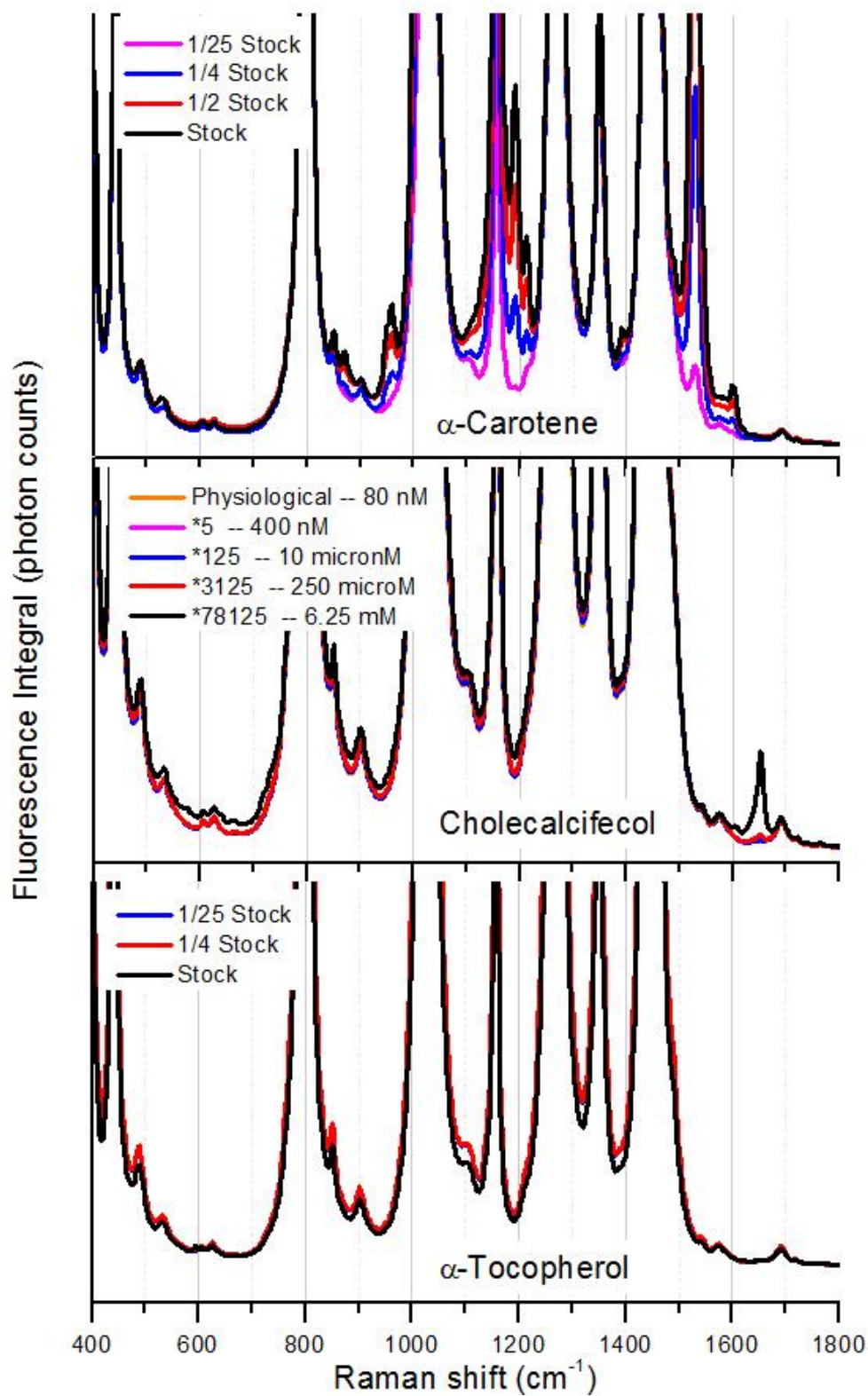
Figure 4-5: NIR spectra of three antioxidants that do not dissolve in water, namely β-carotene, cholecalciferol, and (±)-α-tocopherol. Cyclohexane was used as solvent.
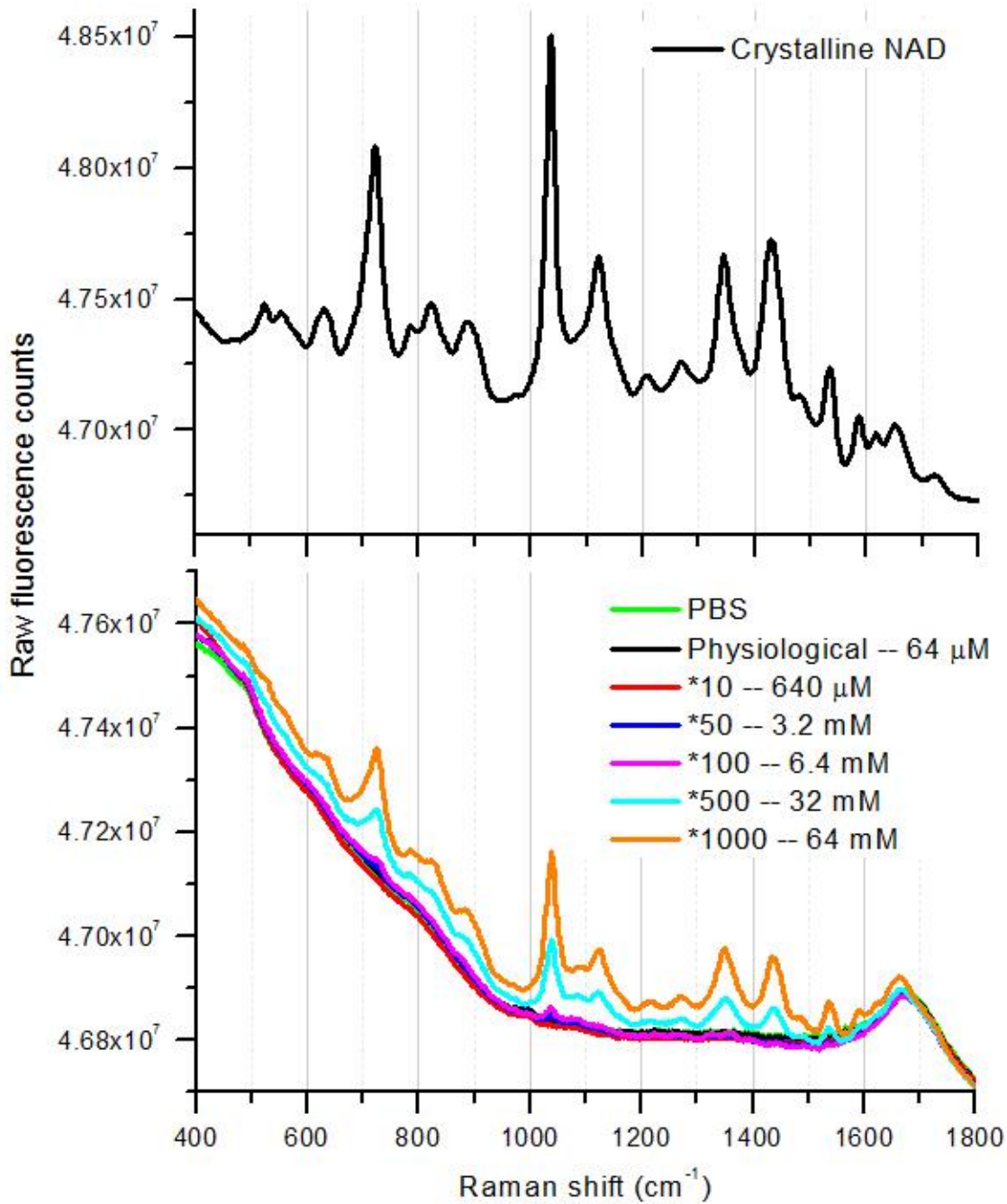
Figure 4-6: NIR raw spectra of crystalline NAD (A, top) and its solutions with various concentrations (B, bottom). In panel B, PBS background is buried within the spectra of four NAD aqueous samples with lower concentrations and thus is invisible.

Except for the samples with the highest concentration which also showed their corresponding Raman features, others showed no difference from the background. Considering their low physiological concentrations, these antioxidants and coenzymes could not contribute to the observed human fingertip autofluorescence under NIR excitation.

4.3.2   Collagen

Figure 4-7 shows a raw spectrum accumulated over 10 min for gelatin powder. As shown in the top panel, the broadband fluorescence stretches through the whole spectra range with Raman features visible on top. This feature is obviously absent from the aforementioned spectra for the pure form antioxidants and coenzymes in Section 4.3.1. Not shown in Figure 4-7 top panel is the flat baseline. Due to the dramatically different amplitudes, such baseline is indistinguishable from the x-axis and thus is left out. The bottom panel showed the Raman spectra for the same solid gelatin. The strong protein peaks, i.e., amide I and amide III around 1668 and 1248 cm^{-1}, are obvious and consistent with literature (119).

Not surprisingly, the fluorescence shown in Figure 4-7 is also concentration dependent in jelly form samples. Figure 4-8 shows the fluorescence integral growth with increasing gelatin concentrations used to prepare ten samples. Although the data has a noticeably big standard deviation, a linear fit still yield a correlation coefficient of 0.8 with a positive slope.
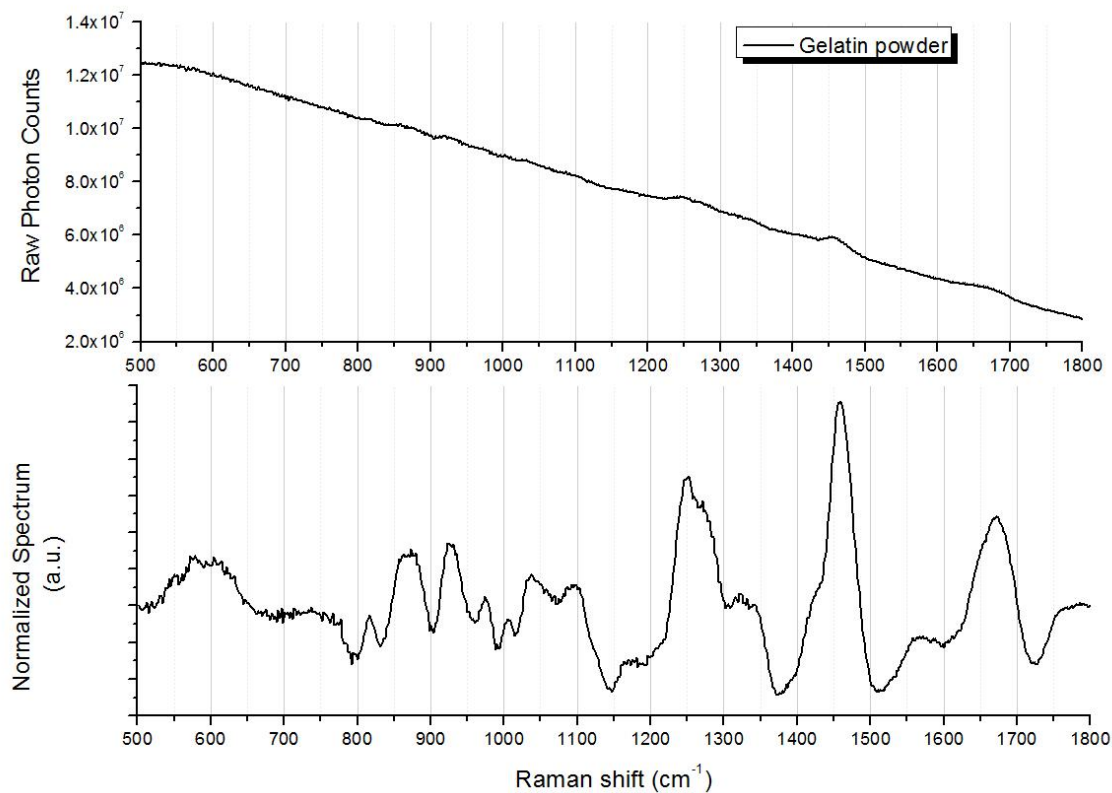
Figure 4-7: Spectra of gelatin powder with 10 min accumulation. (top) Raw spectrum; (bottom) 101-7 smoothed Raman spectrum.

Empirically, the big variation might result from experimental difficulties. Collagen gels were transparent and propagation of the laser within the gel could easily be seen by the naked eye. The penetration depth, i.e., probed volume, plays an important role in determining the yield of fluorescence. To guarantee relatively consistent thickness of the gel samples, customized parallel blades were used to cut the gelatin into a rectangular block with a fixed thickness of 12.5 mm. However, at lower gelatin concentrations the samples contained more water and the watery texture was hard to handle. This partially explains the relatively larger calculated residuals for samples contain less than 0.5 g gelatin per 10 ml water. Therefore, for the purpose of photobleaching experiment that

will be presented next, samples were prepared to contain 0.5 g gelatin per 10 ml water for the convenience of handling.
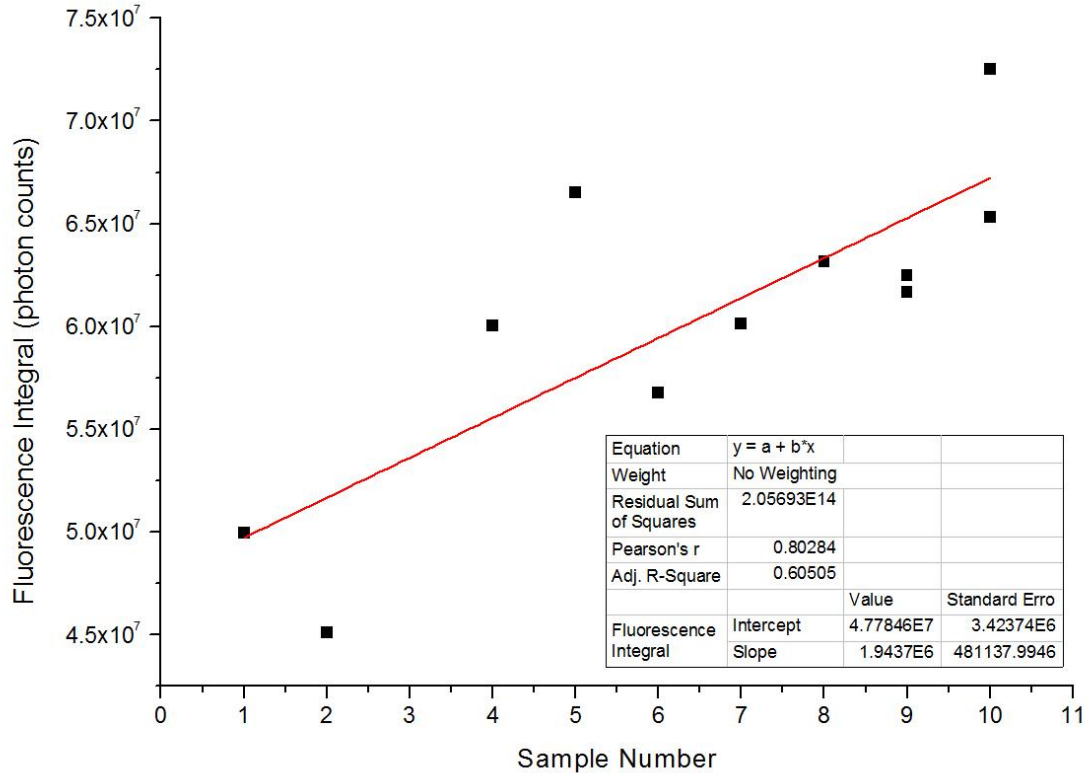
Figure 4-8: Fluorescence integral growth with increasing gelatin concentrations in jelly form. The gelatin concentrations increased by 0.1 g per 10 mL water. The third sample was left out as an outlier. Each spectrum was accumulated for 10 min.

Three bleaching curves are shown in Figure 4-9. Sequence 1 got the laser exposure first and showed a substantial amount (around 8%) of quench in its fluorescence. After 85 min of recovery in complete darkness, although the similar photobleaching pattern was expected, however, sequence 2 and 3 showed only randomly changing fluorescence integrals. Other sets of results from similar experiments also could not give definite answer on whether gelatin, i.e., collagen, fluorescence recovers or not.
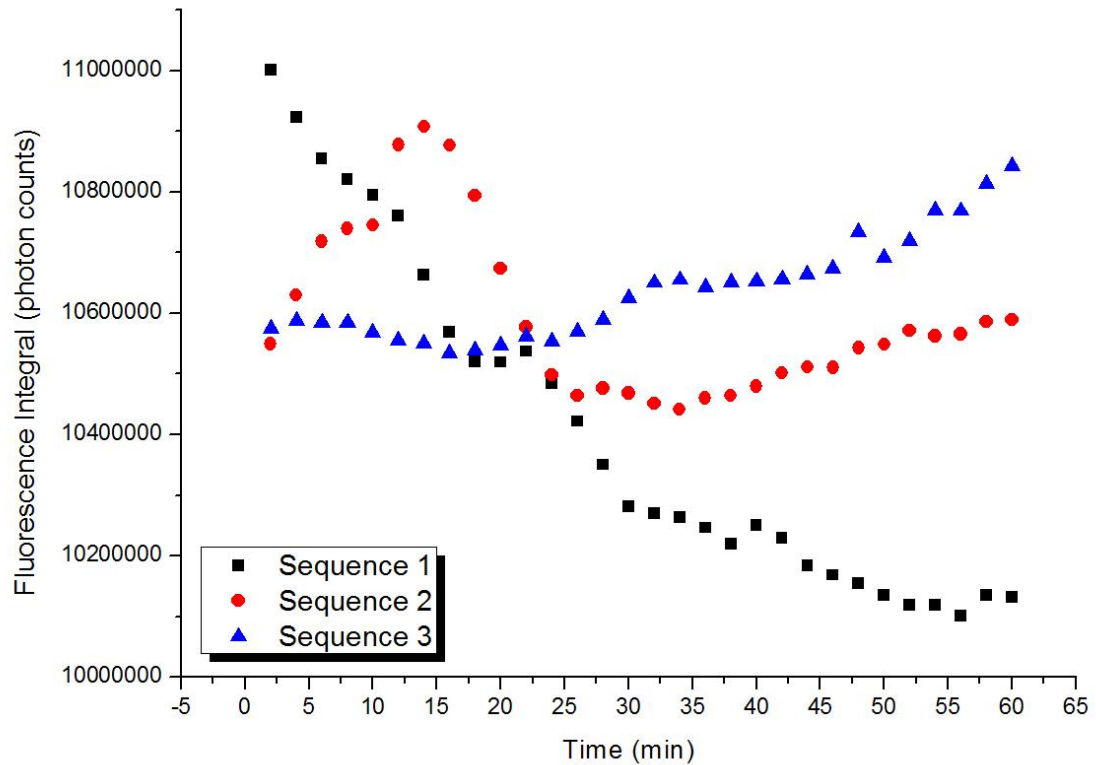
Figure 4-9: Three 1 hr bleaching curves for gelatin. The used gelatin concentration was 0.5 g/10 mL water and spectra were collected every 2 min. Sequence 1 was collected first and followed by an 85 min recovery period, during which the sample was left in complete darkness. Then sequence 2 and 3 were collected continuously afterward.

It is also an empirical fact that gels have some texture change issues if allowed to set in air for substantially long time. To obtain the data shown in Figure 4-9, the gelatin sample was left in air for a total time of almost 4.5 hr. Upon finishing the whole experimental procedure, noticeable sign of dehydration had been observed. To evaluate to what extend such texture change brought to the observed fluorescence, a control experiment was performed following the exact procedure but without laser exposure during the period of the three bleaching sequences in Figure 4-9.
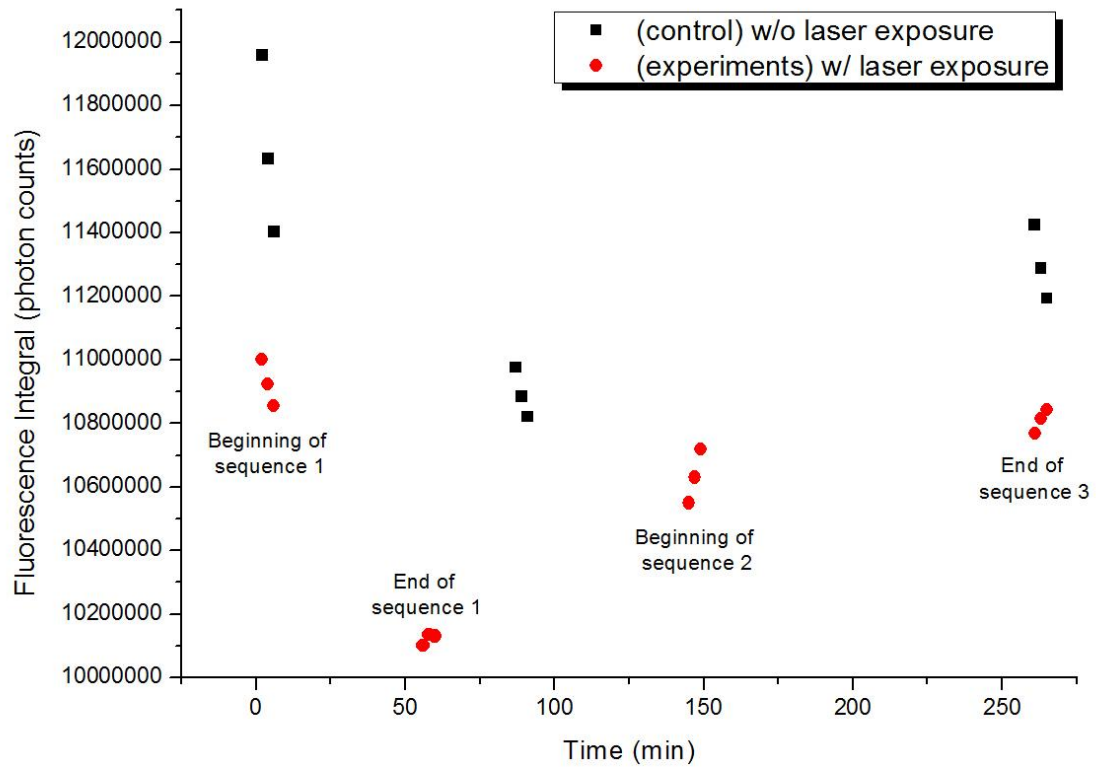
Figure 4-10: Gelatin control experiments showing texture variation during the experiments had nonnegligible influence on the fluorescence integrals.

As shown in Figure 4-10, three 2 min spectra were collected corresponding to three different times along the procedure: i) at the beginning of sequence 1, ii) during the recovery period, and iii) at the end of sequence 3. The range of fluorescence variation for the control group is similar as that for the bleaching experiments. The patterns are also analogous to each other. It is suggested that the influence of gel texture could not be overlooked when interpreting either the bleaching or recovery results shown in Figure 4-9. Laser radiation also introduces artifacts by heating and thus probably melting of the gelatin samples. There is no evidence that the same physical sample is being tested on

successive trials due to melting and resulting physical redistributions of the material, therefore bleaching cannot be evaluated.

Despite of the ambiguity of the bleaching property of gelatin it is clear that collagen fluoresces significantly under NIR excitation. Actually, in the timescale of an *in vivo* experiment, collagen does not show discernible bleach as shown in Figure 4-11. Therefore, it is evident that as a major constitute of extracellular matrix the structural protein collagen contributes as type I fluorophore to the *in vivo* observed fluorescence under NIR excitation.
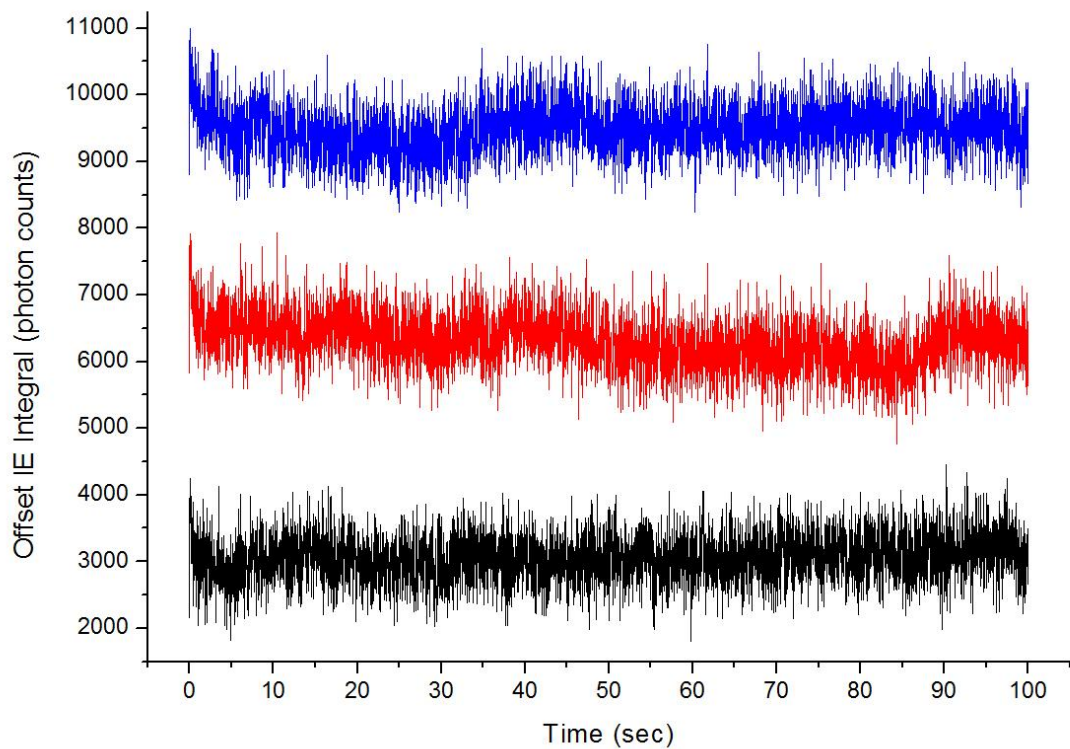
Figure 4-11: Fluorescence of three gelatin samples measured on different days using *in vivo* apparatus showing no sign of photobleaching during a 100 sec short period of time. Y-axis has an offset. Before offset, the average fluorescence of each 20 ms frame was 3053, 2221 and 2350 respectively.

4.3.3 Melanin

Melanin, a chromophore carried in melanocytes, is one of the main light-absorbing pigments in skin and is present only in stratum basale of the epidermis, i.e., it is not possible to excite blood without also irradiating melanocytes. As a skin photoprotectant, melanin absorbs UV/Vis radiation and disperses the energy through ultrafast internal conversion as heat. Microscopically, melanin is a granular biopolymer which is an aggregate of smaller component molecules. The melanin granule also has a much higher refractive index and therefore behaves as a strong scatterer as well as an absorber (108, 120). The fluorescence of melanin under multi-photon excitation has long been observed (121, 122), and it has been acknowledged as one of the major endogenous fluorophores of human skin under UV/Vis excitation.

Figure 4-12 shows the melanin fluorescence spectra under NIR excitation. The Raman and fluorescence from the cuvette and DI water is obvious. Nevertheless, the growth of broadband Raman (Figure 4-12(A)) from melanin at 1380 and 1580 cm^{-1} almost makes the cuvette Raman at 1650 cm^{-1} a shoulder peak in the stock solution. Fluorescence integrals for various melanin concentrations were calculated after the background emission from the DI water containing cuvette was subtracted. As shown in Figure 4-12(B), melanin fluorescence by NIR excitation increases linearly with concentration.
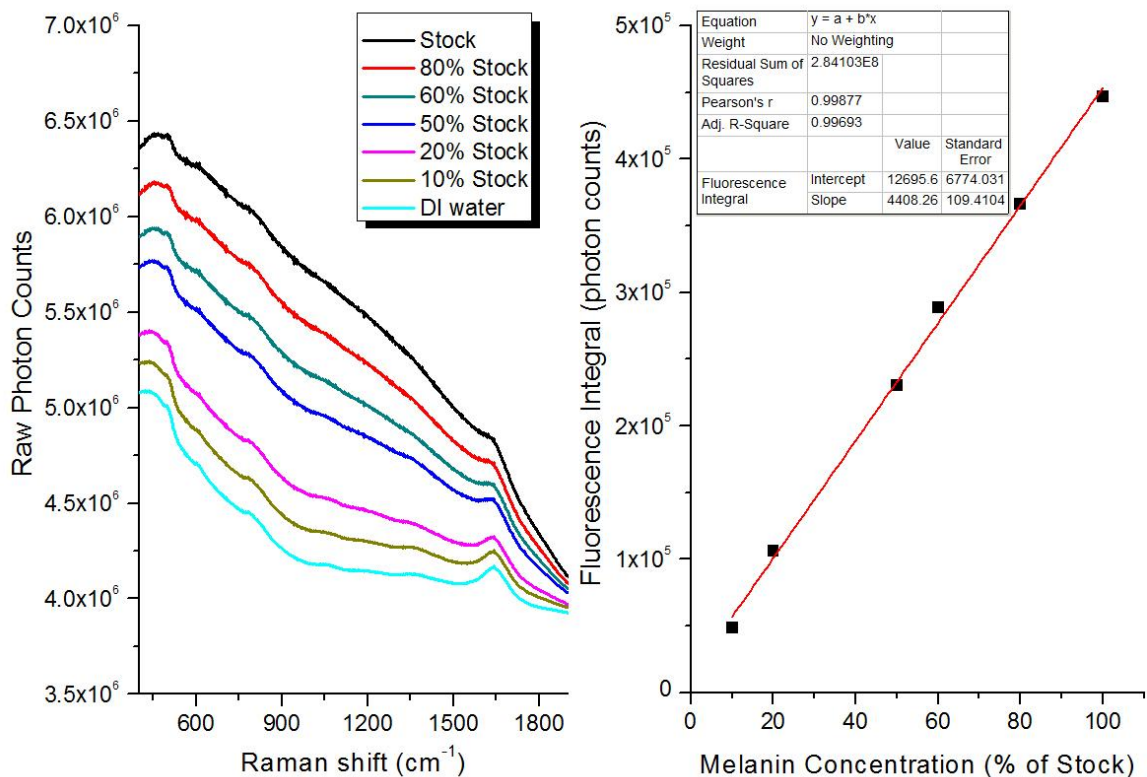
Figure 4-12: (A, left) Raw spectra of melanin solutions (30 min accumulation each) at various concentrations with 100 nm pore-size filtration; (B, right) Linear fit of fluorescence integrals vs. concentration for melanin. All spectra have DI water background subtracted. Correlation coefficient equals 0.999.

Figure 4-13 shows the bleaching curves for 200 nm pore-size filtered water soluble melanin. For both curves, NIR irradiation caused a quench around 25-30% from its original fluorescence. After 2 hr of exemption from the laser irradiation between the first and second exposure, fluorescence integral almost stayed where it was indicating no obvious recovery. Although not shown here, a 24 hr recovery time was also tested and still the same was observed.
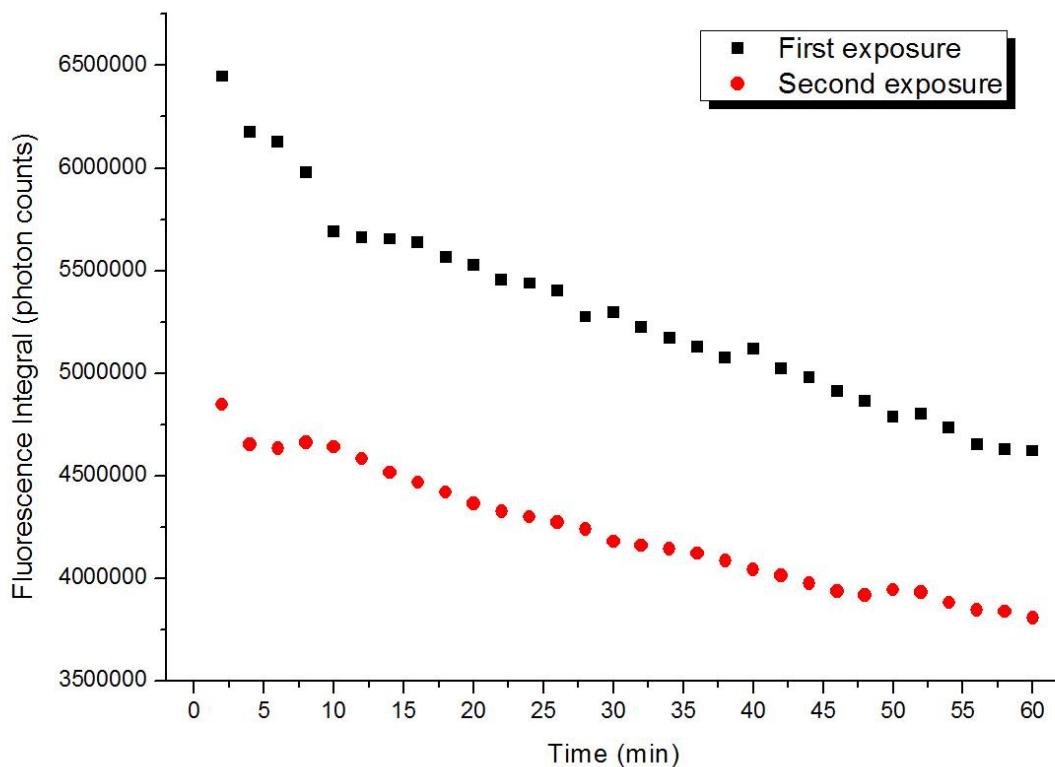
Figure 4-13: Photobleaching of 200 nm pore-size filtered melanin solution. 2 hr recovery time was allowed between the first and second exposure.

As a photoprotectant, melanin is susceptible to get oxidized by exposure to light with the generation of hydrogen peroxide in the photochemical process. It has been reported (123) that oxidation of melanin molecules causes it to fluoresce under UV/Vis excitation. Thus, the role of oxygen in NIR melanin fluorescence was studied by purging oxygen and argon till saturation in the melanin solutions. Results are shown in Figure 4-14. Oxygen purged sample shows no difference in the rate of bleaching from that without any gas purged. It is indicated that oxygen is not involved in the mechanism of melanin photobleaching in the same way as pentosidine that will be demonstrated in Figure 5-17 in Chapter 5.
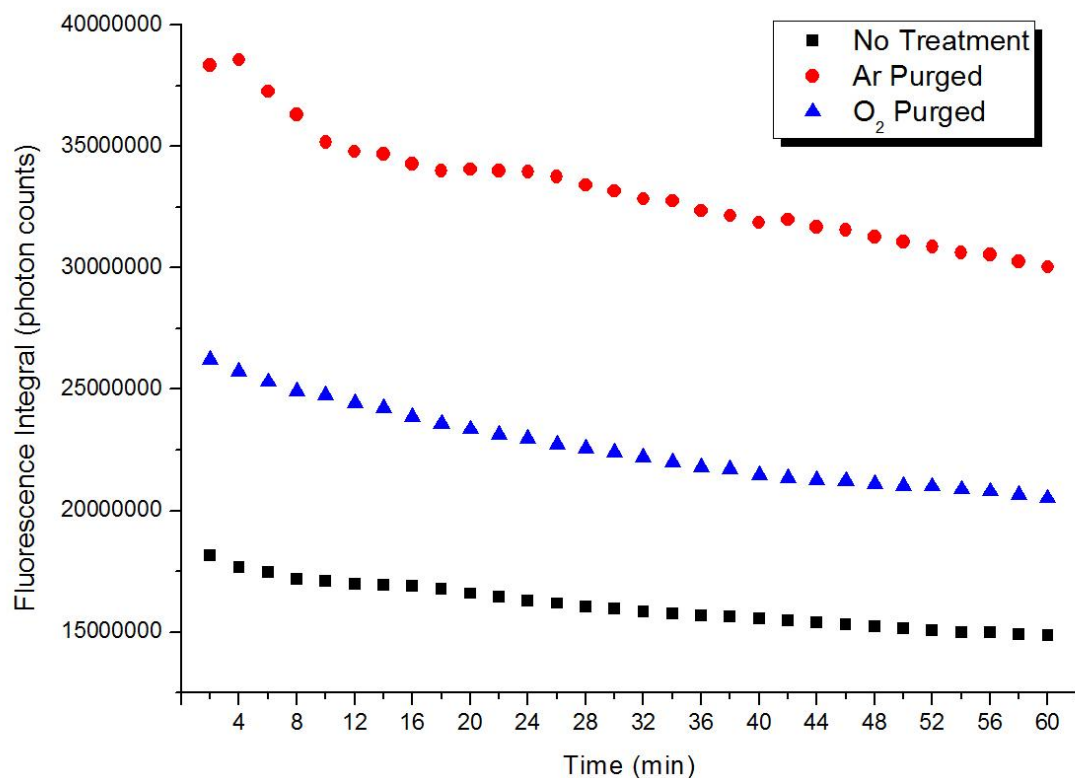
Figure 4-14: Bleaching curves of melanin with argon or oxygen purge.

Once again, it should be emphasized that the melanin samples used in this *in vitro* study are highly diluted water soluble solutions. The *in vitro* observed NIR melanin fluorescence may have limited relevance to the *in vivo* observation. As a strong absorber the melanin absorbance increases exponentially toward the UV/Vis range (124). The absorption of melanin in the NIR is extremely weak. Besides, its fluorescence quantum yield is also low, i.e., in the order of 10^{-4} (125). To this extend, melanin NIR fluorescence may not be a dominant factor *in vivo*. It is also an empirical observation that test subjects with difference skin tones do not always necessarily produce fluorescence that could be related with melanin levels, i.e., the darkness level. Melanin is also known as a tough substrate to be broken down through natural biodegradation process (126). Thus,

unrecoverable bleaching of melanin would have an accumulative effect on test subjects

who frequently participated in this study, i.e., the more often a test subject is exposed to

the NIR laser, the less his/her fingertip fluoresces. However, no such photobleaching

effect has ever built up within the normal metabolic period of skin. Therefore, as a type II

contributor to the *in vivo* human skin autofluorescence, its contribution to the observed

photobleaching might also be limited.

4.3.4   Blood Components

As shown in Figure 4-15, plasma produced copious NIR fluorescence. By contrast,

although not shown here, the NIR fluorescence of the Hb samples actually decreases as

the increase of Hb concentrations. However, it should be noticed that in the NIR spectral

range, Hb absorbs more than 10 times of plasma (10). The mismatch of the refractive

index of the cuvette and the Hb samples formed a shielding effect that reduces the

contribution of the cuvette while the Hb fluorescence increases. Less incident light

reaches the cuvette as the Hb concentration increase. Actually, Hb fluoresces but the

contribution to the total is not adequate to replace the cuvette fluorescence that decrease.
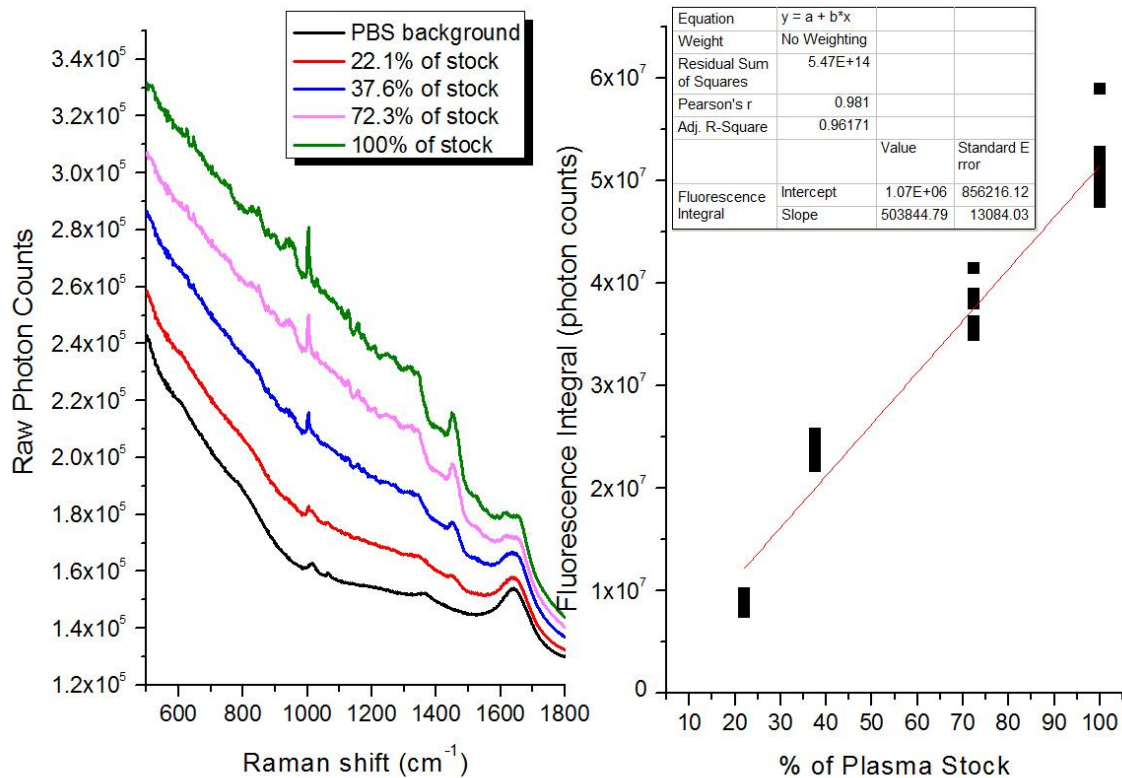
Figure 4-15: NIR fluorescence of plasma at various concentrations. Both raw spectra (A, left) and linear fit to fluorescence integrals (B, right) are presented. Fifteen 1 min spectra were collected for each concentration. The relative percentages were calculated based on the glucose added in to the plasma stock solution as an internal reference.

Nevertheless, evidence of Hb fluorescence could be suggested in the bleaching experiments shown in Figure 4-16(B). An obvious trend of fluorescence loss can be observed in Hb solutions, while in plasma solutions (Figure 4-16(A)) no such pattern is shown and total fluorescence fluctuates randomly. This indicates that it is Hb, not blood plasma, that contributes the most to the photobleaching in whole blood. In Hb samples, about 50% of fluorescence loss happens in the first 5 min. Although photobleaching slows down thereafter, there is no sign for the total fluorescence to become stable at 20 min. The rate of photobleaching is observed to increase with the increased concentration

144

of Hb. The most concentrated sample, which has an Hb concentration of 7.2 g/dL (normal range for human blood Hb level is 12-15 g/dL) bleaches the quickest.
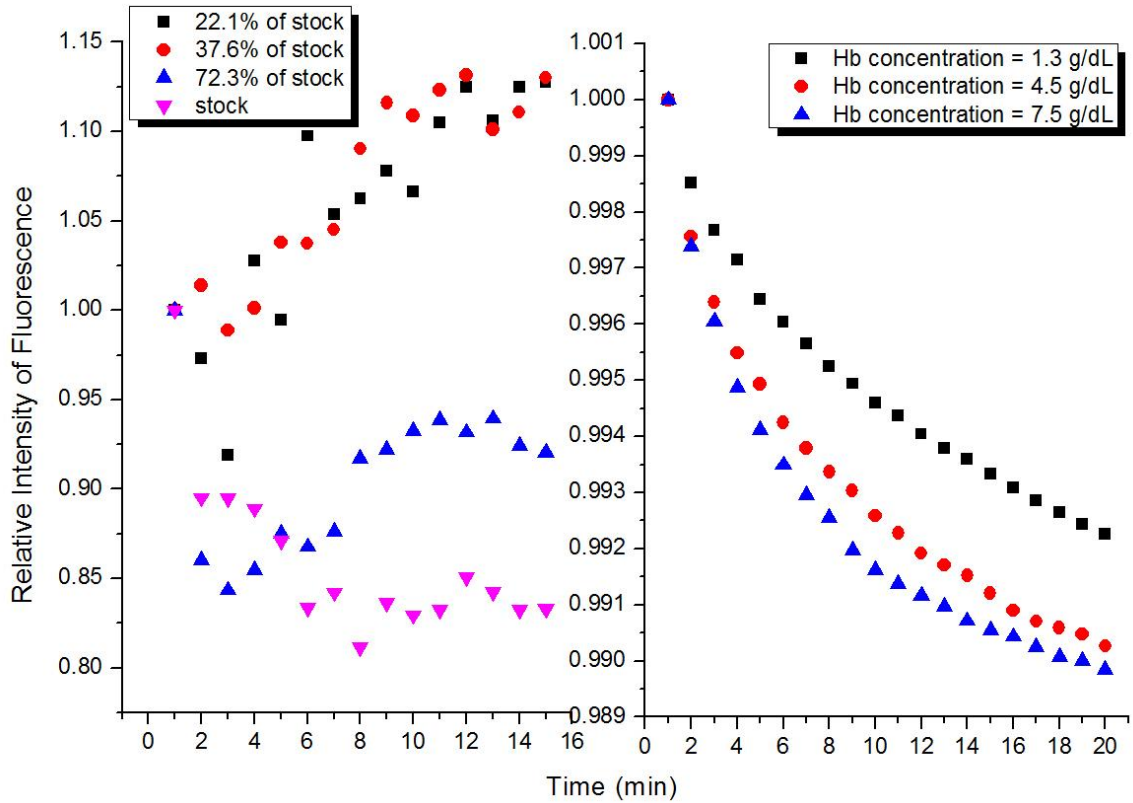
Figure 4-16: Photobleaching study of plasma (A, left) and Hb (B, right). The rate of bleaching is concentration dependent for Hb samples.

To characterize the bleaching properties of Hb NIR fluorescence, the Hb sample was put under laser exposure for 15 min and then left in the same place but without laser exposure to allow any possible recovery for 1.5 hr before the collection of the second spectra sequence. As shown in Figure 4-17 although not fully recovered, the total fluorescence did mostly restore back and the whole bleaching process could be repeated. Another similar overnight experiment also shows the same phenomenon, demonstrating that the observed Hb photobleaching is recoverable, or in other words, is reversible.
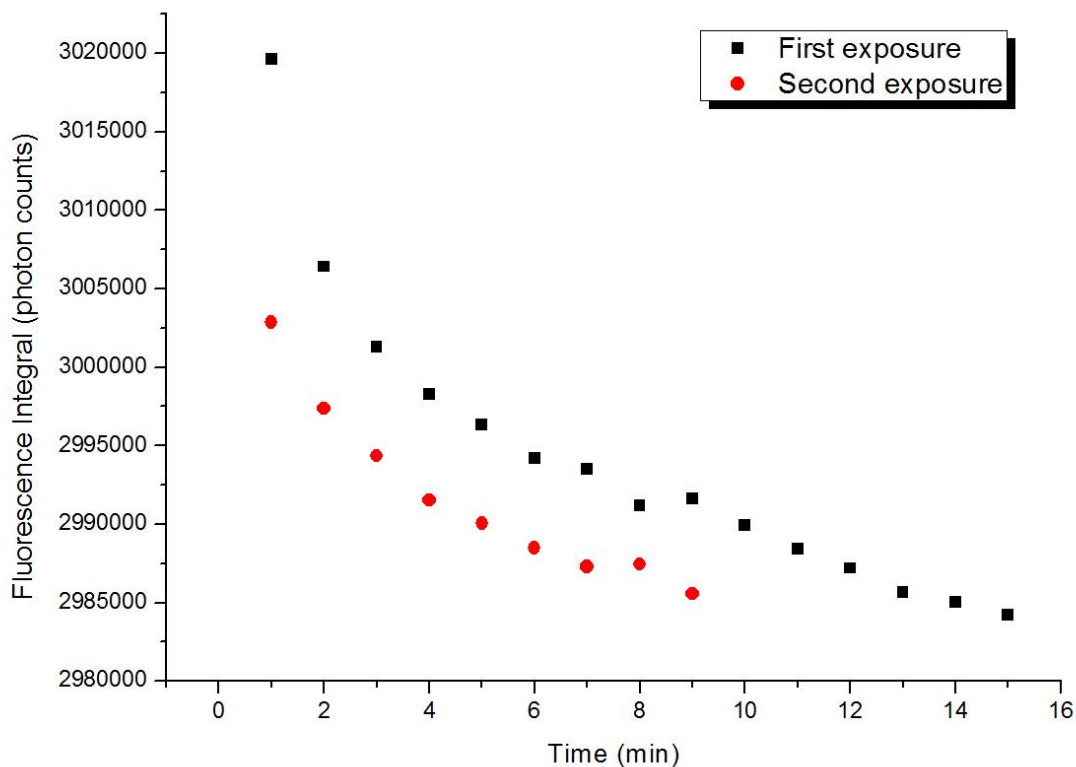
Figure 4-17: Recovery study of Hb photobleaching. The sample was left in complete darkness for 1.5 hr for possible NIR fluorescence recovery.

The photochemical explanation for the observed Hb photobleaching phenomenon is not fully understood. But, aggregation of Hb under laser exposure is observed in higher Hb concentration samples that are close to physiological level (not shown). As a strong absorber, whose absorbance coefficient is at least 10 times larger than that of plasma at 785 nm excitation, the aggregation further facilitates the absorption of excessive laser energy. As reported by Puppels (21, 127) and Franzen (128), a photo-induced aggregation phenomenon could cause the observed Raman spectra of single RBC to change with exposure time. Aggregation of large metal containing molecules in low lying but excited electronic states, perhaps of high spin multiplicities (90) and intrinsically long

emission lifetimes, would certainly create a very large density of vibronic states in which to thermalize electronic excitation and quench fluorescence.

To summarize, similar to collagen, plasma is a type I contributor to the *in vivo* observed human skin autofluorescence. While the bleaching and recovery properties of Hb suggest that the emission from whole blood, reaches a steady state *in vivo* when the laser induced emission is balanced against the photobleaching. Heart driven pulses are always observable *in vivo* and so equilibrium is apparently reached very quickly, relative to heart rate and blood flow rate *in vivo*.

4.4 Discussion

It should be pointed out firstly that *in vitro* solution environments, such as for Hb and melanin, are by no means comparable to their *in vivo* ones, no matter how concentrated the samples could be. Therefore the nature of the tissue fluorescence cannot be described unequivocally *in vitro*. For example in tissue, i.e., RBCs, Hb is tightly packed into erythrocytes, approximately 270 million per cell. Thus, biomolecular photochemistry within a RBC is likely to be much faster and more efficient than any *in vitro* environment which must be more dilute. Therefore, although the photodynamics observed here is capable of offering reference to *in vivo* phenomenon, it is only partially representative and should be interpreted warily in the context of *in vivo* observations.

A variety of antioxidants and free radical scavengers, i.e., vitamins and coenzymes, were also tested *in vitro*. Functionally important *in vivo* (129), surprisingly these materials generally do not produce NIR emission despite producing copious UV/Vis

147

emission. So while not every known metalloprotein was tested, the mere presence of amide linkages without any metal present, even thousands of them, does not seem to offer an explanation for the fact that nearly every protein displays some NIR fluorescence.

Endogenous and exogenous porphyrins (130) may also contribute as porphyrins are well known to produce copious fluorescence under either UV/Vis (123, 124, 131, 132) or NIR excitation. However, their fluorescence properties were not studied since cytochrome species that are found exclusively in the static tissue, i.e., cytosol and mitochondrial membranes, exist only in extremely small quantities (≈3 nM porphyrins per gram tissue) in skin (133, 134). This is not surprising since most of the natural porphyrins in human body are metabolic intermediates, such as protoporphyrin, and photochemical reactions upon irradiation produce reactive oxygen species (ROS) that are toxic to cells. Bacteria are known (130, 131) to produce porphyrins on the skin that for a given test subject could be significant. However, fingertips skin tissue is less prone to have abnormal overproduction of porphyrins through this pathway than facial skin as inflammation and acne vulgaris (135). Therefore, endogenous porphyrins are probably at most a minor contributor to the net *in vivo* fluorescence.

As shown in Figure 4-13 the melanin fluorescence does not recover but for the specific *in vivo* experiments it is noted that there is much less melanin on the volar side of fingertip skin, i.e., ridged skin is generally weakly pigmented if at all. Therefore, it is concluded that most of the observed fluorescence does not originate with melanin. Anecdotally strongly pigmented fingertips have only been observed in certain people, e.g., from the Indian subcontinent, but for most test subjects the pigmentation of ridged skin actually is very low. Furthermore sun induced pigmentation, i.e., sun tan, requires tens of

hours to develop and this timescale is also in disagreement with the *in vivo* characteristics of the fluorescence recovery that have been observed.

It is commonly stated in the cosmetic literature that natural exfoliation limits the lifetime of viable skin cells to about 28 days. Clearly this depends on the type of skin, i.e., smooth body or facial skin is probably well described with ridged skin having a longer lifetime. So skin that is bleached today is unlikely to be exfoliated completely by the next day. Since the penetration is greater than the thickness of the nonviable and viable tissue, i.e., 500-700 μm, the bleached spot should be able to be detected if that is the site of bleaching chemistry and it does not repair overnight. Since we never have had evidence of detecting a bleached spot under such conditions the contribution of the melanin to the bleaching does not seem significant.

Even the dead outer cells of the stratum corneum in direct contact with the atmosphere cannot be guaranteed to remain attached to the irradiated surface. Therefore to obtain the result which is always observed *in vivo* it is suggested that the bleaching behavior occurs below the outermost layers of cells whether they are viable or not. Thus on the basis of direct *in vivo* observations and comparison with specific *in vitro* materials, it is suggested that the fluorescence from so called "static tissue" mostly originates from the cells and extracellular spaces and fluids in contact with the viable tissues.

Most commercially available proteins like gelatin or bovine serum albumin fluoresce although it is possible that they could contain preservatives, e.g., antioxidants, and impurities, e.g., ash. However, according to the manufacturer there are no preservative impurities and the ash is an extremely small percentage of the material so these do not

seem to be viable sources of the observed emission. It should be also noted that many proteinaceous materials as well as nonproteinaceous materials are purified on sucrose or sepharose columns and these could promote the formation of AGEs as will be discussed later in Chapter 5. Therefore freshly harvested serum and plasma were tested. These samples were also found to fluoresce but it is difficult to obtain either plasma or serum *in vitro* that absolutely contains no residual Hb. Therefore, to date it is hypothesized that plasma has intrinsic fluorescence separate from that of RBCs but that it apparently does not bleach. On this basis we suggest that *in vivo* the bleaching of blood that is not impeded in its cardiac driven motion is not as important as tissue bleaching.

4.5 Conclusions

The presence of ubiquitous NIR fluorescence from human skin *in vivo* is well-known but poorly understood at least partly because there are many potential sources with only limited means for separating the different contributions. In this chapter, *in vitro* study on the photochemistry of various blood and static tissue constituents was performed in an effort to narrow down endogenous sources of the observed *in vivo* spontaneous NIR fluorescence from biological tissues. Of all the substances investigated in this chapter, four of them stand out, namely collagen, melanin, plasma and Hb: two major static tissue constituents and two major blood proteins. The major skeletal protein in static tissue, e.g., collagen, and another important blood protein, e.g., plasma, contribute significantly to the non-bleachable part of the baseline *in vivo* observed skin autofluorescence. Based on *in vivo* observations *at the site probed*, it is suggested that melanin fluorescence though not

negligible has only limited influence. Hb fluorescence bleaches but also recovers quickly,

thus it is more likely to form a dynamic equilibrium with cardiac pulses during *in vivo*

measurements. However, no observations or statistics have been reported supporting the

idea that these tissue constituents vary in some way between healthy and diabetic patients.

But, as shown in Figure 3-8 in Chapter 3, it has been observed *in vivo* that there is

considerable difference between the autofluorescence and bleaching properties of healthy

and diabetic patients. Therefore, the photochemistry of another potential fluorophore, e.g.,

AGEs, needs to be investigated.

5. PHOTOCHEMISTRY OF ADVANCED GLYCATION ENDPRODUCTS (AGEs)

5.1 Advanced Glycation Endproducts (AGEs)

5.1.1   Motivation of AGEs Study

It was established in Chapter 3 on the basis of *in vivo* experiments on human volar side fingertip skin that: i) the majority of the photobleached fluorescence does not originate within blood, ii) the bleaching (1/e point) occurs in 10^1-10^2 sec timescale with 200 mW 830 nm excitation, and also iii) a photobleached region remains bleached for at least 45 min but recovers completely within several hours. From the *in vitro* investigations of various tissue and blood constituents in Chapter 4, it was shown that among the constituents that fluorescence under NIR excitation, e.g., collagen, plasma, melanin, and Hb, only the last two show the trend of photobleaching.

In vitro experiments suggest that when disconnected from biochemical processes characteristic of metabolic homeostasis, Hb photobleaching is reversible whereas melanin is not. However, melanin production requires longer than days to accumulate, resulting in inconsistency with respect to the timescale of the fading of the bleached spot observed *in vivo*. Combining these with the fact that volar side ridged skin is not usually strongly pigmented it is suggested that the majority of the bleachable fluorescence that recovers on a several hour to 1 day timescale may be associated with something else.

Among the different ethnic groups encountered, African American, some Indians and Hispanic subjects are more pigmented than Caucasian and Asian. However, *in vivo* spectra collected for tens of test subjects that participated in this study for the past several years have indicated that the baseline IE is not necessarily positively related with skin melanin levels. By saying baseline IE, it means the part of IE that is not modulated by the blood movement. What has been observed in a systematic way is the excessive IE for senior and diabetic patients, similar as what has been reported by others (136).
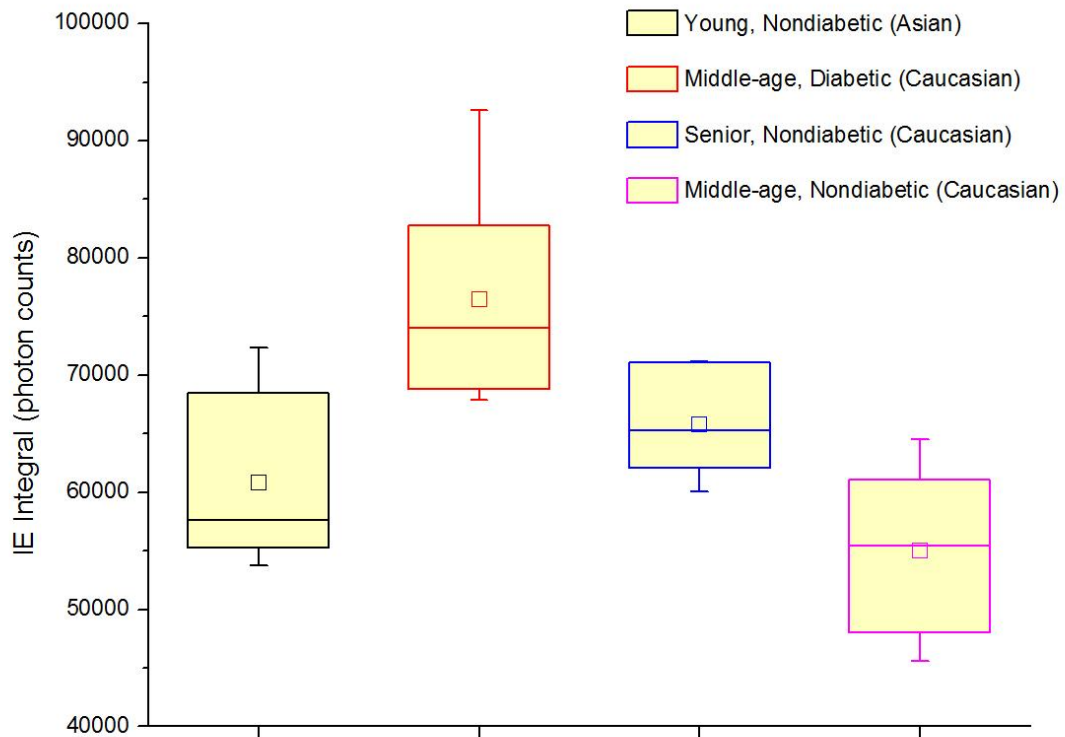
Figure 5-1: IE integrals collected on the same day for four individuals showing the fluorescence from senior and diabetic patients are stronger than others. Six and eight data points are used for non-diabetic and diabetic subjects respectively. Upper and lower edges of box represent 75th and 25th percentile. Smaller square represents mean value. Top and bottom whiskers represent maximum and minimum data respectively.

Figure 5-1 shows the *in vivo* IE integrals for four subjects collected on the same day under the PDPM settings that are optimal for each individual respectively so that differences cannot be attributed to differing blood content, i.e., perfusion. Within the same ethnic group, diabetic patient fluoresces significantly more than healthy people. Though not as distinctive, senior test subject also tends to produce more fluorescence. Such tendency leads us to seek age or diabetes related endogenous tissue constituents that have potential to contribute substantially to the *in vivo* observed fluorescence.

Advanced glycation endproducts, or AGEs, are a family of complex and reactive compounds that result from a chain of chemical reactions started with a glycation reaction (137, 138), i.e., a reaction between certain amino acid side chains, e.g., lysine or arginine, and various sugars, e.g., ribose and glucose. After the formation of AGEs, the accumulation in the tissues is dependent on the half-life of the proteins to which the crosslink is bound (139). Therefore, on long-lived proteins like skin collagen, AGEs accumulate over the lifetime. In the AGEs family, compounds like N-carboxy-methyl lysine (CML) and pentosidine are known to be highly fluorescent in UV/Vis spectral range. But before this work there was no knowledge of the photochemical behavior under NIR excitation. Therefore, it was necessary to investigate the fluorescence features of these compounds under NIR excitation in order to hopefully shed some light in explaining our *in vivo* observations.

5.1.2   Endogenous Formation Pathways of AGEs

The formation of AGEs is part of normal metabolism *in vivo*. Although physiologically there is more than one pathway leading to the ultimate synthesis (109, 140), they all include a glycation step at the early stage, which is called the Maillard reaction. This chemical reaction involves bonding and crosslinking between amino group containing compounds, such as proteins and amino acids, and the carbonyl group of reducing sugars. During this process chemically reversible early glycosylation products with proteins, such as Schiff bases and Amadori adducts, are formed. Over time, these intermediate products undergo slow and complex processes comprising condensation, rearrangement, fragmentation, and oxidation reactions to finally form AGEs. At this stage, the alteration of circulating, cellular, and extracellular matrix proteins is final and irreversible.

Of all reducing carbohydrates and sugars in protein glycation, the physiologically relevant D-glucose is one of the least reactive. That is possibly an evolutionary reason why it is the most important free sugar *in vivo* being widely used in organisms as a source of energy (141). While by contrast, it is well known that D-ribose is much more reactive in the Maillard reaction (109, 142) due to a higher fraction of the more reactive acyclic form. However D-ribose does not elevate in human but D-glucose does when excessive carbohydrates are consumed. Pooling of dietary D-glucose in interstitial fluid or blood flow has been proved to result in an elevated AGEs level (139, 143, 144). Albeit at a slower rate, AGEs formation *in vivo* from glucose is possible through oxidation of glucose to arabinose or even ribose (145).

As shown in Figure 5-2, dietary glucose goes through the pentose phosphate pathway which reduces hexoses into ribose-5-phosphate, and further into pentoses, such as ribose. Although there may be other established metabolic pathways that connect glucose to more reactive sugars, the point here is that ribose is always available for new AGEs formation to replace prior AGEs within hours if they are consumed by the photobleaching reactions reported earlier in Chapter 3. Then through the Maillard reaction, these reducing sugars build crosslinks with the free amino groups of protein and form intermediates. A variety of other AGEs are eventually generated by more thorough and complicated oxidation of these precursors within living organisms.
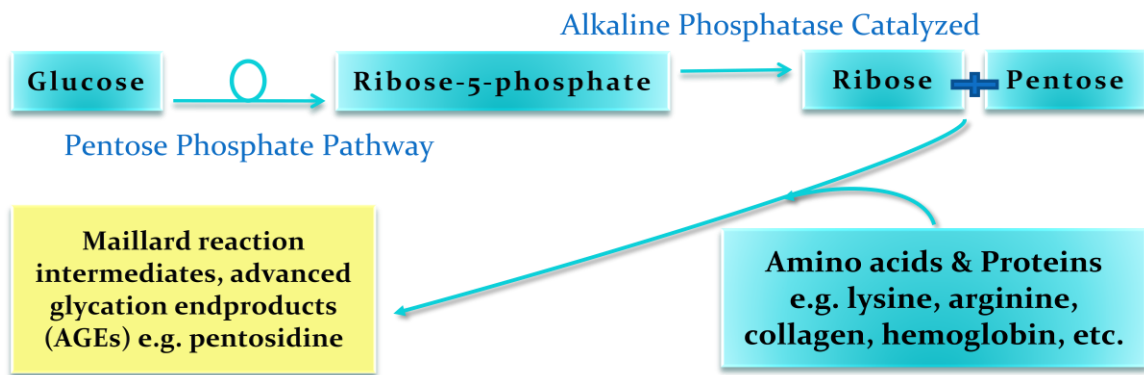
Figure 5-2: One possible endogenous pathway of AGEs formation from the free sugar D-glucose.

5.1.3 Clinical Aspects of AGEs

There are three different mechanisms by which AGEs contribute to some long-term diseases and complications (139): i) binding and crosslinking with a primary amino group of a protein; ii) interaction with AGE receptors (142, 146); and iii) binding to lipoproteins. Of the three mechanisms, the first one brings detrimental pathogenetic effect even in the

process of AGEs formation. Upon bonding with structural protein within the extracellular matrix, e.g., collagen, related tissue and organs lost their original elasticity. In vascular system, increasing stiffness leads to angiosclerosis and related cardiovascular diseases. In tissue, AGEs could cause widespread damage through up-regulation of inflammation and oxidative stress.

As will be shown in Table 5-1, AGEs exist in almost every tissue and organ within human body, with higher concentrations in cartilage, dura mater, vascular base membrane, skin, and the circulatory system. By nature protein glycation is a slow process; however the lifetime of AGEs is determined by the protein to which they are bound. In the circulatory system, e.g., the blood stream, the turnover times for both albumin (15-20 days) and Hb (120 days) are short (147-149). Therefore, the best known AGE hemoglobin H1c (HbA1c), is a biomarker for the 120-day moving average of plasma glucose concentration (150, 151). Yet in long-lived protein as collagen or other structural materials, AGEs could stay for the life time of the organism due to their low clearance rate in kidney (152). It has been well established (143, 153) that AGEs build up with age and the accumulation is increased under long-term hyperglycemia, which is common for many diabetic patients.

Excessive accumulation of AGEs in long lived tissues is believed to play a pivotal role in diabetes (154-156), and even a causative factor in several other age related chronic diseases, such as vascular disease, cardiopathy, neuropathy, nephropathy, retinopathy, cataract, and arthritis (137, 138, 157-159). On the other hand, monitoring the UV/Vis fluorescence of AGEs has been proposed as a marker of inflammation and oxidative stress in renal failure in kidney transplant, or as a substitute for the HbA1c as an indicator

of diabetes duration and time-averaged glycemic status in diabetes mellitus (91, 111, 160-162).

5.1.4   Pentosidine and Tri – Mixture (TMX)

Among the entire AGEs family (163), pentosidine is one of the most frequently studied molecules and has been proposed by Monnier and Sell (153, 160) as a prototypical AGE. *In vivo* pentosidine is derived from a pentose crosslink between arginine and lysine residues in collagen. In late 1980s, Monnier first isolated pentosidine in human collagens and other tissue proteins (153).

Table 5-1: Summary of pentosidine levels in different tissues (153).

TISSUE	YIELD (nmol/g)	TISSUE	YIELD (nmol/g)
Dura mater	117	Skin	27
Tracheal cartilage	142	Cortical bone	9
Aorta	33	Cardiac muscle	29
Lung	29	Liver	12
Kidney medulla	25	Purified isolated glomerular basement membrane	21
Red blood cells	10	Blood proteins	8
Lens	0.7	Placenta (commercial type III, IV, V soluble collagens)	ND

As shown in Table 5-1, it is ubiquitous in all tissues this noninvasive spectroscopic study is interested in, namely skin, RBCs, and blood proteins. Similar to other AGEs, pentosidine is also found to accumulate in tissue (primarily forms crosslink with collagen)

158

with age (143, 144). Its association with aging related processes diseases and diabetes has

been declared over the past decades by multiple individual research groups (155, 160,

164, 165).

The structure of pentosidine molecule is shown in Figure 5-3. Residues from

arginine and lysine are attached to the core imidazo pyridinium ring. Obtaining adequate

quantities of pure pentosidine with which to explore properties and processes relative to

NIR photobleaching effects in skin is presently not practical since the published

syntheses are currently beyond our skill level. Pentosidine is commercially available

though very rarely; it is extremely pricy (2 mg for $450, 5 mg for $1000) and might

contain impurities from living tissues that preclude performing spectroscopic

investigations.
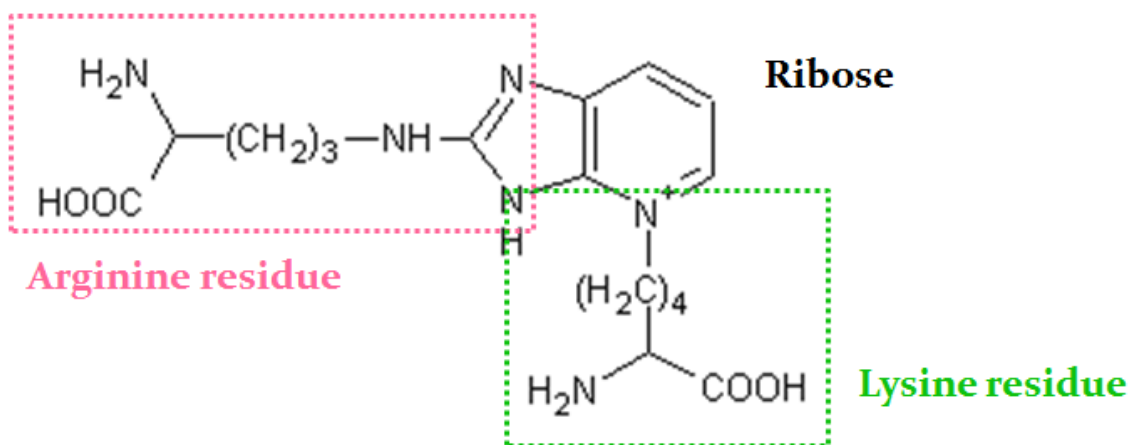
Figure 5-3: Molecular structure of pentosidine. Pentosidine could be synthesized exogenously by heating up ribose, lysine, and arginine and then be purified from this TMX. The structure shows the apparent residues from the two amino acids and the ring structure from the pentose.

Alternatively, pentosidine can be formed following the approach proposed by Monnier (109, 153, 160). Theoretically, all reducing carbohydrates, pentoses, hexoses, and even disaccharides can potentially be involved in the Maillard reaction and ultimately form AGEs. D-ribose is the sugar counterpart in most of the *in vitro* studies, not only because it reacts 30 times faster than D-glucose but also because of its 10 times higher yield. Therefore, in this study an aqueous solution termed as the "tri-mixture" (TMX) is produced in order to study the photochemistry of pentosidine.

TMX is produced by heating L-lysine, L-arginine and D-(-)-ribose in phosphate buffered saline (PBS) solution at 65 °C for at least1 hr under continuous stirring. Further purification of this TMX is available (166) but at extreme reduction of net yield. Nevertheless in living tissues AGEs are accompanied by variety of intermediates. Thus, keeping the unpurified form of TMX could be more appropriate for exploring the source of our *in vivo* observations. As will be shown in Section 5.4, this solution displays many of the properties of skin NIR autofluorescence photobleaching and it allows some *in vitro* experiments that we hope will shed some light on the *in vivo* photobleaching process and our hypotheses concerning volume normalization.

5.2 Singlet Oxygen ($^1O_2$) Chemistry

5.2.1 Triplet Oxygen ($^3O_2$) & Singlet Oxygen ($^1O_2$)

Energetically more favorable, the oxygen molecule has a triplet ground state ($^3O_2$), which is unusual for the vast majority of other molecules. When excited, $^3O_2$ can get to two singlet excited states, 95 kJ/mol and 155 kJ/mol above the ground state respectively.

However, in the condensed phase the singlet state which is 155 kJ/mol above the ground state is not significant because of the increased chance of radiationless deactivation to the lower 95 kJ/mol singlet state. Therefore, $^1O_2$ is usually referred to the lower lying singlet excited state of molecular oxygen.

Among the few species that exhibit a triplet electronic ground state, molecular oxygen is the one that actively participates in a variety of chemical and biochemical processes. During the normal metabolism of oxygen, the natural byproduct $^1O_2$ is generated, which has been known to play an important role in cell signaling and homeostasis (167, 168). In fact $^1O_2$ is way more reactive than ground state oxygen. It can initiate a plethora of events that lead to cell death. Therefore, one of its major clinical applications is to kill cancerous cells in photodynamic therapy (PDT) (169-172). In this radiation treatment, $^1O_2$ sensitizer is injected into the blood flow and depending on the absorption property of the sensitizer either UV/Vis or NIR radiation from a laser or light emitting diode (LED) is guided to the site of operation. When radiated, the sensitizer excites the oxygen molecules in the surrounding tissue to $^1O_2$. Malignant cancer tissue and cells are characterized with high metabolic rate, thus are over-plethoric and highly oxygenated. More $^1O_2$ molecules are generated in cancer than in normal tissue. Therefore, an effective treatment is achieved.

5.2.2   Photosensitized Process of $^1O_2$ Formation

$^1O_2$ could be generated by direct photoexcitation from triplet ground state oxygen (173). Alternatively, energy could be gained during the collision of $^3O_2$ with another

excited molecule to ultimately form reactive $^1O_2$. The whole process always includes a

step that enables the nonradiative transitions between two electronic states with different

spin multiplicity, which is known as intersystem crossing (ISC).

Inter-nuclear Separation (r)
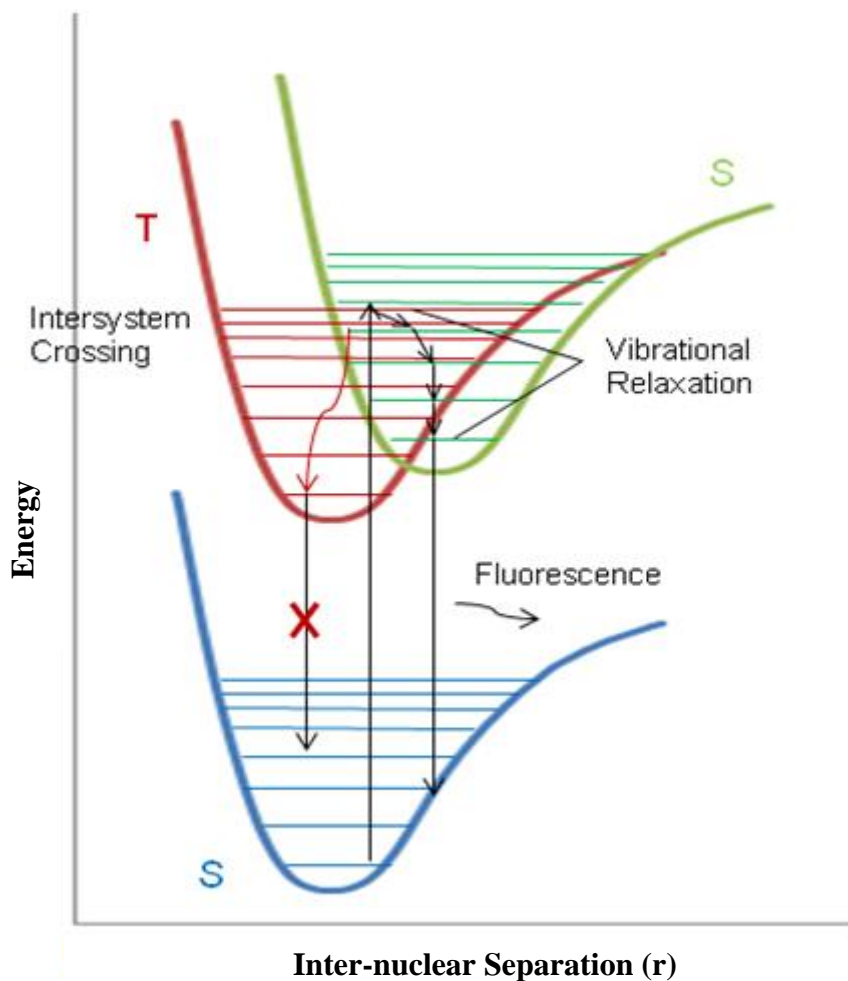
Figure 5-4: Normal processes of electron interaction with light inside a molecule. Most of
the time the ground state (blue curve) of a molecule has singlet spin coupling. (S: singlet;
T: triplet) Although not always favorable, the energy could be transferred to a
neighboring triplet excited state through ISC.

As shown in Figure 5-4, normally the absorption of photon(s) excites a ground state

molecule to its singlet excited electronic state. Most of the time, the energy of absorbed

photons is directly spent on fluorescence emission. However, for some heavy-atom

molecules, such as metal containing porphyrins and some iodine/bromine bearing

molecules, overlapping singlet and triplet excited vibrational levels exist. In this case, the

probability of ISC occurring is more favorable. Thus, the absorbed energy is transferred

from the singlet excited state to a metastable excited triplet state without any photon

emission.

ISC is one of the slowest forms of relaxation with a time scale on the order of 10^{-8} to

10^{-3} sec (174). In an isolated molecule, as a result of ISC, energy is trapped in the triplet

state since the electron transition from an excited triplet state to a singlet ground state is

quantum mechanically forbidden. However, phosphorescence still occurs at a

significantly slower rate (10^3 to 10^0 sec) for such "forbidden" transition (85). In a solvent

system where molecular oxygen is present, the trapped energy could be transferred to the

ground state oxygen through the well-known triplet-triplet annihilation (TTA) process,

which gives rise to $^1O_2$ (175). A schematic drawing of this complete process of $^1O_2$

photosensitization is shown in Figure 5-5. It is also the working principles of

photodynamic therapy (PDT) in treating cancer (172, 176).

Molecules that are capable of generating $^1O_2$ by photosensitizing $^3O_2$ are called

singlet oxygen sensitizer, or photosensitizing dye. To be a singlet oxygen sensitizer, the

molecule should first of all have two overlapping singlet and triplet excited states, since

in the ISC transition little or no energy must be gained or lost. In addition, the triplet

excited state of a sensitizer should be slightly higher than that of $^1O_2$ relative to the

ground state to achieve effective energy transfer (177). Finally, its lifetime should be long

enough to undergo the TTA with ground state oxygen. For a sensitizer to be used in *in*

vivo PDT, not only should it be water soluble but also be able to exhibit a high quantum yield of $^1O_2$, leading to the death of a cell or biological tissue. Hypericin, rose bengal diacetate, and methylene blue are all among the most efficient reagents for $^1O_2$ generation.
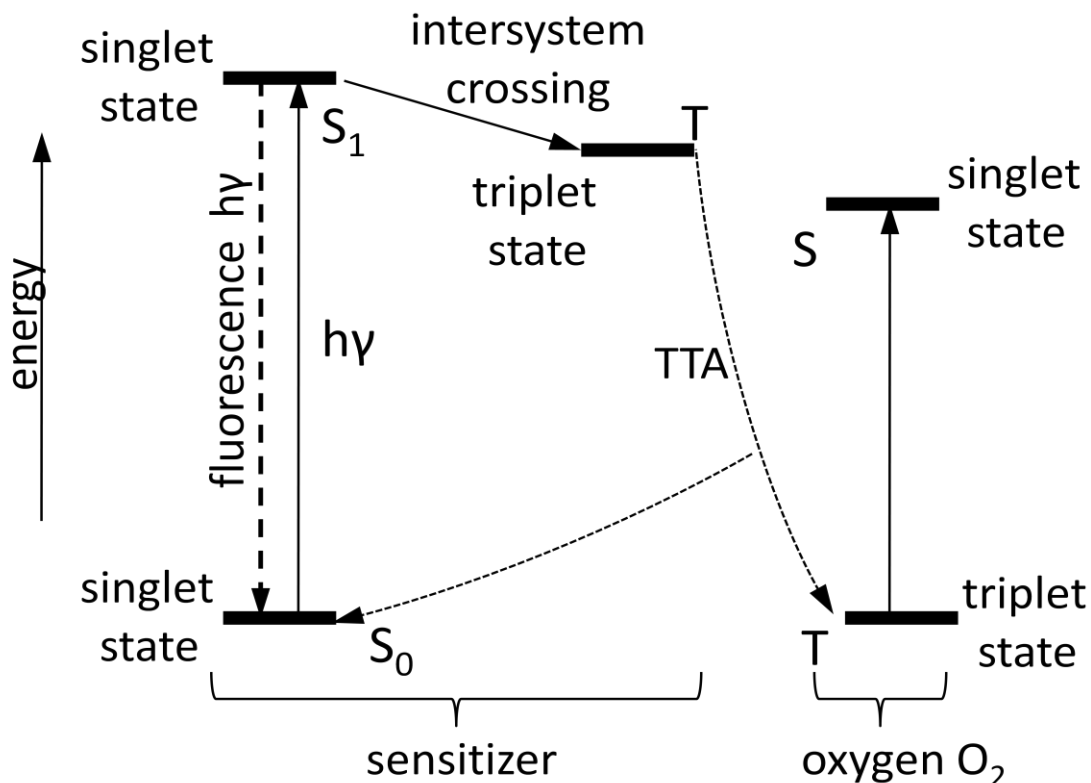
Figure 5-5: Schematic drawing of singlet oxygen photosensitization. S_0: singlet ground state; S_1: singlet excited state; T: triplet state; S: singlet state. Destination of the energy from the absorbed photons: 1) emits as fluorescence; 2) goes through ISC, TTA and finally excite the $^3O_2$ to $^1O_2$.

5.2.3   Detection of $^1O_2$

Singlet oxygen can be directly detected by its characteristic NIR luminescence at 1270 nm, corresponding to its lower singlet state at 95 kJ/mol. The chemiluminescent emission is so weak that highly sensitive optical system is needed in order to detect it.

Such system usually has a high power fast repetition rate Nd:YAG pulsed laser source

and an IR sensitive photomultiplier (169, 171). In low pressure gas phase, $^1O_2$ has an

extremely long lifetime around 72 mins (178). In condensed phase, however, its lifetime

is significantly shortened to microseconds or even nanoseconds (179), and is highly

dependent on the medium. In water, the lifetime of $^1O_2$ is around 2 to 3 ms (180).

Therefore, D_2O is widely used as solvent to extend its lifetime to 10-fold longer (181,

182) for the detection purpose. However the fluorescence quantum yield is still extremely

low.

To overcome this limiting feature, one solution is to use fluorescent probes that

chemically trap $^1O_2$ and consequently form compounds that bear different fluorescent

features from the original probes. Recently, some research groups (183, 184) have been

using a novel commercial $^1O_2$ marker, called Singlet Oxygen Sensor Green [®] (SOSG).

Unlike other fluorescence and chemiluminescent reagents, SOSG is designed to be highly

selective for $^1O_2$ and shows no appreciable response to other reactive oxygen species

(ROS) like peroxide. Although the exact structure of SOSG is not disclosed by the

commercial source, according to literature speculation it consists of two components

tethered together (184-186).

Figure 5-6 shows a suggested SOSG structure and its mechanism of detecting singlet

oxygen (185). Prior to the reaction with $^1O_2$, the bonding between the chromophore and

dimethylanthrancene derivative quenches the fluorescence by electron transfer (ET) from

the trapping moiety. Thus, only weak emissions at 395 and 416 nm are observed.

However, upon reacting with $^1O_2$ the formed endoperoxide can no longer be an

intramolecular electron donor. Therefore, strong emission at 525 nm (green) with UV/Vis

excitation is observed (187). The greater the 525 nm emission the greater the $^1O_2$

concentration but it must be noted that the immediate product of SOSG and $^1O_2$ by itself

is also a sensitizer. Therefore, the background response must be understood for each

system to obtain acceptable results.
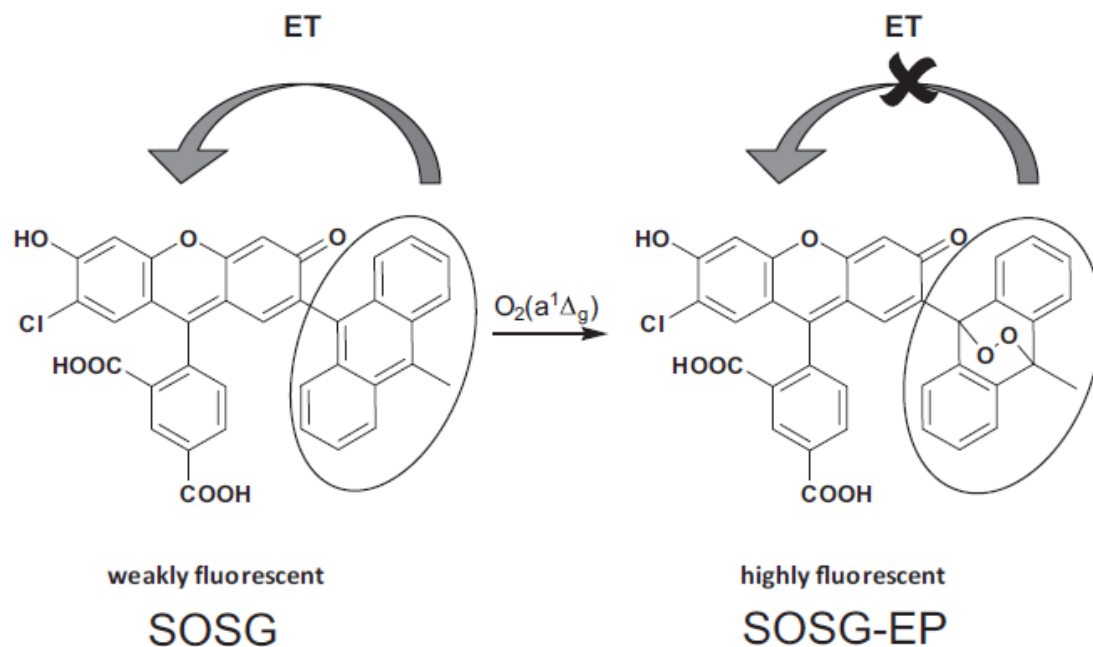
Figure 5-6: Mechanism of SOSG reacting with $^1O_2$. Upon reaction with $^1O_2$, endoperoxide (EP) forms in the anthrancene moiety, forbidding the intramolecular election transfer (ET). Therefore, the chromophore starts a strong green emission at 525 nm. That fluorescence peak is an indicator of $^1O_2$ capture.

5.3 Experimental

While there is extensive literature on the UV/Vis photochemistry of relevant

biomolecules there is much less involving direct one photon NIR excitation as what

occurs in biomedical spectroscopic applications. In this study a range of techniques are

employed to explore the role of oxygen in the NIR fluorescence and photobleaching of

the TMX system. In the subsequent paragraphs, experimental apparatus and setups will be described before the results are presented.

First of all, TMX stock solution was produced by exogenous synthesis following the procedure described by Monnier (153, 160). 25 mM (in some cases 100 mM) L-lysine (16,971-4 or L6001), L-arginine (A5006) and D-(-)-ribose (R7500, all from Sigma-Aldrich Co. LLC., St. Louis, MO, USA) solution was mixed in PBS and heated at 65 ℃ for 2 hrs under continuous stirring. Since pentosidine is sensitive to ambient light, the flask is kept in dark by shielding with aluminum foil throughout the process. Both temperature and pH have an influence on the final yield of pentosidine. Based on Monnier, in a slightly alkaline environment (pH=9) the yield (3.9%) is higher (153), yet the more neutral environment is closer to physiological pH in living tissues and organs. Under pH=7.8, a yield of 2.75% could still be achieved and a pentosidine concentration on the order of several hundreds of micro molar could be anticipated in the TMX at equilibrium. After stopping the reaction, the remaining amino acids and ribose might continue to produce pentosidine and drive subsequent reactions to produce larger agglomerates. However there is no evidence that they are involved in the observed chemistry, which is an assumption at this point. During the synthesis, 5 mL TMX was sampled every 20 min and investigated using the *in vitro* apparatus described in Section 4.2.2 of Chapter 4. It will be shown later in Section 5.4.1 that as described by Monnier the mixture started out a colorless, transparent solution and then turned brown with a little bit red hue toward the end. Further characterization and experimentation with this TMX is described below.

UV/Vis absorption spectra of various TMX stock concentrations were collected using Cary 50 UV/Vis spectrophotometer (Varian Inc., now Agilent Technologies, Santa Clara, CA 95051). A medium sweep rate of 600 nm/min with 1 nm wavelength resolution was set for all the UV/Vis absorption data that were collected. The fluorescence spectra were collected using a PTI fluorimeter system (Photon Technology International, Inc., Birmingham, NJ). The entrance and exit lit widths were kept constant for all data collected. Most of the time regular excitation or emission scans were performed at a scan rate of 1 nm/sec. For the results shown in Section 5.5.3, each solution was monitored consecutively 1) for emission at 525 nm for 30 sec under 488 nm excitation without the laser present, and then 2) set in the dark without any excitation for 20 sec before repeating step 1. This "baseline" cycle was repeated 4 times before actually irradiating the solution with 500 mW 830 nm CW laser (Innovative Photonic Solutions, Monmouth Junction, NJ, USA) during step 2 beginning 250 sec into the experiment.

The $^1O_2$ reagent SOSG is extremely sensitive to light. It is packaged in sets of 10 vials of 100 μg effective compound. It was stored desiccated and protected from light at below -20 ℃ until required for use. The SOSG stock solutions were prepared immediately before use in 33 μL methanol due to its limited solubility in water. This yielded a concentration of about 5 mM. The stock was further diluted by 500 or 1000 times in either PBS or water to get the suggested working solution concentration of 5-10 μM. No reuse of SOSG occurred and all solutions were disposed at the end of each work session. It should be noted that the SOSG is provided as a small amount crystalline material and great care must be taken in order to insure that *all the crystals* are dissolved for consistent and reproducible baseline.

To observe the effect of the laser irradiation (450 mW, either 780 nm or 830 nm) on the dissolved oxygen concentration, a Model DO-166MT-1SXS micro dissolved oxygen electrode (LAZAR Research Laboratories Inc., Los Angeles, CA) is used. The oxygen electrode produces a voltage reading proportional to the partial pressure of molecular oxygen in contact with a semi-permeable membrane. The data logging system automatically saves the data every 1 sec into an Excel workbook. A 10 cm long square fused silica open top cuvette was used in this study for the convenience of gas purging. Pure oxygen and argon was bubbled into the TMX samples in an extremely low flow rate to avoid overflow. Although the TMX samples would be purged completely within couple minutes, for all the samples tested in this study at least 30 min of either oxygen or argon was bubbled before any measurements were taken to guarantee gas saturation. The purged samples are sealed with Parafilm M$^®$ all-purpose laboratory film to reduce gas exchange. The cuvette was also fully covered with aluminum foil leaving only a 5 mm by 10 mm rectangular window for laser to enter if necessary.

An *ab initio* electronic structure calculation using Gaussian 03 program with restricted Hartree Fock, 3-21G basis set (Revision E.01, Gaussian, Inc., Wallingford, CT, USA) was also performed in order to guide our speculation of the possible underlying photochemistry. The ground state singlet molecular structure was optimized for all bond lengths and angles in Figure 5-3 before the energies of the lowest excited singlet and triplet states were calculated (ZINDO) using that optimized ground state structure.

5.4 Results

5.4.1 TMX Fluorescence with NIR excitation

UV/Vis fluorescence of pentosidine and other AGEs has long been observed *in vivo*, and has been proposed (111, 161) as a measure of long-term diabetic compliance of individuals with physician directed treatment. However, no obvious absorption and fluorescence is reported in NIR. In the following sections, AGEs fluorescence in NIR regime will be studied in great detail.

Along the process of preparing the TMX stock, aliquots were taken every 20 min, as shown in Figure 5-7, the colorless mixture of 100 mM arginine, lysine, and ribose in PBS gradually gained some browning color and darker toward the end. Browning in color indicated the forming of crosslinks between reduced sugars and amino acid. This explains why in food chemistry the Maillard reaction is frequently referred as "browning reaction".

Figure 5-7: Browning of the TMX along the timeline of preparing the stock. From left to right, aliquots were taken from 0 min to 120 min in 20 min interval. 100 mM of each of the three reactants were used.
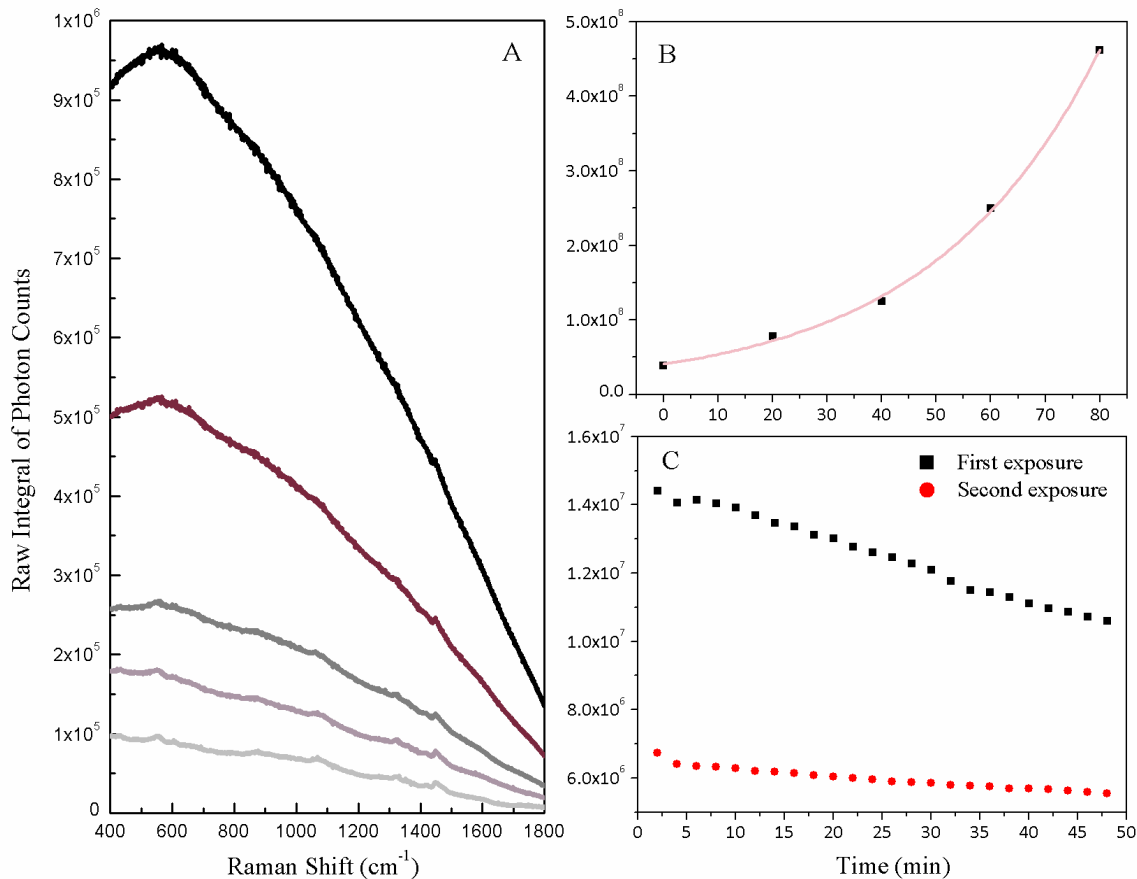
Figure 5-8: Fluorescence and bleaching properties of the TMX. (A) Raw spectra across 400-1800 cm^{-1} Raman shift range at various time points (0 min, 20 min, 40 min, 60 min and 80 min respectively) along the reaction course, shown in increasing gray scale. (B) Total fluorescence integral at each five time point, fitting with a simple exponential curve. (C) 50 min photobleaching curve (square dots) followed by the second profile (round dots) taken after an overnight recovery.

Spectra shown in Figure 5-8(A) was obtained by examining the aliquots using the *in vitro* Raman system detailed in Section 4.2.2 of Chapter 4. As observed, the fluorescence increases rapidly with the level of intermediate or final Maillard reaction. Upon the end of TMX stock preparation, the bleaching experiment as described in detail in Section 4.2.1 of Chapter 4 was performed. As shown in Figure 5-8(C), its fluorescence is bleachable and not easily recoverable for as long as 24 hrs. For *in vivo* skin tissue

fluorescence, although no recovery is observed for up to 1 hr, it is usually impossible to locate the bleached spot from the previous day. The time scale for *in vitro* and *in vivo* seems quite different. Nevertheless, one should realize that AGEs, though at a slow rate, are constantly forming *in vivo*. While *in vitro*, once consumed there is no newly formed pentosidine to replenish the quenched fluorescence. Since stirring introduce disturbance, no attempt was tried to facilitate the mixing and diffusion of the exhausted molecules, either pentosidine or dissolved oxygen, in and out of the irradiated volume *in vitro*.
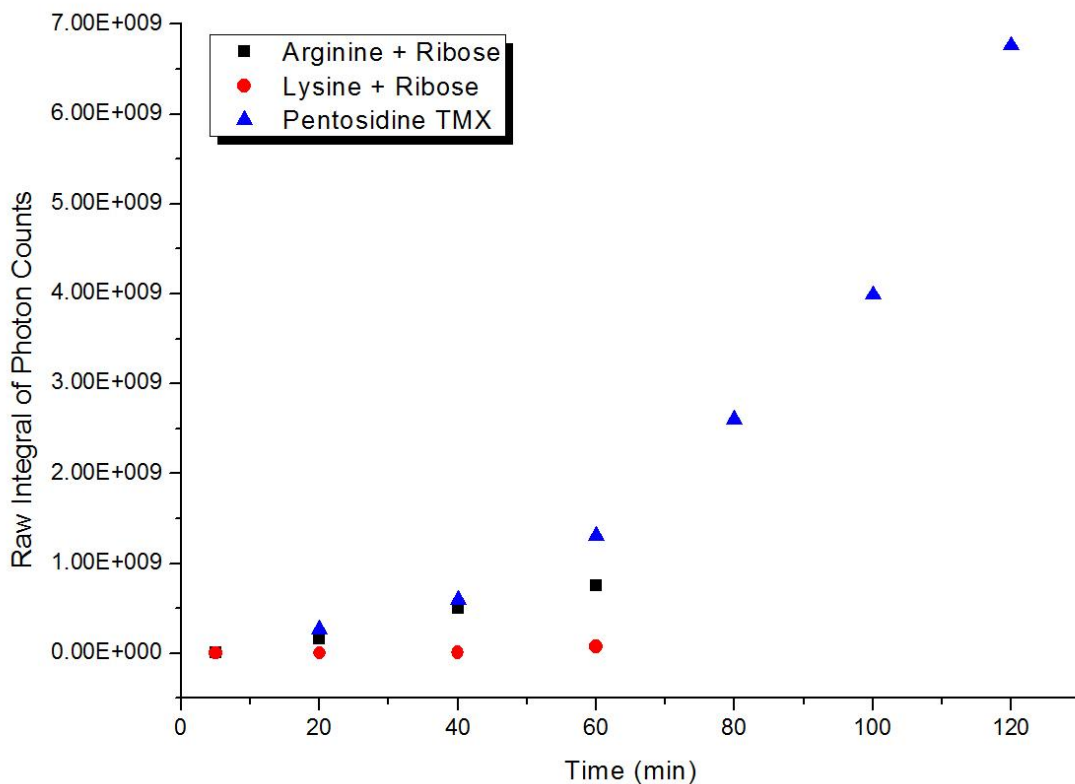
Figure 5-9: Fluorescence yields for various lysine, ribose, and arginine combinations. The reactant molarity was 25 mM for all three combinations. Since no browning effect was observed for arginine + ribose (black square) and lysine + ribose (red triangle) solutions, the synthesis was stopped at 60 min.

Various combinations of the three reactants, i.e., lysine, arginine, and ribose, were tested to establish the mechanism of pentosidine and possibly other fluorescent compounds formation. Not surprisingly, as shown in Figure 5-9, pentosidine yield in TMX increased almost exponentially, but the combination of lysine and ribose for example barely gave rise to any pentosidine product. The combination of arginine and ribose did get some nonnegligible yield, but was by no ways comparable to the yield from TMX. Thus, it is suggested that the observed TMX fluorescence comprises of mostly that from the formed AGE, i.e., pentosidine.

5.4.2   TMX UV/Vis Absorption

Fluorescence is a process that involves two steps, the first of which is the absorption of a photon. Therefore, Figure 5-10 also checked the growth of the UV/Vis absorption spectra for aliquots taken along the timeline. The successive increase of absorbance is found to be consistent with that observed by Monnier and Sell (109, 153) as the concentration of pentosidine increases for an identical TMX. Notice that also in Figure 5-10, the size of the 335 nm peak was comparable with that of 300 nm at the beginning of the reaction. But the 300 nm absorption peak grew in faster toward the end, thus resulting in a slight shifted absorption center.
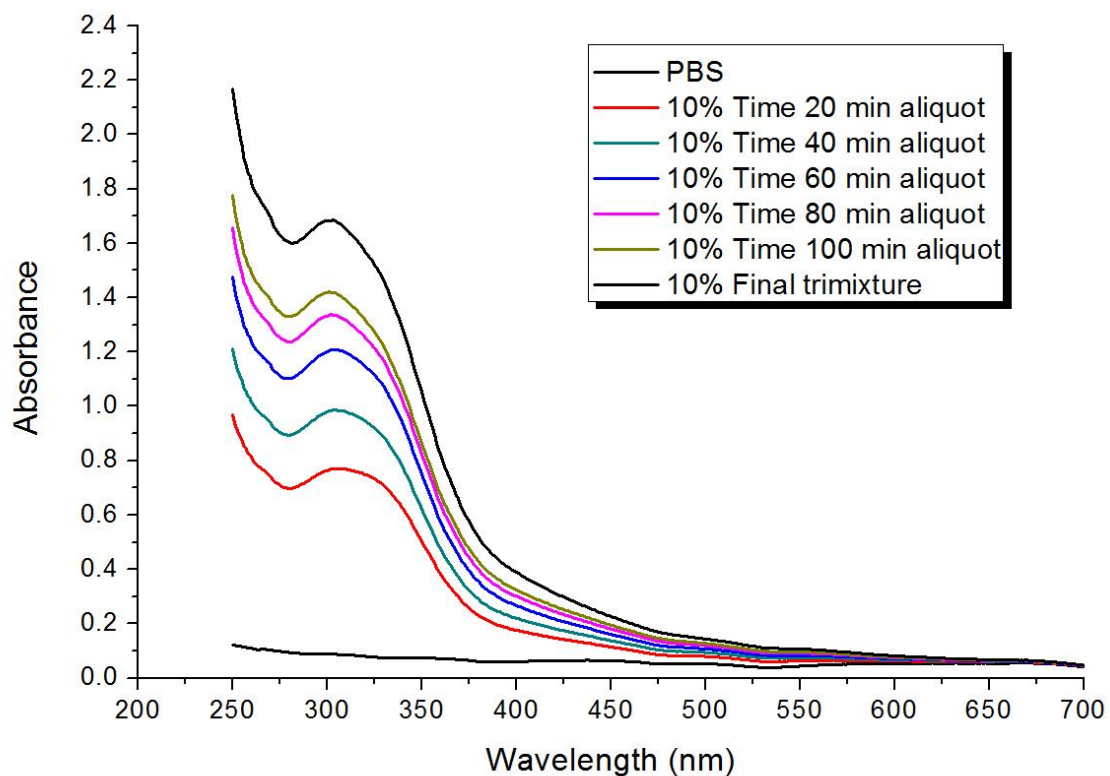
Figure 5-10: UV/Vis absorption peak growth for aliquots taken every 20 min during the process of TMX synthesis. Notice that all the aliquots were diluted in PBS to 10% of the original concentration to avoid saturation.

Since special interest of this study lies in the absorption characteristic in the NIR range, extended spectral range up to 1100 nm is shown in Figure 5-11 for the final TMX products after 2 hours of synthesis. The shoulder peak at 335 nm proves the existence of pentosidine while a stronger peak to the left at 300 nm may reflect the absorption of other AGEs or intermediate products. Yet, there are only very weak clump-like spectral features to the red of 600 nm. Although the readily observed fluorescence and photobleaching with 785 nm excitation as shown in Figure 5-8 implies absorption in NIR should exist to some extent, the empirical result showed difficulty in detecting it.
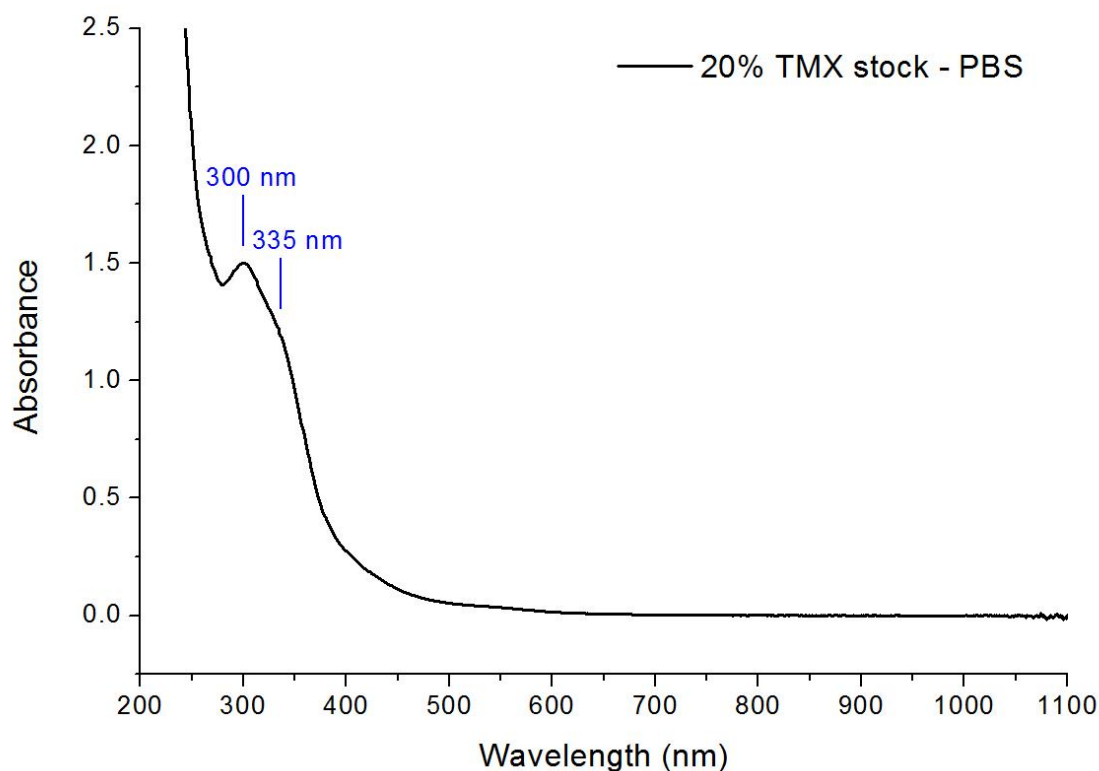
Figure 5-11: Baseline corrected absorption spectrum of pentosidine producing TMX. The sample tested used 25 mM reactants to produce the stock and then diluted to 20% using PBS.

If the same solution is irradiated with 500 mW 785 nm loosely focused light in a roughly 200 μm diameter spot for 20 min and another UV/Vis absorption spectrum is obtained, the difference between that spectrum and the original spectrum is shown in Figure 5-12. In order to more clearly observe the spectral changes to the red of 400 nm a relatively high starting TMX concentration (20% of stock) was chosen for study even though the absorption spectrum blue of 400 nm was saturated in some regions. It is observe that the difference spectrum in Figure 5-12 has the same strong peaks as the starting TMX solution (with some distortion blue of 250 nm because of saturation effects) but also there are some broad and diffuse absorption features starting at about 600 nm

175

and extending to the red limit of the instrument. These features might also be evident in the starting TMX spectrum but more discernible in the difference spectrum. The strength of the absorption in the 600 nm and longer range is about 5% of that at about 335 nm which is not too saturated at that wavelength. It is noticeable that the stronger absorption peak at 300 nm is almost completely subtracted off in the difference spectrum, suggesting the laser induced chemistry is mostly related with pentosidine, probably not other as yet unknown compounds and intermediates.
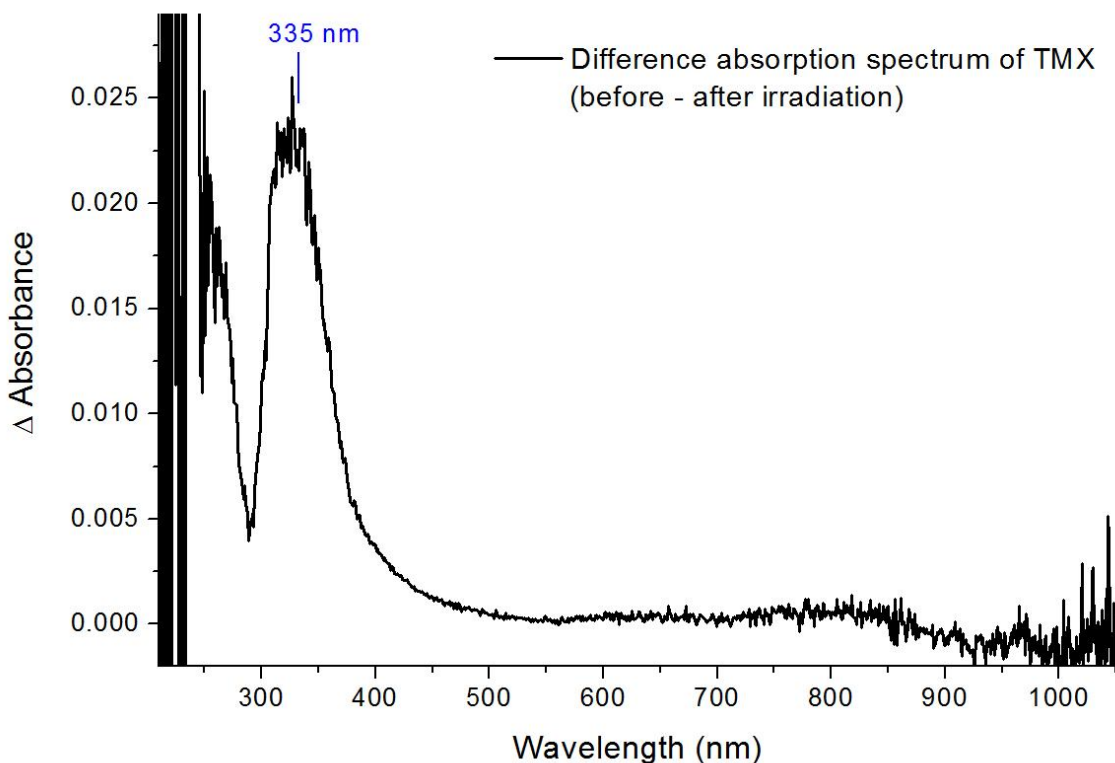
Figure 5-12: Difference absorption spectrum obtained by subtracting UV/Vis absorption spectrum of TMX obtained after irradiation with 785 nm laser from UV/Vis obtained before irradiation as described in the text.

5.4.3 TMX Fluorescence with UV/Vis Excitation

The fluorescence excitation and emission spectra of TMX were collected and shown in Figure 5-13, Figure 5-14, and Figure 5-15. The excitation/emission peak pair is consistent with that reported by other groups (153). In addition, the emission was extended into NIR spectral range to check the appearance of any possible emission.
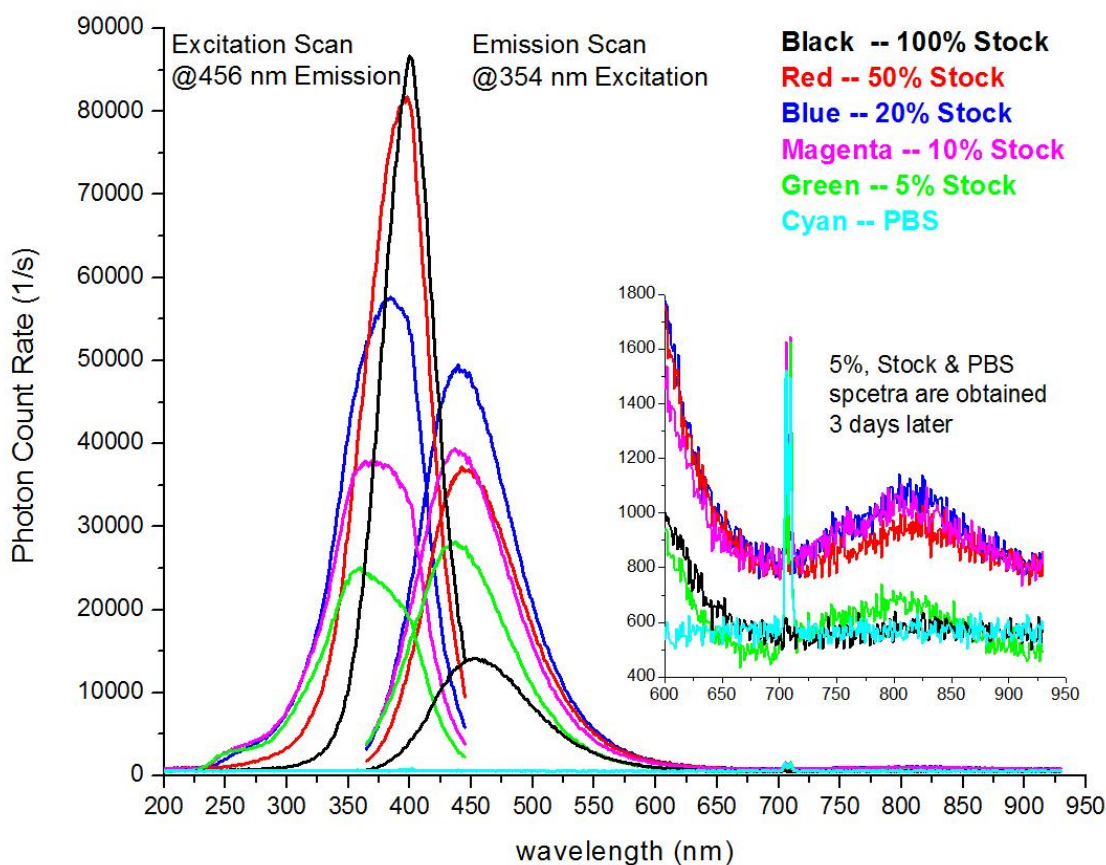
Figure 5-13: Emission and excitation scans in UV/Vis spectral range for TMX at various concentrations. The emission scans were extended to NIR range to check whether emission could be observed. The insert is a close-up of the NIR spectral range from 600 nm to 950 nm. Though weak, fluorescence emission was observed.
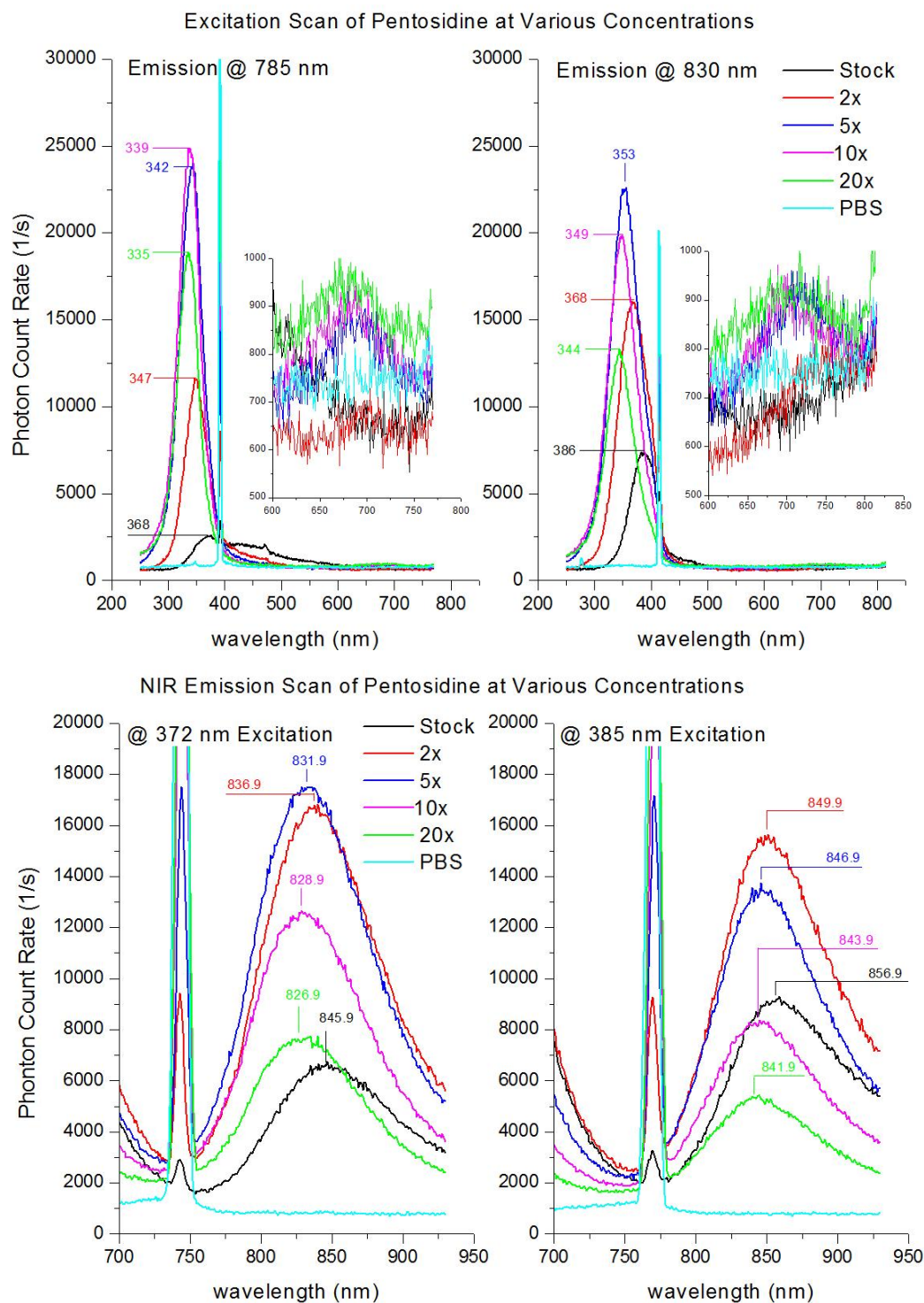
Figure 5-14: NIR fluorescence of TMX at various concentrations. (top) Excitation scans by detecting fluorescence emission at 785 nm and 830 nm respectively. These two wavelengths correspond to the laser wavelengths used either *in vivo* or *in vitro*. (bottom) Emission scans at two more UV/Vis excitation wavelengths, 372 nm and 385 nm.

As shown in the insert of Figure 5-13, compared to the PBS baseline, TMX samples show various sizes of NIR emissions (from at least 720 nm to 920 nm) according to the concentration gradient. The sharp peak at 708 nm is an excitation artifact caused by overlapping grating orders. When the grating at the emission end steers to selectively pass the preset excitation at 354 nm, any wavelengths that are whole number multiples of excitation will also be selected to pass at the same time, such as the 708 nm in Figure 5-13.

Also noticed, not only in Figure 5-13 but also Figure 5-14, is the much weaker emission for higher concentrated sample, especially the TMX stock, no matter in UV/Vis or NIR. As shown in Figure 5-7, TMX stock is highly colored. Although not shown in figures, the absorption of the stock solution in UV/Vis was extremely high and saturated at every wavelength below 400 nm. Based on empirical experience, to make comparable fluorescence spectra, however, the optical density, i.e., absorbance, of each sample should be around 1, which is obviously not the case for stock solution. Compensation for absorption loss requires the quantum yield of TMX fluorescence of the spectral range of correction, which is not available. Therefore, direct quantitative comparison between the fluorescence of various TMX concentrations has to take the absorption loss compensation into consideration. Despite of that, NIR fluorescence of TMX could still be characterized.

Corresponding to the two NIR wavelengths used in all *in vivo* and *in vitro* experiments, i.e., 785 nm and 830 nm, excitation scans as shown in Figure 5-14 were collected. For both wavelengths, weak but still discernible NIR excitation beyond noise level was observed. Comparing the excitation peaks from 350 to 390 nm, the amplitude

for generating NIR emission (20000 – 25000 photons per second) is much less than that for UV/Vis emission (80000 – 90000 photons per second) shown in Figure 5-13.

Two more emission scans under UV/Vis wavelengths, 372 nm and 385 nm respectively, were collected. Since only NIR range was investigated, data acquisition time was much shortened, allowing the collecting of multiple spectra to get smoother curves. The sizes of the emission are of the same order of magnitude as the one shown in the inserted graph in Figure 5-13.
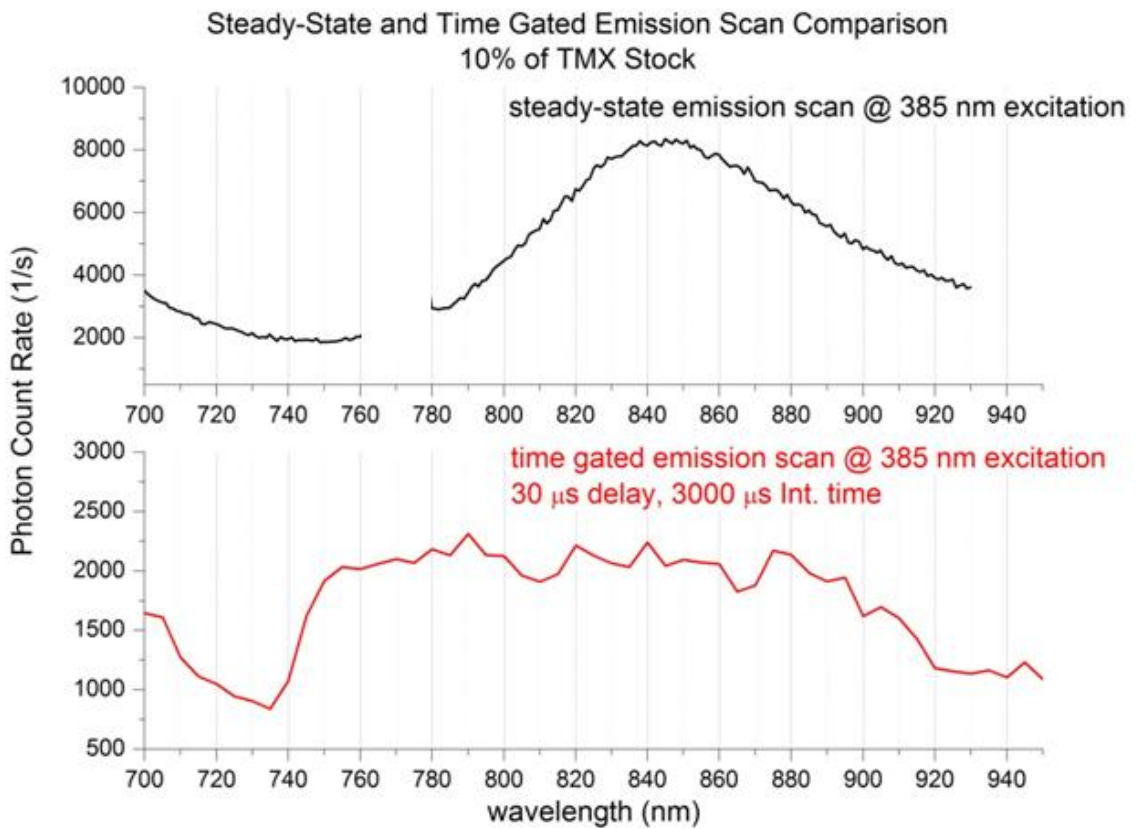
Figure 5-15: (top) Steady state and (bottom) time gated emission of 10% TMX stock after excitation at 385 nm.

In addition to the observation of NIR emission from pentosidine containing TMX in steady state fluorescence spectra, time correlated experiments as shown in Figure 5-15 showed the same emission, but with a 30 μs to 100 μs (no shown) delay. The time scale of the delayed emission matches that of ISC mentioned in Section 5.2.2. This might indicate a photochemical process involving the oxygen molecules dissolved in the solvent system.

5.5 $^1O_2$ Involved Photochemistry of Pentosidine

5.5.1 Role of Dissolved Oxygen in Pentosidine Photobleaching

The observation of delayed emission encourages the consideration of a possible role of dissolved gases. Given that most bleaching phenomena are oxidation reactions (175, 188-190), it is natural to explore the role of oxygen in the NIR excited autofluorescence and photobleaching of TMX, i.e., pentosidine. Figure 5-16 shows a schematic depiction of a hypothesis, where pentosidine acts as both a $^1O_2$ sensitizer and scavenger. As detailed in Section 5.2.2, ground state pentosidine gets excited by the incident photon to its singlet excited state. Through ISC of a time scale from tenth to hundredth of seconds, energy is transferred to a neighboring triplet excited state. If such triplet state satisfies all the requirements as described in Section 5.2.2 to be a sensitizer, then the oxygen molecules that are dissolved within the solvent can be excited to $^1O_2$.
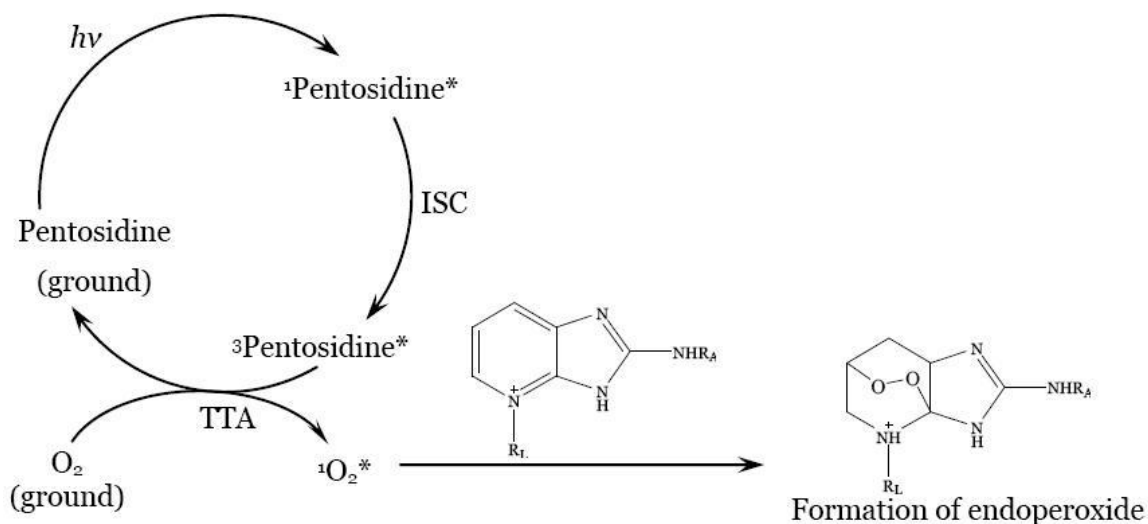
Figure 5-16: Hypothetical photochemical process between pentosidine and oxygen. ISC: intersystem crossing; TTA: triplet-triplet annihilation; R_L: lysine residue; R_A: arginine residue.

Notice that although pentosidine participates in this process by playing the critical role of photo-sensitizer, there is no consumption of the molecule by itself. Excited pentosidine molecule finally relaxes to its ground state without giving any emission. Meanwhile, the indole ring structure within the pentosidine molecule has long been known to quench $^1O_2$ (191) and form endoperoxide (192). Thus, the generated $^1O_2$ could readily get captured by pentosidine again and forms an endoperoxide, which does not fluoresce in NIR.

The hypothesized mechanism could explain what have been observed in the previously presented results in Section 5.4, and would also help the understanding the photobleaching of fingertip tissue autofluorescence *in vivo*. The following sections will try to build evidences to support this hypothesis.

5.5.2 Rate of Dissolved Oxygen Loss

To support the involvement of dissolved oxygen in pentosidine bleaching process as proposed in Section 5.5.1, the effect of purging the TMX solutions with various gases is summarized in Figure 5-17. Purging entails bubbling the specified gas through the solution for a sufficiently long enough time to ensure saturation, i.e., no further change in the concentration of the particular gas. This actually is a fast process since the diffusion coefficient of dissolved O_2 in water is on the order of 10^5 cm^2/sec (193).
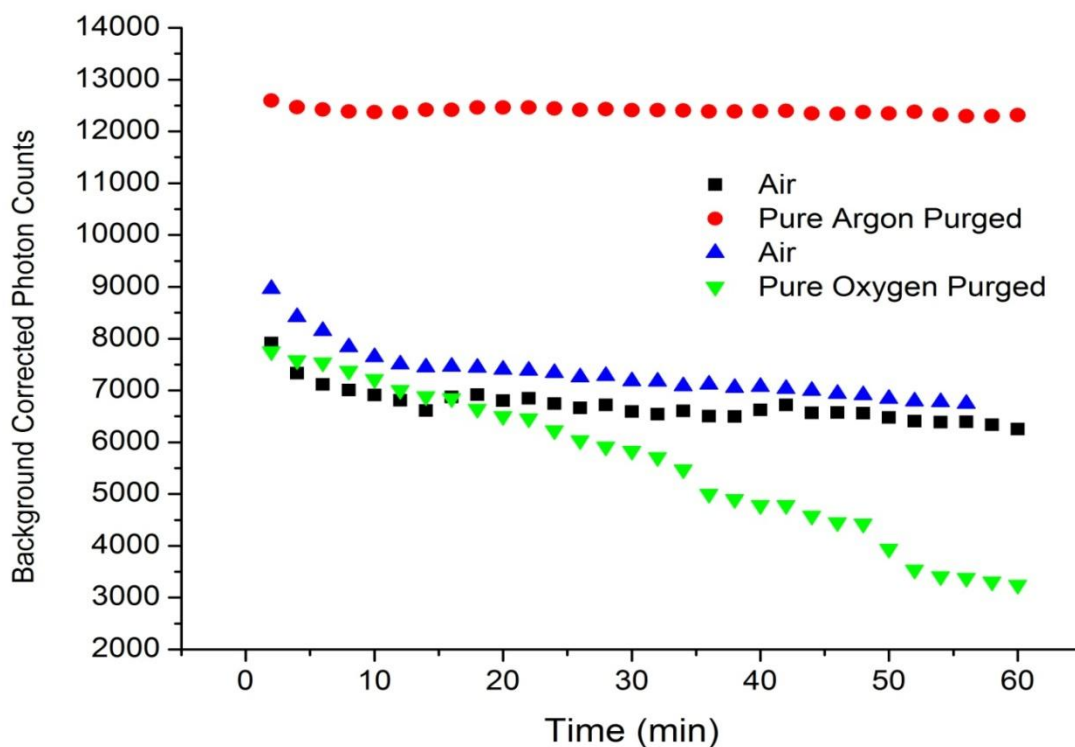
Figure 5-17: Integrated emission, i.e., between 400 to 1900 cm^{-1} Stokes shift, using 785 nm excitation, as a function of time, for solutions saturated with gases in the legend.

It is shown that an argon purged solution has very little decrease in fluorescence intensity over 60 min of irradiation with 785 nm radiation. The oxygen purged solution

produces less IE than the solution in contact with air and only about half of that observed from the argon purged solution. All solutions have a quick initial drop as if some emitting species within the irradiated zone are quickly bleached and the later loss of emission are slowed by the need for species to diffuse into the excitation-observation zone. Once again, bear in mind that no stirring of mixing while bleaching curves were recorded. Purging with oxygen produces an over 50% decrease during the same interval and purging with air produces a decrease approximately 1/5 as much as the pure oxygen.

Given the obvious effect of oxygen on the bleaching of the TMX solution, i.e., the decrease in fluorescence, an electrochemical oxygen sensor was employed to directly observe the effect of 785 nm light irradiation on the oxygen concentration. It must be noted from the outset that obtaining a saturated solution of a gas is much easier than obtaining and maintaining any particular lesser concentration. Given this practical challenge and limitation in experimental technique and methodology, the decrease in oxygen partial pressure was still able to be observed in the irradiated volume of the TMX solution for varying starting pressures of oxygen and dilutions of the TMX stock solution.

The best data are shown graphically in Figure 5-18 and Table 5-2. These four runs compare the initial rates of oxygen loss, i.e., the slopes of the lines fit to the O_2 vs. time data in Figure 5-18, for varying TMX (in units of stock) and the same starting O_2 concentration (in mV). Similarly, comparison could also be made to see the effect of varying initial O_2 concentrations with the same TMX concentration as shown in Table 5-2. The results in Table 5-2 are consistent with the empirical rate law given in Equation 5-1 in which the net rate of dissolved O_2 loss is first order in both pentosidine and O_2 concentration. Notice that the data in Figure 5-17 which is based on loss of fluorescence

184

and not electrochemically detected O_2 loss are also consistent with the proposed rate law, i.e., there is no variation in pentosidine concentration but there is in O_2.

$$d(O_2)/dt = -k[O_2][pentosidine] = d(IE)/dt \qquad \text{Equation 5-1}$$
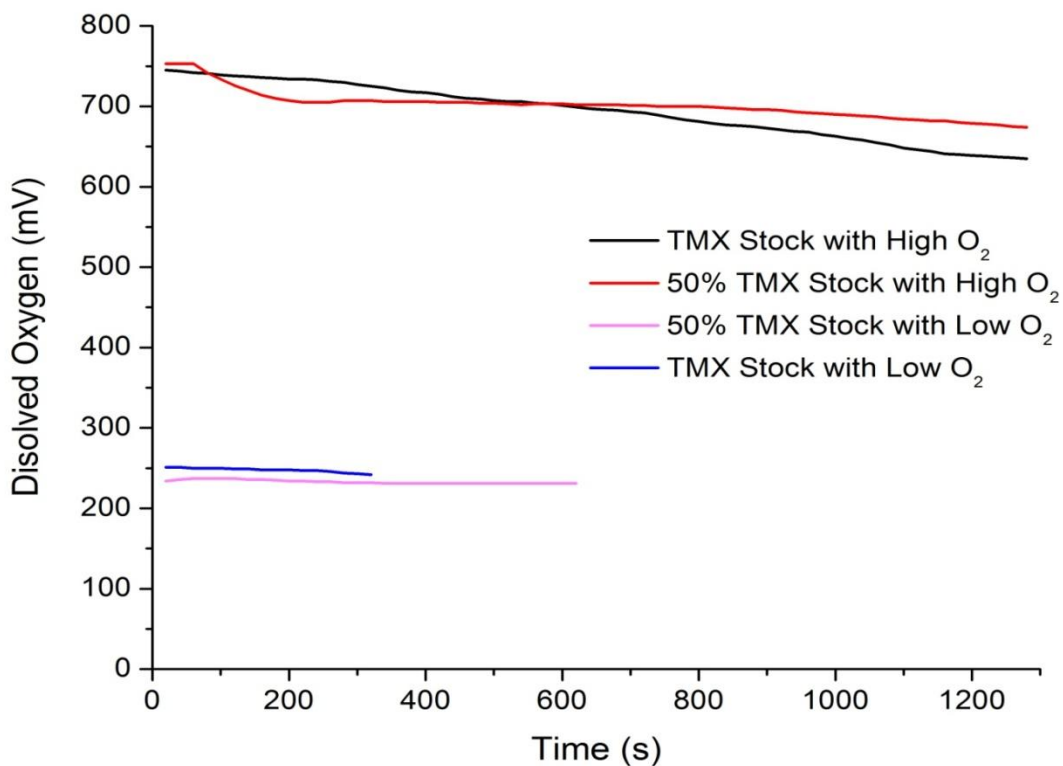
Figure 5-18: Oxygen electrode response as a function of time for various starting combinations of O_2 concentration and TMX dilutions. Laser power was constant at 0.5 W 785 nm in all cases.

Anecdotally we found that under ambient conditions the partial pressure of dissolved oxygen in any TMX solution is always 10% or less than that in ambient water or in contact with ambient air. That means TMX solutions are always hypoxic and ≈90% depleted in dissolved oxygen relative to water.

Table 5-2: Rates of dissolved oxygen loss from various starting concentrations of TMX and oxygen based on the data shown in Figure 5-18. The rates are the slopes of the linear fits to the data and all had a correlation coefficient r>0.88 and p<0.001.

TMX Concentration (% stock)	O_2 (mV)	Rate of O_2 Loss (mV/sec)	Error (mV/sec)
100	750	-0.09	0.001
100	250	-0.027	0.002
50	750	-0.04	0.003
50	250	-0.011	0.001

5.5.3   Generation of $^1O_2$ in TMX

To probe specifically for a role for singlet oxygen in particular, a commercially available sensor system (187) known as SOSG was employed. In order to see the effect of 830 nm excitation, each solution was monitored using the systematic method described in the experimental Section 5.3. The 500 mW NIR laser irradiation during the 20 sec in step 2 was continued for 6 ½ cycles as can be seen in Figure 5-19 and Figure 5-20.

In order to illustrate the response of a known $^1O_2$ sensitizer, a run was completed using saturated and filtered aqueous solution of dicarboxylated porphyrin (T1239, Frontier Scientific, Inc., Logan, UT, USA). The cycle when the 830 nm excitation begins is obvious. The baseline signal using D_2O for solvent is greater than for H_2O as expected due to the extended $^1O_2$ lifetime in presence of D_2O. More SOSG emission is observed for the TMX solutions, unfiltered greater than filtered, but both are much less than that for the porphyrin.
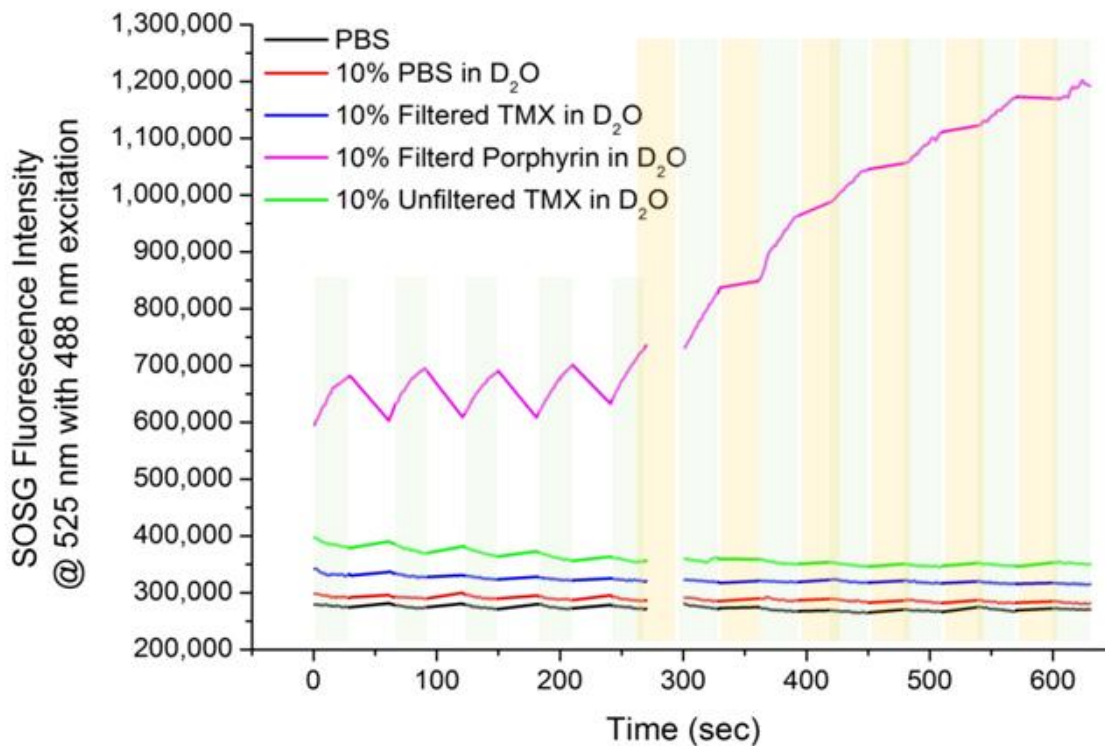
Figure 5-19: SOSG monitoring of $^1O_2$ for different solutions with and without NIR laser irradiation. Blue stripes indicate the 30 sec 488/525 nm excitation/emission fluorometer measurement cycle. Yellow stripes indicate 20 sec 500 mW 830 nm CW laser irradiation.

Whereas laser irradiation of porphyrin produced a large sustained increase in reported emission and thus $^1O_2$ signal, both TMX solutions only produced a decrease in the loss of emission. Porphyrin produces a stronger SOSG response than TMX does partially because of a greater porphyrin concentration. Also, pentosidine appears much more vulnerable to be attacked by $^1O_2$. Thus in Figure 5-19 there is no evidence for pooling of $^1O_2$ for the TMX samples.
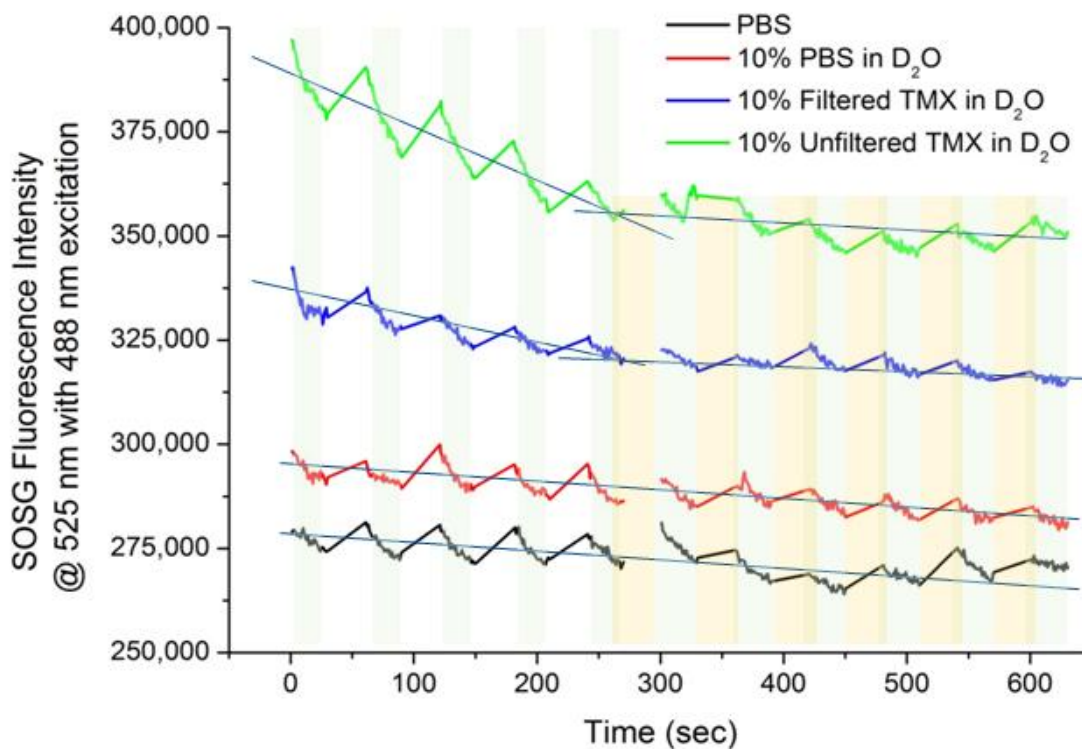
Figure 5-20: A close-up view of the same data sets shown in the bottom of Figure 5-19. Linear fit trend lines for laser-irradiated and non-laser-irradiated cycles are shown to facilitate the interpretation of the data.

However, by taking a closer look at Figure 5-20, under NIR laser irradiation the rate of SOSG sensor fluorescence is obviously slowed down. This indicates the generation of $^1O_2$ in the TMX. However, the pentosidine molecule is very vulnerable to $^1O_2$. Thus, the quickly formed endoperoxide trapped the newly excited $^1O_2$ within its structure. SOSG has to compete with pentosidine in trapping $^1O_2$ in order to emit green fluorescence. In this sense, although it is clear that $^1O_2$ production could be sensitized by pentosidine, a better understanding of how efficiently pentosidine works is hard to get using this approach. The influence of the probe thus should be taken into consideration also. As shown in Figure 5-20, the decline in SOSG emission for the two PBS baselines results

from the consuming of $^1O_2$ by SOSG itself. The situation is certainly not completely understood and more work is needed to determine between porphyrin and pentosidine which produces $^1O_2$ more efficiently, i.e., with greater net quantum yield.

5.5.4   Gaussian Calculation of Pentosidine Electronic States

In order to approach the relevant photochemistry of pentosidine, the electronic structure was calculated using standard Gaussian calculation with the most salient points summarized graphically in Figure 5-21.
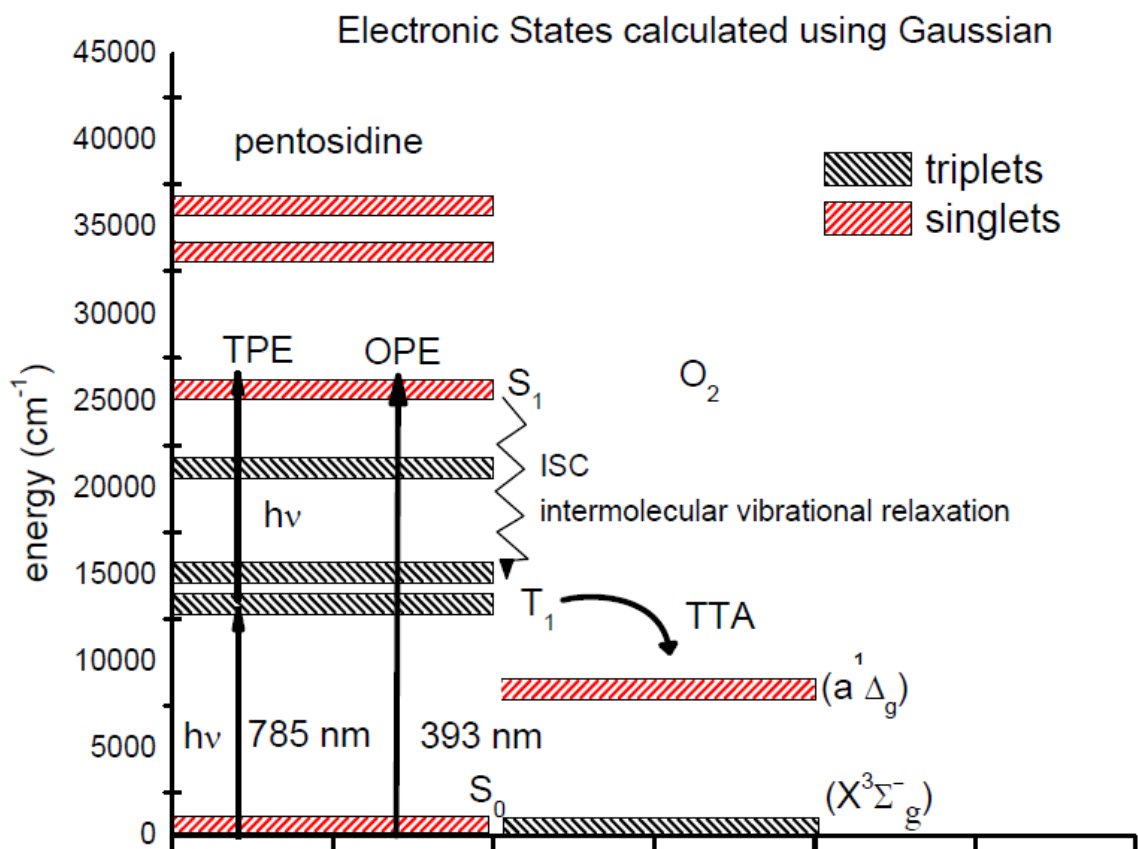
Figure 5-21: Jabronski diagram of Gaussian calculated pentosidine singlet and triplet excited states showing the $^1O_2$ formation through photochemical reactions with pentosidine.

The positions of the strongest UV/Vis absorption features in Figure 5-11 could be rationalized given calculated positions of the singlet states and strengths, i.e., f values of the transitions from the ground states ($f = 0.30$). According to the Gaussian calculation for pentosidine there are no allowed one photon transitions involving NIR excitation at all. Nevertheless the observed photobleaching and other observed "actions" caused by NIR irradiation are obvious and energetically well-defined. For example it is clear from difference spectrum in Figure 5-12 that one of the carriers of the spectrum in Figure 5-11, i.e., pentosidine, is consumed by the action of the laser. The ratio of the two calculated f values for the $S_0 \rightarrow T_1$ ($f = 0.02$) and $S_0 \rightarrow S_1$ ($f = 0.30$) transitions is roughly equal to the ratio of the induced NIR absorption near ≈ 800 nm to that near ≈ 390 nm in the difference spectrum in Figure 5-12. This reinforces the suggestion that 1) the difference spectrum is that of a single species, i.e., pentosidine, and 2) that pentosidine itself is consumed by the $^1O_2$.

Figure 5-13 and Figure 5-15 also show that direct one photon excitation (OPE) into the predicted lowest excited singlet state (385 nm) produces copious UV/Vis emission as reported by Monnier but also delayed emission across a wide range of NIR wavelengths in accord with the predicted presence of relatively low lying triplet states for pentosidine across the appropriate energy range. Because this emission can be observed in steady state and in single photon time resolved mode, it can be concluded that NIR excitation produces a long lived species associated with NIR emission that actually pools to some undetermined extent.

The requirement that this species might be connected to oxygen is clearly demonstrated by the purging experiments and the oxygen electrode experiments. That

D_2O produced greater evidence of this species than experiments in H_2O solvent in Figure 5-20 is also a specific connection to known $^1O_2$ photochemistry. The specificity of SOSG for singlet oxygen as opposed to superoxide, or any peroxide strongly supports the mechanism depicted in Figure 5-16 and Figure 5-21.

To explain this mechanism and the subsequent reaction sequence that results in photobleaching it is first asserted that in condensed phases, NIR or UV/Vis absorption features are broad and that 5-10 nm variation in exact wavelength of excitation is not of any consequence. Furthermore, the accuracy of the Gaussian calculations is far from perfect. Small differences between the experimental results and the calculation are quite consistent with the explanation provided.

Indeed, the ZINDO formalism applied to this problem is inappropriate to the extent that the molecule is charged since ZINDO is only applicable to closed shell systems. There are a number of resonance structures for pentosidine and some are charged and others are not. The value of this calculation is to validate the possibility that pentosidine has low lying triplet states available to participate in singlet oxygen sensitization. Future experiments with solutions of the pure authentic material can reveal the solution ionization states and these are planned.

It is essential to realize that two photon excitation (TPE) using a continuous wave (CW) laser is commonplace in fluorescence microscopy (194, 195) and as shown in Figure 5-21, the energy of two NIR photons is roughly resonant with the lowest energy allowed one photon transition. The presence of near resonant interactions between lower lying states and the incident photons makes the absorption of addition photons after the

first much more facile. In this case there is a symmetry allowed but spin forbidden transition almost resonant with the incident photons.

Despite being spin forbidden the $S_0 \rightarrow T_1$ transition from the ground state singlet has a calculated $f = 0.02$ whereas the lowest energy fully allowed transition, i.e., the $S_0 \rightarrow S_1$, only has $f = 0.30$, i.e., just 15 times stronger. The presence of $^3O_2$ opens the possibility of 1) direct excitation of the oxygen itself to $^1O_2$, or 2) the pentosidine to the T_1, or 3) production of T_1 by ISC if S_1 pentosidine is actually produced. It seems probable that some pentosidine is first excited to S_1 by TPE and then relaxes nonradiatively into T_1 which can undergo TTA with ground state molecular oxygen, i.e., $^3O_2$, to produce $^1O_2$. Otherwise pentosidine has its interaction with the incident NIR photons interrupted at the T_1 level and undergoes TTA with $^3O_2$ to produce the $^1O_2$. In either case, after transfer of some energy to the solvent, vibrationally hot pentosidine and $^1O_2$ are produced. The $^1O_2$ goes on to attack pentosidine itself producing a non-NIR fluorescing endoperoxide. This is the mechanism proposed earlier in Section 5.5.1 for the photobleaching of AGEs in TMX that also leads directly to the delayed TMX NIR emission as shown in Figure 5-15, and presumably *in vivo* too.

Figure 5-22 shows the power dependence of TMX fluorescence yield of two different starting reactants concentrations, e.g., 25 mM and 100 mM, respectively. The less than 1 non-integer slopes of the linear fit to the double logarithmic plots indicate that the fluorescence probably in a great extent results from an OPE process by direct excitation of pentosidine molecule from S_0 to T_1. However, the dissolved oxygen partially consumes the excited pentosidine that leads to fluorescence quenching, thus the fitted slopes show power indexes smaller than 1. While in 100 mM TMX the slope is

0.93 which is fairly close to 1, the power index in 25 mM TMX is only 0.69. This might

be related with the limited availability of dissolved oxygen compared to the

overwhelming amount of excited pentosidine molecule in a higher concentrated sample.

Thus the $^1O_2$ induced fluorescence bleaching has less significance on the power index in

the more concentrated TMX solution.
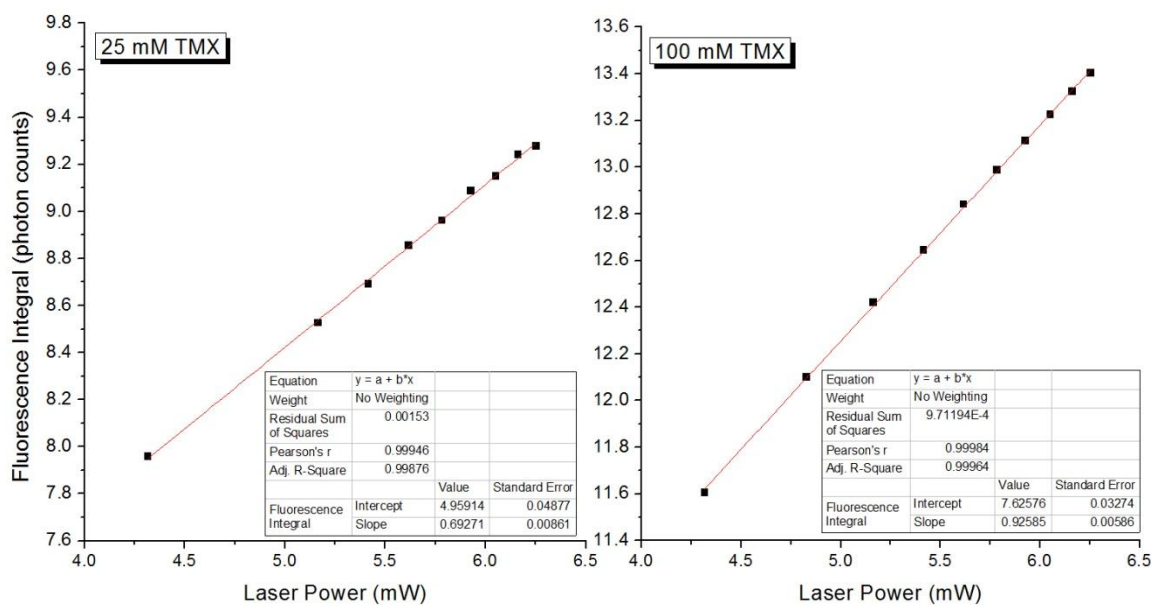
Figure 5-22: Double logarithmic plots showing the laser power dependence of TMX
fluorescence under 450 mW 785 nm laser excitation. (A, left) TMX stock solution with
25 mM starting reactants; slope equals 0.69; (B, right) TMX stock solution with 100 mM
starting reactants; slope equals 0.93.

Note that as shown in Figure 3-7 of Chapter 3 the double logarithmic plot of the

incident laser power and the observed NIR fluorescence *in vivo* is linear with a slope of

0.74. Given the interactions that can occur involving excited pentosidine and $^3O_2$ between

the absorption of the first and second photons (90), this is not surprising that a

inconsistent with an overall linear dependence of the emission on the incident power.

5.6 Conclusions

Nonenzymatic glycation and oxidation of ubiquitous proteins *in vivo* leads to irreversible formation of AGEs. Due to their relatively long half life and low clearance rate AGEs tend to accumulate within static tissues and the circulatory system. Spectra obtained using 830 nm NIR excitation suggest that the so-called "autofluorescence" from all tissues has a finite number of sources. But the fact that senior and diabetic subjects produce more than other members of the general population suggests that a significant portion of the total autofluorescence from all sources originates from AGEs. Using pentosidine generated in a reaction mixture as representative, an *in vitro* study unveiled very similar fluorescence and photobleaching pattern as observed for autofluorescence *in vivo*. A series of oxygen, air and argon purging experiments on the TMX suggest that pentosidine is a singlet oxygen sensitizer and secondary reactions between the pentosidine itself and/or other fluorophores and the photosensitized singlet oxygen explain the observed photobleaching. *Ab initio* Gaussian calculations on pentosidine reveal the existence of low-lying triplet excited states required for the sensitization of ground state oxygen. A commercially available product known as SOSG that specifically serves as a singlet oxygen detection reagent suggests the generation of singlet oxygen from NIR irradiated pentosidine TMX. This study provides one definite chemical mechanism for understanding *in vivo* human skin autofluorescence and photobleaching.

6. Overall Discussion, Future Work and Conclusions

6.1 Overall Discussion

The goal of the research presented in the dissertation is to better understand and hopefully overcome two major obstacles, i.e., fluorescence and human factors, in noninvasive *in vivo* blood analysis using Raman spectroscopy. Therefore, the research seeks solutions in two seemingly irrelevant fields: one is more engineering and the other one is more chemistry. Nevertheless, they are both critical to this study due to their close relationships with the underlying physiological process, in other words, the human tissue properties and blood flow dynamics.

We have established that maintaining a good contact and steady pressure helps generate data with less random errors and uncertainty. With better reproducibility of the collected spectra, it could be expected to reduce the experimental length. And this could in turn further alleviates the influence of human factors. However, one should be aware of the fact that the selection of optimal pressure is of equal importance. Since the optical geometry of our *in vivo* apparatus only allows a penetration to less than 200 μm of the most superficial blood-filled volume of the epidermis, the delicate capillary wall is sensitive to tissue deformation either related with external pressure or not.
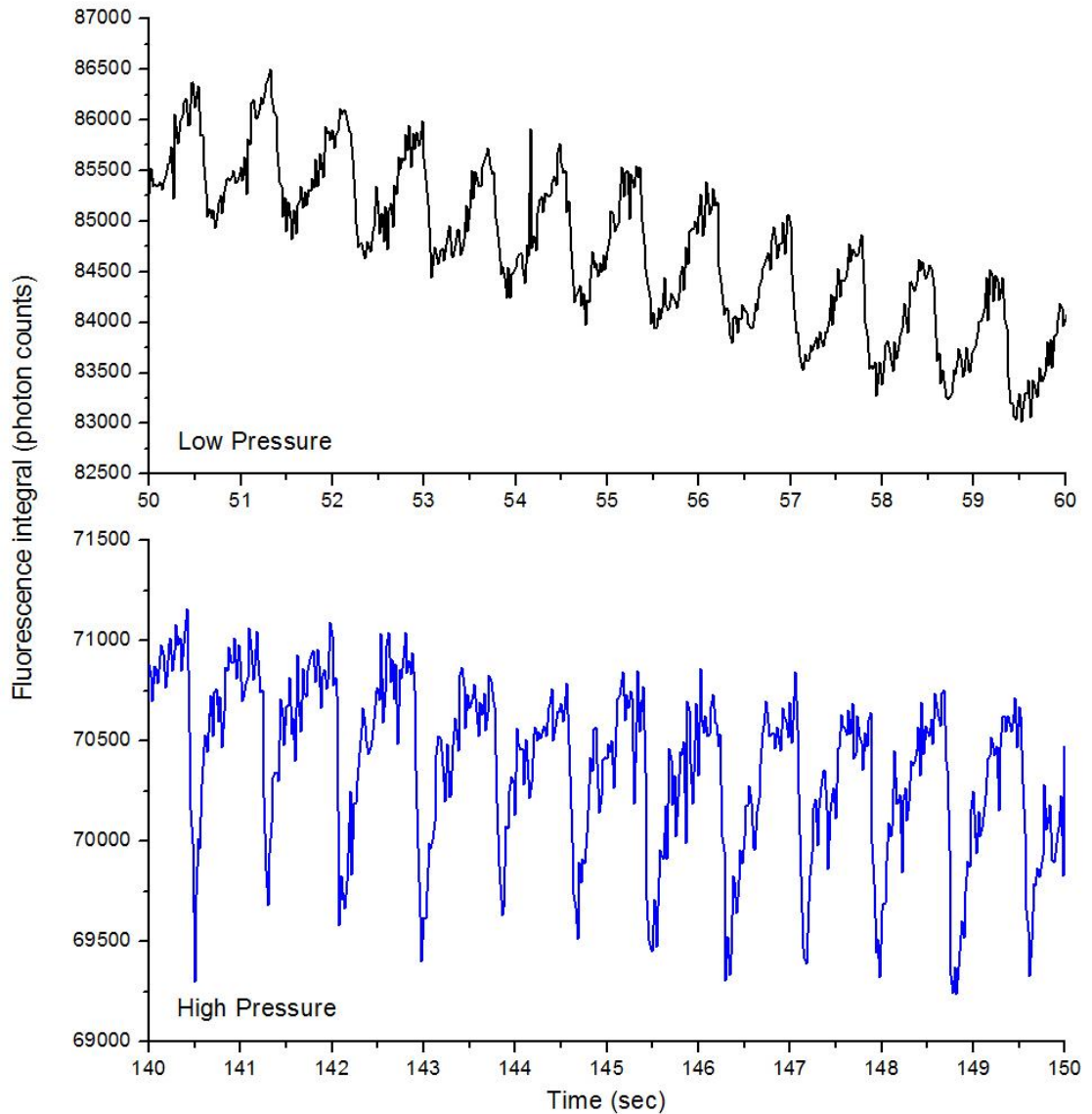
Figure 6-1: IE vs. Time curves showing different shapes of pulses under two pressures, a low and a high, in a single tissue modulated experiment for a test subject. Excitation wavelength is 805 nm.

As shown in Figure 6-1, the optical pulses on an IE vs. Time curve for a single test subject vary in a 200 sec tissue modulated experiment. On the first half when the pressure is low, the pulses though sitting on top of a bleaching baseline show no sign of impedance. However, on the second half when the pressure is high, the down-stroke of a

pulse is much sharper than the up-stroke. Although it has not been verified, we speculate that under high modulated pressure the capillaries are constantly squeezed but depending on the relative pressures they get dilated upon arrivals of cardiac pulses. However, halfway between relaxing from systolic to diastolic, the external pressure forces the blood vessels to close, thus causing the abrupt drops on the optical pulses.

The phenomenon observed in Figure 6-1 not only further validates that our spectra do contain information directly from blood but also justified the importance of controlling experimental conditions including human factors. The two quantities that we extract useful information from, i.e., EE and IE, are very sensitive to the relative volume fraction changes of the three phases, i.e., static tissue, plasma and RBCs. And these volume fractions could be easily disturbed by not tightly controlled human factors. Thus, without proper apparatus, i.e., PDPM, that could address these issues, random errors could not be effectively controlled which might lead to inaccurate interpretation of the spectral results. This is of extreme importance in our noninvasive *in vivo* Hct monitoring protocol.

However, it has to be pointed out that in order to allow PDPM perform the way it is supposed to, the test subject should act passively pretending to be unconscious. Practically, no automated self-compensated human machine interface could possibly function without the compliance of the subjects. To facilitate evaluating the compliance, real-time pressure, force and contact areas are logged along the acquisition of spectral signals. These could be used as a separate piece of information to rule out any collected spectra that are suspicious to involve human interference.

Another important finding of this research concerns the *in vivo* observed photobleaching. Autofluorescence from biological tissues has been observed to be ubiquitous, nevertheless photobleaching has been reported by more than one group besides us, such as Morris (95) from University of Michigan and Feld and Dasari (93) from MIT. In fact, it is not only observed *in vivo* in tissue. Our lab collaborated in a separate project in which chemical changes during glial scar formation were investigated using Raman spectroscopy. Figure 6-2 shows the *ex vivo* fluorescence of a saline perfused rat spinal cord used in that project. The spectra were taken by exposing the spinal cord at the same spot continuously for up to one hour under 200 mW 785 nm NIR laser. As shown in the right panel of Figure 6-2, the fluorescence photobleaches more than 30% and shows no sign of reaching final steady state in 1 hr, which is even deeper bleaching than most of the *in vivo* tissues.
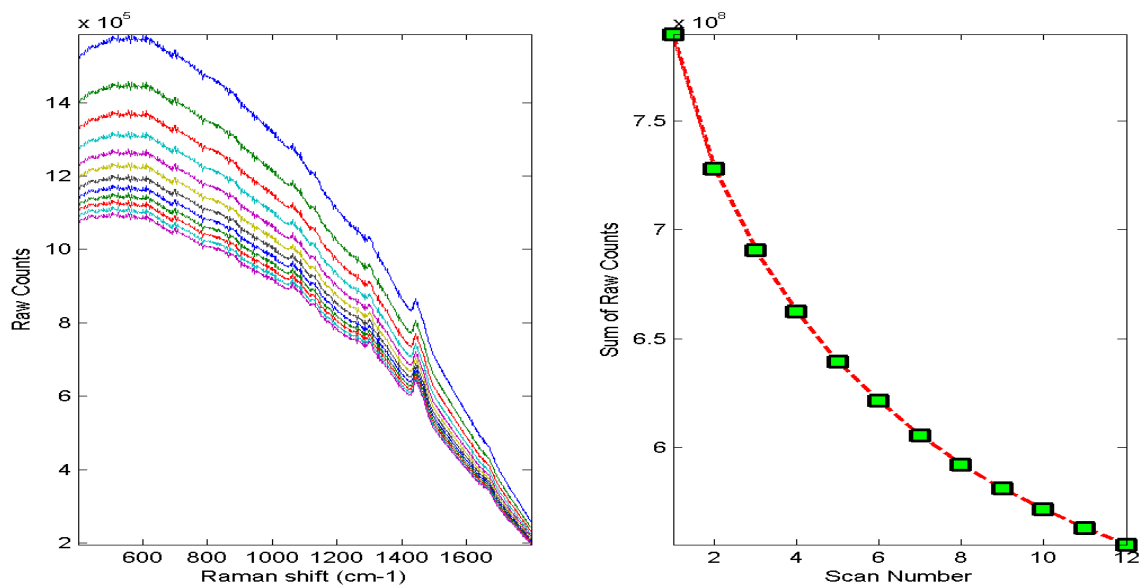
Figure 6-2: Sequence of 5 min raw spectra (left) and fluorescence integrals (right) from extended irradiation by a 200 mW 785 nm NIR laser of a single point on a saline perfused rat spinal cord.

The first thing to mention is that the spinal cord was thoroughly perfused with saline water before testing. Therefore, little blood if any is present in such *ex vivo* sample. But still, substantial photobleaching is observed. Although central nervous system tissue bears very different cell types from skin tissues, the chemical constituents of cytosol and extracellular matrix (113) are not that distinct at all. Therefore, in another angle the photobleaching observed in Figure 6-2 supports our conclusion that it is static tissue not blood that contributes the majority of the fingertip tissue photobleaching.

Another interesting phenomenon is that the fluorescence from saline perfused cord not only bleaches but also bleaches in significant amount. Based on our *in vitro* study in Chapter 4 and 5, only five major tissue constituents, i.e., plasma, Hb, melanin, collagen, and AGEs, are narrowed down as contributors to the observed skin fluorescence and photobleaching. Obviously, there is no melanin in spinal cord and only trace amounts of Hb and plasma in the saline perfused rate spinal cord. Spinal cord does have collagen in its extracellular matrix, but our *in vitro* results show that collagen by itself does not bleach. However, when it gets crosslinked with sugars the resulting AGEs fluoresce and also bleach substantially. As shown in Table 5-1, the outmost layer of the meninges surrounding spinal cord, i.e., dura mater, contains the second highest levels of pentosidine among the tissues investigated (153). Thus, it is speculated that photobleaching of AGEs may play an important part here.

In the effort to associate our *in vivo* observed fingertip autofluorescence photobleaching with static tissue and blood constituents, we performed a series of systematic *in vitro* studies. Comparing Hb bleaching curves shown in Figure 4-16 with pentosidine and melanin bleaching curves in Figure 5-8 and Figure 4-13, Hb only

bleaches 1% within 20 min while pentosidine and melanin bleaches more than 15% in an hour. Both melanin and AGEs show stronger potential of photobleaching than Hb. But, as stated previously, the *in vitro* environment of these tissue constituents are quite different from *in vivo*. Therefore, these results could only offer limited explanations to what is happening *in vivo*.

For purposes of understanding the role of the autofluorescence and photobleaching in the technology of noninvasive blood and tissue analysis by NIR spectroscopy, the results suggest that NIR emission *per unit volume* likely changes somewhat from test subject to test subject. Nevertheless, our study shows that the possible interferences are not that serious and can be overcome. For a single test subject in comparison with him or herself, using fluorescence as a volume normalizer is quite adequate. Since the bleached tissue does not easily recover after up to several hours, utilizing a reasonable prebleaching period in a consistent manner in order to remove the contribution of the bleachable components could provide a consistent basis for utilizing the fluorescence as a volume normalizer.

With regard to calibration across test subjects the situation is more complicated. Whereas the disposition of many of the most potent chromophores, specifically AGEs, are defined by homeostasis in relation to eating, lifestyle and other habits, as well as other factors like test subject disease state, i.e., whether the test subject is diabetic or not. The AGE emission has the appropriate characteristics to account for all of the *in vivo* observations. Clearly, whatever else occurs *in vivo* it is occurring in addition to the possible sources we have described in this thesis.

So while we project no pretense that the experiments described in this paper are exhaustive for all potential NIR chromophores, we do suggest that it is possible that we have identified the major related cause of the observed *in vivo* NIR emission and its characteristics. Indeed the fluorescence and bleaching under UV/Vis excitation are the basis for new devices and protocols proposed by other researchers to screen for diabetes (162), and the statistics for the success of these approaches are reasonable so far. Thus it is clear that the effects and manifestations of AGEs must be large enough *compared to all other contributors*.

Clearly the photobleaching issue matters in all measurements where IE is involved quantitatively, such as our glucose measurements as well as the newly proposed noninvasive *in vivo* Hct monitoring algorithm. Utilizing the separated IE and EE light that carry two independent physical and chemical properties of the irradiated tissue, we provided empirical calibrations for our noninvasive Hct algorithm based on a model that is consistent with the anatomy, function of the skin and the geometry of the probing. Our primary goal is simply to show that it is possible to monitor changes in the Hct by analyzing scattering intensities. And its feasibility has been well justified.

The results presented in this thesis suggest an ability to monitor Hct continuously on a 20 ms or less measurement time scale and with apparently high sensitivity, i.e., Hct change of 0.02 in tens of seconds. This is encouraging but much needs to be done to assess the true accuracy, precision, and sensitivity of this measurement. We note that fluorescence based techniques are essentially zero background measurements that typically permit 100–1000 times smaller detection limits (196) for absolute concentrations and changes in concentration compared to absorption-based techniques.

However, so far absolute Hct values could not be offered directly from our approach. Nevertheless, Leypoldt et al. (99) have demonstrated that potentially useful clinical information is contained in monitoring relative variation from homeostasis of Hct and fluid volumes, which are the earliest indicators of internal hemorrhage.
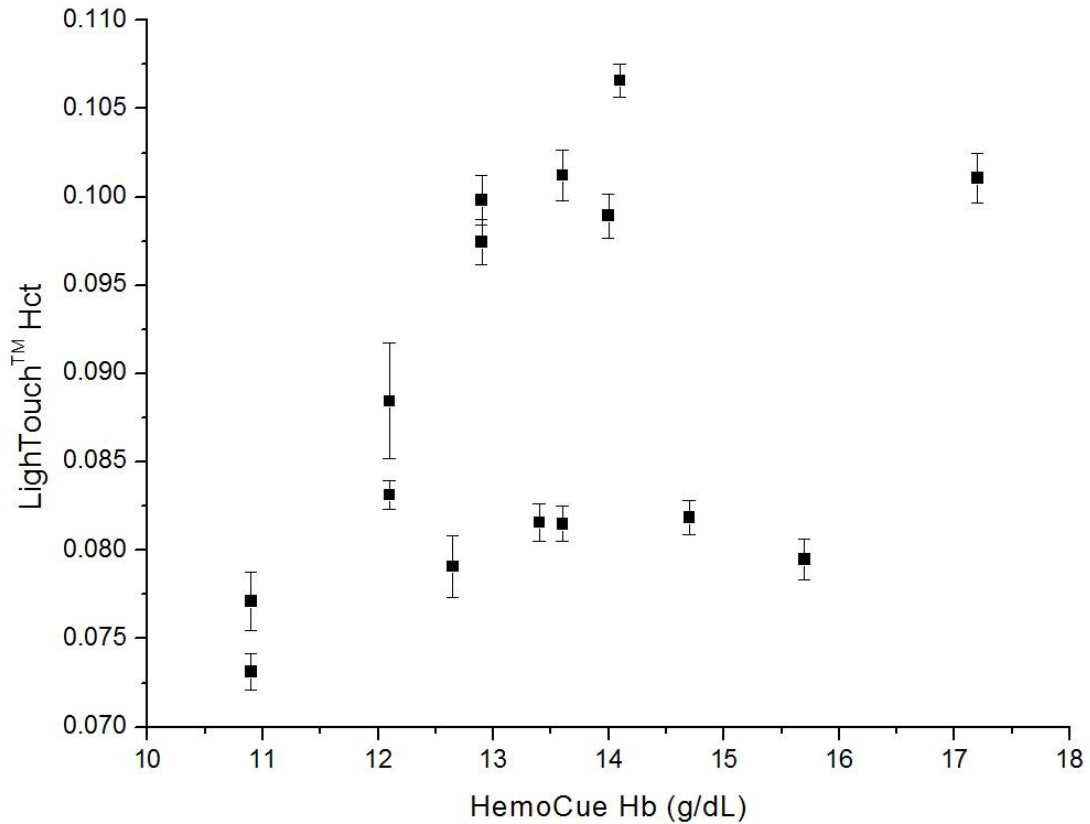
Figure 6-3: Correlation between standard HemoCue Hb hemoglobin measurements and LighTouch[TM] Hematocrit measurements.

As shown in Figure 6-3, although there is clearly a correlation between LighTouch[TM] Hct measurements and HemoCue hemoglobin readings, the physiological implications of changes (197) in the two quantities are what determines the utility of their measurement to a practitioner. Total Hb relates more to the oxygen-carrying capacity of

the blood, whereas Hct relates more to the viscosity of the blood and may therefore present more unambiguous indications of impending circulatory collapse.

Recognizing the unique and irreplaceable clinical values of Hct, other groups have been exploring ways to realize noninvasive Hct monitoring (99-101, 198). Leypoldt et al.(99) have analyzed extracorporeal blood in the ultrafiltration unit to guide dialysis therapy in renal patients. This approach is only "noninvasive" to a dialysis patient. Using a truly noninvasive transcutaneous optical approach Jeon et al. (101) reported an absolute mean percent error in estimating absolute Hct within ±8.3% (σ±3.67). However, to our knowledge, all these currently existing noninvasive optical approaches to Hct exploit the coupled oxy/deoxy Hb absorption spectra using at least one Hb isosbestic point(s) (e.g., at 569 or 805 nm). Since Hct could not be measured based only on one piece of Hb absorption information, empirical calibrations of Twersky's treatment (199) is applied, in which it is assumed that the Hb concentration (in g/dL) is 35 times of Hct.

Table 6-1: Erythrocytometric values for "apparently healthy" white and black subjects of different ages (42).

Subjects	Erythrocytes				Hct		Hb concentration in whole blood		Mean corpuscular Hb concentration	
	Number concentration in whole blood		Mean corpuscular volume							
	Mean	95% range	Mean	95% range	Mean	95% range	Mean	95% range	Mean	95% range
	10^{12}/L		fL				g/dL			
Adults Men	5.1	4.3-5.9	90	80-100	0.47	0.39-0.55	15.1	13.9-16.3	34	31-37
Adults Women	4.5	3.5-5.5	88	79-98	0.42	0.36-0.48	13.5	12.0-15.0	35	30-36

As shown in Table 6-1, this pulse oximeter signal based approach simply makes the assumption that the mean corpuscular Hb concentration is constant at 35 g/dL for all subjects, regardless of age, gender, or even healthy conditions. Therefore, in practical purposes Hct calculated this way offers no different information from Hb measurement. Moreover, the 95% range of mean corpuscular Hb concentration (30-37 g/dL across gender) is wide enough to lead to significantly different Hct estimations as shown in Figure 6-4. This means that even if the Hb concentrations for two different healthy test subjects are the same, e.g., 14 g/dL, the Hct could still be very different, not to mention patients whose mean corpuscular Hb concentration may fall out of the 95% range.
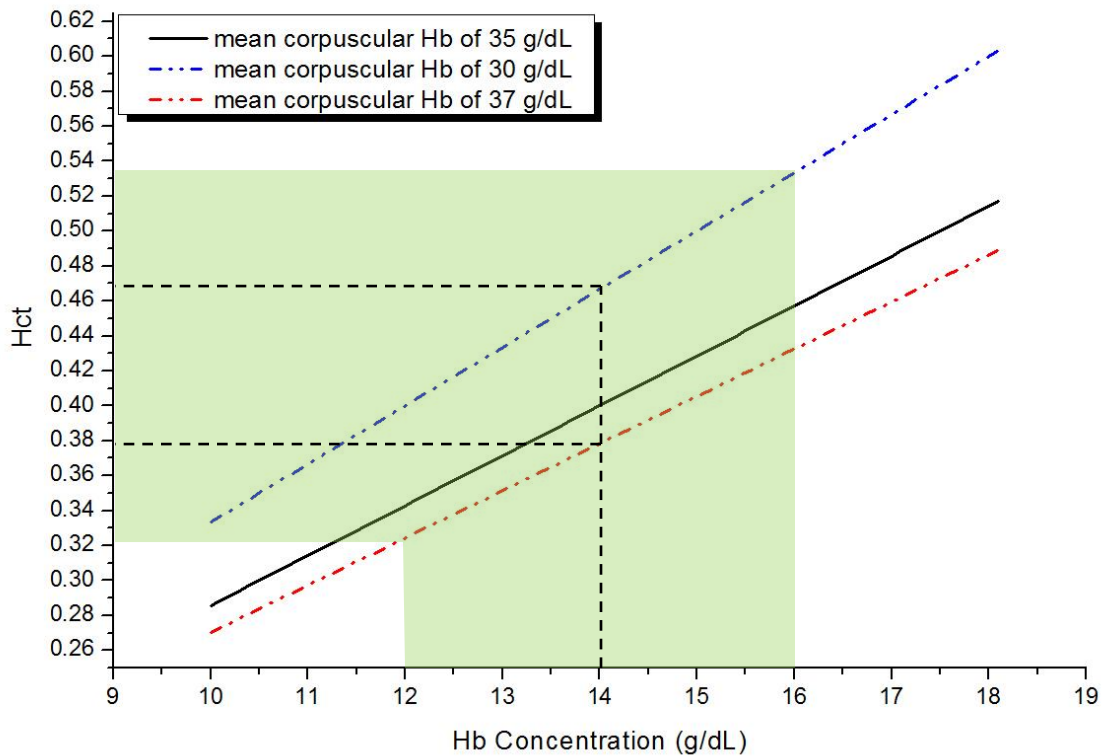
Figure 6-4: Hct estimations from measured Hb concentrations based on various assumptions on mean corpuscular Hb concentrations. According to Table 6-1, the averaged value of mean corpuscular Hb concentration is 35 g/dL with a 95% range from 30-37 g/dL. Green shaded area: maximum Hct variation range within normal physiological Hb concentrations based on 30-37 g/dL corpuscular Hb assumption.

In fact, invasive approaches that give traditionally acceptable data (103, 104) are also quite variable due mostly to sampling and handling issues (105). Nevertheless, devices such as oximeters (200, 201) and hemoglobinometers (198, 202) produce results that are apparently not sufficiently sensitive, precise, or accurate regarding blood changes to give unambiguous indications to clinicians for diagnosis of internal hemorrhage and determining the need for a transfusion. On the other hand, the Hct monitoring approach introduced in this thesis adopts a totally different approach which is based fundamentally on the photophysical and photochemical properties of RBCs and plasma. Therefore, it has a pragmatic potential to monitor the Hct variation.

Finally, because the perfusion is affected by many things, experiments should explore the variation of the observed spectra with systematic variation in the mechanical coupling to the skin surface. Combining our findings in human factors control and *in vivo* skin tissue fluorescence properties, it is apparent that a standard pre-experiment procedure will be beneficial to follow. First of all, when necessary, such as for test subject with dry skin or experiments taken in dry season like winter, a thin layer of regular skin lotion or moisturizer could be applied to increase skin conductivity. Although blinking dots caused by poor contact introduce unnecessary force compensation, empirical experience has proved this to be an effective way to avoid such problem. However, be cautious of any spectral ambiguity that might be introduced by the lotion itself.

Then, before the taking of any spectral data, it is suggested to measure the BP and heart rate from each test subject. Our research shows that for each individual both optical and mechanical pulses happens when the applied pressure is around the mean arterial

pressure (MAP), which is close to the mean of the systolic and diastolic pressure. Also, the force needed to apply MAP for a test subject with regular fingertip size is also in the range that has been proved to cause moderate blood flow modulation. Thus the pre-taken blood pressure could be used to guide the target pressure set-up that is optimized to each individual. For the best outcome from a normal noninvasive glucose measurement, it is optimal to set the target pressure of the unpressed part to the lowest pressure sufficient enough to maintain fingertip stability, and that of the pressed part to the MAP. From a purely engineering standpoint it would be very easy to incorporate blood pressure and heart rate measurements in the LighTouch^{TM} device itself using the plethysmographic data already collected using the PDPM.

When the fingertip is properly positioned, the laser could be switched on after the test subject is informed. The pre-experimental laser exposure is made on purpose to prebleach the skin region under investigation. Then a PDPM set-up procedure is performed to take fingertip under initial pressure registration. The whole set-up step usually takes less than 20 sec. Thus a separate 20 sec more prebleaching step is added to bleach the skin even deeper. Although the total time of prebleaching is still less than what is needed to reach a steady state fluorescence equilibrium which could be as along as hundreds of seconds, the fast bleaching process should be done at this point.

Then another ridge set-up procedure follows, during which the fingertip will be dragged back and forth by a motored micro actuator to take topographic scan. In our current version, the second detected ridge will be located to guarantee the closest vicinity to 53 °incident angle. Once these steps are all done, either a regular single glucose measurement or a continuous Hct monitoring could start. The research in this thesis

suggests that following these steps has promise to greatly improve the experimental reproducibility and generate more accurate blood glucose concentration predictions. These ideas need to be verified in the future work.

6.2 Future Work

As mentioned in the proceeding context of this thesis, while the current research has led to many interesting observations and the *in vivo* apparatus is capable of performing precise and reproducible glucose and Hct measurements, there is still room for both technical refinements and conducting continuous study on the unsolved problems.

From the instrumental point of view, it could be envisioned that the next generation of PDPM will be able to perform automatic target modulation pressure set-up. Using the hardware of the current PDPM to fulfill this function, the step motor and solenoid system could exert gradually increasing pressure under programmed pressure gradient. Meanwhile the mechanical pulses are monitored and the amplitudes of these pulses are fed into a BP measuring algorithm. Using the same principle as the oscillometric approach in determining BP, the MAP as well as the pulse rate could be obtained simultaneously.

Although we have been logging the force, pressure, and contact area signals that come directly from the transducer, we have never used these sensor outputs as the criteria in real-time automatic active data rejection. We have shown in Chapter 2 that the amplitude of force variation caused by involuntary tremor is much bigger than cardiac pulses and normal modulation. Therefore, abnormal force fluctuation could be an

indicator of poor test subject compliance. Either a checkup toward the end of an experiment or a real-time monitoring of suspicious force variation would be beneficial and time-saving.

Besides the two aforementioned refinements, there is still one obstacle that needs to be overcome. In our effort to modify experimental skills and improve the procedure along the way for making the *in vivo* findings presented in this thesis, we have been adapting most of the aforementioned steps of the proposed standard pre-experiment procedure, except the ridge set-up. This is simply because anatomic difficulties we encountered when trying to implement our current ridge set-up procedure. In this procedure, the transverse motored micro actuator is first positioned at a position called "center". This is where the test subject originally positioned their finger. Upon starting of the ridge scan, the actuator, together with the finger, first backs up about 2 mm and then scans unidirectionally form the joint to end. While performing a topographic scan, the IE vs. Time curve records the position of the ridges and the actuator drags the finger back to where the ridge index is logged.

Although this sounds plausible, in reality this procedure is hard to perform because there exists a tissue stretching issue. We noticed that moving finger together with the actuator always needs to overcome the initial stretching of the skin tissue that is also in contact with the printed circuit board surface before it actually begins to move. In other words, the distance travelled does not correspond to the logged actuator steps. Besides, upon finishing the first scan the finger is dragged in the opposite direction. This time the skin must restore to its original state first and then once again overcome the same stretching as the first time. Thus, the final position could easily be far from a ridge.

To solve this problem, we have to seek new approaches in locating fingertip ridges. Supposedly, the fingertip could be dragged to travel in only one direction in a much slower pace to allow short "move-measure" cycles. In other words, the actuator moves one step and CCD camera takes spectra to calculate IE. When this "move-measure" cycle is finished, the actuator drags the fingertip to the next step and repeats the cycle. Since our laser is not shuttered or synchronized with the actuator, at least 2 frames need to be allowed each step since the first frame IE may have some timing issues relating with CCD clearing. Both the absolute IE and the first derivatives need to be logged and calculated in real-time in order to stop advancing forward when a sufficient amount of decline in IE is observed.

It can be foreseen that this ridge set-up procedure will be time-consuming, i.e., it might require as much as 20-30 seconds, but it has the potential to guarantee a ridge could be located accurately each time. However, how to select the parameters, such as thresholds and criteria needed to stop the scan, could be tricky. Each test subject's fingerprints have unique widths and depths, and the fluorescence baseline could vary to an even bigger extent. Therefore, substantial testing will be necessary in order to realize this procedure in practical application.

Concerning noninvasive Hct monitoring, as a practical matter, the spectroscopic experimental requirements for obtaining EE and IE measurements that are adequate for application of this algorithm do not seem to be very stringent. The main requirement is a clean separation of the EE and IE, with no need to separate the Raman contribution from the fluorescence; this would not require spectrographs or very narrow line width lasers or even particularly stable laser sources. Probably, simple filters and simple lasers may be

used and the measurement system can use fiber-coupled incoming laser and outgoing IE and EE light. Therefore, although the Hct results presented in this thesis were obtained using CCD detection, it would be feasible to use optical fiber, an optical filter, a low-grade laser, or possibly only a LED and two photodiode detectors to access the same information. A system using these simplified optical components will greatly decrease the complexity and price of a real product while increasing the portability and convenience for clinical applications.

As to the empirical calibrations for the *in vivo* noninvasive Hct algorithm, there are definitely more than the two approaches proposed in this thesis. Actually, the second assumption about the blood modulated by a typical pressure modulation is somehow related with the first assumption about cardiac pulses. In the process of testing the sensitivity of the algorithm, it is clear that we can use the tourniquet experiment as a separate calibration method. First of all, conventional fingerstick references can be compared in parallel with the spectra data. Absolute Hct change can be fed directly into the algorithm. Although errors do exist depending on how the tourniquet is performed and blood is sampled, it could be expected that this approach is at least more accurate than assumptions. Moreover, the tourniquet experiment by far shows the most obvious blood disturbance ever observed *in vivo*. A calibration based on this is expected to yield a more reliable set of parameters *a-f*.

Another limitation of our *in vivo* Hct algorithm calibration is the narrow range of Hct variation. Even with the tourniquet trials, the biggest change before and after a tourniquet is only approximately 0.03. For one test subject, the Hct increase from 0.38 to 0.41 after the blood flow has been block by a tourniquet for 1 min. Although theoretically feasible,

we never know whether our algorithm is able to track Hct to an extreme level. To investigate that, an animal model needs to be employed. We have currently proposed a protocol for Institutional Animal Care and Use Committee (IACUC) approval to perform an animal study at Syracuse University.

In this propose study, the rats will be exsanguinated while a portable Hct device will be used to simultaneously monitor IE and EE changes. Notice that losing blood does not necessarily cause an immediate change of Hct since the change will not happen until the compensatory phase (203, 204) is initiated. During this physiologically manifested body fluid compensation process, compartment-scale fluid shifts, surface fluid redistribution, and change in blood composition happens to compensate for blood volume loss, and thus result in Hct change. To actively control the rat Hct, body fluid replacements with Normocarb™, plasma, and whole blood are also planned.

It is also noteworthy that, during the compensatory phase of hemorrhagic shock, protein and glucose concentration in the plasma are known to increase precipitously; measurement of the IE offers the possibility of simultaneously monitoring both Hct and analyte concentrations. The amide I Raman band at ≈ 1670 cm^{-1} Raman shift, is a measure of protein content over all three phases. The Raman features of the IE we have long used for glucose monitoring could also be useful in this context as an indicator of whether a compensatory mechanism is triggered or not in an internal hemorrhage case.

Measuring the IE and EE simultaneously and applying the algorithm leads to a sensitive probe for volume changes of not only RBCs, but also plasma. Detection of Hb or RBCs is of course routine, but to our knowledge obtaining a plasma volume

simultaneously is unique. Normalizing to the internally consistent and turbidity-corrected plasma volume fraction calculated from our algorithm offers the possibility of calculating concentrations of various analytes, including but not limited to glucose. It could turn out to be a more accurate and straightforward volume normalizer than directly utilizing undifferentiated inelastic emission, but further validation needs to be planned for our future studies.

Due to the importance of prebleaching, we have been thinking about solutions to shorten the time needed to reach the steady state fluorescence baseline. It is natural to propose using higher laser powers since the power dependence of photobleaching has been established (91). Shorter wavelength laser could also be tried. As shown in Figure 3-11, using 805 nm laser the skin bleached about twice as much as that with 830 nm laser in 100 sec for two healthy test subjects, and the power used for 805 nm excitation is only half of 830 nm laser. However, laser safety concerns arise when trying to increase the power or using shorter wavelength. The American National Standards Institute (ANSI) allowed maximum permissible exposure is determined by laser wavelength, exposure length and incident spot size (205). Therefore, one possible solution is to use laser sources that are not tightly focused or the ones that originally have big spot sizes. By reducing the power density, higher allowable power is possible. Prebleaching over a broader area could be preferred from an engineering standpoint to implement the ridge set-up procedure.

Finally, interesting chemistry between dissolved oxygen and pentosidine (possibly other AGEs or Maillard reaction intermediates) has been observed. However, there are some technical difficulties involved in this study. First of all, the TMX turns out to be

very efficient at depleting dissolved oxygen and extremely sensitive to light. Therefore, in the process of making the stock solution it is critical to keep the TMX out of any possible light source. Moreover, our results show that pentosidine bearing TMX has very similar photobleaching properties as what we observed *in vivo*. Therefore, the bleaching behavior of pentosidine itself is conceivably useful in order to quantify the fluorescence and thereby assign a volume numerically to the probed volume. These are presently under review but we believe a better understanding of the bleaching chemistry itself is necessary to proceed. And this leads to our further investigation of the pure form of pentosidine, the synthesis of which has recently been achieved by our collaborators (206).

To explain the pentosidine fluorescence properties under NIR excitation, ZINDO calculations on the singlet and triplet excitation states was performed. Although the results support our speculation of that interesting physical chemistry underlies the fluorescence and photobleaching phenomenology, such as TPE and singlet oxygen sensitizing, more proof is needed to be certain. Actually, the ZINDO formalism applied to this problem could be inappropriate since the pentosidine molecule may be charged under physiological conditions but ZINDO is only applicable to closed shell systems. The power dependence of autofluorescence production is also consistent with our proposed involvement with pentosidine but more work is required to obtain greater confidence in the hypothesis.

In the thesis, we proposed a hypothesized pentosidine photochemical pathway in which it reacts with dissolved oxygen as a sensitizer and also a scavenger. The research presented demonstrates its potential as a sensitizer but only provides limited evidence to support the formation of the endoperoxide. Therefore, traditional analytical approaches,

such as mass spectroscopy and high-performance liquid chromatography, could be used to perform the product analysis. These studies will have real potential to unveil the role of dissolved oxygen in pentosidine photochemistry.

Without question, there are many possibilities to use the outcomes presented in this thesis to explore a much broader range of possible applications, either *in vivo* or *in vitro*. Continued work along the lines of this project will further advance the development of such noninvasive blood analytes monitoring systems for final clinical availability.

6.3 Conclusions

This research is part of an ongoing project aimed at the application of combined NIR Raman and fluorescence spectroscopy to noninvasive *in vivo* blood analysis including but not limited to glucose monitoring. Coping with practicalities of human factors and exploring ways to obtain and use knowledge gained about autofluorescence to improve algorithms for blood and tissue analysis are the general goals of this research.

Firstly, the study investigated the various sources of human factors pertinent to our concerns, such as fingerprints, turgor, skin hydration and pigmentation. We then introduced specialized *in vivo* apparatus including means for precise and reproducible placement of the tissues relative to the optical aperture, i.e., the PDPM. Based on solid instrumental performances, appropriate methodology is now provided for applying and maintaining pressure to keep surface tissues immobile during experiments while obtaining the desired blood content and flow.

Secondly, *in vivo* human fingertip skin autofluorescence photobleaching under 200 mW 830 nm NIR irradiation is observed and it is characterized that: i) the majority of the photobleached fluorescence originates from static tissue not blood, ii) the bleaching (1/e point) occurs in 10^1-10^2 sec timescale, and also iii) a photobleached region remains bleached for at least 45 min but recovers completely within several hours. A corresponding extensive but not exhaustive *in vitro* systematic study narrowed down the major contributors of such fluorescence and bleaching to collagen, melanin, plasma and Hb: two major static tissue constituents and two major blood proteins.

Thirdly, we established that measuring the IE and EE simultaneously leads to a sensitive probe for volume changes of both RBCs and plasma. An algorithm based on measurements obtained while performing research needed for this thesis, as well as some empirical calibration approaches, was presented. The calibrated algorithm showed real potential to track Hct variations in cardiac pulses, centrifugal loading, blood vessel blockage using tourniquet, and even during as subtle an occurrence as a Valsalva maneuver.

Finally, NIR fluorescence and photochemistry of pentosidine, a representative of the AGEs which accumulate with age and hyperglycemia, was studied. The results indicate that oxygen plays a pivotal role in its photobleaching process. We hypothesized and offered proofs showing that pentosidine is a $^1O_2$ sensitizer that is also subject to attack by the $^1O_2$ resulting in the photobleaching that is observed when probing tissue using NIR. The photobleaching reaction is kinetically first order in pentosidine and ground state oxygen, and *in vivo* effectively first order with NIR irradiation also.

APPENDIX A: LOAD CELL CALIBRATION PROCEDURE

In order to allow PDPM measure absolute force and pressure, the load cell (LCGC-150G, Omega Engineering Inc., Stamford, CT, USA) needs to be properly calibrated. Figure A-1 shows a simplified drawing of load cell mounting and working scheme. A lever system is used and the aperture is positioned between the fulcrum and the tip of the load cell. The drawing is not to scale, but the distance between the aperture and the fulcrum is the same as that between the load cell and the fulcrum. According to the law of lever, displacement at the tip of the load cell is twice of that at the aperture. Therefore, the force measured by the load cell is twice of that is actually applied at the back of the fingertip. However, as will be shown later, the calibration procedure has naturally incorporate this ratio in the calibrating process. Therefore, no further scaling is necessary.

Two screws are used to hold the spring steel board in position. While the screw close to the end of fulcrum (referred as "calibration screw" thereinafter) is used to fasten the board down, the other one between the aperture and the load cell is just loosely fitted to keep the board properly oriented. A rubber O-ring is used while tightening the calibration screw down. The fulcrum is designed to have the same height as the tip of load cell transducer and also the rubber O-ring, Therefore, the spring steel board is almost parallel to the aluminum main body. The side-view of the spring steel board shown in Figure A-1 has a much exaggerated angle.
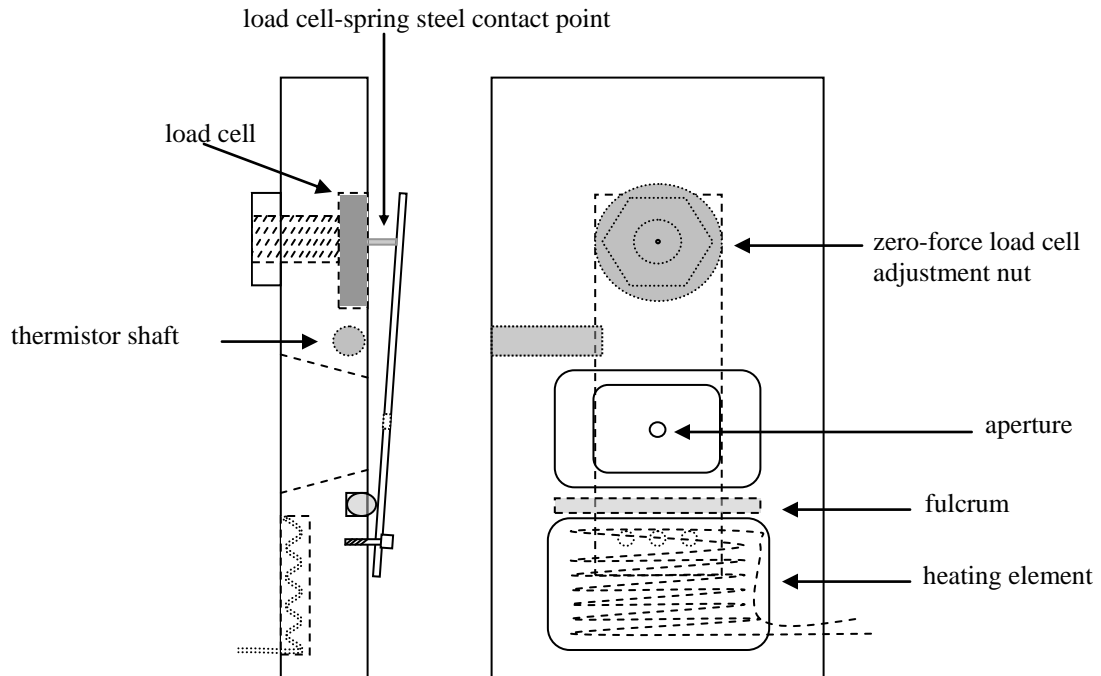
Figure A-1: Simplified drawing, not to scale, of tissue modulator. Main body is aluminum with load cell, thermistor shaft and stainless steel rod/fulcrum shown in gray tone. The angle between the spring steel modulating plate is exaggerated for clarity. Nut is used to adjust zero position of load cell and ensure that spring steel is always in contact with transducer tip.

Whenever the calibration screw is adjusted, a load cell calibration is required to be performed. A yearly periodical calibration is also recommended and the frequency of calibration is determined by how extensively the PDPM is used. We perform the following steps for the load cell force calibration:

i)   Open the "PDPM Settings" panel as shown in Figure A-2 under "File" in the menu bar of the LighTouch[TM] GUI. Make the "PDPM Feed Back" window visible at the same time.
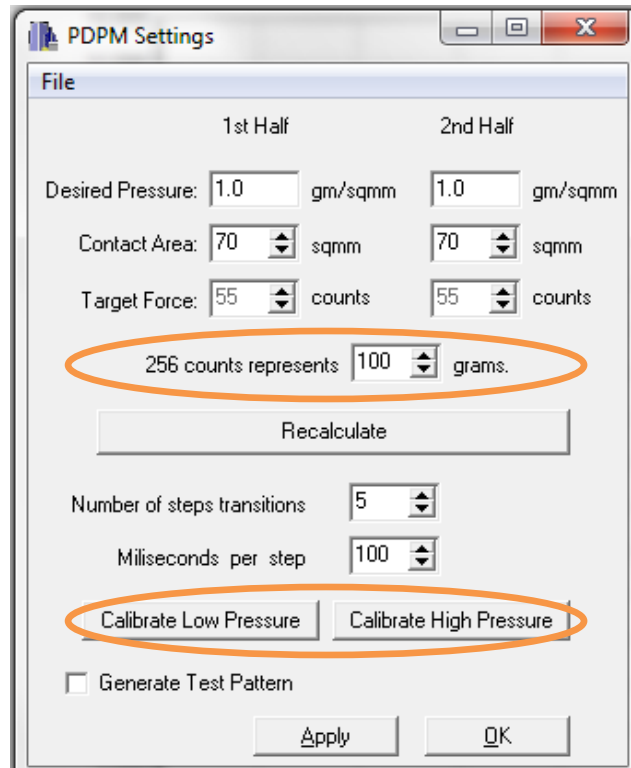
Figure A-2: Screenshot of the "PDPM Settings" panel on the LighTouch[TM] GUI. In the load cell calibration process, the button "Calibrate Low Pressure", "Calibrate High Pressure" and "256 counts represents ___ grams" are the ones that will be used.

ii)   Adjust the calibration screw when a slight turn shows force variation on the low end of the slide bar in the "PDPM Feed Back" window of the LighTouch[TM] GUI click "Calibrate Low Pressure". Alternatively, electronic signal from the load cell could be directly displayed on an oscilloscope. In this case, voltage variation could be referenced.

iii)   Put standard weights (100 g, 200 g or 250 g) on the aperture to saturate on the real-time force slide bar and click "Calibrate High Pressure". The manufacture specification of the LCGC-150G load cell is to output 20 mV for 150 g force.

iv) Put the weight number used for the calibration in the "256 counts represents __
grams". The 256 counts represent the A/D converter (up to 12-bit capacity)
numbers that will be used to control the PDPM as shown in Figure A-3. By
doing this, the analog voltage outputs from the load cell are converted into
digitized numbers ranging from 0 to 255.
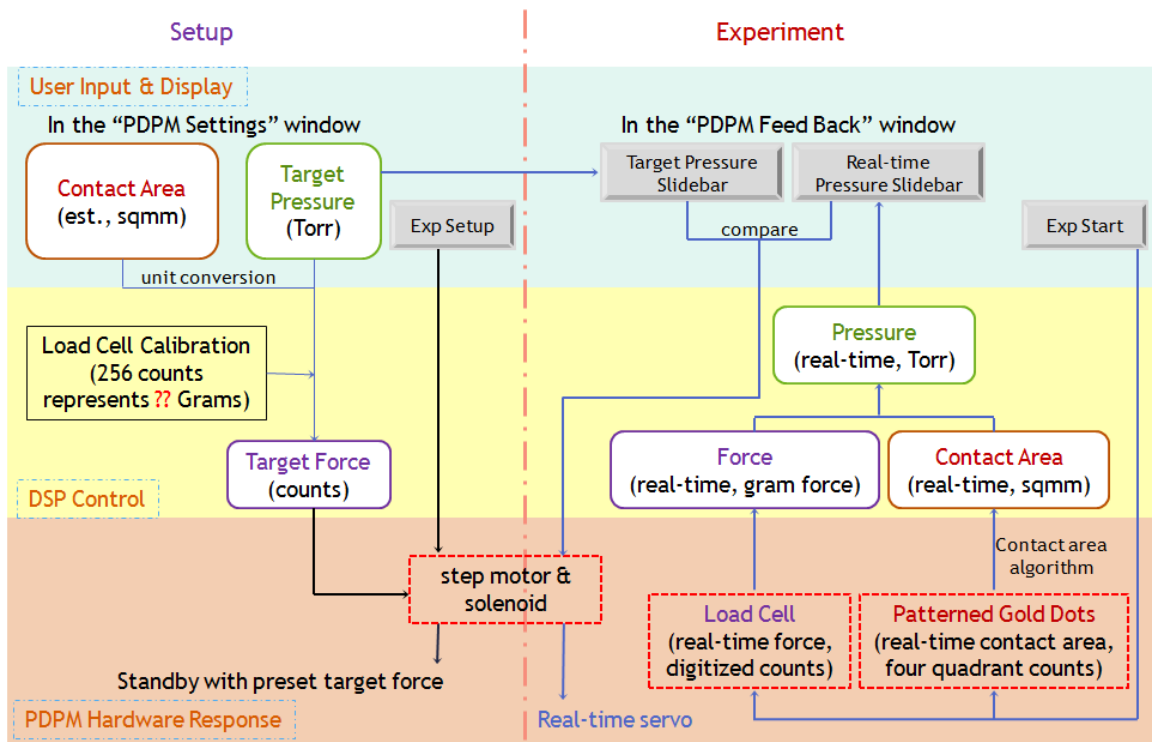
Figure A-3: Schematic drawing of PDPM feedback cycle in set-up and experiment
process. The load cell calibration is used in converting the inputs into digitized numbers
using A/D converter.

When the target pressure (in gf/mm^2) is set, the following equation will be used to
convert it into dimensionless digitized target force numbers:

$$\text{"Target Force"} = \text{"Contact Area"} \times \text{"Desired Pressure"} \times 256 / \text{"??"}$$
$$\text{(counts)} \qquad \text{(mm}^2\text{)} \qquad \text{(gf/mm}^2\text{)} \qquad \text{(counts/gf)}$$

The underscored part is derived from the load cell calibration. Currently, the force and pressure logged in the .sen and .dtl files are in dimensionless converted digital numbers. Therefore, the load cell calibration equation needs to be used reversely to get the meaningful force with proper unit.
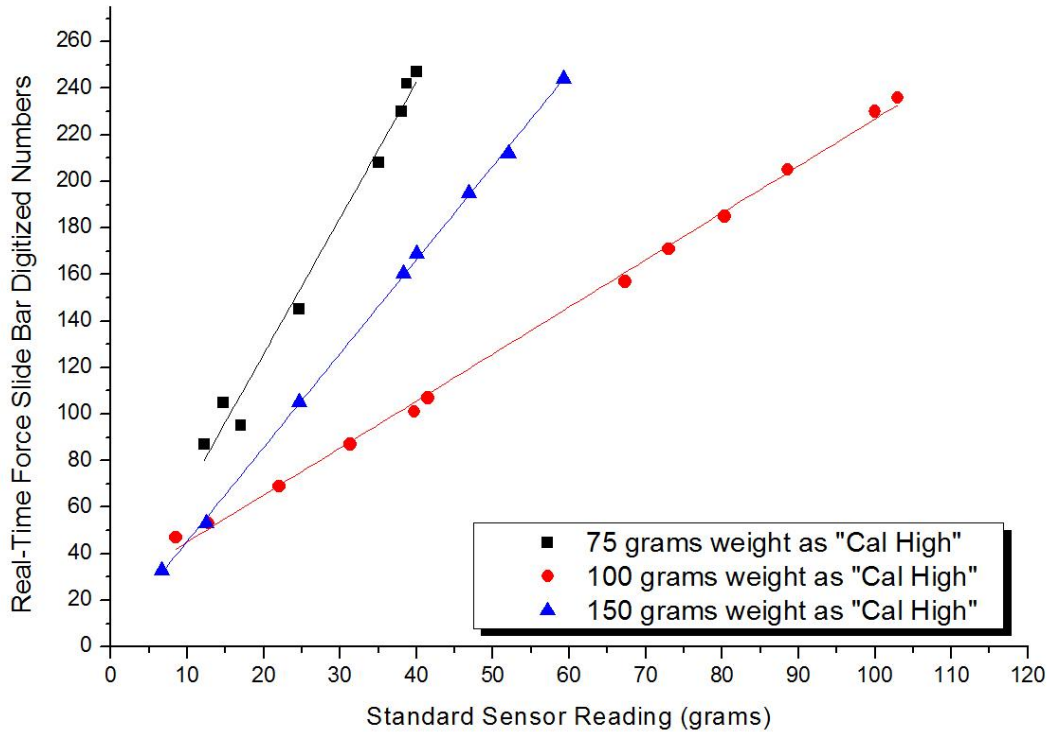
Figure A-4: Calibration curves of using different standard weights as "Calibrate High Pressure". Using heavier weight extends the dynamic range, while using lighter weight increase the sensitivity.

Usually after a load cell calibration is done, another load cell connected to a single channel signal conditioner-indicator (Model GM, SENSOTEC Inc., Columbus, OH, USA) will be used to check the linearity, sensitivity, and dynamic range of the calibration. Examples of typical curves are shown in Figure A-4. It is obvious that how much standard weights used as "Calibrate High Pressure" determines the dynamic range and

sensitivity of the PDPM module. Using heavier weights could extend the dynamic range, while using lighter weights increase the sensitivity. There is a tradeoff and the selection of calibration weight should be based on needs. Besides, extra attention needs to be paid on the drift of calibrated zero.

APPENDIX B: DATA STRUCTURE SPECIFICATION FOR HEMO MODE

The LighTouch^{TM} GUI could run under two modes: "Glucose" mode and "Hemo" mode. To select mode, the configuration file (with a suffix of ".cfg") needs to be loaded manually before the collection of any data. For the current version of LighTouch^{TM} GUI (v 11.06), "Glucose" and "Hemo" modes share the same configuration file but are different in the setting of "Experiment Length" as circled in a screenshot in Figure B-1.

Figure B-1: Screenshot of LighTouch^{TM} GUI showing the "Configuration Parameters" panel popped up upon loading a configuration file.

To take a single measurement as it is normally done under "Glucose" mode, the experiment length is usually set between 20 sec to 200 sec. Typically 100 or 200 sec acquisition should be used to collect sufficient number of frames for tissue modulated

Raman calculation. The maximum length of an experiment that could be performed under "Glucose" mode is 200 sec.

"Hemo" mode allows continuous data collection until quitting the mode by clicking "Stop Hemo". Under this mode, the setting of "Experiment Length" means the length of a hemo cycle. The hemo cycle will be repeated and data will be generated for each cycle and automatically pooled under the designated folder specified by the initiation file, i.e., "LighTouch.ini".

Under both modes, spectral and mechanical transducer data will be logged in frame basis. The amount of frames generated is determined by two settings: experiment length and shutter time. Both of them could be set in the configuration panel shown in Figure B-1. Frames logged in each hemo cycle could be calculated using Equation B-1 and the same equation could be applied to data collected under "Glucose" mode.

$$\text{frames per hemo cycle} = \text{"Experiment Length"} / \text{"Shutter Time"} \qquad \text{Equation B-1}$$

At the end of a single "Glucose" experiment, .ccd and .sen files will be allowed to be manually saved in local hard drive. The .ccd file contains all frames of spectra captured by the CCD camera. The.sen file contains force, pressure, quadrants and contact area information detected by the mechanical transducers. Data processing procedure and MATLAB routines used to bulk convert these binary format files will be elaborated in following APPENDIX C.

Back to the hemo data structure issue, it is important to know the number of frames per hemo cycle for a successful MATLAB implement. Although 40 ms shutter time has been occasionally used for better SNR, 20 ms is of primary preference since such setting

give better data density per pulse. Therefore, for every hemo cycle, typically 3 sec, 150 CCD frames will be recorded and automatically saved as a miniature .ccd file. Usually, when "Hemo" mode is started, the experiment will uninterruptedly collect data and output the calculated RBC volumes, plasma volumes and Hct results into a consecutively updating graph within the GUI. Meanwhile, .ccd and .dtl files are logged sequentially in the designated directory every hemo cycle. The structure of the .dtl file is specified below in Table B-1.

In Table B-1, the "Hemo Cycle Size" in .dtl file equals the "frames per hemo cycle" determined by Equation B-1, while "Hemo Cycle Instance" represents the relative position of a particular hemo cycle within a continuous Hct monitoring experiment. The Hct, plasma volumes and RBC volumes calculated from IE and EE integrals as elaborated in Chapter 3 are also logged in each hemo cycle. Notice that no .sen file is logged since the basic PDPM feedbacks, such as pressure, contact area, and quadrants, have been backed up in .dtl file. Force is not logged since it could be readily calculated based on the pressure and contact area. Pressure values are represented by dimensionless digitized numbers that come directly from A/D converter. Absolute real-time pressure with meaningful units could be got by applying the aforementioned force load cell transducer calibration in APPENDIX A. Finally, two more fields are included to save the data collected from the two channels, TP9 and TP10, of a commercial pulse oximeter (Nellcor® N200, Nellcor Inc., Pleasanton, CA, USA) for parallel comparison with LighTouch™ signals.

Table B-1: "Hemo" mode detail log file structure (.dtl) based on version 1.4 update

Item Number	Item Name	File Granularity	Logging Granularity	Data Type	Type Size (byte)	Data Size (byte)	Notes
1	File Revision Tag	Cycle	Once	int	4	4	
2	Hemo Cycle Size	Cycle	Once	int	4	8	**Header**
3	Hemo Cycle Instance	Cycle	Once	int	4		
4	Red Blood Cell Volume	Cycle	Frame	float	4	24	**Data** Fields 4 - 12 are written as a set for each frame and consist of 24 bytes of data
5	Plasma Volume	Cycle	Frame	float	4		
6	Hct Result	Cycle	Frame	float	4		
7	Pressure	Cycle	Frame	float	4		
8	Contact Area	Cycle	Frame	float	4		
9	Quadrant "Down" Contact Count	Cycle	Frame	char	1		
10	Quadrant "Up" Contact Count	Cycle	Frame	char	1		
11	Quadrant "Out" Contact Count	Cycle	Frame	char	1		
12	Quadrant "In" Contact Count	Cycle	Frame	char	1		
13	Test Point 9 (TP9)	Cycle	Frame	short	2	4	Fields 13 & 14 are new to REV2
14	Test Point 10 (TP10)	Cycle	Frame	short	2		
File Size (bytes):						4 + 8 + (24 + 4) * (Hemo Cycle Size)	

Thus, based on the lasted update (v1.4) on .dtl file structure, the detail file size (in bytes) of each hemo cycle can be calculated. For example, assuming 150 frames of data are generated for each cycle (3 sec hemo cycle length and 20 ms shutter time), then 4212 bytes or 4.11 KB .dtl file will be logged. Meanwhile, 622 KB (637320 bytes) .ccd file will also be backed up simultaneously. Bear in mind that these just calculated storage spaces needed for logged data are only for a single hemo cycle, i.e., 3 sec. Thus, for a 1 min monitoring under "Hemo" mode, about 18.34 MB of data will be logged.

However, in order to monitor the Hct fluctuation of a test subject, one experiment normally takes tens of minutes, or much longer if necessary. This will eventually generate thousands of CCD and detail files and also take up a tremendous amount of hard disk spaces. While at the R&D phase raw data are favorable in optimizing parameters that feed into the algorithm and evaluating system performance, the redundancy of data logging could be significantly reduced once the testing phase ends.

At the end of one Hct monitoring trial, a summary file with a suffix of .sum is logged. The .sum file only backs up the final results and the most important system operation parameters. Table B-2 shows the structure of a summary file. "Hemo Cycle Counts" records the total number of hemo cycles one continuous monitoring has taken. Parameters *a-f* are predetermined constants using the approaches elaborated in Section 3.3 of Chapter 3. These numbers are fetched directly from .ini file where the six parameters are set. The "CCD Exposure Time" is another expression of the aforementioned "Shutter Time". Different from the .dtl file, the Hct, plasma volumes and RBC volumes in the .sum file are the average for each cycle and could be plotted readily in the LighTouch^{TM} GUI at the end of an experiment.

Two Boolean fields, i.e., "Bleach" and "Stable", are also included in the .sum, representing the fingertip tissue photobleaching status and compliance of the test subjects respectively. A "0" is false and "1" is true. The Hct related fields are only calculated when both of the fields are true. Therefore, no output could be shown during a monitoring process if one or both of the red LED lights on the GUI lit up. IE0 and EE0 will be recalculated once a new cycle that passes the two tests starts. The .sum file takes much less hard drive spaces compared to the .dtl and .sum files generated along the data acquisition process.

Finally, the data structures listed in Table B-1 and Table B-2 for .dtl and .sum files respectively should be used as references for implementing the MATLAB routines in hemo data processing. Changes in MATLAB codings should be made accordingly whenever there is a change to these structures.

Table B-2: "Hemo" mode summary log file structure (.sum) based on version 1.4 update

Item Number	Item Name	File Granularity	Logging Granularity	Data Type	Type Size (byte)	Data Size (byte)	Notes
1	File Revision Tag	Procedure	Once	int	4	4	
2	Hemo Cycle Count	Procedure	Once	int	4		
3	Hemo Cycle Size	Procedure	Once	int	4		
4	Parameter A	Procedure	Once	float	4		
5	Parameter B	Procedure	Once	float	4		
6	Parameter C	Procedure	Once	float	4		**Header**
7	Parameter D	Procedure	Once	float	4	40	Laser Power in mW
8	Parameter E	Procedure	Once	float	4		CCD Exposure in ms
9	Parameter F	Procedure	Once	float	4		
10	Laser Power	Procedure	Once	float	4		
11	CCD Exposure Time	Procedure	Once	float	4		

Table B-2 (Continued): "Hemo" mode summary log file structure (.sum) based on version 1.4 update

Item Number	Item Name	File Granularity	Logging Granularity	Data Type	Type Size (byte)	Data Size (byte)	Notes
12	Hemo Cycle Instance	Procedure	Cycle	int	4		
13	Red Blood Cell Volume	Procedure	Cycle	float	4		
14	Plasma Volume	Procedure	Cycle	float	4		
15	Hct Result	Procedure	Cycle	float	4		**Data** Fields 12-22 are written as a set for each cycle and consist of 32 bytes of data; For Bleached and Stable fields, a value of 0 indicates false and a value of 1 indicates true.
16	CCD Exposure Temp (°C)	Procedure	Cycle	float	4	32	
17	IE0 Value	Procedure	Cycle	float	4		
18	EE0 Value	Procedure	Cycle	float	4		
19	Bleached	Procedure	Cycle	char	1		
20	Stable	Procedure	Cycle	char	1		
21	Spare1	Procedure	Cycle	char	1		
22	Spare2	Procedure	Cycle	char	1		
File Size (bytes):						4 + 40 + (32 * Hemo Cycle Size)	

APPENDIX C: IN VIVO DATA PROCESSING PROCESSURE

The excessive headers in the .ccd and .sen files generated *in vivo* either using "Glucose" or "Hemo" mode could be cleaned using a C++ based command line tool called "ConversionTool.exe". Either a .ccd, or .sen file, or a path to a folder which has these files could be specified to implement this command. More than one file or folder could be specified at the same time by adding them as arguments.

The format of the .sec file, which is the converted file from .sen data, is:

> Frame Count (16 bit unsigned int)
> % Then the sensor data for each frame
> % Sensor Frame Data Format:
> Force (32 bit int)
> Pressure (32 bit int)
> Contact Area (32 bit int)   % scaled by multiplying by 1000
> Q1 Sum (32 bit int)   % scaled by multiplying by 1000
> Q2 Sum (32 bit int)   % scaled by multiplying by 1000
> Q3 Sum (32 bit int)   % scaled by multiplying by 1000
> Q4 Sum (32 bit int)   % scaled by multiplying by 1000

The format of the .vec file, which is the converted file from .ccd data, is:

> Frame Count (16 bit unsigned int)
> Frame 1 Data (1024 32 bit signed values)
> ...
> Frame n Data (1024 32 bit signed values)

Only the .vec and .sec files could be recognized by the MATLAB routines for bulk processing. Therefore, file type conversion is a must. To use the "ConversionTool.exe", follow the following steps:

i) Open a "Command Prompt" window.

ii) Direct the path to where "ConversionTool.exe" is located. For example, it is located under the root directory of disk C:\, then input in the command line:

iii) > C:\ConversionTool.exe "C:\2011-06-20 data" (assuming data is also saved under the root directory of disk C:\).

iv) The program should then tell you it is converting the files and that they were successfully converted in to the original folder.

The following MATLAB routines and subfunctions are used to bulk convert the binary formatted .dtl, .sum and the converted .vec data files into summarized Excel files. It is important to *modify the routine according to any changes made to the data structures* as shown in APPENDIX B.

1. Main function: Hemolog.m

% Save binary Hemo log files (.vec,.dtl,.sum) into .xlsx with captions;
% Hemo Cycle Size means the number of CCD frames in a single Hemo cycle;
% Hemo Cycle Size can be found in the Hemo.cfg settings;
% Bin Deng 6/28/2010

```
function HemoLog()
clc;
clear all;

% Changed the current directory for Matlab
cd('C: \LighTouch Data\2011-06-20');

% Default Hemo Cycle Size is 3 sec, 20ms per frame, thus 150 frames
FramesPerCycle = 150;

Summary;
Detail_LT(FramesPerCycle);
CCD(FramesPerCycle);

msgbox('Conversion is done!')
end
```

2. Subfunction – Summary.m

```
% Subfunction for HemoLog.m
% Process of .sum for each Hemo experiment
% Based on v1.4 .sum file data structure
% Bin Deng 6/28/2010

function Summary

Files = dir('*.sum');

for n=1:length(Files);
    SumID = fopen(Files(n).name, 'r', 'ieee-le');
```

% the equation below is determined by the .sum file structure

% TotalHemoCycle = (SumCount-44)/32; % the number of Hemo cycles run for each experiment

```
FileRevisionTag = {fread(SumID,[1,4],'*char')}; % header for each .sum is '1VER'
HemoCycleCount = fread(SumID,1,'int32');
HemoCycleSize = fread(SumID,1,'int32'); % The number of CCD frames in each
Hemo cycle
ParaA = fread(SumID,1,'float32'); % The six parameters for the Hemocrit caculation
algorithm
ParaB = fread(SumID,1,'float32');
ParaC = fread(SumID,1,'float32');
ParaD = fread(SumID,1,'float32');
ParaE = fread(SumID,1,'float32');
ParaF = fread(SumID,1,'float32');
LaserPower = fread(SumID,1,'float32'); % in volts, can be convert to milliwatts
using the calibration curve
CcdExposureTime = fread(SumID,1,'float32'); % in milliseconds
```

```
% define the data space for all the variables
HemoCycleInstance = zeros(HemoCycleCount,1);
RBCVolume = zeros(HemoCycleCount,1);
PlasmaVolume = zeros(HemoCycleCount,1);
HctResult = zeros(HemoCycleCount,1);
CcdExposureTemp = zeros(HemoCycleCount,1);
IE0 = zeros(HemoCycleCount,1);
EE0 = zeros(HemoCycleCount,1);
BleachStatus = zeros(HemoCycleCount,1);
StabilityStatus = zeros(HemoCycleCount,1);
Unused1 = zeros(HemoCycleCount,1);
```

233

```
Unused2 = zeros(HemoCycleCount,1);


for i=1:HemoCycleCount;
    HemoCycleInstance(i,1) = fread(SumID,1,'int32');
    RBCVolume(i,1) = fread(SumID,1,'float32'); % RBC,plasma volume & Hct is the
average for each Hemo cycle
    PlasmaVolume(i,1) = fread(SumID,1,'float32');
    HctResult(i,1) = fread(SumID,1,'float32');
    CcdExposureTemp(i,1) = fread(SumID,1,'float32'); % in celsius
    IE0(i,1) = fread(SumID,1,'float32'); % IE0 & EE0 used for the Hct calculation
    EE0(i,1) = fread(SumID,1,'float32');
    BleachStatus(i,1) = fread(SumID,1,'bool'); % 1 is true, 0 is false
    StabilityStatus(i,1) = fread(SumID,1,'bool');
    Unused1(i,1) = fread(SumID,1,'*char'); % two unused variables for future
expension
    Unused2(i,1) = fread(SumID,1,'*char');
end


Title1 = {'File Revision Tag';'HemoCycleCount';'Hemo Cycle Size';'Parameter
A';'Parameter B';'Parameter C';'Parameter D';'Parameter E';'Parameter F';'Laser
Power';'CCD Exposure Time'};
Title2 = {'Hemo Cycle Instance' 'Red Blood Cell Volume' 'Plasma Volume' 'Hct
Result' 'CCD Exposure Temp' 'IE0 Value' 'EE0 Value' 'Bleach Status' 'Stability
Status' 'Unused_1' 'Unused_2'};
xlswrite([Files(n).name,'_summary','.xls'],Title1,[Files(n).name,'_summary'],'A1');
xlswrite([Files(n).name,'_summary','.xls'],FileRevisionTag,[Files(n).name,'_summar
y'],'B1');
xlswrite([Files(n).name,'_summary','.xls'],HemoCycleCount,[Files(n).name,'_summa
ry'],'B2');
xlswrite([Files(n).name,'_summary','.xls'],HemoCycleSize,[Files(n).name,'_summary
'],'B3');
```

234

```
xlswrite([Files(n).name,'_summary','.xls'],ParaA,[Files(n).name,'_summary'],'B4');
xlswrite([Files(n).name,'_summary','.xls'],ParaB,[Files(n).name,'_summary'],'B5');
xlswrite([Files(n).name,'_summary','.xls'],ParaC,[Files(n).name,'_summary'],'B6');
xlswrite([Files(n).name,'_summary','.xls'],ParaD,[Files(n).name,'_summary'],'B7');
xlswrite([Files(n).name,'_summary','.xls'],ParaE,[Files(n).name,'_summary'],'B8');
xlswrite([Files(n).name,'_summary','.xls'],ParaF,[Files(n).name,'_summary'],'B9');
xlswrite([Files(n).name,'_summary','.xls'],LaserPower,[Files(n).name,'_summary'],'B
10');
xlswrite([Files(n).name,'_summary','.xls'],CcdExposureTime,[Files(n).name,'_summ
ary'],'B11');
xlswrite([Files(n).name,'_summary','.xls'],Title2,[Files(n).name,'_summary'],'D1');
xlswrite([Files(n).name,'_summary','.xls'],HemoCycleInstance,[Files(n).name,'_sum
mary'],'D2');
xlswrite([Files(n).name,'_summary','.xls'],RBCVolume,[Files(n).name,'_summary'],'
E2');
xlswrite([Files(n).name,'_summary','.xls'],PlasmaVolume,[Files(n).name,'_summary'
],'F2');
xlswrite([Files(n).name,'_summary','.xls'],HctResult,[Files(n).name,'_summary'],'G2'
);
xlswrite([Files(n).name,'_summary','.xls'],CcdExposureTemp,[Files(n).name,'_summ
ary'],'H2');
xlswrite([Files(n).name,'_summary','.xls'],IE0,[Files(n).name,'_summary'],'I2');
xlswrite([Files(n).name,'_summary','.xls'],EE0,[Files(n).name,'_summary'],'J2');
xlswrite([Files(n).name,'_summary','.xls'],BleachStatus,[Files(n).name,'_summary'],'
K2');
xlswrite([Files(n).name,'_summary','.xls'],StabilityStatus,[Files(n).name,'_summary']
,'L2');
xlswrite([Files(n).name,'_summary','.xls'],Unused1,[Files(n).name,'_summary'],'M2');
xlswrite([Files(n).name,'_summary','.xls'],Unused2,[Files(n).name,'_summary'],'N2');
warning off MATLAB:xlswrite:AddSheet
```

```
fclose(SumID);
end
end
```

3. Subfunction – Detail.m

```
% Subfunction for HemoLog.m
% Process of .dtl for each Hemo Cycle
% Based on v1.4 .dtl data structure
% Bin Deng 12/10/2010


function Detail_CL(FramesPerCycle)


% define the data space for all .dtl variables
RBCVolume = zeros(FramesPerCycle,1);
PlasmaVolume = zeros(FramesPerCycle,1);
HctResult = zeros(FramesPerCycle,1);
QuadrantCount = zeros(FramesPerCycle,4);
Pressure = zeros(FramesPerCycle,1);
ContactArea = zeros(FramesPerCycle,1);
TP9 = zeros(FramesPerCycle,1);
TP10 = zeros(FramesPerCycle,1);


% get all the .dtl files
Files = dir('*.dtl');
TotalFrames = length(Files)* FramesPerCycle;


% define the data space for all the summary variables
HemoCycleInstanceAll = zeros(TotalFrames,1);
RBCVolumeAll = zeros(TotalFrames,1);
PlasmaVolumeAll = zeros(TotalFrames,1);
```

```
HctResultAll = zeros(TotalFrames,1);

PressureAll = zeros(TotalFrames,1);

ContactAreaAll = zeros(TotalFrames,1);

QuadrantCountAll = zeros(TotalFrames,4);

TP9All = zeros(TotalFrames,1);

TP10All = zeros(TotalFrames,1);


for n=1:length(Files);
    DtlID = fopen(Files(n).name, 'r', 'ieee-le');
    [DtlData, DtlCount] = fread(DtlID);


    Count = 12+28*FramesPerCycle; % calculate supposed total data bytes
    if DtlCount ~= Count; %
        errordlg('Wrong File Size: Please check Hemo Cycle Size','File Error');
    else
        DtlID = fopen(Files(n).name,'r','ieee-le'); % relocate the pointer to the begining
        FileRevisionTag = {fread(DtlID,[1,4],'char*1')}; % header for each .dtl is
'1VER'
        HemoCycleSize = fread(DtlID,1,'int32'); % HemoCycleSize should be equal to
FramesPerCycle
        HemoCycleInstance = fread(DtlID,1,'int32');
        for i=1:HemoCycleSize;
            RBCVolume(i,1) = fread(DtlID,1,'float32');
            PlasmaVolume(i,1) = fread(DtlID,1,'float32');
            HctResult(i,1) = fread(DtlID,1,'float32');
            Pressure(i,1) = fread(DtlID,1,'float32');
            ContactArea(i,1) = fread(DtlID, 1, 'float32');
            QuadrantCount(i,:) = fread(DtlID,[1,4],'*char');
            TP9(i,1) = fread(DtlID, 1, 'short');
            TP10(i,1) = fread(DtlID, 1, 'short');
```

237

```matlab
        k=(n-1)*HemoCycleSize+i;
        HemoCycleInstanceAll(k,1) = HemoCycleInstance;
        RBCVolumeAll(k,1) = RBCVolume(i,1);
        PlasmaVolumeAll(k, 1) = PlasmaVolume(i,1);
        HctResultAll(k,1) = HctResult(i,1);
        PressureAll(k,1) = Pressure(i,1);
        ContactAreaAll(k,1) = ContactArea(i,1);
        QuadrantCountAll(k,:) = QuadrantCount(i,:);
        TP9All(k,:) = TP9(i,1);
        TP10All(k,:) = TP10(i,1);
    end
  end


fclose(DtlID);


% Title1 = {'File Revision Tag' 'Hemo Cycle Size' 'Hemo Cycle Instance' 'Frame
Count' 'Red Blood Cell Volume' 'Plasma Volume' 'Hct Result' 'Pressure' 'Contact
Area' 'Quadrant Down' 'Quadrant Up' 'Quadrant Out' 'Quadrant In'};
% FrameCount = transpose(1:FramesPerCycle);
% xlswrite([Files(n).name,'.xls'],Title1,[Files(n).name],'A1');
% xlswrite([Files(n).name,'.xls'],FileRevisionTag,[Files(n).name],'A2');
% xlswrite([Files(n).name,'.xls'],HemoCycleSize,[Files(n).name],'B2');
% xlswrite([Files(n).name,'.xls'],HemoCycleInstance,[Files(n).name],'C2');
% xlswrite([Files(n).name,'.xls'],FrameCount,[Files(n).name],'D2');
% xlswrite([Files(n).name,'.xls'],RBCVolume,[Files(n).name],'E2');
% xlswrite([Files(n).name,'.xls'],PlasmaVolume,[Files(n).name],'F2');
% xlswrite([Files(n).name,'.xls'],HctResult,[Files(n).name],'G2');
% xlswrite([Files(n).name,'.xls'],Pressure,[Files(n).name],'H2');
% xlswrite([Files(n).name,'.xls'],ContactArea,[Files(n).name],'I2');
% xlswrite([Files(n).name,'.xls'],QuadrantCount,[Files(n).name],'J2');
warning off MATLAB:xlswrite:AddSheet
```

```
    end


    Title2 = {'Hemo Cycle Instance' 'Frame' 'RBC Volume' 'Plasma Volume'
    'Hematocrit' 'BV' 'RBC' 'TP9' 'TP10'};
    FrameCount2 = transpose(1:TotalFrames);
    xlswrite(['Frame by Frame Summary','.xlsx'],Title2,['Hct'],'A1');
    xlswrite(['Frame by Frame Summary','.xlsx'],HemoCycleInstanceAll,['Hct'],'A2');
    xlswrite(['Frame by Frame Summary','.xlsx'],FrameCount2,['Hct'],'B2');
    xlswrite(['Frame by Frame Summary','.xlsx'],RBCVolumeAll,['Hct'],'C2');
    xlswrite(['Frame by Frame Summary','.xlsx'],PlasmaVolumeAll,['Hct'],'D2');
    xlswrite(['Frame by Frame Summary','.xlsx'],HctResultAll,['Hct'],'E2');
    xlswrite(['Frame by Frame Summary','.xlsx'],TP9All,['Hct'],'H2');
    xlswrite(['Frame by Frame Summary','.xlsx'],TP10All,['Hct'],'I2');


    Title3 = {'Hemo Cycle Instance' 'Frame' 'Pressure' 'Contact Area' 'Quadrant Down'
    'Quadrant Up' 'Quadrant Out' 'Quadrant In'};
    xlswrite(['Frame by Frame Summary','.xlsx'],Title3,['PDPM'],'A1');
    xlswrite(['Frame by Frame Summary','.xlsx'],HemoCycleInstanceAll,['PDPM'],'A2');
    xlswrite(['Frame by Frame Summary','.xlsx'],FrameCount2,['PDPM'],'B2');
    xlswrite(['Frame by Frame Summary','.xlsx'],PressureAll,['PDPM'],'C2');
    xlswrite(['Frame by Frame Summary','.xlsx'],ContactAreaAll,['PDPM'],'D2');
    xlswrite(['Frame by Frame Summary','.xlsx'],QuadrantCountAll,['PDPM'],'E2');


    end
```

4. Subfunction -- CCD.m

```
    % Subfunction for HemoLog.m
    % Process of .ccd files for each Hemo Cycle
```

```
% .ccd needed to be converted to .vec file using the conversion tool first!!
% Excel 2003: max rows = 65,536; max columns = 256
% Excel 2007: max rows = over 1 million; max columns = 16,384
% Bin Deng 6/28/2010

function CCD(FramesPerCycle)

% get all the .vec files
Files = dir('*.vec');
TotalFrames = length(Files)* FramesPerCycle;

% define BV and RBV start and end cell (.cfg number +1)
% the following sets of params are for the old LT system
BVStart = 401;
BVEnd = 926;
RBCStart = 96;
RBCEnd = 105;

% the following sets of params are for the new Hct-1 system
% BVStart = 226;
% BVEnd = 701;
% RBCStart = 98;
%RBCEnd = 104;

% define the data space for all the summary variables
BV = zeros(FramesPerCycle,1);
RBC = zeros(FramesPerCycle,1);
BVAll = zeros(TotalFrames,1);
RBCAll = zeros(TotalFrames,1);

for n=1:length(Files);
```

```matlab
    CcdID = fopen(Files(n).name, 'r', 'ieee-le');
    HemoCycleSize = fread(CcdID, 1, 'uint16');
        if  HemoCycleSize ~= FramesPerCycle; %
            errordlg('Wrong File Size: Please check Hemo Cycle Size','File Error');
        else
            CcdData = fread(CcdID,[1024,HemoCycleSize],'int32');
            for i=1:HemoCycleSize;
                BV(i,1) = sum(CcdData(BVStart:BVEnd,i));
                RBC(i,1) = sum(CcdData(RBCStart:RBCEnd,i));


                k=(n-1)*HemoCycleSize+i;


                BVAll(k,1) = BV(i,1);
                RBCAll(k, 1) = RBC(i,1);
            end
        end
        fclose(CcdID);


        %Title = {'Frame Count' 'BV' 'RBC'};
        %FrameCount = transpose(0:FramesPerCycle-1);
        %xlswrite([Files(n).name,'.xls'],Title,[Files(n).name],'A1');
        %xlswrite([Files(n).name,'.xls'],FrameCount,[Files(n).name],'A2');
        %xlswrite([Files(n).name,'.xls'],BV,[Files(n).name],'B2');
        %xlswrite([Files(n).name,'.xls'],RBC,[Files(n).name],'C2');
end

xlswrite(['Frame by Frame Summary','.xlsx'],BVAll,['Hct'],'F2');
xlswrite(['Frame by Frame Summary','.xlsx'],RBCAll,['Hct'],'G2');

% Wavelength Calibration using 5th order polynomial
% y0,A1,A2,A3,A4,A5 can be found in .cfg file
```

```
% UPDATE whenever new calibration is made
% PixelNumber = transpose(0:1023);
% y0 = -392.516970725087;
% A1 = 4.43554354246831;
% A2 = -0.00710683854527714;
% A3 = 1.91473348286739E-5;
% A4 = -2.74128188255463E-8;
% A5 = 1.5003258140181E-11;
% RamanShift =
y0+A1*PixelNumber+A2*PixelNumber.^2+A3*PixelNumber.^3+A4*PixelNumber
.^4+A5*PixelNumber.^5;

% Title = {'Pixel Number' 'Raman Shift' 'Raw CCD Counts'};
% xlswrite([fName,'.xls'],Title,[fName,'_CCD'],'A1');
% xlswrite([fName,'.xls'],PixelNumber,[fName,'_CCD'],'A2');
% xlswrite([fName,'.xls'],RamanShift,[fName,'_CCD'],'B2');
% xlswrite([fName,'.xls'],CcdData,[fName,'_CCD'],'C2');
warning off MATLAB:xlswrite:AddSheet

end
```

These routines can also be revised in multiple ways to bulk convert the .ccd and .sen files generated under "Glucose" mode. Since only minimal changes are needed in order to do so, redundant codes will not be included in this appendix.

REFERENCES

1. B. T. Andrews, *Intensive care in neurosurgery*, Thieme ; Ill. : American association of neurological surgeons, New York [etc.]; Rolling Meadows (2003).

2. W. Lippincott and Wilkins, *Handbook of diseases*, Lippincott Williams & Wilkins, Springhouse, Pa. (2003).

3. C. Cothren, E. Moore, H. Hedegaard and K. Meng, "Epidemiology of Urban Trauma Deaths: A Comprehensive Reassessment 10 Years Later," *World Journal of Surgery* **31**(7), 1507-1511 (2007)

4. A. Sauaia, F. A. Moore, E. E. Moore, K. S. Moser, R. Brennan, R. A. Read and P. T. Pons, "Epidemiology of trauma deaths: a reassessment," *The Journal of trauma* **38**(2), 185-193 (1995)

5. L. C. Cancio, A. I. Batchinsky, J. Salinas, T. Kuusela, V. A. Convertino, C. E. Wade and J. B. Holcomb, "Heart-Rate Complexity for Prediction of Prehospital Lifesaving Interventions in Trauma Patients," *The Journal of Trauma: Injury, Infection, and Critical Care The Journal of Trauma: Injury, Infection, and Critical Care* **65**(4), 813-819 (2008)

6. M. Martin, J. Oh, H. Currier, N. Tai, A. Beekley, M. Eckert and J. Holcomb, "An Analysis of In-Hospital Deaths at a Modern Combat Support Hospital," *The Journal of Trauma: Injury, Infection, and Critical Care The Journal of Trauma: Injury, Infection, and Critical Care* **66**(Supplement), S51-S61 (2009)

7. V. V. Tuchin, *Tissue Optics: Light Scattering Methods and Instruments for Medical Diagnosis*, SPIE PRESS, Bellingham, WA (2000).

8. V. V. Tuchin, *Optical clearing of tissues and blood*, SPIE PRESS, Bellingham, WA (2005).

9. V. V. Tuchin, *Handbook of optical sensing of glucose in biological fluids and tissues*, CRC PRESS, Taylor & Francis Group, Boca Raton, FL (2008).

10. J. Chaiken and J. Goodisman, "On probing human fingertips in vivo using near-infrared light: model calculations," *J Biomed Opt* **15**(3), 037007 (2010)

11. M. A. Arnold and G. W. Small, "Noninvasive glucose sensing," *Anal Chem* **77**(17), 5429-5439 (2005)

12. O. S. Khalil, "Spectroscopic and clinical aspects of noninvasive glucose measurements," *Clin Chem* **45**(2), 165-177 (1999)

13. R. R. Anderson and J. A. Parrish, "THE OPTICS OF HUMAN-SKIN," *Journal of Investigative Dermatology* **77**(1), 13-19 (1981)

14. R. R. Anderson, *Optics of the Skin*, Marcel Dekker, New York (1993).

15. A. K. Amerov, J. Chen, G. W. Small and M. A. Arnold, "Scattering and absorption effects in the determination of glucose in whole blood by near-infrared spectroscopy," *Anal Chem* **77**(14), 4587-4594 (2005)

16. M. A. Arnold and J. T. Olesberg, "Method for generating a net analyte signal calibration model and uses thereof," U. S. P. Application, Ed., p. 20, United States (2006).

17. K. Maquelin, C. Kirschner, L. P. Choo-Smith, N. van den Braak, H. P. Endtz, D. Naumann and G. J. Puppels, "Identification of medically relevant microorganisms by vibrational spectroscopy," *Journal of Microbiological Methods* **51**(3), 255-271 (2002)

18. L. P. Choo-Smith, H. G. Edwards, H. P. Endtz, J. M. Kros, F. Heule, H. Barr, J. S. Robinson, H. A. Bruining and G. J. Puppels, "Medical applications of Raman spectroscopy: from proof of principle to clinical implementation.," *Biopolymers* **67**(1), 1-9 (2002)

19. K. Maquelin, L. P. Choo-Smith, H. P. Endtz, H. A. Bruining and G. J. Puppels, "Rapid identification of Candida species by confocal Raman microspectroscopy.," *J Clin Microbiol* **40**(2), 594-600 (2002)

20. P. J. Caspers, G. W. Lucassen and G. J. Puppels, "Combined in vivo confocal Raman spectroscopy and confocal microscopy of human skin," *Biophysical journal* **85**(1), 572-580 (2003)

21. B. R. Wood, P. Caspers, G. J. Puppels, S. Pandiancherri and D. McNaughton, "Resonance Raman spectroscopy of red blood cells using near-infrared laser excitation," *Anal Bioanal Chem* **387**(5), 1691-1703 (2007)

22. B. W. de Jong, T. C. Schut, K. Maquelin, T. van der Kwast, C. H. Bangma, D. J. Kok and G. J. Puppels, "Discrimination between nontumor bladder tissue and tumor by Raman spectroscopy.," *Anal Chem* **78**(22), 7761-7769 (2006)

23. I. Barman, G. P. Singh, R. R. Dasari and M. S. Feld, "Turbidity-Corrected Raman Spectroscopy for Blood Analyte Detection," *ANALYTICAL CHEMISTRY - WASHINGTON DC-* **81**(11), 4233-4240 (2009)

24. I. Barman, C. R. Kong, G. P. Singh, R. R. Dasari and M. S. Feld, "Accurate Spectroscopic Calibration for Noninvasive Glucose Monitoring by Modeling the Physiological Glucose Dynamics," *Analytical Chemistry* **82**(14), 6104-6114 (2010)

25. I. Barman, C. R. Kong, N. C. Dingari, R. R. Dasari and M. S. Feld, "Development of Robust Calibration Models Using Support Vector Machines for Spectroscopic Monitoring of Blood Glucose," *Analytical Chemistry* **82**(23), 9719-9726 (2010)

26. M. V. Schulmerich, K. A. Dooley, M. D. Morris, T. M. Vanasse and S. A. Goldstein, "Transcutaneous fiber optic Raman spectroscopy of bone using annular illumination and a circular array of collection fibers.," *J Biomed Opt* **11**(6), 060502 (2006)

27. A. Carden, R. M. Rajachar, M. D. Morris and D. H. Kohn, "Ultrastructural changes accompanying the mechanical deformation of bone tissue: a Raman imaging study.," *Calcif Tissue Int* **72**(2), 166-175 (2003)

28. N. J. Crane, V. Popescu, M. D. Morris, P. Steenhuis and M. A. Ignelzi, "Raman spectroscopic evidence for octacalcium phosphate and other transient mineral species deposited during intramembranous mineralization.," *Bone* **39**(3), 434-442 (2006)

29. E. M. Kanter, E. Vargis, S. Majumder, M. D. Keller, E. Woeste, G. G. Rao and A. Mahadevan-Jansen, "Application of Raman spectroscopy for cervical dysplasia diagnosis,"

30. A. Mahadevan-Jansen, K. Mariapphan and P. Konrad, "Methods and devices for optical stimulation of neural tissues," p. 16, Vanderbilt University, United States (2005).

31. C. P. Richter, A. I. Matic, J. D. Wells, E. D. Jansen and J. T. Walsh, "Neural stimulation with optical radiation," *Laser Photonics Reviews* **5**(1), 12 (2011)

32. R. L. McCreery, *Raman spectroscopy for chemical analysis*, John Wiley & Sons, New York (2000).

33. ADA, "Diabetes Statistics," http://www.diabetes.org/diabetes-basics/diabetes-statistics/?loc=DropDownDB-stats (2011).

34. O. S. Khalil, "Non-invasive glucose measurement technologies: an update from 1999 to the dawn of the new millennium," *Diabetes technology & therapeutics* **6**(5), 660-697 (2004)

35. A. Tura, A. Maran and G. Pacini, "Non-invasive glucose monitoring: Assessment of technologies and devices according to quantitative criteria," *Diabetes Research and Clinical Practice* **77**(1), 16-40 (2007)

36. K. Rebrin and G. M. Steil, "Can interstitial glucose assessment replace blood glucose measurements?," *Diabetes technology & therapeutics* **2**(3), 461-472 (2000)

37. H. W. Vesper, P. M. Wang, E. Archibold, M. R. Prausnitz and G. L. Myers, "Assessment of trueness of a glucose monitor using interstitial fluid and whole blood as specimen matrix," *Diabetes technology & therapeutics* **8**(1), 76-80 (2006)

38. S. J. Yeh, C. F. Hanna and O. S. Khalil, "Monitoring blood glucose changes in cutaneous tissue by temperature-modulated localized reflectance measurements," *Clinical chemistry* **49**(6), 924-934 (2003)

39. K. Kajiwara, T. Uemura, H. Kishikawa, K. Nishida, Y. Hashiguchi, M. Uehara, M. Sakakida, K. Ichinose and M. Shichiri, "Noninvasive measurement of blood glucose concentrations by analysing Fourier transform infra-red absorbance spectra through oral mucosa," *Medical & biological engineering & computing* **31**(17-22 (1993)

40. S. F. Malin, T. L. Ruchti, T. B. Blank, S. N. Thennadil and S. L. Monfre, "Noninvasive prediction of glucose by near-infrared diffuse reflectance spectroscopy," *Clinical chemistry* **45**(9), 1651-1658 (1999)

41. P. Williams, *Gray's anatomy*, Chuichill Livingston, New York (1999).

42. C. Lentner, *Geigy Scientific Tables Vol. 3: Physical Chemistry, Composition of Blood, Hematology, Somatometric Data*, CIBA-GEIGY, West Caldwell, NJ (1984).

43. W. J. Cliff, *Blood vessels*, Cambridge University Press, Cambridge, United Kingdom of Great Britain (1976).

44. D. Van Wynsberghe, C. R. Noback and R. Carola, *Human anatomy and physiology*, McGraw-Hill, New York (1995).

45. J. Chaiken, W. F. Finney, K. P. Peterson, C. M. Peterson, P. E. Knudson, R. S. Weinstock and P. Lein, "Noninvasive in-vivo near-infrared vibrational spectroscopic study of lipid and aqueous phases of skin and near-surface tissues," *Proceedings of SPIE* 3907), 89-97 (2000)

46. J. Chaiken, W. F. Finney, C. M. Peterson, K. P. Peterson, P. E. Knudson, R. S. Weinstock and P. Lein, "Noninvasive in-vivo tissue-modulated near-infrared

vibrational spectroscopic study of mobile and static tissues: blood chemistry," *Proceedings of SPIE* 3918), 135-145 (2000)

47. J. Chaiken, W. F. Finney, P. E. Knudson, K. P. Peterson, C. M. Peterson, X. Yang and R. S. Weinstock, "Noninvasive blood analysis by tissue-modulated NIR Raman spectroscopy," *Proceedings of SPIE* 4368), 134-145 (2001)

48. J. Chaiken, W. F. Finney, P. E. Knudson, K. P. Peterson, C. M. Peterson, X. Yang and R. S. Weinstock, "Noninvasive in-vivo tissue-modulated Raman spectroscopy of human blood: microcirculation and viscosity effects," *Proceedings of SPIE* 4254), 106-118 (2001)

49. J. Chaiken, W. F. Finney, P. E. Knudson, K. P. Peterson, C. M. Peterson, R. S. Weinstock and D. Hagrman, "Progress in the noninvasive in-vivo tissue-modulated Raman spectroscopy of human blood," *Proceedings of SPIE* 4254), 216-227 (2001)

50. J. Chaiken, W. Finney, P. E. Knudson, R. S. Weinstock, M. Khan, R. J. Bussjager, D. Hagrman, P. Hagrman, Y. Zhao, C. M. Peterson and K. Peterson, "Effect of hemoglobin concentration variation on the accuracy and precision of glucose analysis using tissue modulated, noninvasive, in vivo Raman spectroscopy of human blood: a small clinical study," *J Biomed Opt* **10**(3), 031111 (2005)

51. J. Chaiken, K. Ellis, P. Eslick, L. Piacente and E. Voss, "Noninvasive in vivo tissue and pulse modulated Raman spectroscopy of human capillary blood and plasma," *Proceedings of SPIE* 6093), 609305 (2006)

52. B. D. Beier and A. J. Berger, "Method for automated background subtraction from Raman spectra containing known contaminants.," *Analyst* **134**(6), 1198-1202 (2009)

53. C. A. Lieber and A. Mahadevan-Jansen, "Automated method for subtraction of fluorescence from biological Raman spectra," *Appl Spectrosc* **57**(11), 1363-1367 (2003)

54. W. F. Finney, "Noninvasive in vivo tissue modulated quantitative Raman spectroscopy of human blood," in ProQuest Dissertations and Theses, p. 311 p., Syracuse University, United States -- New York (2002).

55. J. J. Burmeister and M. A. Arnold, "Evaluation of measurement sites for noninvasive blood glucose sensing with near-infrared transmission spectroscopy," *Clin Chem* **45**(9), 1621-1627 (1999)

56. S. Prahl, "Tabulated molar extinction coefficient for hemoglobin in water," M. R. C. L. compiled by Scott Prahl using data from W. B. Gratzer, Holly Hill, London, and N. Kollias, Wellman Laboratories, Harvard Medical School, Boston, Ed., Oregon Medical Laser Center, Portland, Oregon (1998).

57. R. R. Anderson and J. A. Parrish, "The Optics Of Human Skin," *Journal of Investigative Dermatology* **77**(1), 13-19 (1981)

58. K. A. Pasyk, S. V. Thomas, C. A. Hassett, G. W. Cherry and R. Faller, "Regional differences in capillary density of the normal human dermis," *Plast Reconstr Surg* **83**(6), 939-945; discussion 946-937 (1989)

59. S. I. Yum and J. Roe, "Capillary blood sampling for self-monitoring of blood glucose," *Diabetes Technol Ther* **1**(1), 29-37 (1999)

60. G. Von Hagen, "Body Worlds: the original exhibition of real human bodies," http://www.plastination-products.com/Blood-vessel-configuration/Human-blood-vessel-configuration/Art-objects/Blood-vessel-configuration-of-a-human-hand::1620.html.

61. L. A. Jones and S. J. Lenderman, *Human hand function*, Oxford University Press, Inc., New York, New York (2006).

62. V. V. Tuchin, *Tissue Optics: Light Scattering Methods and Instruments for Medical Diagnosis*, SPIE PRESS, Bellingham, WA (2007).

63. A. J. Jaap, A. C. Shore, A. J. Stockman and J. E. Tooke, "Skin capillary density in subjects with impaired glucose tolerance and patients with type 2 diabetes," *Diabet Med* **13**(2), 160-164 (1996)

64. A. M. Enejder, T. G. Scecina, J. Oh, M. Hunter, W. C. Shih, S. Sasic, G. L. Horowitz and M. S. Feld, "Raman spectroscopy for noninvasive glucose measurements," *J Biomed Opt* **10**(3), 031114 (2005)

65. G. C. Holst, *CCD Arrays, Cameras, and Displays*, JCD Publishing (1998).

66. J. Chaiken, E. Voss, R. J. Bussjager and G. Shaheen, "Towards an improved assignment of spectral features in tissue modulated non-invasive Raman spectroscopy of human fingertips," *Proceedings of SPIE* 6430), 643004 (2007)

67. J. Chaiken and C. M. Peterson, "Method for determining lipid and protein content of tissue," LighTouch Medical, Inc., United States (2002).

68. H. F. a. E. Society, "Definition of Human Factors and Ergonomics," http://www.hfes.org/Web/EducationalResources/HFEdefinitionsmain.html.

69. S. J. Barker, ""Motion-resistant" pulse oximetry: a comparison of new and old models," *Anesth Analg* **95**(4), 967-972, table of contents (2002)

70. Masimo, "Signal extraction technology (SET)," M. Corporation, Ed., http://www.masimo.com/pdf/whitepaper/LAB1035R.PDF (2002).

71. U. S. FDA, "General Human Factors Information and Resources," http://www.fda.gov/MedicalDevices/DeviceRegulationandGuidance/HumanFactors/ucm124829.htm (2012).

72. D. Ashbaugh, "Friction skin anatomy," http://ridgesandfurrows.homestead.com/friction_skin.html (2004).

73. P. C. Burridge, "Question of fingerprints," in NZ Security, New Zealand (2002).

74. H. N. Ho and L. A. Jones, "Modeling the thermal responses of the skin surface during hand-object interactions," *J Biomech Eng* **130**(2), 021005 (2008)

75. O. Jay and G. Havenith, "Differences in finger skin contact cooling response between an arterial occlusion and a vasodilated condition," *J Appl Physiol* **100**(5), 1596-1601 (2006)

76. S. A. Mascaro and H. H. Asada, "Measurement of finger posture and three-axis fingertip touch force using fingernail sensors," *Robotics and Automation, IEEE Transactions on* **20**(1), 26-35 (2004)

77. S. A. Mascaro and H. H. Asada, "The common patterns of blood perfusion in the fingernail bed subject to fingertip touch force and finger posture," *Haptics-e: the Electronic Journal of Haptics Research* **4**(3), 1-6 (2006)

78. J. D. Bronzino, *Medical devices and systems*, CRC Press, Boca Raton, FL (2006).

79. K. Brandis, "Fluid Physiology," http://www.anaesthesiamcq.com/FluidBook/index.php.

80. J. Chaiken, B. Deng, J. Goodisman, G. Shaheen and R. J. Bussjager, "Analyzing near-infrared scattering from human skin to monitor changes in hematocrit," *J Biomed Opt* **16**(9), 097005 (2011)

81. J. Chaiken, J. Goodisman, B. Deng, R. J. Bussjager and G. Shaheen, "Simultaneous, noninvasive observation of elastic scattering, fluorescence and inelastic scattering as a monitor of blood flow and hematocrit in human fingertip capillary beds," *J Biomed Opt* **14**(5), 050505 (2009)

82. I. Barman, G. P. Singh, R. R. Dasari and M. S. Feld, "Turbidity-Corrected Raman Spectroscopy for Blood Analyte Detection," *Analytical Chemistry* **81**(11), 4233-4240 (2009)

83. R. Steponavicius and S. N. Thennadil, "Extraction of chemical information of suspensions using radiative transfer theory to remove multiple scattering effects: application to a model two-component system," *Anal Chem* **81**(18), 7713-7723 (2009)

84. C. Reble, I. Gersonde, C. A. Lieber and J. Helfmann, "Influence of tissue absorption and scattering on the depth dependent sensitivity of Raman fiber probes investigated by Monte Carlo simulations," *Biomed Opt Express* **2**(3), 520-533 (2011)

85. J. R. Lakowicz, *Principles of fluorescence spectroscopy*, Springer, New York, NY (2006).

86. E. Salomatina, B. Jiang, J. Novak and A. N. Yaroslavsky, "Optical properties of normal and cancerous human skin in the visible and near-infrared spectral range," *J Biomed Opt* **11**(6), 064026 (2006)

87. M. Meinke, G. Müller, J. Helfmann and M. Friebel, "Optical properties of platelets and blood plasma and their influence on the optical behavior of whole blood in the visible to near infrared wavelength range," *J Biomed Opt* **12**(1), 014024 (2007)

88. S. L. Jacques, "Origins of tissue optical properties in the UVA, Visible, and NIR regions," in OSA TOPS on Advances in Optical Imaging and Photon Migration R. R. Alfano and J. G. Fujimoto, Eds., pp. 364–369, Optical Society of America, Washington, D.C. (1996).

89. C. D. Forbes and G. D. O. Lowe, *Physics in Medicine and Biology Encyclopedia*, Pergammon Press, New York (1986).

90. J. Chaiken, "Laser chemistry of organometallic species: conceptual framework and overview," in *Laser chemistry of organometallics* J. Chaiken, Ed., American Chemical Society, Washington, DC (1993).

91. H. Zeng, C. MacAulay, D. I. McLean, B. Palcic and H. Lui, "The dynamics of laser-induced changes in human skin autofluorescence--experimental measurements and theoretical modeling," *Photochem Photobiol* **68**(2), 227-236 (1998)

92. B. Deng, C. Wright, E. Lewis-Clark, G. Shaheen, R. Geier and J. Chaiken, "Direct noninvasive observation of near-infrared photobleaching of autofluorescence in human volar side fingertips in vivo," *Proceedings of SPIE* 7560), 75600P (2010)

93. I. Barman, C. R. Kong, G. P. Singh and R. R. Dasari, "Effect of photobleaching on calibration model development in biological Raman spectroscopy," *J Biomed Opt* **16**(1), 011004 (2011)

94. S. Gupta, Bhawna, P. Goswami, A. Agarwal and A. Pradhan, "Experimental and theoretical investigation of fluorescence photobleaching and recovery in human breast tissue and tissue phantoms," *Appl Opt* **43**(5), 1044-1052 (2004)

95. K. Golcuk, G. S. Mandair, A. F. Callender, N. Sahar, D. H. Kohn and M. D. Morris, "Is photobleaching necessary for Raman imaging of bone tissue using a green laser?," *Biochimica et Biophysica Acta* **1758**(868-873 (2006)

96. B. Deng, A. Simental, P. Lutz, G. Shaheen and J. Chaiken, "Singlet oxygen induced advanced glycation end-product photobleaching of in vivo human fingertip autofluorescence," in Biomedical Vibrational SpectroscopyV: Advances in Research and Industry A. Mahadevan-Jansen and W. Petrich, Eds., p. 82190D, Proceedings of SPIE, San Francisco, CA (2012).

97. T. Schlosser, K. Pagonidis, C. U. Herborn, P. Hunold, K. U. Waltering, T. C. Lauenstein and J. Barkhausen, "Assessment of left ventricular parameters using 16-MDCT and new software for endocardial and epicardial border delineation," *AJR Am J Roentgenol* **184**(3), 765-773 (2005)

98. G. F. Birchard, "Optimal hematocrit: theory, regulation and implications," *Amer. Zool.* **37**(65-72 (1997)

99. J. K. Leypoldt, A. K. Cheung, R. R. Steuer, D. H. Harris and J. M. Conis, "Determination of circulating blood volume by continuously monitoring hematocrit during hemodialysis," *J Am Soc Nephrol* **6**(2), 214-219 (1995)

100. M. Nogawa, S. Tanaka and K. Yamakoshi, "Development of an optical arterial hematocrit measurement method: pulse hematometry," *Conf Proc IEEE Eng Med Biol Soc* **3**(2634-2636 (2005)

101. G. Yoon and K. J. Jeon, "Noninvasive hematocrit monitoring based on parameter-optimization of a LED finger probe," *J. Opt. Soc. Korea* **9**(107-110 (2005)

102. B. Y. Creer, H. A. Smedel and R. C. Wingrove, "Centrifuge study of pilot tolerance to acceleration and effects of acceleration on pilot performance," NASA Tech. Note No. D-337, NASA, Washington, DC (1960).

103. A. M. Lardi, C. Hirst, A. J. Mortimer and C. N. McCollum, "Evaluation of the HemoCue for measuring intra-operative haemoglobin concentrations: a comparison with the Coulter Max-M," *Anaesthesia* **53**(4), 349-352 (1998)

104. H. Gehring, C. Hornberger, L. Dibbelt, A. Rothsigkeit, K. Gerlach, J. Schumacher and P. Schmucker, "Accuracy of point-of-care-testing (POCT) for determining hemoglobin concentrations," *Acta Anaesthesiol Scand* **46**(8), 980-986 (2002)

105. Hema Metrics, "Crit-Line hematocrit accuracy," Hema Metrics[TM] Tech Note (2003).

106. J. M. Fritsch-Yelle, V. A. Convertino and T. T. Schlegel, "Acute manipulations of plasma volume alter arterial pressure responses during Valsalva maneuvers," *J Appl Physiol* **86**(6), 1852-1857 (1999)

107. M. J. Noordzij, J. D. Lefrandt, R. Graaff and A. J. Smit, "Dermal factors influencing measurement of skin autofluorescence," *Diabetes Technol Ther* **13**(2), 165-170 (2011)

108. V. V. Tuchin, "Light scattering study of tissues," *Physics-Uspekhi* **40**(5), (1997)

109. S. K. Grandhee and V. M. Monnier, "Mechanism of formation of the Maillard protein cross-link pentosidine. Glucose, fructose, and ascorbate as pentosidine precursors," *J Biol Chem* **266**(18), 11649-11653 (1991)

110. E. Gebel, "High blood glucose and diabetes complications: the buildup of molecules known as AGEs may be the key link," *Diabetes Forecast* **63**(2), (2010)

111. J. Blackwell, K. M. Katika, L. Pilon, K. M. Dipple, S. R. Levin and A. Nouvong, "In vivo time-resolved autofluorescence measurements to test for glycation of human skin," *J Biomed Opt* **13**(1), 014004 (2008)

112. B. D. Beier and A. J. Berger, "Method for automated background subtraction from Raman spectra containing known contaminants," *Analyst* **134**(6), 1198-1202 (2009)

113. T. Saxena, B. Deng, D. Stelzner, J. Hasenwinkel and J. Chaiken, "Raman spectroscopic investigation of spinal cord injury in a rat model," *J Biomed Opt* **16**(2), 027003 (2011)

114. M. J. Goetz, G. L. Coté, R. Erckens, W. March and M. Motamedi, "Application of a multivariate technique to Raman spectra for quantification of body chemicals," *IEEE Trans Biomed Eng* **42**(7), 728-731 (1995)

115. H. Iwata, S. Nishio, M. Yokoyama, A. Matsumoto and M. Takeuchi, "Solubility of uric acid and supersaturation of monosodium urate: why is uric acid so highly soluble in urine?," *J Urol* **142**(4), 1095-1098 (1989)

116. I. R. Lewis and H. G. M. Edwards, *Handbook of Raman spectroscopy: from the research laboratory to the process line*, Marcel Dekker, Inc., New York (2001).

117. Z. Huang, H. Lui, X. K. Chen, A. Alajlan, D. I. McLean and H. Zeng, "Raman spectroscopy of in vivo cutaneous melanin," *J Biomed Opt* **9**(6), 1198-1205 (2004)

118. Z. Matuszak and M. Wasilewska-Radwanska, "Optical properties of melanin solutions, estimation of polymer particles size," in Symposium on Photonics Technologies for 7th Framework Program A. Popiolek-Masajada, Ed., pp. 533-537, Oficyna Wydawnicza Politechniki Wroclawskiej, Wroclaw, Poland (2006).

119. B. G. Frushour and J. L. Koenig, "Raman scattering of collagen, gelatin, and elastin," *Biopolymers* **14**(2), 379-391 (1975)

120. R. Drezek, A. Dunn and R. Richards-Kortum, "Light scattering from cells: finite-difference time-domain simulations and goniometric measurements," *Appl Opt* **38**(16), 3651-3661 (1999)

121. B. R. Masters, P. T. So and E. Gratton, "Multiphoton excitation fluorescence microscopy and spectroscopy of in vivo human skin," *Biophys J* **72**(6), 2405-2412 (1997)

122. H. G. Breunig, H. Studier and K. König, "Multiphoton excitation characteristics of cellular fluorophores of human skin in vivo," *Opt Express* **18**(8), 7857-7871 (2010)

123. P. Kayatz, G. Thumann, T. T. Luther, J. F. Jordan, K. U. Bartz-Schmidt, P. J. Esser and U. Schraermeyer, "Oxidation causes melanin fluorescence," *Invest Ophthalmol Vis Sci* **42**(1), 241-246 (2001)

124. J. Riesz, J. Gilmore and P. Meredith, "Quantitative scattering of melanin solutions," *Biophys J* **90**(11), 4137-4144 (2006)

125. M. Scholz, G. Stankovic, G. Seewald and D. Leupold, "Uncovering of melanin fluorescence in human skin tissue," *Proceedings of SPIE - OSA Biomedical Optics* **6633**(663321 (2007)

126. A. Slominski, D. J. Tobin, S. Shibahara and J. Wortsman, "Melanin pigmentation in mammalian skin and its hormonal regulation," *Physiol Rev* **84**(4), 1155-1228 (2004)

127. B. R. Wood, L. Hammer, L. Davis and D. McNaughton, "Raman microspectroscopy and imaging provides insights into heme aggregation and denaturation within human erythrocytes," *J Biomed Opt* **10**(1), 14005 (2005)

128. S. Franzen, S. E. Wallace-Williams and A. P. Shreve, "Heme charge-transfer band III is vibronically coupled to the Soret band," *J Am Chem Soc* **124**(24), 7146-7155 (2002)

129. L. Chen, J. Y. Hu and S. Q. Wang, "The role of antioxidants in photoprotection: A critical review," *J Am Acad Dermatol* (2012)

130. S. Ramstad, N. Le Anh-Vu and A. Johnsson, "The temperature dependence of porphyrin production in Propionibacterium acnes after incubation with 5-aminolevulinic acid (ALA) and its methyl ester (m-ALA)," *Photochem Photobiol Sci* **5**(1), 66-72 (2006)

131. M. Zandomeneghi, C. Festa, C. Angelletti, G. Menconi, T. Sicuro and I. Cozzani, "Detection of near-infrared porphyrin fluorescence excited in experimental animal tumour by the HeNe laser," *Lasers in Medical Science* **3**(1), 3 (1988)

132. H. Ou-Yang, G. Stamatas and N. Kollias, "Spectral responses of melanin to ultraviolet A irradiation," *J Invest Dermatol* **122**(2), 492-496 (2004)

133. G. Goerz, A. Link-Mannhardt, K. Bolsen, M. Zumdick, C. Fritsch and N. Y. Schürer, "Porphyrin concentrations in various human tissues," *Exp Dermatol* **4**(4 Pt 1), 218-220 (1995)

134. H. Liu, C. Macaulay, H. Zeng, D. I. Mclean and R. Bissonnette, "Photoacitivation of endogenous porphyrins for treatment of psoriasis," p. 22, The University of British Columbia, USA (2001).

135. N. Kollias, B. Choi, H. Zeng, R. S. Malek, B. J. Wong, J. F. R. Ilgner, K. W. Gregory, G. J. Tearney, L. Marcu, H. Hirschberg and S. J. Madsen, "Fluorescence spectroscopy for endogenous porphyrins in human facial skin," in Photonic Therapeutics and Diagnostics V, p. 716105, Proceedings of SPIE, San Jose, CA, USA (2009).

136. R. Na, I. M. Stender, M. Henriksen and H. C. Wulf, "Autofluorescence of human skin is age-related after correction for skin pigmentation and redness," *J Invest Dermatol* **116**(4), 536-540 (2001)

137. R. Singh, A. Barden, T. Mori and L. Beilin, "Advanced glycation end-products: a review," *Diabetologia* **44**(2), 129-146 (2001)

138. J. L. Wautier and P. J. Guillausseau, "Advanced glycation end products, their receptors and diabetic angiopathy," *Diabetes Metab* **27**(5 Pt 1), 535-542 (2001)

139. R. Meerwaldt, T. Links, C. Zeebregts, R. Tio, J. L. Hillebrands and A. Smit, "The clinical relevance of assessing advanced glycation endproducts accumulation in diabetes," *Cardiovasc Diabetol* **7**(29 (2008)

140. S. J. Cho, G. Roman, F. Yeboah and Y. Konishi, "The road to advanced glycation end products: a mechanistic perspective," *Curr Med Chem* **14**(15), 1653-1671 (2007)

141. H. F. Bunn and P. J. Higgins, "Reaction of monosaccharides with proteins: possible evolutionary significance," *Science* **213**(4504), 222-224 (1981)

142. J. V. Valencia, S. C. Weldon, D. Quinn, G. H. Kiers, J. DeGroot, J. M. TeKoppele and T. E. Hughes, "Advanced glycation end product ligands for the receptor for advanced glycation end products: biochemical characterization and formation kinetics," *Anal Biochem* **324**(1), 68-78 (2004)

143. D. G. Dyer, J. A. Dunn, S. R. Thorpe, K. E. Bailie, T. J. Lyons, D. R. McCance and J. W. Baynes, "Accumulation of Maillard reaction products in skin collagen in diabetes and aging," *J Clin Invest* **91**(6), 2463-2469 (1993)

144. R. D. Semba, E. J. Nicklett and L. Ferrucci, "Does accumulation of advanced glycation end products contribute to the aging phenotype?," *J Gerontol A Biol Sci Med Sci* **65**(9), 963-975 (2010)

145. D. G. Dyer, J. A. Blackledge, S. R. Thorpe and J. W. Baynes, "Formation of pentosidine during nonenzymatic browning of proteins by glucose. Identification of glucose and other carbohydrates as possible precursors of pentosidine in vivo," *J Biol Chem* **266**(18), 11654-11660 (1991)

146. J. W. Nin, A. Jorsal, I. Ferreira, C. G. Schalkwijk, M. H. Prins, H. H. Parving, L. Tarnow, P. Rossing and C. D. Stehouwer, "Higher plasma soluble Receptor for Advanced Glycation End Products (sRAGE) levels are associated with incident cardiovascular disease and all-cause mortality in type 1 diabetes: a 12-year follow-up study," *Diabetes* **59**(8), 2027-2032 (2010)

147. M. W. Turner and B. Hulme, *Plasma proteins: an introduction*, Pitman Medical (1971).

148. J. Shaller, S. Gerber, U. Kaempfer, S. Lejon and C. Trachsel, *Human blood plasma proteins: structure and function*, Wiley (2008).

149. T. J. Peters, *All about albumin: biochemistry, genetics, and medical applications*, Academic Press, San Diego, CA (1995).

150. A. D. Association, "Executive summary: standards of medical care in diabetes--2011," *Diabetes Care* **34 Suppl 1**(S4-10 (2011)

151. M. L. Larsen, M. Hørder and E. F. Mogensen, "Effect of long-term monitoring of glycosylated hemoglobin levels in insulin-dependent diabetes mellitus," *N Engl J Med* **323**(15), 1021-1025 (1990)

152. T. Miyata, Y. Ueda, A. Yoshida, S. Sugiyama, Y. Iida, M. Jadoul, K. Maeda, K. Kurokawa and C. van Ypersele de Strihou, "Clearance of pentosidine, an advanced glycation end product, by different modalities of renal replacement therapy," *Kidney Int* **51**(3), 880-887 (1997)

153. D. R. Sell and V. M. Monnier, "Structure elucidation of a senescence cross-link from human extracellular matrix. Implication of pentoses in the aging process," *J Biol Chem* **264**(36), 21597-21602 (1989)

154. M. Sensi, F. Pricci, C. Pugliese, M. G. De Rossi, F. S. Celi, A. Cristina, S. Morano, D. Andreani and U. Di Mario, "Enhanced nonenzymatic glycation of eye lens proteins in experimental diabetes mellitus: an approach for the study of protein alterations as mediators of normal aging phenomena," *Arch Gerontol Geriatr* **15 Suppl 1**(333-337 (1992)

155. D. R. Sell, E. C. Carlson and V. M. Monnier, "Differential effects of type 2 (non-insulin-dependent) diabetes mellitus on pentosidine formation in skin and glomerular basement membrane," *Diabetologia* **36**(10), 936-941 (1993)

156. P. Ulrich and A. Cerami, "Protein glycation, diabetes, and aging," *Recent Prog Horm Res* **56**(1-21 (2001)

157. N. J. McIntyre, L. J. Chesterton, S. G. John, H. J. Jefferies, J. O. Burton, M. W. Taal, R. J. Fluck and C. W. McIntyret, "Tissue-Advanced Glycation End Product Concentration in Dialysis Patients," *Clinical Journal of the American Society of Nephrology* **5**(1), 51-55 (2010)

158. A. Goldin, J. A. Beckman, A. M. Schmidt and M. A. Creager, "Advanced glycation end products: sparking the development of diabetic vascular injury," *Circulation* **114**(6), 597-605 (2006)

159. A. Prasad, P. Bekker and S. Tsimikas, "Advanced Glycation Endproducts and Diabetic Cardiovascular Disease," *Cardiol Rev* (2012)

160. D. R. Sell, R. H. Nagaraj, S. K. Grandhee, P. Odetti, A. Lapolla, J. Fogarty and V. M. Monnier, "Pentosidine: a molecular marker for the cumulative damage to proteins in diabetes, aging, and uremia," *Diabetes Metab Rev* **7**(4), 239-251 (1991)

161. L. Y. Xu, L. Zhu, L. Zhang, F. Yu, Y. Liu, G. Zhang and L. S. Wu, "Design of advanced glycation endproducts fluorescence spectrum detecting system," *Guang Pu Xue Yu Guang Pu Fen Xi* **29**(8), 2298-2301 (2009)

162. E. Hull, M. Ediger, A. Unione, E. Deemer, M. Stroman and J. Baynes, "Noninvasive, optical detection of diabetes: model studies with porcine skin," *Opt Express* **12**(19), 4496-4510 (2004)

163. I. Nemet, "AGE database," p. 30, IMARS, http://www.imars.org/ (2008).

164. S. Taneda and V. M. Monnier, "ELISA of pentosidine, an advanced glycation end product, in biological specimens," *Clin Chem* **40**(9), 1766-1773 (1994)

165. R. H. Nagaraj, T. S. Kern, D. R. Sell, J. Fogarty, R. L. Engerman and V. M. Monnier, "Evidence of a glycemic threshold for the formation of pentosidine in diabetic dog lens but not in collagen," *Diabetes* **45**(5), 587-594 (1996)

166. J. R. Requena, D. L. Price, S. R. Thorpe and J. W. Baynes, "Measurement of pentosidine in biological samples," *Methods Mol Med* **38**(209-217 (2000)

167. J. R. Hoidal, "Reactive oxygen species and cell signaling," *Am J Respir Cell Mol Biol* **25**(6), 661-663 (2001)

168. R. Tuma, "The two faces of oxygen," *Sci Aging Knowledge Environ* **2001**(1), oa5 (2001)

169. M. Niedre, M. S. Patterson and B. C. Wilson, "Direct near-infrared luminescence detection of singlet oxygen generated by photodynamic therapy in cells in vitro and tissues in vivo," *Photochem Photobiol* **75**(4), 382-391 (2002)

170. H. Messmann, E. Endlicher, C. M. Gelbmann and J. Scholmerich, "Fluorescence endoscopy and photodynamic therapy," *Dig Liver Dis* **34**(10), 754-761 (2002)

171. J. Baier, T. Maisch, M. Maier, E. Engel, M. Landthaler and W. Bäumler, "Singlet oxygen generation by UVA light exposure of endogenous photosensitizers," *Biophys J* **91**(4), 1452-1459 (2006)

172. S. Mathai, T. A. Smith and K. P. Ghiggino, "Singlet oxygen quantum yields of potential porphyrin-based photosensitisers for photodynamic therapy," *Photochem Photobiol Sci* **6**(9), 995-1002 (2007)

173. S. Jockusch, N. J. Turro, E. K. Thompson, M. Gouterman, J. B. Callis and G. E. Khalil, "Singlet molecular oxygen by direct excitation," *Photochem. Photobiol. Sci.* **7**(235-239 (2008)

174. D. A. McQuarrie and J. D. Simon, *Physical chemistry: a molecular approach*, University Science Books, Sausalito, CA (1997).

175. L. Guo, C. N. Coretsopoulos and A. B. Scranton, "Measurement of the dissolved oxygen concentration in acrylate monomers with a novel photochemical method," *Journal of Polymer Science: Part A: Polymer Chemistry* **42**(1285-1292 (2004)

176. J. C. Dabrowiak, *Metals in Medicine*, John Wiley & Sons, Ltd, West Sussex, United Kingdom (2009).

177. W. Spiller, H. Kliesch, D. Wohrle, S. Hackbarth, B. Roder and G. Schnurpfeil, "Singlet oxygen quantum yields of different photosensitizers in polar solvents and micellar solutions," *Journal of Porphyrins and Phthalocyanines* **2**(2), 145-158 (1998)

178. C. Schweitzer and R. Schmidt, "Physical mechanisms of generation and deactivation of singlet oxygen," *Chem Rev* **103**(5), 1685-1757 (2003)

179. J. Kopecky, *Organic photochemistry: a visual approach*, Wiley-VCH Verlag GmbH, Weiheim (1992).

180. M. A. J. Rodgers and P. T. Snowden, "Lifetime of oxygen $O_2(^1\delta_g)$ in liquid water as determined by time-resolved infrared luminescence measurements," *J. Am. Chem. Soc.* **104**(20), 5541-5543 (1982)

181. J. G. Parker and W. D. Stanbro, "Optical determination of the rates of formation and decay of $O_2(^1\Delta_g)$ in H_2O, D_2O and other solvents," *Journal of Photochemistry* **25**(2-4), 545-547 (1984)

182. S. C. Ameta, P. B. Punjabi, C. S. Chobisa, N. Mangal and R. Bhardwaj, "Singlet molecular oxygen," *Asian Journal of Chemistry Reviews* **1**(2), 106-124 (1990)

183. C. Flors, M. J. Fryer, J. Waring, B. Reeder, U. Bechtold, P. M. Mullineaux, S. Nonell, M. T. Wilson and N. R. Baker, "Imaging the production of singlet oxygen in vivo using a new fluorescent sensor, Singlet Oxygen Sensor Green," *J Exp Bot* **57**(8), 1725-1734 (2006)

184. A. Gollmer, J. Arnbjerg, F. H. Blaikie, B. W. Pedersen, T. Breitenbach, K. Daasbjerg, M. Glasius and P. R. Ogilby, "Singlet Oxygen Sensor Green®: photochemical behavior in solution and in a mammalian cell," *Photochem Photobiol* **87**(3), 671-679 (2011)

185. X. Ragàs, A. Jiménez-Banzo, D. Sánchez-Garcá, X. Batllori and S. Nonell, "Singlet oxygen photosensitisation by the fluorescent probe Singlet Oxygen Sensor Green," *Chem Commun (Camb)* 20), 2920-2922 (2009)

186. X. Chen, X. Tian, I. Shin and J. Yoon, "Fluorescent and luminescent probes for detection of reactive oxygen and nitrogen species," *Chem Soc Rev* **40**(9), 4783-4804 (2011)

187. "Singlet Oxygen Sensor Green Reagent," M. Probes, Ed., pp. 1-2, http://tools.invitrogen.com/content/sfs/manuals/mp36002.pdf (2004).

188. H. J. Lee, M. H. Lee, S. G. Han, H.-Y. Kim and Y. H. Won, "Photo-oxidation in the photobleaching process of a non-linear optical polymer," *Thin Solid Films* **283**(1), 247-250 (1996)

189. N. B. Vicente, J. E. Diaz Zamboni, J. F. Adur, E. V. Paravani and V. H. Casco, "Photobleaching correction in fluorescence microscopy images," *Journal of Physics: Conference Series* **90**(012068 (2007)

190. L. Song, E. J. Hennink, I. T. Young and H. J. Tanke, "Photobleaching kinetics of fluorescein in quantitative fluorescence microscopy," *Biophys J* **68**(6), 2588-2600 (1995)

191. Z. Matuszak, M. A. Bilska, K. J. Reszka, C. F. Chignell and P. Bilski, "Interaction of singlet molecular oxygen with melatonin and related indoles," *Photochem Photobiol* **78**(5), 449-455 (2003)

192. N. Soh, "Recent advances in fluorescent probes for the detection of reactive oxygen species," *Anal Bioanal Chem* **386**(3), 532-543 (2006)

193. W. Y. NG and J. Walkley, "Diffusion of gases in liquids: the constant size bubble method," *Canadian Journal of Chemistry* **47**(1075-1077 (1969)

194. D. B. Nowak, A. J. Lawrence and E. J. Sánchez, "Apertureless near-field/far-field CW two-photon microscope for biological and material imaging and spectroscopic applications," *Appl Opt* **49**(35), 6766-6771 (2010)

195. S. W. Hell, M. Booth, S. Wilms, C. M. Schnetter, A. K. Kirsch, D. J. Arndt-Jovin and T. M. Jovin, "Two-photon near- and far-field fluorescence microscopy with continuous-wave excitation," *Opt Lett* **23**(15), 1238-1240 (1998)

196. J. D. Ingle and S. R. Crouch, *Spectrochemical Analysis*, Prentice Hall, Englewood Cliffs, NJ (1988).

197. O. K. Baskurt, O. Yalcin, F. Gungor and H. J. Meiselman, "Hemorheological parameters as determinants of myocardial tissue hematocrit values," *Clin Hemorheol Microcirc* **35**(1-2), 45-50 (2006)

198. J. W. McMurdy, G. D. Jay, S. Suner and G. Crawford, "Noninvasive optical, electrical, and acoustic methods of total hemoglobin determination," *Clin Chem* **54**(2), 264-272 (2008)

199. V. Twersky, "Absorption and multiple scattering by biological suspensions," *J Opt Soc Am* **60**(8), 1084-1093 (1970)

200. Q. J. Milner and G. R. Mathews, "An assessment of the accuracy of pulse oximeters," *Anaesthesia* **67**(4), 396-401 (2012)

201. S. J. Barker and K. K. Tremper, "Pulse oximetry: applications and limitations," *Int Anesthesiol Clin* **25**(3), 155-175 (1987)

202. E. Gayat, A. Bodin, C. Sportiello, M. Boisson, J. F. Dreyfus, E. Mathieu and M. Fischler, "Performance evaluation of a noninvasive hemoglobin monitoring device," *Ann Emerg Med* **57**(4), 330-333 (2011)

203. G. Gutierrez, H. D. Reines and M. E. Wulf-Gutierrez, "Clinical review: hemorrhagic shock," *Crit Care* **8**(5), 373-381 (2004)

204. B. R. Soller, Y. Yang, O. O. Soyemi, K. L. Ryan, C. A. Rickards, J. M. Walz, S. O. Heard and V. A. Convertino, "Noninvasively determined muscle oxygen saturation is an early indicator of central hypovolemia in humans," *J Appl Physiol* **104**(2), 475-481 (2008)

205. American National Standards Institute (ANSI), "Safe use of lasers in health care," pp. ANSI Z136.133-2011 (2011).

206. A. Rosenberg and D. Clark, "manuscript in preparation," (2012).

VITA

NAME OF AUTHOR: Bin Deng

PLACE OF BIRTH: Luoyang, Henan, China

EDUCATION:

- Bachelor of Science in Biomedical Engineering, 2004, Tianjin University
- Master of Science in Measuring and Testing Technology and Instrument, 2007, Tianjin University

AWARDS AND HONORS:

- 1999   Academic Excellence Award, Tianjin University
- 2004-2006   Merit Student Scholarship, Tianjin University
- 2009-2011   WiSE Future Professoriate Program Award , Syracuse University

PROFESSIONAL EXPERIENCE:

- 2007-2008   Teaching Assistant, Department of Biomedical and Chemical Engineering, Syracuse University

- 2010   Teaching Assistant, Department of Chemistry, Syracuse University
- 2010-2012   Vise President, Student Chapter of Society for Biomaterials, Syracuse University

CONFERENCE ATTENDED:

- SPIE Photonics West – BiOS, San Francisco, CA, Jan 23-28, 2010
- XXII ICORS, Boston, MA, August 8-13, 2010
- SPIE Photonics West – BiOS, San Francisco, CA, Jan 21-26, 2012

PUBLICATIONS:

1. **Bin Deng**, Anabel Simental , Patrick Lutz, George Shaheen, <u>Joseph Chaiken</u>, Singlet oxygen induced advanced glycation endproduct photobleaching of in vivo human fingertip autofluorescence, Proc. of SPIE, Vol. 8219, 82190D, 2012

2. <u>Joseph Chaiken</u>, **Bin Deng**, Jerry Goodisman, George Shaheen, Rebecca J. Bussjager, Analyzing near infrared scattering from human skin to monitor changes in hematocrit,

Proc. of SPIE, Vol.8219, 821908, 2012

3. Joseph Chaiken, **Bin Deng**, Jerry Goodisman, G. Shaheen, R. J. Bussjager, Analyzing near-infrared scattering from human skin to monitor changes in hematocrit, Journal of Biomedical Optics, 16(9), 097005, 2011

4. Tarun Saxena, **Bin Deng**, Dennis Stelzner, Julie Hasenwinkel, Joseph Chaiken, Raman spectroscopic investigation of spinal cord injury in a rat model, Journal of Biomedical Optics, 16(2), 027003, 2011

5. Tarun Saxena, **Bin Deng**, Kyle Hoellger, Eric Lewis-Clark, Julie M. Hasenwinkel, Joseph Chaiken, Near infra-red Raman spectroscopic study of reactive gliosis and the glial scar in injured rat spinal cords, Proc. of SPIE, Vol.7560, 75600I, 2010

6. **Bin Deng**, Colin Wright, Eric Lewis-Clark, George Shaheen, Roman Geier, Joseph Chaiken, Direct noninvasive observation of near infrared photobleaching of autofluorescence in human volar side fingertips in vivo, Proc. of SPIE, Vol. 7560, 75600P, 2010

7. Joseph Chaiken, **Bin Deng**, Rebecca J. Bussjager, George Shaheen, David Rice, Dave Stehlik, John Fayos, Instrument for near infrared emission spectroscopic probing of human fingertips in vivo, Review of Scientific Instruments, 81, 034301, 2010

8. Joseph Chaiken, Jerry Goodisman, **Bin Deng**, Rebecca J. Bussjaeger, George Shaheen, Simultaneous, noninvasive observation of elastic scattering, fluorescence and inelastic scattering as a monitor of blood glow and hematocrit in human fingertip capillary beds, Journal of Biomedical Optics, 14(05), 050505, 1st Sep. 2009

9. Wenliang Chen, **Bin Deng**, Rong Liu, Xiaoyu Gu, Kexin Xu, Methodology of effective glucose-specific signal extraction in complicated sample, Proc. of SPIE, Vol. 6445, 64450L, 14th Feb. 2007

10. Xiaoyu Gu, **Bin Deng**, Lin An, Wenliang Chen, Kexin Xu, The feasibility investigation of non-invasive blood glucose sensing based on near-infrared spectroscopy, Proc. of SPIE, Vol. 6094, 60940J, 27th Feb. 2006

11. Rong Liu, **Bin Deng**, Wenliang Chen, Kexin Xu, Next step of non-invasive glucose monitor by NIR technique from the well controlled measuring condition and results, Optical and Quantum Electronics, 37, 1305-1317, 2005